Università di Modena e Reggio Emilia

Dipartimento di Scienze Fisiche, Informatiche e Matematiche

Corso di laurea Magistrale in Fisica

Towards Spin-resolved/Time-resolved Photoelectron Spectroscopy at the fs time scale: construction and commissioning of the ULTRASPIN apparatus

Relatore:
Chiar. mo Prof. Sergio Valeri

Correlatore:
Chiar. mo Prof. Giorgio Rossi

Autore:
Tommaso Pincelli

Anno Accademico 2013/2014

Contents

Introduction

This thesis reports on the construction and commissioning tests of the novel experimental set-up needed for a long term research project, named ULTRASPIN, aiming at establishing time resolved spin-resolved photoemission measurements with ultra-short (10^{-14} s) photon pulses from Free Electron Laser beamlines or from table-top UV/Soft-X beamlines.

The ULTRASPIN project started in the summer 2013, building on competences and instrumentation in part available from the APE-beamline group of IOM-CNR at Elettra, and with the partial support of an European contract (EXSTASY-EXperimental STation for the Analysis of the Spin Dynamics, Grant agreement N.PIIF-GA-2012-326641) and related fellowship of a world-expert of Mott scattering.

I have been involved from the beginning in the final design, in the construction and commissioning of a novel stray-field free UHV apparatus for preparing and hosting atomically clean surfaces and for measuring the spin-polarization of the photo-emitted electrons with "single pulse" sensitivity down to the 10^{-14} s time scale, as well as in the standard high frequency spectroscopy mode. In the commissioning phase I have participated to test experiments on ULTRASPIN as well as to relevant experiments conducted in other apparatuses.

In the following chapter, a short description of the environment in which the ULTRASPIN project is set will be given, with an attention to the possible outcomes of such work. Finally, the range of the work described in this thesis will be defined, detailing its relevance in the project's context.

Photoemission

The broad area of spectroscopy in which the machine is expected to work is *X-ray photoelectron spectroscopy* from solid surfaces. This term defines the class of "photon-in, electron-out" techniques, where a source of photons of suitable energy illuminates a sample of interest and the resulting electrons ejected by photoelectric effect[1] are measured. This kind of experiments have to be performed in vacuum, because the mean free path of electrons is very short in air at ambient pressure, and in fact in Ultra High Vacuum

[1]The study of photoelectric effect holds the legacy of an authoritative and noble line of research: it was experimetally discovered by H. Hertz [1] and was explained as a manifestation of the quantum nature of the light by Einstein in [2], one of the seminal papers published in the *annus mirabilis* 1905, and the only awarded with a Nobel prize in 1921.

(UHV) if one wants to retrieve signal from "atomically clean surfaces". One can think of the process in the time-dependent perturbation theory scheme.

- The initial states, remote in time and space from the interaction, are defined by the characteristics conferred to the photon beam and the physical state of the sample.
- During the interaction, the photon impinges on the target and is absorbed by an electron. If the photon energy is sufficient, the electron is excited from a core level into an empty band of the solid, travels towards the surface, crosses the surface barrier and is ejected in the free space.
- The ejected electron enters a continuum of states in which is freely propagating in vacuum. After a long time (with respect to the interaction duration) and far from the interaction region, the particle is detected.

The interaction process is, in general, very complicated, because the emitted electron interacts with the coulomb force and it is affected by virtually all the other charges in the solid. Thus all the processes to which the electron undergoes before emerging from the surface should be treated coherently as a single process, accounting for all the possible interactions. This single step picture can anyway be broken down in three basic steps, that can be described by the dominant processes intervening, in what is called the "three steps model":

1. electrons are photoexcited in the solid
2. electrons are transported to the surface of the solid
3. electrons cross the surface barrier and are emitted in vacuum.

if one supposes to consider only electrons that didn't interact again with the solid during the last two steps, the total energy, the total momentum and the total angular momentum are conserved, and the picture is greatly simplified. To achieve an insight in the sample intrinsic characteristics, it is then necessary to measure some of the characteristics of the initial or final states of the process. The free-particle states for photons and electrons posses in general four degrees of freedom: momentum, which is a three dimensional vector, and spin[2].

X-ray Photoelectron Spectroscopy

In what is called X-ray photoelectron spectroscopy (XPS), the photon energy, polarization and direction of incidence are kept fixed (i.e. the initial states) throughout the experiment, while the characteristics of the emitted electrons are resolved. In the chronological

[2]In sect.1.1 and sect.1.2 it is described how this fourth degree of freedom has been discovered for electrons. For photons the situation is slightly different, because they are vector bosons and therefore posses an integer spin which would be a three dimensional vector. The special relativity rules for a massless particle, however, force it to assume only the two values of ± 1, thereby making spin again a single degree of freedom.

development of this technique, the first characteristic to be studied was kinetic energy, in the work of Kai Siegbahn[3], who developed the double focusing magnetic analyser. The use of this system enabled him to select and send to an electron counter only particles within a very precise energy window (ΔE) centred on a selectable energy value (E), with a high resolution ($\Delta E/E = 10^{-4}$). This, and the use of a source with a relatively low spread in energy, allowed him to measure the first XPS spectrum in 1954.

In the simplified, non-interacting electron picture, it is straightforward to study the balance of energies for a photoemitted electron:

$$E_{kin} = h\nu - \Phi - |E_b| \tag{1}$$

where E_{kin} is the kinetic energy of the electron, $h\nu$ is the energy of the absorbed photon, Φ is the work function (the energy required to the electron to reach the vacuum level of the system) and E_b is the binding energy of the electron in the solid. As a matter of fact, two work functions are present: the one of the analyser (Φ_a) and the one of the sample (Φ_s). During the XPS experiment, the detector and the sample are in electrical contact, and thus their Fermi levels (and not their vacuum levels) are aligned: for this reason Φ_a and Φ_s can be different. The kinetic energy that is measured is the one of the vacuum states of the detector, and thus in Eq. 1 one must use Φ_a for Φ. The difference $\Phi_s - \Phi_a$ defines, instead, the minimum kinetic energy that can be measured (if $\Phi_s - \Phi_a \leq 0$ the minimum kinetic energy is zero).

An XPS spectrum is a plot of electron counts as a function of E, which is scanned in small steps in an interval defined by the experimenter. This curve presents a series of sharp peaks emerging from a smooth background. The main features of the spectrum can be understood by looking at Fig.1.

At lower kinetic energies (0-200 eV), a very broad peak with a high amount of counts is present. This is formed by electrons that have undergone many collisions before exiting the sample, and can not be treated in the "three steps model" picture. These electrons do not carry information retrievable in a single particle picture, because it is dissipated in various interactions. In intermediate energy regions, numerous sharp peaks are present on a smooth background. The peaks are originated from excitation of electrons from the core-levels of atoms in the solid, that have emerged from the sample without further interactions[4]. Finally, at energy close to the primary photon energy a very broad peak is present that terminates in a very sharp cut-off. This corresponds to emission from the valence band of the solid, and the cut-off is given by the Fermi level of the system.

As displayed in Fig. 1, the intensity of electron emission as a function of energy, in an angle integrated experiment, can be connected[5] with the *density of states* (DOS) of

[3]Prof. Siegbahn was awarded the Nobel prize in 1981 for his contribution in this field.

[4]The probability that an electron can emerge from the solid without interacting decreases rapidly (exponentially) as the distance from the surface (depth) increases. This is due to the fact that electrons in solids have relatively short mean free paths (see Fig. 6.6 in sect. 6.2.2), and electrons generated deeper than 5-10 nm give a very small contribution to the signal.

[5]The XPS signal, however, is determined also by many effects originated from the real physical process of photoelectron emission, such as inelastic secondary electron emission, spectral broadening due to analyzer resolution, etc. A more detailed description of these effects and how they are overcome is demanded to sect 6.2.2, where the use of this technique for characterization of samples is discussed.

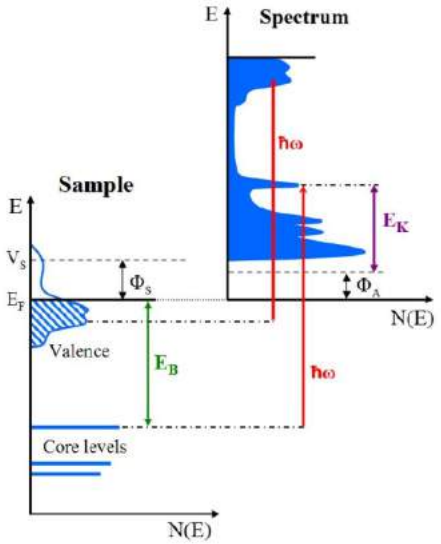

Figure 1. *Scheme expressing the concept of XPS. On the left, the DOS of the solid, on the right the resulting XPS spectrum. Adapted from [3].*

the solid. The DOS contains an extremely big amount of information, as the energy distribution of the core-levels is characteristic of each single element, and through an accurate exam it is possible to individuate the atomic species present at the surface and in the near surface region of the solid. Considering that the relative intensities through the atomic photoionization cross sections can be associated with the relative amounts of the different atomic species present in the sampled volume of the solid, XPS can be used to detect, non-distructively, the near surface composition of a sample. If the energy resolution of source and analyser is sufficient, it is possible to observe small modifications in the peaks (shifts in energy, lineshape variations) that are connected with the presence of different chemical or physical environments of the elements. For this reason, the technique was originally named ESCA (Electron Spectroscopy for Chemical Analysis).

The technique was diffused by Siegbahn's publications, and it rapidly became a widespread instrument for the surface analysis, in particular after the development of the electrostatic hemispherical analysers[6]. With its diffusion, XPS immediately started to be studied from many different points of view, triggering a long standing theoretical work aiming at describing and simulating the spectra with as much accuracy as possible. At the same time, on the experimental side, scientists started to push its limits, trying to widen the range of electron's characteristics measured simultaneously[7]. In the context of this expansion of XPS, the spin-resolution and angle-resolution are the most important

[6]For a more detailed description of these detectors see Chap. 3.

[7]Despite the undoubted charm and elegance of experiments that require only a very small amount of information extracted from the system to demonstrate a complete understanding of a phenomenon, these are generally the beautiful result of very rare conditions. In most of the cases, when a highly complex and not well understood process is under study, it is desirable to obtain an amount of information as rich as possible, and the modern technological advancements, that allow to control enormous fluxes of data, are more and more opening amazing possibilities in this sense.

progresses.

Spin resolution

Spin resolution is historically the first expansion of XPS[8], and yet probably one of the most challenging ones. The realization of spin polarimetry[9], i.e. the ability to select electrons on the basis of their intrinsic angular momentum state, is indeed very difficult, because it is not possible to apply the magnetic separation techniques that are used for neutral particles[10], and the development of efficient experimental techniques required a long and continued effort of experimentalists from all over the world, coupled with constant upgrading with the most recent technologies.

The implementation of spin resolution offers a great number of possibilities, that can be divided in two main classes:

1. The reconstruction of the density of states with spin resolution of the solid and of each element in it is possible. This allows to shed light on the magnetic interactions at a microscopic level: spin-orbit splitting of core-levels can be studied, eventually resolving peaks that in spin integrated spectroscopy are not easily distinguishable, or observing the modifications in the peaks shape and position when external physical and chemical conditions are varied. Another application consists in the study of exchange-split bands in ferromagnets, characterizing with a high precision the polarization at the Fermi energy. Finally the studies of effects arising from quantum confinement are of extreme interest and importance: the study of the surface states of magnetic and non-magnetic materials, the effects of adsorbates, the modifications induced by nanopatterning or nanoislands and the investigation of quantum well states are only some of the potentialities of this technique[11].

2. The study of the very low energy end of the secondary electrons peak ($E_k = 0 - 10\ eV$), instead, contains very valuable informations on the incoherent transport inside a material. In this range, in fact, are present electrons which have undergone a high number of interactions with the solid. This allows to evaluate the mean free path of electrons with spin resolution, that can be extremely different both in magnetic and in non-magnetic materials.

Both these areas of application have recently witnessed a huge raise in interest. Since the advent of spintronics[12], the new development of electronics in which the carriers spin is used to carry information (in particular, to read and to record permanently the data bits), indeed, the attention to the spin polarized states close to the Fermi energy has increased significantly. These particular states are, in fact, involved in transport of electrons across

[8] See Chap.1.
[9] Described accurately in Part I of this thesis.
[10] See Sect.1.2.
[11] For an accurate review, combined with an extremely deep insight on the technique, one can refer to [4]. For a more sketchy, but more up to date discussion, [5].
[12] See [6].

the material, and the present ability in controlling materials both geometrically and chemically, combined with the knowledge that can be retrieved with the use of these techniques, holds promises for extraordinary technological improvements.

Angle resolution

The second expansion of XPS consists in the resolution of the momentum of electrons: not only the kinetic energy is detected, but the complete $\mathbf{k}$ vector in the three dimensions. The technique is called Angle Resolved Photoelectron Spectroscopy (ARPES)[13], because the implementation of momentum resolution boils down to a symultaneous measurement of kinetic energy and angle of emission of electrons. Indeed, if one considers step 1 of the three steps model, the conservation laws hold, besides Eq. 1, also:

$$\mathbf{k}_f - \mathbf{k}_i = \mathbf{k}_{ph} \tag{2}$$

i.e. the difference between electron's momentum in the initial ($\mathbf{k}_i$) and final ($\mathbf{k}_f$) state must equal the photon momentum ($\mathbf{k}_{ph}$). Usually, however, most of the ARPES experiments are performed with a relatively low energy primary photon (100-10 eV), which has negligible momentum with respect to electrons'. Eq. 2 can then be rewritten as:

$$\mathbf{k}_f = \mathbf{k}_i \tag{3}$$

i.e. the three-dimensional momentum is conserved in the photoexcitation process. Step 2 of the model accounts for the extreme surface sensitivity of ARPES: electrons in the range 10-100 eV have the shortest mean free path in solids, and most of the signal comes from the topmost two or three atomic layers. Finally, step 3 defines what actually can be observed in an experiment: the surface breaks the translational symmetry, creating a potential step in the vertical (z) direction. For this reason, the momentum that can be measured by the detector does not retain explicitly the full three dimensional information of step 1, but loses information on k_z[14].

These details make ARPES particularly suited for the study of dispersion relations of the valence bands in 2-dimensional structures, such as surfaces, ultra-thin films, etc. The sensitivity to the low-binding energy part of the spectrum allows ARPES to assess low-energy single-particle and collective excitations, a powerful insight on the effects that determine the solid propertiers in the most common (and realizable) conditions[15]. The great amount of information that can be collected may be organized in many different ways, giving importance to different characteristics of the solid: one particularly interesting method is to reconstruct the density of states at the Fermi energy in the Brillouin zone (2D or 3D). This procedure, called *Fermi surface mapping* is of extreme relevance for the

[13] [7], [3], [8].

[14] The k_z component can anyhow be retrieved by the use of some assumptions on the dispersion of the free-electrons propagating to the analyser and writing k_z as a function of the other quantities that can be measured during an experiment. This method requires anyway the use of fitting techniques, and, particularly when the parabolic assumption is made, is not always adhering to the experimental reality.

[15] For example ARPES is an invaluable tool for the study of complex superconducting materials, able to individuate the superconducting gap [8].

understanding of the transport, and is a very powerful instrument for advanced electronics research.

Experimentally, the momentum resolution is achieved by the use of electrostatic spectrometers that (besides the pass energy) are able to select the angle of emission, counting only electrons taking-off with a very precise direction defined by two polar angles. Modern detectors do not require rotation of the sample (or of the spectrometer) for both angles to realize a complete characterization. The implementation of parallel acquisition electron counters mounted at the end of a large acceptance spectrometer, indeed, allowed for the acquisition of 2D snapshots, in which energy is dispersed along one direction and one component of momentum along the other. This development of the detectors, that improved significantly the resolution and at the same time reduced the duration of the experimental routine, gave significant impulse to this technique, which achieved results of extraordinary scientific relevance.

Angle resolution can be combined with spin resolution to realize a so-called *Complete Photoemission Experiment*[16]. This name is originated from the fact that in such kind of measurements all the four degrees of freedom of the emitted electrons are measured, thus completely determining the final states. Only few of these experiments and apparatuses have been realized up to now, but the strong demand by the research on spintronics is now triggering the realization of new experimental set-ups and some are already in commissioning. The possibilities given by this technique are extremely wide, and allow to observe absolutely new phenomena in solids, such as the appearance of spin-orbit split surface states in non-magnetic materials (Rashba Effect [10]).

Sources

The sources used for XPS have a huge impact on the overall performance of the experiment: a lack of monochromaticity[17] imposes an intrinsic loss of sensitivity to electrons' energy shifts, a lack of intensity[18] reduces the stoichiometric sensitivity according to the photoionization cross sections, the *brilliance*[19] allows to concentrate the intensity on small surface areas therefore favouring the angular resolution, i.e. the parallel momentum resolution. Two kinds of X-ray sources have been developed to maximize brilliance, and are used to measure XPS.

The first class of sources, by chronological order and by diffusion in laboratories all over the world, is the X-ray tube. The electrons emitted by a heated cathode are accelerated to hundreds of keV, and impact on an anode made of (or covered with) a highly pure

[16] [9],[10],[11].

[17] i.e. a source that produces photons in a wide range of energies, introducing an indetermination on the excitation energy.

[18] i.e. the source generates a small flux of photons [W/m^2].

[19] The term brilliance (or *brightness*) indicates a very precise quantity, which is the number of photons delivered by the source per unit time, per unit solid angle and per unit area in a bandwidth (BW) of 0.1% of the central energy [$ph/(s\ sr\ m^2\ BW\ 0.1\%)$]. This means that, the higher the brilliance, the higher is the flux of photons concentrated in a small area, with a small angular divergence, and very close in energy to the central value. This number sums-up many of the required characteristics of a photon source. In the rest of the text, the sake of readability, these units of measurement will be omitted, as there won't be ambiguity.

material. The electron excite strongly the atoms of the material, generating X-ray emission from the core levels, which has a characteristic energy. The main limit of these sources is the stopping of electrons in the anode: the electrons are slowed down and thus lose energy by *bremsstrahlung*, generating a very broad photonic background and, at the same time, deliver a significant load of thermal power on the anode. The local increase of temperature limits strongly the maximum working power that an X-ray tube can achieve before undergoing damages on the anode. Several solutions have been experimented to increase the maximum working power, such as anode cooling, rotating anode or metal jet methods. The maximum brightness obtained from these systems is between 10^8 and 10^{10}, depending on the design. Where a high energy resolution is required, techniques, appropriate for the wanted wavelength, are employed.

The second class is formed by the three generations of synchrotron radiation (SR) sources. They are all based on the emission of X-rays generated in an ultrarelativistic electron when its trajectory is bent[20]. Originally [13], the radiation was extracted from e^+ - e^- colliders, i.e. accelerators designed for high energy physics experiments (*first generation*). Then *storage rings* of larger size with extended straight section were used both for high energy collisions and for installing *insertion devices* to complement the *bending magnet sources* in the parasitic mode of operation of synchrotron radiation as well as in the dedicated runs (*second generation*). The light emitted by electrons passing through a bending magnet is extremely intense, has a very low angular spread and is focussed in a very sharp beam, but it possesses an extremely broad spectrum and must be monochromatized before the use for XPS. Despite the reduction of intensity associated with the selection of only a part of the spectrum, bending magnets achieve extremely high brilliances[21], from 10^{11} to 10^{15}.

The great success of the synchrotron radiation spectroscopy and X-ray scattering has promoted the so called *third generation* of storage rings entirely designed for optimal SR production, with further development of insertion devices. These systems allow electrons to undergo many deflections in a sinusoidal fashion, so that the average trajectory is straight: initially thought as a way to increase the number of emission points in a single accumulation ring[22], they turned out to have an incredibly deeper impact on X-rays generation and control. In particular *undulators*, formed by arrays of permanent magnets that can be moved closer to or further from the beam, generate an oscillatory path with a very small amplitude, so that the electron bunches and the photons propagate almost collinearly. The radiation emitted in the various points of the trajectory can thus interfere constructively or destructively, giving raise to a spectrum in which the intensity is concentrated in a very sharp peak (*fundamental*) and a few integer multiples (*harmonics*). The radiation still needs to be monochromatized, but here most of the power carried by the accelerated electrons is concentrated around the energy of interest, giving a very high

[20] A very long discussion should be started here, in order to give appropriate space to the knowledge on this matter that the beamline staff transferred to me. However, the aim of this chapter is not to describe in detail the operation of a synchrotron. For a very complete description of the complex mechanisms involved in the working of such big facilities, see [12].

[21] Not to mention the advantages of having a tunable source of X-rays: the chance to use the desired primary photon energy opens a great number of different possibilities for the experimenter.

[22] The first insertion devices, indeed, where *wigglers*, i.e. arrays of strong electromagnets, that generated radiation with characteristics very similar to the one from bending magnets.

brightness (up to 10^{21}). The tunability, great advantage of free-electron sources, is anyhow not lost: the fundamental's energy is dependent on the characteristics of the path and mechanical movements of the magnets allow to shift it to higher or lower values[23]. The radiofrequency power transferred to the electron beam to maintain it into the storage ring determines a pulse structure (bunches) of the current and therefore of the synchrotron radiation emission. It must be noted that a synchrotron is a pulsed source. The typical bunch length of the electron current translates in photon burst durations of the order of 10^{-11} s 10^{-12} s (or picoseconds ps).

The extraordinary achievements in the manipulation of X-ray photons, however, have proceeded much further than the realization of third generation synchrotron sources: these years are witnessing a revolution towards the delivery of spatially coherent, highly brilliant (up to 10^{35}), ultrashort (down to few tens of femtoseconds) radiation pulses. This will allow all the techniques based on photoexcitation to expand in a new direction: the *time resolution*.

Time resolution

Time resolution is the experimental approach to identify non-equilibrium transient effects by probing the electronic, optical, magnetic, structural properties of matter with ultrashort pulses whose duration selects a "stage" in a transient phenomenon that occurs more slowly. The key experimental feature that enables time resolution is the duration of the energy pulse that probes the matter: conventional synchrotron radiation beamlines deliver pulsed radiation with 50ps-long pulses (minimum time resolution) and 500 MHz repetition rates (few ns intervals in between pulses). Laser sources operate ps or shorter pulses, down to fs and as. Nowadays table-top laser sources can reach the UV and soft-X energy range with 10-100 fs pulse duration and KHz or higher repetition rates. Free Electron Lasers can generate X-rays with 10-100 fs duration and 10-120 Hz repetition rates. The superconducting accelerator of teh XFEL will yield SASE pulses at 4.5 KHz.

The photoemission process[24] excites the bound electron very rapidly (less than one femtosecond, 1 $fs = 10^{-15}s$) in the free space: for this reason, the shortening of the pulse allows to obtain an XPS signal coming from a very precise instant[25]. This is therefore a resolution originated uniquely by the characteristics of the source, and does not hold information on the final states (that are still supposed to be steady, plane waves), but rather on the particular transient condition of the system: the state of the solid is sampled on a timescale which can be smaller than the times typical of nuclear motion and thus it is possible to "freeze" even non-equilibrium states.

When a solid is suddenly put under new physical or chemical conditions, it reacts by

[23]These are the state of the art sources of SR. A general upgrade to the novel design for high-brilliance (low emittance) rings based on multiple-bend achromat magnetic lattices is underway or planned for the next few years.

[24]Photoemission is only one of the processes that are used in time resolved techniques: photon-out spectroscopies (ranging from time resolved optical reflectivity measurements to ultrafast XRD) have an even wider application, as the implementation is often simpler.

[25]Intended here as a time interval much shorter than the duration of the examined processes, and thus approximable as a point-like event.

relaxation, i.e. it reaches the closest accessible relative minimum in the total internal energy landscape. This is called a stable equilibrium if the achieved minimum is absolute, or meta-stable equilibrium if the minimum is only local. Meta-stable equilibrium states have a well-defined lifetime i.e. the system remains in the state only for a finite time, and then it relaxes back to a stable equilibrium. Meta-stable equilibria are generally formed when the fastest relaxation process is suppressed, and the system can reach stability only through processes that have a lower probability. The typical times and channels of relaxation vary widely, because a solid is a complex and often highly correlated material, possessing a high number of degrees of freedom.

Photoemission experiments without a pulsed source are made under the assumption that if the experimenter varies the physical or chemical surroundings, the system will be measured once it has reached the stable equilibrium, or at least a very long-lifetime metastable configuration, and the transient relaxation process can not be observed. But if the source is pulsed, and the delay between the modification of the external conditions and the X-ray pulse can be controlled accurately on the scale of femtoseconds, most of the relaxation processes can be followed during their evolution: only the fastest electronic processes are one order of magnitude faster, and happen on the timescale of hundreds of attoseconds[26] ($1\ as = 10^{-18} s$).

Thus time resolution is achieved if:

1. the system is driven out of the equilibrium very rapidly
2. the time required to probe the state of the solid is very short
3. the delay between the the excitation of the system and its measurement can be controlled to a high degree.

the most widespread method to achieve this is the *pump-probe method*: the system is excited by a *pump-pulse* that "prepares the sample in an excited state" (e.g. an infrared fs-laser pulse to excite phonons) and it is subsequently probed by a controllably delayed *probe-pulse* (e.g. a soft X- ray or XUV radiation pulse to excite final states measureable in the laboratory). In many situations the two pulses come from the same *femtosecond laser system* (the *master oscillator*); the wavelenghts can be modified by non-linear optics or by harmonic-generation in gases, and the relative delay is generated by sending the photon beams to different optical paths, adjustable by motorized optical elements[27]. The repetition rate of any kind of femtosecond laser, anyhow, does not allow to record the full time-evolution of the system after a single excitation: instead, the system is measured only one time after pumping, at a specific delay; then the delay is changed, and the system is re-prepared by another pump pulse. The measurement is, therefore, based on

[26] The most recent developments of XPS spectroscopy have already started to explore even this regime, achieving a stunning time resolutions of few as [14], [15]. When breaking below the limit of the fs scale, however, the XPS technique is changed very deeply, because the evolution of the same photoemission process has these characteristics times (for example, in [15] the different times required for electrons from different parts of the spectrum to reach the surface are measured). As a matter of fact, the so called "attosecond science" is now focussing more in deepening the comprehension of the dynamics of the photoemission process, rather than studying solids' behaviour.

[27] At the speed of light in vacuum, a difference of 1 μm corresponds to a delay of 3.3 fs.

a silent assumption that each time the system is pumped, it is excited always in the same condition, but as long as transient and non-linear processes are involved in this experiments, it is possible that this hypothesis is not satisfied: careful attention must be paid to the experimental condition in order to have reproducible data.

Femtosecond lasers

The realization of femtosecond time-resolved XPS experiments is a rather difficult task, because the generation of ultra short pulses is achievable only through the advanced optical control guaranteed by laser systems. On the other hand, however, the processes that can generate the short wavelengths needed are very few[28]. It is very useful to give a sketch of their characteristics here.

The most common system is a table-top solid state femtosecond laser. This system is formed by few main components.

1. *Oscillator*. It is the laser that generates the first ultrashort pulse. It consists of a normal laser cavity, in which the laser crystal[29] is placed between two mirrors. The output mirror is called *output coupler* and is partially transmissive. For the realization of ultrashort pulses, usually *passive mode-locking* is employed: the mirror at the back of the cavity is made of a particular material, called *saturable absorber* (SA). This is a medium that is absorbing in most conditions, except when the laser light achieves an intensity higher than a certain value (*saturation intensity*): in this conditions, it abruptly becomes strongly reflective. In this way, the SA mirror turns off the cavity emission unless a pulse of sufficient intensity hits its surface, thus actually shaping the cavity emission in ultrashort bursts. Thanks to advanced optical techniques the central wavelength of these pulses can be tuned in the infrared range, between 650 nm and 1100 nm, with typical values around 800 nm.

2. *Amplifier*. The pulse generated by the oscillator is still too weak to give the high brightness required in XPS experiments, and requires amplification. This stage is normally realized through the use of *chirped-pulse amplifiers*. These systems, generally also based on a Ti:sapphire crystal pumped by a green laser, exploit the huge gain bandwidth of the crystal to achieve enormous increase in intensity[30]: before entering in the amplifier the pulse is stretched in time in a controlled way[31], then it is amplified through several pass in the laser crystal[32], and then is compressed again[33] to femtosecond durations. The introduction of a chirped pulse allows to

[28] As noted before, the time structure of synchrotron radiation can achieve at best 1-10 *ps* time resolution.

[29] The laser crystal is the optical element in which the stimulated emission is produced. For these systems it often consists of a Ti-doped sapphire (Ti:sapphire) crystal, although also other materials are used, ranging from doped optical fibres to garnet crystals. The population inversion necessary for lasing is achieved by optical pumping with a continuous wave green laser (around 532 nm).

[30] It is possible to generate pulses of few mJ energy and fs duration, i.e. peak powers of several terawatts.

[31] The pulse is spread over durations of a nanosecond, distributing the shorter wavelength first and the longer last (*chirp*) by the use of controlled dispersion. This operation is performed by an element called *stretcher*

[32] The laser cavity is gated by an optical switch: the experimenter can decide how many trips the pulse makes in the cavity before being sent out.

[33] By a *compressor*, with an opposite dispersion to the *stretcher*.

realize very high amplifications without the occurrence of non-linear distortions or crystal damage.

3. *Beam splitter.* A passive optical component that divides the beam in two synchronized beams. Depending on the applications the repartition of the intensities can vary. Generally the highest is used for the probe pulse, because the up-conversion of photons energy induces a very significant loss of intensity.

4. *Delay-line.* One of the two beams is sent through a motorized system with two fixed mirrors and two moving mirrors that create a "U" path, in which the length of the vertical traits can be controlled. This determines the pump-probe delay.

5. *Frequency up-conversion stage.* The probe pulse is at this point still in the infrared range, not sufficient to overcome the work function of the solid. Thanks to the strong non-linearities that can be achieved with the use of high power ultrashort pulses, anyway, it is possible to increase the central wavelength of the pulse by the generation of harmonics, at the price of a strong reduction of intensity. The techniques will be described in the following paragraphs.

6. *Realignment and focussing optics.* The two beams are then focussed appropriately. The pump beam must be much wider than the probe beam, both because the probe must sample only an area with uniform density of excitation, and because the an excessively focused power can permanently damage the sample. Generally, a high collinearity is also required, because different incidence angles generate a lower time resolution. The two beams are sent trough a series of optical elements (designs vary) that allow to achieve the desired configuration.

Harmonics Generation

Solid state One of the ways to generate UV light is through the use of particular non-linear effects in crystals with broken inversion symmetry. In these systems is possible, under appropriate optical conditions, that the wave impinging on the lattice excites a non-linear dielectric polarization wave[34] part of which oscillates at a double frequency of the external field, and radiates consequently. This is called *second harmonic generation* (SHG). If the phase of such emission is accurately tailored throughout the medium so that the emission always adds up constructively (i.e. *phase matching* is realized), the process can be highly efficient and does not significantly effects the beam parameters, both in terms of the pulse duration and bandwidth and in terms of geometrical and coherence properties. The output beam contains anyway a remaining part of the primary beam that must be separated trough some form of monochromatization.

[34]Here non-linear is used in the sense that the relationship between the polarization vector $\mathbf{P}$ and the external electric field $\mathbf{E}$ is not linear as usually assumed: one must consider

$$P_i(t) = \sum_j \chi_{ij} E_j(t) + \sum_{j,k} \chi^{(2)}_{ijk} E_j(t) E_k(t)$$

and the $\chi^{(2)}$ tensor gives the non-linear effects.

Second harmonic generation from a 800 nm ($h\nu = 1.5\ eV$), giving 400 nm ($h\nu = 3\ eV$) is not sufficient, however, to overcome the typical work function of a metal (4-5 eV). For long time experiments were performed using the Two-Photon-Photoemission (2PPE) technique, in which the electrons having absorbed two photons are observed. This method, however, requires that the electrons are excited firstly in an empty state still bound to the solid, and then, through a second photoexcitation, are emitted in vacuum. This complicates severely the data analysis, because the density of the empty states is involved, because one of the two photons can be a pump photon, and because electronic relaxation processes can occur when the electron is in the empty states. Furthermore, the probability of 2PPE processes is very low, giving very low statistics. Recently the amplifiers have reached sufficient power that has become possible to cascade two SHG crystals to obtain FHG, achieving about 6 eV, sufficient to explore the upper limit of the valence band. The repetition rate of systems based completely on solid state is not limited by the frequency multiplication, and thus is dependent on the performance of the oscillator and amplifier: few systems can achieve even the MHz range, but normally it is limited to few kHz.

High harmonics generation from gases A radically different approach consists in the exploitation of non-linear effects in gases. As it was discovered in 1987 by McPherson et al. [16], if a laser pulse of sufficient intensity is strongly focussed (with optical intensities of $10^{14} W/cm^2$) on a low-pressure gas, the emitted spectrum results in a very peculiar structure, shown in Fig. 2 b, i.e. it presents strong peaks at odd harmonics of very high order (up to 50-60) of the driving laser frequency, all of them with intensity not decreasing significantly until a certain cut-off is reached, at which point it fades rapidly. The full explanation of this process that surprised the investigators at first [17], is based on a time dependent resolution of the Schrödinger equation and requires mostly the use of computation, but a classical picture that can give a sufficiently detailed picture has been developed and is depicted in Fig 2 a.

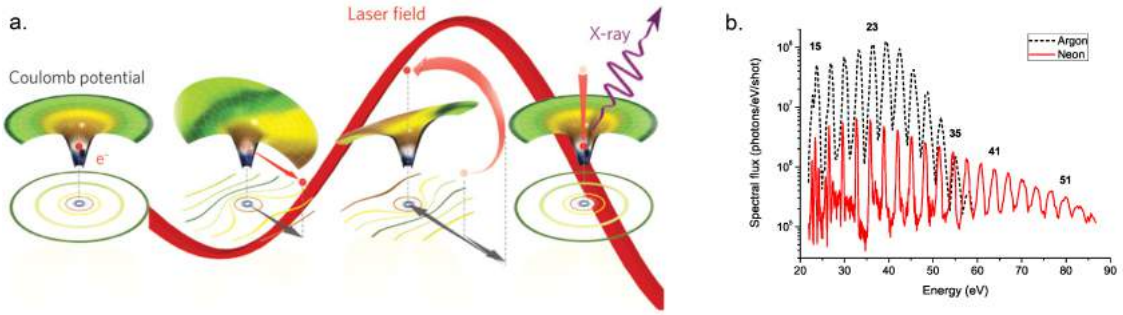

Figure 2. *a. Schematics of the classical interpretation of HHG process. [17] b. Typical spectrum of an HHG source in the XUV range, for different emitting gases, Argon (dashed black) and Neon (solid red) the cut-off is more evident for Argon [18].*

When the atom is exposed to the large oscillating field of the infrared pulse, its coulomb potential is severely distorted during the part of the optical cycle in which the electrical field is high. The distortion is sufficiently severe to generate a ionization of the atom, because an electron is able to escape the lowered barrier by quantum-mechanical tunnelling.

The free electron is then accelerated by the driving field, but soon the driving field enters a phase in which the electric vector is in the opposite direction, and the electron is accelerated back to the parent ion. If the driving field characteristics are set appropriately, there is then a high probability that the electron will recombine with the ion, decaying radiatively from the high kinetic energy state in which was driven by the external field. In this way the system generates a high number of odd-harmonics[35] of the driving frequency.

One must note that, being originated from a single optical cycle, the HHG bursts are most of the times shorter than the duration of the driving pulse: actually, the HHG method is the one that yields the highest temporal resolution ever reached, and theoretical studies hint at the possibility of it entering the zeptosecond range [19]. However, the laser pulses are limited by the fact that the shorter is their duration, the broader is their spectrum (*transform limit* or *Fourier limit*[36]): if one wants to concentrate the emission power in a small bandwidth (tenths of eV), then must accept lower time-resolutions (few fs).

The HHG, exactly as SHG, requires phase matching to be effective. This is realized by several different designs of the geometry with which the laser irradiates the gas. The most used ones are a differentially pumped gas cell or a hollow fibre with a continuous flow of gas: they both allow to achieve good phase matching without complicated optical manipulations, and can be used in vacuum. The UV-light and soft X-rays are in fact absorbed by air, and the optical system downstream to the HHG must be kept in high vacuum.

To realize photoemission, monochromatization is needed: the HHG pulse is then sent to a mirror monochromator[37] before being focussed on the sample. In this way, pulses of very short duration (tens of fs), low energy spread (tenths of eV), rather high energy (up to hundred of eV), high spatial and temporal coherence can be obtained. The repetition rate is slightly smaller than that of solid state frequency multiplication, because an excessive stimulation of the gas can destroy the delicate conditions in which the process is efficient, but it is anyway in the kHz range (normally between 5 and 10). The HHG holds now the potential to become very important complementary sources to those based on electron accelerators for the realization of photon-in spectroscopies.

Free-Electron Laser

A third method to obtain ultrashort laser pulses relies on a completely different approach. Originated from undulator radiation research in 1971 [20] and demonstrated with infrared radiation few years later [21], the Free-Electron Laser is a process of generation of highly coherent radiation by relativistic electron bunches in a linear accelerator. The sponaneous undulator radiation used by third generation synchrotron sources can, in fact, be still

[35] The harmonics are only the odd ones for symmetry reasons: the gas has an inversion symmetry that precludes even-harmonics generation.

[36] This is an unavoidable effect: the more the pulse is confined in time, the higher is the number of frequencies that must be superposed to create the sharp envelope curve. Ideally, only a stationary wave can be perfectly monochromatic.

[37] Monochromatization can significantly increase the time duration of a pulse. However, recently, special designs have been specifically developed [18] to keep to a minimum this effect, so that pulses limited only by the Fourier-transform relation can be obtained.

improved. If one considers the power emitted by an undulator, it can be written as [22]:

$$P \propto \left| \sum_{j=1}^{N} E_j \, e^{i\phi_j} \right|^2 = \sum_{j=1}^{N} E_j^2 + \left| \sum_{j=1}^{N} \sum_{k=1}^{N} E_j E_k \, e^{i(\phi_j + \phi_k)} \right|^2 \tag{4}$$

with $j \neq k$. Here ϕ_j are the relative phases of the emitted radiation electric fields E_j, with N number of electrons in the bunch. For the typical synchrotron undulator described above the phases are uncorrelated and thus the second term, containing a very relevant contribution (N^2 terms) is cancelled by destructive interference, and the total power is only the sum of the emissions from the N independent electrons. The FEL process manages to achieve a condition in which the phases are approximately identical for all the electrons, unlocking a gain of many orders of magnitude in brilliance and producing spatial coherence.

A FEL system presents three main elements: a photocathode, an high energy accelerator stage, and a very long undulator (or a sequence of them). In the photocathode, a UV laser generates very short free electron bunches (*macrobunches*), which are sent to the acceleration stage. Here the bunch is adjusted in geometrical shape, in angular and energy spread, and is accelerated to GeV energies. The high energy beam is then sent to a system of undulators. When travelling trough the periodic magnetic fields, the electrons interact with the light generated by the same bunch, slowly exchanging energy. It can be shown that electrons separated by half a radiation period have opposite rates of change, i.e. some are accelerated, some are slowed down [22].

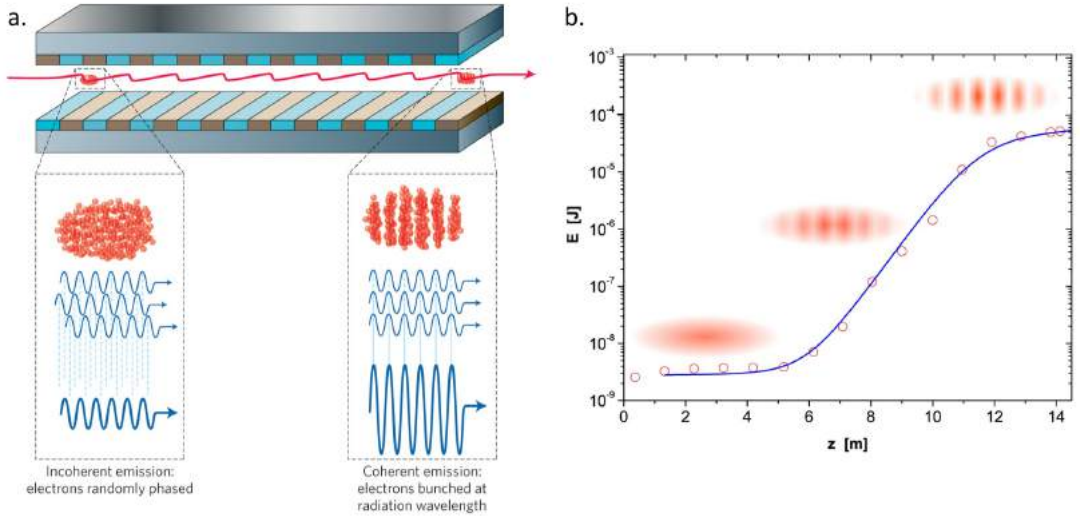

Figure 3. *a. Schematics of the FEL process. [22] b. Gain in intensity (energy per pulse) of emission from an electron as a function of the length travelled in a undulator, from DESY website.*

This process forces the electron macrobunch to subdivide into smaller bunches (*microbunches*) distanced by a radiation wavelength as shown in Fig. 3 a. The forces will initially be small, and in principle not able to effectively create a significant microbunching, but an even slight variation of the density of electrons in the macrobunch can trigger the

process[38] and the more the electrons are accumulated in the microbunches, the stronger the coherent emission (and therefore the bunching forces) will be, thus driving the system in an exponential positive feedback loop. The feedback will proceed (increasing emission of several order of magnitude) until the saturation is reached, as can be seen in Fig. 3 b. At this point all the bunches are separated ad emit coherently at the fundamental wavelength. The pulse duration depends on temporal length of the electron bunch (i.e. it spatial length in the direction of propagation divided by its velocity): trough particular sections of the accelerator called *bunch compressors*, pulses of less than 100 fs can be achieved.

As it can be seen from Fig. 3 b, it is necessary to use very long (even longer for higher energy X-rays: at XFEL the undulators are expected to reach more than 100 m) magnets arrays. This, combined with the fact that the bunches must have very high temporal compression that cannot be maintained if electrons pass many times per second in the undulators as in a circular accelerator would be, requires the accelerators used for FEL to be linear. Being such big facilities, the design of experimental access to the radiation is similar to synchrotron lightsources: once exited from the undulator, the photons are separated from the electrons by a magnet, and the laser beam is transported to few beamlines. Here, it is monochromatized[39], often characterized by non-destructive diagnostics, and focussed on the samples. Free-Electron Lasers, also called *fourth-generation lightsources* are then able to deliver a highly spatially coherent, highly brilliant, tunable ultrafast radiation. This is the only apparatus that can achieve, with these characteristics, the hard X-ray region. These sources are arising a widespread interest, and many of the big scientific facilities are operating, commissioning or designing one of such systems[40]. The repetition rate, however, is rather low, ranging from few tens Hz to hundreds Hz.

The perspectives for the realization of time resolved XPS rely mainly on two complementary sources, HHG lasers and Free-Electron lasers:

- HHG provides a table-top source that is very sharply time-resolved, possesses a good tunability, high spatial and temporal coherence and has an elevated repetition rate. It is however limited (in most of the cases) to the XUV range or very soft X-rays (it is very difficult to reach more than 100 eV) and in the photon flux.

- FEL radiation has a slightly lower time-resolution, a very-good (continuous) tunability and spatial coherence (temporal coherence is achieved only in seeded FELs). The repetition rate depends on the electron accelerator (from 10-120 Hz of "warm" accelerators to 4.5 MHz of "cold" superconducting accelerators like the EU-XFEL

[38] If this is generated by a spontaneous fluctuation in the macrobunch at the entrance of the undulator, the FEL is said to be in *Self-Amplified Spontaneous Emission* (SASE) operation. If, otherwise, a pulsed laser (for example from solid state sources) is sent in the undulator in coincidence with the macrobunch, this drives the microbunching process, and the FEL is in *seeded* operation. The seeded operation is far superior by temporal phase coherence and intensity stability, as shown by the performance of FERMI FEL-1 [23]; however it is very difficult to create seed lasers in the shortest wavelengths and thus for hard X-rays the SASE scheme is used.

[39] Having generally much longer pulse durations than HHG signals, the energy resolution can be much higher without reducing the time-resolution.

[40] For a comprensive table of the FEL facilities in the world, see the FEL table of the FEL project at UCSB.

under construction. The photon flux is extremely high and combined with outstanding brilliance. Finally FELs able to reach even hard X-rays are already operating (LCLS and SACLA) as well as under construction (EU-XFEL, Swiss-FEL).

ULTRASPIN Project

The ULTRASPIN project[41] aims at the realization of an experimental station dedicated to the study of ultrafast spin dynamics in solids by analysis of the spin polarization of the photoelectrons excited by individual XUV or soft X-ray pulses (from both FEL and HHG sources). The core instruments of the apparatus will be two:

- A four-axis Mott spin-polarimeter[42] working in a energy integrated mode (thereby operating in the class 2 of spin-resolved photoelectron spectroscopy, according to the classification described above) allowing for a full vectorial reconstruction of the spin-polarization vector both in the static and dynamic (with a pump-probe scheme) modes. In the expected regime of operation, the electrons photoemitted from the surface will be collected, focussed and accelerated in a periaxial beam by a system of electrostatic lenses. The particles will then scatter at high energy (40-50 keV) onto two orthogonal gold targets. The elastically backscattered electrons from each target are then counted by four high-speed detectors selecting right/left solid angles at 120° with respect to the incoming beams. Spin-polarization will then be assessed as an asymmetry in the counts of the relevant right/left couple of detectors, obtaining four vectorial projections of the three dimensional polarization vector (one component is redundant and used for intensity normalization between the two target scatterers). This system based on modifications of an existing apparatus already operational in spectroscopic mode at APE beamline, and implementing a completely new signal pick-up and amplification electronics, that can handle adequately the intense charge flux peak reaching the detectors after the short light bursts.

- A new apparatus able to retrieve the maximum amount of information from a single photoelectron pulse, detecting in a single shot the energy distribution (via time-of-flight, or TOF, energy analysis), the angular distribution (via two-dimensional parallel acquisition), and, on a successive step, spin. In the expected operation regime, the photoelectrons will be collected by a system of lenses that will image the sample on a two-dimensional detector. The electron bunch, initially of fs duration, will stretch to occupy few hundreds of nanoseconds when reaching the electron counter, as an effect of the free propagation of charges with different energies. The realization of a very fast two dimensional detector (i.e. able to acquire a full 2D image every few hundreds of picoseconds[43]) should then allow to acquire a standard

[41] The details of the Ultraspin project can be read in the attachment to the agreement between the two main collaborating institutions (Istituto Officina dei Materiali and Università di Roma Tre).

[42] A description of the principle of operation of these systems and of the state of the art in spin detectors will be given in Part I of this dissertation, in particular in sect. 2.3 and subsect. 3.1.1.

[43] The use in applications very close to this of such detector has already been demonstrated [24] and is based on the outstanding performance of a cross-delay anode detector.

XPS spectrum[44] or a complete ARPES spectrum[45] within a single electron shot. The further implementation of a spin-filtering method could allow to achieve simultaneous energy, angle, spin and time resolution. This system will be built from scratch (and at the moment of writing is still in the design phase), in a close collaboration between IOM, CNR and University of Rome III.

These two instruments will be hosted in a complete and independent modular endstation, featuring an analysis chamber and a sample preparation chamber, that will allow to perform measurements in a UHV environment efficiently screened from external perturbations (in particular stray magnetic fields), and to perform in situ modifications of the sample, ranging from simple cleaning by sputtering to the evaporation of simple materials. The project is designed to be very versatile, allowing for variation of the sample environment (application of controlled electrical and magnetic fields, cryogenic cooling) and for the parallel realization of photon-in photon-out techniques (fluorescence yield XAS, time-resolved magneto-optical Kerr effect). The station is designed to be extremely compact, allowing it to be moved easily giving the possibility of connecting it with many different lightsources such as HHG (for example the CITIUS laboratory HHG beamline [24]), or FEL (for example one of the FERMI @ Elettra beamlines or the future beamlines at the European X-FEL in Hamburg).

Scientific questions addressed

The scientific potentialities of such an apparatus are huge, because it is expected to extract an unprecedented amount of informations from the sample. The main direction of investigation is, however, the study of spin dynamics, and in particular the study of ultrafast magnetism, a very active field which has potential applications in electronics development. The on-going research on electronics is now providing new, extremely compact and efficient devices which operate at ever-increasing frequencies (GHz), thus managing to perform operations at the nanosecond timescale. This is creating a significant gap with respect to the data storage technologies that are limited to the range of microseconds (or MHZ frequencies): the bottle-neck on the data manipulation is thus when magnetic processes are involved to record the bits. The research on ultrafast magnetism is thus trying to push down the limit of the typical magnetization reversal (2 ps), exploiting magnetic phenomena that happen on a femtosecond timescale. In particular, a close connection with the science and technology of spintronics is present because both benefit from a deep understanding of the relaxation processes of the spin degree of freedom in charge carriers and from a nanoscale spatial manipulation of magnetic materials.

Ultrafast magnetism research was triggered by the seminal experiment of J. Y. Bigot and E. Beaurepaire in 1996 [25] in which the evolution of magnetization in Ni film was observed in a pump-probe configuration as the time dalay from the pump pulse was increased. The resulting behaviour is shown in Fig. 4. As it can be observed, the magnetization is *quenched* very rapidly, reaches a minimum and then starts to recover. An explanation of

[44] Integrating each 2D picture and converting the time of arrival at the detector in kinetic energy, one obtains the spectra with the TOF technique (described in subsect. 3.1.2 with more detail).

[45] Measuring the distribution of electrons with respect to both polar angles and energy.

the behaviour of the magnetization was given on the basis of a phenomenological thermodynamic model, the *three-temperature model*. In this scheme, the spin degree of freedom, the thermal energy of the electrons and the thermal energy of the lattice are considered as three independent reservoirs coupled by three heat transfer equations. The laser pulse optically excites the electron reservoir, which absorbs the infrared energy mostly by intraband transitions in metals. The energy is then transferred to the spin degrees of freedom on an extremely rapid way, generating the ultrafast quenching of the magnetization. Finally, the energy is relaxed to the lattice, and then the system slowly (hundreds of ps) moves towards the equilibrium.

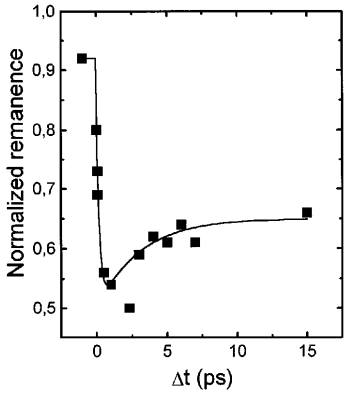

Figure 4. *The transient magnetization of a* $Ni(20\ nm)/MgF_2(100\ nm)$ *film [ref.] as measured with a time-resolved magneto-optical Kerr effect (TR-MOKE) set-up. The signal is normalized to the signal measured in the absence of pump beam. The line is a guide to the eye.*

The research that started from this observation is progressing towards two main directions: the deepening of the understanding of the complex processes involved, giving sufficient insight to go beyond the phenomenological model described above; and the application of ultrafast processes to the realization of magnetic devices working at high frequencies (on this, particular attention is given to the realization of ultrafast switching, in particular by all-optical methods [26]). The developement of these studies relies heavily on optical (photon-in photon-out) methods in reflection, such as TR-MOKE[46], or in absorption, maily because the availability of ultrafast pulses with photon energies sufficient to generate photoemission is very recent[47].

The optical methods that have been deployed up to now, however, despite having been mastered by few groups to very advanced level, are intrinsically limited:

- they probe only collective properties, an are not able to describe the behaviour of single particles; they thus do not give straightforward answers to the questions that arise in the development of an accurate microscopic description of the processes,
- the pump and the probe interact with the material via the same channels i.e. the optical ones; this often creates spurious modification of the probe signal generated

[46]The basis of this technique will be described in subsect.6.1.1.

[47]Nonetheless, many experiments of 2PPE have been performed during these years with ultrafast sources [27].

by the pump pulse (for example, *optical bleaching*, i.e. the saturation of a particular transition that distorts the measurements),

- optical methods are often not element-specific; despite in some special cases, and thanks to the deep knowledge of the method, the dynamical behaviour of different elements can be separated, this is not a common feature.

The ULTRASPIN project aims then to participate to the research by the use of a different technique, which can offer an insight complementary to the optical ones. Time-resolved photoelectron spectroscopy measurements in the field of ultrafast magnetism have already started to be performed in these years, giving exciting results[48]. In particular, the main themes at reach of the project will be:

1. The resolution of fundamental questions on ultrafast dynamics, on the correlation between electronic, spin and lattice degrees of freedom, and the analysis of magnetic order in nanostructures.

2. The analysis of time dependent phenomena near the phase transitions in complex materials.

3. The study of spintronics devices or magnetic nanostructures when in working conditions (*in-operando* measurements).

The work reported in this thesis focuses on the the construction and commissioning of such an instrument. In particular I took part to the assembling of a new suite of UHV vessels the integration of the four-axial Mott detector. The subsequent work, that still in progress, has been to test the new signal acquisition mode capable to handle short intense pulses for a time-resolved operation as well as capable of more conventional "spectroscopy mode", i.e. time integrated pulse counting. Mott detectors are, even at present, very challenging set-ups, that detect a very small spin-orbit scattered signal on the top of a large intensity of charge scattered electrons. The Mott detector has to run very efficiently and reliably for very long times. It is essential to achieve a detailed understanding of the set-up and to establish reliable operation in the described way before implementing time-resolved sources, so that troubleshooting can deal with one issue at a time and progress more quickly towards full commissioning and qualification of the set-up.

I participated to the first exploratory experiments related to the take-off of the project. I could grow, optimize and characterize a system with high spin polarization and high stability in UHV conditions, Fe(001)-p(1x1)O on MgO(001), to be used as a reference sample for static and dynamic spin-polarization measurements, and that also represents a system of potential technological applications. It is in fact the chosen target of another detection apparatus, the VLEED polarimeter. This allowed me the uncommon possibility of participating to the realization of two different kinds of detectors, and obtaining a broad overview of the operation of such kind of detectors. Finally, I had the possibility to partake to the first experiments on the dynamical behaviour of a complex magnetic oxide, $La_{0.7}Sr_{0.3}MnO_3$, which is now of relevant use in spintronics research [6] and holds promises

[48] As an example experiments of TR-ARPES have been performed on Gd [28].

to be high interest in its dynamical behaviour, in particular close to the ferromagnetic-paramagnetic phase transition.

Riassunto

Questa tesi descrive la costruzione e la messa in opera del nuovo set-up sperimentale sviluppato per un progetto di ricerca a lungo termine, chiamato ULTRASPIN, il cui scopo è di inaugurare la tecnica della fotoemissione risolta in tempo ed in spin tramite impulsi luminosi ultrabrevi (10^{-14} s) estratti dalle beamlines di un Free Electron Laser o da laser table-top negli UV o Raggi-X soffici.

Il progetto ULTRASPIN è entrato nella fase realizzativa nell'estate 2013, avvalendosi di competenze e strumentazione in parte già disponibile presso il gruppo della beamline APE dell'Istituto Officina dei Materiali-CNR ad Elettra, e con il parziale sostegno di un contratto europeo (EXTASY-EXperimental STation for the Analysis of the Spin Dynamics) e la fellowship di un esperto mondiale di polarimetria Mott.

Dall'inizio della mia partecipazione, sono stato coinvolto nelle fasi finali della progettazione, nella costruzione e nella messa in opera di un innovativo apparato da ultra alto vuoto (UHV) altamente schermato dai campi magnetici esterni: tale sistema ha la funzione di preparare e alloggiare superfici atomicamente pulite e di misurare la polarizzazione in spin degli elettroni foto-emessi risolvendo ogni singolo impulso con sensibilità alla scala temporale di 10^{-14} s, allo stesso tempo mantenendo la capacità di operare nella modalità standard della spettroscopia con sorgenti ad alta frequenza (sincrotrone) o continue. Nella fase di messa in opera, ho partecipato sia agli esperimenti di test su ULTRASPIN sia ad altri esperimenti finalizzati allo sviluppo delle tecniche di misura dello spin elettronico e dell'utilizzo di impulsi ultrabrevi e condotti presso APE ad Elettra e presso l'Università di Regensburg.

Il lavoro esposto in questa tesi è quindi consistito di due fasi principali, una di sviluppo

tecnologico della strumentazione e una di realizzazione di esperimenti volti a studiare le capacità della macchina, a produrre sistemi facilmente misurabili con questo strumento e a esplorare le possibili direzioni di ricerca future.

Strumentazione

La end station di ULTRASPIN è formata da un sistema di due camere da ultra-alto vuoto (UHV) di forma sferica collegate tra loro da un tubo passante e valvolato che permette il trasferimento di campioni dall'una all'altra. Una, detta camera di preparazione campioni, è dedicata alla strumentazione necessaria per preparare, crescere e modificare i campioni in UHV.

La seconda, detta camera di analisi, è quella in cui vengono realizzate le misure di polarimetria di spin. Il campione è posizionato al suo interno tramite un manipolatore verticale con quattro gradi di libertà: esso può essere mosso linearmente nelle tre dimensioni spaziali e ruotato attorno all'asse verticale. La camera presenta un sistema di flange orientate in direzione radiale, in modo che gli strumenti montati su di esse puntino tutti verso il centro: in questa maniera è possibile effettuare più misure e operazioni contemporaneamente o con piccole movimentazioni del campione. La camera può essere connessa a diverse sorgenti di luce con una grande flessibilità nella scelta delle geometrie e del posizionamento degli strumenti.

Su questa camera è montato lo strumento centrale del sistema ULTRASPIN, ovvero un *Diffusore di Mott vettoriale*. Si tratta di un polarimetro di spin in grado di raccogliere gli elettroni foto-emessi da un campione e di misurarne la polarizzazione in spin. Misurare la polarizzazione di un fascio di elettroni significa determinare qual'è la percentuale di particelle con proiezione dello spin in una delle direzione spaziale (*asse di quantizzazione*) rispetto alla percentuale di quelle con proiezione di spin in direzione opposta. Nello spazio tridimensionale, le direzioni rispetto a cui può essere misurata la polarizzazione sono tre: si tratta dunque di determinare le tre componenti, date da un numero compreso fra -1 e 1, di un vettore, detto vettore di polarizzazione. Lo strumento è quindi definito vettoriale in quanto è in grado di valutare la polarizzazione rispetto a tutte le tre direzioni spaziali

e di ricostruire la posizione spaziale del vettore di polarizzazione.

La misura della polarizzazione è basata sulla asimmetria nello scattering ad alta energia degli elettroni con il nucleo di un materiale ad elevato numero atomico, derivante da effetti di spin-orbita. Quando infatti un elettrone di alta energia (tra i 10 e i 200 keV) si approssima alla carica positiva del nucleo di un atomo, esso risente di un potenziale di interazione di tipo coulombiano. La diffusione dell'elettrone determina un moto relativo di tipo orbitale fra elettrone e nucleo e quindi "accende" anche l'interazione di spin-orbita. Se ci si limita ai processi in cui l'elettrone conserva la sua energia (*scattering elastico*), è possibile ragionare sulla geometria, cioè sull'angolo di diffusione, in modo semi-classico.

La direzione dell'elettrone incidente e quella dell'elettrone deflesso definiscono un piano (detto *piano di scattering*) in cui è contenuto anche il nucleo: fra di esse, è presente un angolo detto *angolo di scattering*. Gli effetti associati allo spin in questi processi (detti *scattering di Mott*) hanno la loro massima intensità relativamente allo scattering di carica, e quindi la massima misurabilità, quando l'angolo di scattering delle particelle è molto elevato, pari a circa 120°. In queste condizioni, dato che il nucleo è di dimensioni molto ridotte, si può supporre che la carica lo superi mantenendolo alla sua destra e venendo deflessa verso destra, oppure mantenendolo a sinistra e venendo deflessa verso sinistra. In questo modo, nel sistema di riferimento dell'elettrone, il nucleo viene visto come una carica positiva in moto, che genera un campo magnetico: la direzione del campo indotto sarà quindi ortogonale al piano di scattering e rivolta verso l'alto se l'elettrone mantiene il nucleo alla sua sinistra, mentre sarà rivolta verso il basso se l'elettrone supera il nucleo mantenendolo alla sua destra (Fig. 5 a.). Gli spin degli elettroni incidenti sono associati a loro volta ad un piccolo momento magnetico, dunque gli elettroni con spin orientati nella direzione del campo magnetico indotto interagiscono con esso; in particolare i momenti magnetici allineati al campo interagiranno con un potenziale effettivo più intenso di quelli allineati in direzione opposta (Fig. 5 b.). Gli elettroni che hanno spin up saranno quindi deflessi verso sinistra con maggiore probabilità rispetto agli elettroni con spin down; viceversa, gli elettroni con spin down saranno deflessi con maggiore probabilità verso destra rispetto a quelli con spin up.

Se quindi un fascio di elettroni di alta energia viene fatto incidere su un bersaglio

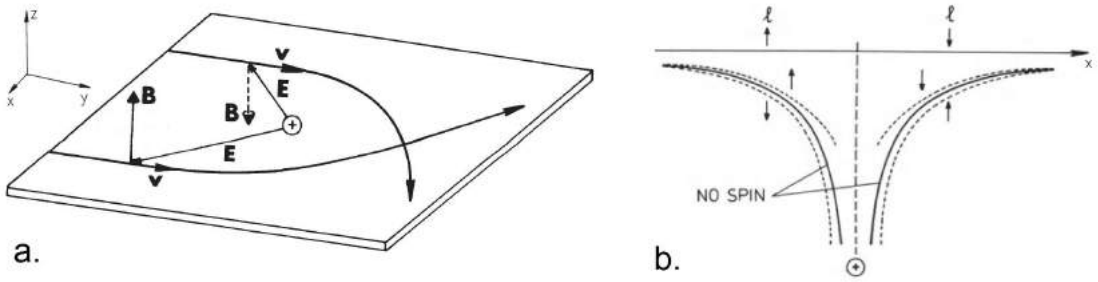

Figure 5. *a. Schema dei vettori coinvolti nello scattering Mott. La forma* $\bigoplus$ *rappresenta il nucleo, mentre i vettori indicati con* **v** *mostrano le direzioni e le velocità dei possibili elettroni incidenti. I vettori indicati con* **B** *mostrano la direzione dei campi indotti, mentre i vettori indicati con* **E** *rappresentano la direzione del campo elettrostatico generato dal nucleo. b. Potenziale di spin-orbita come viene visto da elettroni con spin-up o down (linee tratteggiate) o da particelle prive di spin che incidono sui due lati di un nucleo (corrispondenti a momenti angolari positivi o negativi).*

formato da atomi i cui nuclei hanno una forte carica positiva, e gli elettroni deflessi a 120° a destra e a sinistra vengono contati separatamente, è possibile osservare una asimmetria dovuta alla polarizzazione del fascio incidente rispetto alla direzione perpendicolare al piano di scattering.

Nella sua applicazione sperimentale questo viene realizzato raccogliendo gli elettroni e formando un fascio periassiale tramite un sistema di lenti elettrostatiche[49] che viene portato ad incidere perpendicolarmente alla superficie di un film estremamente sottile d'oro e disponendo dei contatori di elettroni ad angoli di 120° rispetto alla direzione del fascio incidente. Naturalmente possono essere definiti due piani di scattering ortogonali tra loro, dunque posizionando quattro detector è possibile determinare la polarizzazione del fascio rispetto a due assi di quantizzazione. Questa è la struttura centrale di un diffusore o polarimetro di Mott.

La polarizzazione lungo la direzione del fascio incidente, tuttavia, non può essere misurata in questa geometria. Nel diffusore Mott vettoriale questo problema è risolto utilizzando due polarimetri Mott disposti in modo che le direzioni dei fasci incidenti sui bersagli siano l'una perpendicolare all'altra. I due polarimetri Mott condividono una parte del sistema di lenti e solo alla fine il fascio di elettroni viene inviato nell'uno o nell'altro tramite una lente detta di switch, controllabile dall'esterno. Grazie al fatto che

[49]Solo le lenti elettrostatiche possono essere usate per lo studio dello spin perché l'attraversamento di esse non modifica lo stato di spin degli elettroni. L'uso di lenti magnetiche porterebbe invece a modificare l'informazione sullo spin.

la direzione del vettore polarizzazione viene conservata indipendentemente dalla direzione di moto nell'attraversare le lenti elettrostatiche, il polarimetro Mott vettoriale riesce a misurare coerentemente (e senza richiedere movimenti del campione o dello strumento) quattro componenti del vettore polarizzazione, di cui tre sono indipendenti, mentre una è ridondante.

Nella camera di ULTRASPIN, il primo elemento accelerante del sistema di lenti elettrostatiche per la formazione del fascio periassiale è posta in prossimità della superficie del campione e raccoglie gli elettroni emessi dalla superficie formando un fascio che si propaga ad un angolo di 45° rispetto alla direzione normale alla superficie, accelerandoli e trasportandoli fino ai due polarimetri Mott che ricevono alternativamente il fascio e permettono la misura della polarizzazione di spin.

Un'attenzione particolare deve essere dedicata ai contatori di elettroni e all'elettronica utilizzata per leggere il loro segnale. Nel polarimetro Mott vettoriale, infatti, il particolare schema utilizzato nel disporre gli alti voltaggi necessari ad osservare l'asimmetria fa sì che i contatori di elettroni debbano essere mantenuti ad un alto voltaggio (40-70 kV) rispetto al potenziale di terra. Inoltre questi sistemi devano essere in grado di valutare non solo l'arrivo di un elettrone, ma anche la sua energia, al fine di selezionare unicamente gli elettroni elastici che, come si è detto, sono gli unici a portare l'informazione riguardante la polarizzazione.

I contatori di elettroni utilizzati nel polarimetro Mott vettoriale sono dei rilevatori PIPS (Passivated Implanted Planar Silicon), formati da sottili (500 μm) wafer di silicio drogati sulla faccia superiore da impurezze accettrici e sulla faccia inferiore da impurezze donatrici. La regione in cui sono presenti impurezze è di dimensioni estremamente ridotte in prossimità della superfici (circa 5 nm), grazie all'uso della tecnica dell'impiantazione ionica. Se alle due superfici viene applicato un voltaggio polarizzando la giunzione in modalità inversa, si crea una profonda regione di svuotamento fra le due. Quando un elettrone energetico incide sulla faccia superiore, esso penetra nella regione di svuotamento e perde tutta la sua energia all'interno di essa, creando coppie elettrone-lacuna: queste vengono separate ed accelerate verso le due superfici e raccolte come un impulso di carica elettrica.

La quantità di carica contenuta nell'impulso è proporzionale all'energia dell'elettrone primario assorbito. Di conseguenza, attraverso l'elettronica che legge e amplifica i segnali, è possibile conteggiare gli elettroni incidenti e valutarne l'energia. Attraverso uno schema intelligente di alimentazione e l'uso di fibre ottiche, è possibile far funzionare i PIPS mentre essi sono flottanti ad alta tensione (50 kV) e conteggiare unicamente gli elettroni elastici diffusi dal bersaglio d'oro. Calcolando la differenza (normalizzata) fra il numero di elettroni misurati fra due detector opposti e appartenenti allo stesso piano di scattering, si può così ottenere la polarizzazione del fascio lungo una direzione come:

$$P_{\perp} = \frac{1}{S_{eff}} \frac{N_l - N_r}{N_l + N_r} \tag{5}$$

Dove $1/S_{eff}$ è un fattore moltiplicativo, detto *funzione di Shermann efficace* che viene valutato sperimentalmente tramite misure di calibrazione. L'uso di detector avanzati come questi ha permesso di migliorare nettamente il rapporto segnale rumore rispetto agli apparati precedenti e di ridurre l'energia dello scattering. Infatti il rapporto tra l'asimmetria e l'intensità totale misurata cresce al crescere dell'energia nel range 10-200 keV, fornendo al polarimetro Mott un segnale più ampio e un rumore più ridotto: si può quindi passare senza riduzione delle prestazioni da un sistema con detector standard operante a 100 keV ad uno con detector PIPS operante a 40 keV. La riduzione dell'energia di scattering e dunque delle tensioni acceleranti permette di ridurre l'ingombro geometrico dell'apparato, rendendo estremamente compatti questi polarimetri.

I diffusori Mott sono stati costruiti e pensati operare in presenza di sorgenti continue, cioè ricevendo un certo flusso di elettroni al secondo. L'elettronica che legge i segnali, pertanto, integra l'impulso di carica, per poi confrontarlo con un valore regolabile dall'esterno (discriminator level): se è maggiore, significa che un elettrone elastico deve essere contato, se è minore, significa che l'elettrone ha ceduto energia al nucleo, non porta informazione sulla polarizzazione, e deve essere scartato. Questa tecnica richiede, però, che il flusso di elettroni sia tale da riuscire a distinguere l'arrivo di ognuno di essi. I PIPS sono contatori di elettroni con una risposta molto rapida (dell'ordine di poche centinaia di picosecondi), ma che richiedono lunghe distanze temporali se si vuole separare accuratamente gli im-

pulsi (dead-time), poiché avendo sostanzialmente la struttura di un condensatore, dopo l'arrivo di una particella è necessario un certo tempo di carica perché il detector torni nelle condizioni iniziali (alcune centinaia di ns). Se un PIPS è esposto ad un flusso tropo elevato di particelle, esso entra in *saturazione*, e il segnale di asimmetria è perso.

Questo costituisce un problema per l'applicazione di questi detector con sorgenti impulsate, soprattutto nel caso dei FEL, in cui i fotoelettroni sono concentrati in impulsi di grande intensità, della durata inziale di alcuni fs e che si allungano durante la propagazione nelle lenti fino a qualche ns. I due impulsi che raggiungono i PIPS per la misura della polarizzazione portano quindi una grandissima quantità di elettroni in un brevissimo tempo, e la saturazione porterebbe a contare un unico elettrone con una elevatissima quantità di carica. Per gestire un segnale con questa struttura temporale, tuttavia, non è necessario usare altri detectors. È infatti stato scoperto, dal gruppo di Y. Acremann presso ETH Zürich, che se un impulso breve (1-10 ns) di elettroni viene inviato nei PIPS, al loro output viene prodotto un impulso di corrente la cui struttura temporale è proporzionale (con un fattore di amplificazione di circa 10^4) alla struttura dell'impulso originario. Se dunque un'elettronica in grado di registrare la struttura temporale della corrente prodotta dai PIPS viene sostituita a quella basata sui discrimination levels, è possibile acquisire un segnale non saturato, utilizzabile per le misure di asimmetria. Come descritto in Fig. 6, nel regime impulsato si avranno quindi dei pacchetti di elettroni che raggiungono il bersaglio d'oro, vengono diffusi a destra e a sinistra a seconda della loro polarizzazione in spin, e vengono misurati separatamente da due PIPS detectors. Le distribuzioni del flusso di cariche in funzione del tempo, possono poi essere analizzate via sofware, studiando l'asimmetria tra le due curve, riconducibile alla polarizzazione del pacchetto in ingresso.

L'ambizioso progetto di ULTRASPIN è quindi quello di realizzare, per la prima volta, un Compact Classical Vectorial Mott detector in grado di operare in regime impulsato, utilizzando una elettronica di questo tipo sviluppata dal Gruppo del Dott. Cautero al Laboratorio di Strumentazione e Detector del Sincrotrone Elettra a Trieste. Il nuovo sistema di acquisizione sarà inoltre in grado di operare anche con sorgenti continue, per non precludere nessuna possibilità d'uso ad ULTRASPIN. Al di là dello straordinario vantaggio di poter operare in condizioni time-resolved tramite esperimenti di fotoemissione con tecnica

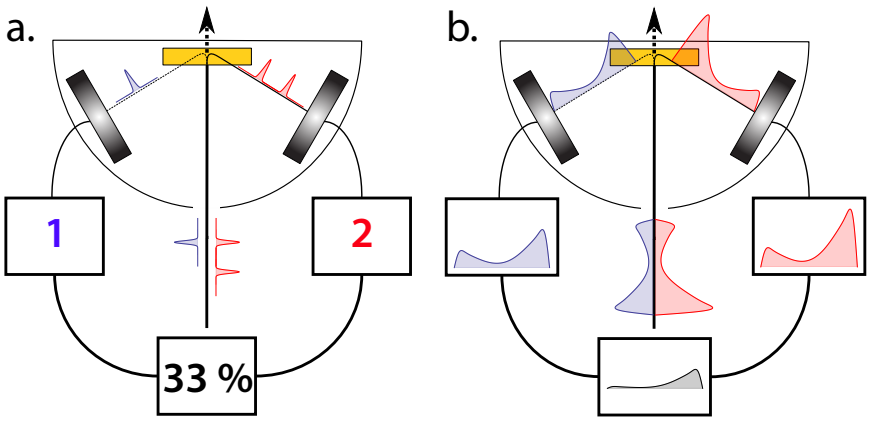

Figure 6. *a. Modalità di operazione continua. Un flusso costante di elettroni raggiunge il target ed è diviso nei due fasci filtrati in spin che raggiungono i contatori di elettroni. L'elettronica converte immediatamente l'impulso di carica in un numero di elettroni al secondo che permettono di calcolare la polarizzazione. b. Modalità impulsata. L'impulso incide sul bersaglio e si divide in due impulsi filtrati in spin. La nuova elettronica acquisisce istante per istante la corrente uscente dai PIPS. Le due curve sono poi mandate ad un computer che permette di calcolare la polarizzazione dell'impulso conservando la struttura temporale.*

pump-probe, esplorando l'evoluzione temporale delle eccitazioni nella materia, è anche possibile che dalla struttura temporale dell'impulso si possa ricostruire la distribuzione in energia degli elettroni, permettendo ad ULTRASPIN di estrarre quattro spettri XPS con risoluzione in spin rispetto a due direzioni di quantizzazione ortogonali per ogni impulso della sorgente.

Durante il lavoro della mia tesi ho potuto partecipare al montaggio e alla messa in opera di tutta la strumentazione di ULTRASPIN. Particolare attenzione è stata naturalmente dedicata al polarimetro Mott. Esso è stato posto in condizioni operative, testato e caratterizzato in modalità continua con l'uso di un cannone elettronico. Il sistema di lenti elettrostatiche di trasporto è stato riconfigurato, raggiungendo la condizione ottimale per la misura. Nello studiare il sistema di lenti è anche stata posta speciale attenzione nel far sì che esso potesse essere in grado di adattarsi alle diverse intensità ed esigenze delle possibili sorgenti. Dal termine della mia attività lo strumento è in grado di entrare in funzione rapidamente, riducendo al minimo i tempi morti fra una misura e l'altra, e presenta ottime caratteristiche di stabilità del segnale, sia nel tempo, sia per piccoli spostamenti nella posizione del campione. Sono inoltre stato coinvolto nella realizzazione dei primi test della nuova elettronica di read-out, preparativi al raggiungimento del funzionamento

impulsato.

Per collaudare l'effettivo funzionamento dello spin detector in modalità continua, sono state effettuate misure di polarimetria di spin sugli elettroni secondari emessi da un campione di materiale magnetico utilizzando come eccitazione un cannone elettronico. Questa tecnica si basa sul fatto che gli elettroni secondari, emessi dagli atomi del materiale del solido a causa dell'energia depositata dagli elettroni primari, debbano viaggiare all'interno del solido stesso prima di poter raggiungere la superficie ed essere emessi. Dal momento che nei materiali magnetici la struttura a bande è differente per gli elettroni con lo spin nella direzione del vettore magnetizzazione e per quelli con spin in direzione opposta, risulta differente anche la propagazione degli uni e degli altri all'interno del solido. In particolare, può essere fortemente spin-dipendente quello che viene chiamato *inelastic mean free path*, ovvero la distanza che un elettrone percorre in media prima di subire una collisione con scambio di energia. Per questo motivo, gli elettroni che si trovano nell'intervallo di energie più basso dello spettro sono fortemente spin-polarizzati, con valori che arrivano fino al 50% nel caso di superfici pulite di Fe. Dal momento che la differenza nella struttura a bande è principalmente originata dall'interazione di scambio ed è quindi associata alla magnetizzazione, la polarizzazione in spin degli elettroni secondari di bassa energia può essere impiegata per seguire la rotazione del vettore magnetizzazione quando un campo esterno viene applicato al materiale. Il polarimetro vettoriale Mott può quindi essere utilizzato come un magnetometro vettoriale in grado di studiare il magnetismo alla superficie.

Le misure svolte utilizzando questa tecnica hanno permesso di registrare le isteresi di un campione di test, una lega priva di struttura cristallina chiamata *amorphous metal*, verificando la performance del detector. La polarizzazione di spin degli elettroni emessi ha mostrato di essere molto piccola, possibilmente a causa della rugosità della superficie. Questo ha però consentito di mettere alla prova la capacità dello strumento di misurare accuratamente segnali piccoli: in una tipica misura con la ripetizione del ciclo di isteresi di 20 volte, variazioni della polarizzazione di meno del 2% sono state registrate con un'incertezza che si è dimostrata essere di origine puramente statistica, attorno al 0,2%. Isteresi misurate con tecniche sensibili alla magnetizzazione del volume hanno esibito campi coercitivi molto differenti rispetto a quelle ottenute con il Mott Detector, mostrando la radicale differenza

che intercorre tra il magnetismo nel volume e quello nella superficie.

Esperimenti

Parallelamente allo sviluppo della strumentazione sono stati svolti due diversi tipi di esperimenti, su altri apparati sperimentali, strettamente correlati alle tecniche di polarimetria di spin e ai processi fisici sui quali le future misure realizzabili con l'apparato di ULTRASPIN saranno applicate.

Il primo esperimento è consistito nella crescita, caratterizzazione e ottimizzazione di una superficie di ferro passivato nella struttura Fe(001)-p(1x1)O. Questo sistema nasce dall'esigenza di mantenere, per un intervallo di tempo compatibile cin l'esecuzione di esperimenti di fisica delle superfici, le proprietà di una superficie magnetica altamente spin-polarizzata senza che esse vengano degradate dalla presenza di contaminanti. La superficie di ferro, infatti, possiede una struttura a bande con un elevato splitting tra gli stati con spin opposto dovuto all'interazione di scambio. In particolare, gli stati vuoti presentano un gap tra i 4 e i 10 eV al di sopra dell'energia di Fermi, che può essere utilizzato per la realizzazione di un tipo differente di spin detector, detto Very Low Energy Electron Diffraction Polarimeter (*VLEED Polarimeter*).

Se infatti elettroni di bassa energia vengono mandati su una superficie cristallina, essi subiscono un processo di scattering coerente e non vengono diffusi con omogeneità nello spazio, ma vengo concentrati in fasci altamente direzionali (*Low Energy Electron Diffraction*, o LEED). Se si impiega una superficie di Fe e l'energia viene scelta in modo da cadere esattamente nel summenzionato gap (ovvero si usano fasci primari di circa 6 eV), allora si può ottenere un unico fascio riflesso, la cui intensità è molto prossima a quella del fascio primario, poichè gli elettroni incidenti non trovano stati energetici accessibili nel materiale, e il loro assorbimento è soppresso. Dal momento che le bande sottostanti sono splittate dall'interazione di scambio spin-spin, però, il fascio primario trova in realtà un gap completo solo per uno stato di spin (quello allineato con la magnetizzazione del Fe, ossia lo stato di spin-majority), mentre per lo spin opposto (spin-minority) sono presenti stati energetici possibili. Questo fa sì che gli elettroni con spin antiparallelo siano assorbiti

facilmente, mentre quelli con spin parallelo siano riflessi con alta probabilità. Se dunque viene registrata l'intensità riflessa dalla superficie con la magnetizzazione diretta in due direzioni opposte, è possibile estrarre una asimmetria proporzionale alla polarizzazione di spin del fascio iniziale.

I detector VLEED possono valutare la polarizzazione degli elettroni con una efficienza molto maggiore rispetto ai polarimetri Mott. La loro geometria, con un solo fascio riflesso misurato in due momenti separati, li rende tuttavia meno adatti alle misure con sorgenti FEL, in cui l'intensità può variare significativamente tra un impulso e l'altro. Per misure continue, tuttavia, essi presentano performance molto elevate, e lo staff della beamline APE ha deciso di montare uno di questi sistemi sul nuovo analizzatore utilizzato per la spettroscopia ARPES (*Angle-Resolved Photoelectron Spectroscopy*), al fine di realizzare la tecnica Spin Polarized ARPES ad alta risoluzione in energia e in momento.

La superficie libera del Fe si contamina tuttavia molto rapidamente, anche in UHV. All'aumentare della contaminazione della superficie, si perdono rapidamente le caratteristiche di polarizzazione della struttura a bande e, con essa, l'asimmetria misurata dal sistema VLEED. Per ovviare a questo problema, è stata sviluppata una forma di passivazione controllata della superficie del Fe, in cui si produce l'adsorbimento di un unico strato atomico di atomi d'ossigeno. Il sistema assume, nel piano, una struttura ordinata con gli atomi di ossigeno posizionati negli spazi vuoti tra gli atomi di Fe, come mostrato in Fig. 7.

Questa struttura conferisce alla superficie una elevata stabilità chimica, ma non solo. L'effetto dell'ossigeno nella struttura a bande del solido è quello di accrescere la presenza di strutture spin-polarizzate, aumentando il momento magnetico del Fe e la riflettività della superficie. I target per la realizzazione di detector VLEED sono quindi realizzati con questa struttura che è in grado di mantenerne inalterate le proprietà per molte settimane in UHV e può essere rinnovata con una procedura di annealing in situ.

Ho quindi avuto la possibilità di studiare e sviluppare la tecnica di crescita di questa superficie, che potrà essere utilizzata sia come target per il nuovo VLEED detector, sia come campione di riferimento per il Mott detector di ULTRASPIN, che, data la sua elevata polarizzazione e stabilità, può essere usato per svolgere misure di calibrazione. La

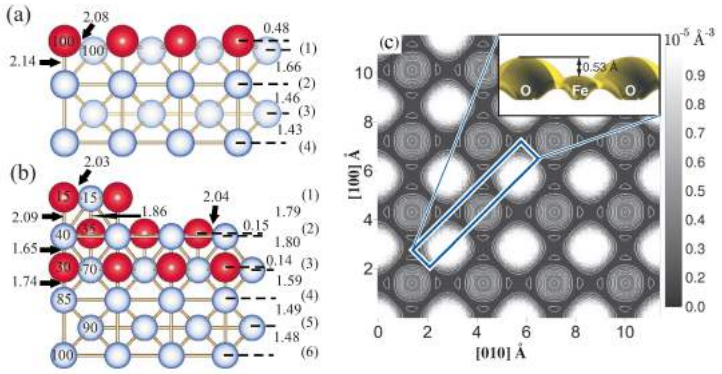

Figure 7. *a. Schema strutturale di una sezione trasversale della superficie di Fe(001)-p*$(1 \times 1)O$ *. Le sfere rosse e azzurre rappresentano rispettivamente gli atomi di ossigeno e di Fe. Le distanze sono in Å e i numeri tra parentesi rappresentano i fattori di occupazione i percentuali di un monolayer. b. Stesso diagramma per la fase disordinata dovuta all'ossidazione. c. Mappa bidimensionale della densità di carica al livello di Fermi calcolata in vuoto 4 Å al di sopra della superficie. Le aree chiare mostrano la posizione degli atomi di ossigeno, mentre quelle scure i siti del Fe. Nell'inserto, il profilo verticale a densità di carica costante nel piano (110).*

struttura effettiva che viene utilizzata è quella di film di Fe cresciuti su MgO lappato nella forma:

$$\mathrm{MgO(001)/Fe(001)(100nm)/O-p(1x1)}$$

Questo sistema viene realizzato pulendo la superficie dell'MgO, evaporando 100nm di Fe su di essa ed eseguendo un annealing per ripristinare la struttura cristallina del Fe. La superficie pulita di Fe viene poi esposta ad un flusso di ossigeno e nuovamente sottoposta ad annealing per desorbire l'ossigeno in eccesso. Dopo aver evaporato alcuni film più sottili di prova, al fine di ottimizzare le procedure di pulizia dei substrati e verificare l'epitassia della crescita, la struttura è stata cresciuta nella sua forma completa, caratterizzandola ad ogni step della preparazione con misure LEED, XPS, XAS, XMCD e magnetometria XMCD. Dall'analisi delle misure ottenute si è compreso che la superficie è stata passivata correttamente, realizzando un sottile (1.5 Å) strato di ferro ossidato, principalmente nello stato Fe^{2+}. La contaminazione da carbonio presente sulla superficie dopo l'evaporazione viene sostanzialmente ridotta dopo l'esposizione all'ossigeno. È stata anche osservata una piccola contaminazione di tungsteno, derivante dal filamento dell'evaporatore. Le curve XMCD, sensibili alla polarizzazione degli stati vuoti al di sopra dell'energia di Fermi, mostra che la polarizzazione non è ridotta nella struttura Fe(001)-p(1x1)O, ma anzi legger-

mente aumentata. Il campione è quindi stato lasciato per 4 settimane in UHV per testare la procedura di rinnovamento della superficie. La contaminazione di carbonio, cresciuta con l'esposizione ai gas residui presenti nella camera, è stata rimossa dalla procedura di annealing in situ, e il valore di polarizzazione di spin della superficie è stato recuperato. Tuttavia, gli spettri XPS portano a concludere che la copertura di ossigeno sia diminuita, eventualmente portando ad aree scoperte di Fe sulla superficie. Questo potrebbe portare ad una ricontaminazione più rapida della superficie. Per migliorare questa procedura, potrebbe essere efficace lo svolgimento di anneling in presenza di una pressione parziale di ossigeno.

Il secondo esperimento è consistito nello studio della dinamica di magnetizzazione dell'ossido magnetico $La_{0.67}Sr_{0.33}MnO_3$. Esso è stato svolto al fine di esplorare alcune delle possibili prospettive di ricerca nelle quali l'apparato ULTRASPIN può dare un contributo rilevante, dando la possibilità di osservare da un punto di vista differente i processi di magnetismo ultraveloce. Come si è discusso precedentemente, infatti, la polarimetria di spin è in grado di studiare il comportamento magnetico delle superfici. Questa tecnica può quindi studiare l'evoluzione temporale delle caratteristiche magnetiche, ottenendo informazioni in maniera diretta dallo stato di spin degli elettroni, se combinata con tecniche pump-probe, in cui un impulso ultrabreve di luce infrarossa raggiunge il campione seguito, ad una differenza temporale controllata, da un impulso di luce con energia sufficiente a generare fotoemissione. Le misure che saranno svolte da ULTRASPIN, quindi, saranno complementari a quelle ottenute con tecniche più tradizionalmente applicate al magnetismo ultrafast, come il Time-resolved MOKE.

Un argomento particolarmente interessante in questa direzione è lo studio della dinamica di magnetizzazione degli *half-metals*. Questi sistemi sono caratterizzati da una struttura a bande che presenta un gap in corrispondenza dell'energia di Fermi per uno solo degli stati di spin degli elettroni, mentre per quello opposto la conduzione è possibile. Questo significa che gli elettroni all'energia di Fermi possiedono una elevatissima percentuale di polarizzazione di spin, prossima al 100%. Materiali di questo tipo sono di altissimo interesse tecnologico, con applicazioni nella spintronica, in cui sono richiesti per questa proprietà, dimostrandosi in grado di generare, controllare e assorbire corrente a

seconda del loro stato di magnetizzazione.

Uno dei più studiati fra gli half-metals è l'$La_{1-x}Sr_xMnO_3$ (LSMO), un composto derivato dal drogaggio della manganite $LaMnO_3$ in cui Sr è incluso sostituzionalmente agli ioni di La, agendo come impurezza accettrice. La struttura cristallina è di tipo perovskitico e in essa il manganese è presente in due forme ioniche Mn^{3+} e Mn^{4+}, separati da atomi di O. È proprio questa struttura che origina il magnetismo nell'LSMO e che ne determina anche le proprietà di trasporto. Infatti, la forma di interazione magnetica che caratterizza l'LSMO è detta *double exchange*, una delle forme di magnetismo in cui sono i portatori introdotti dal drogante a creare la correlazione fra gli ioni magnetici. Nella sua configurazione di drogaggio più diffusa, $La_{0.67}Sr_{0.33}MnO_3$, il sistema è ferromagnetico a basse temperature, e diventa un metallo paramagnetico una volta superata la temperatura di Curie (circa 370 K). Quando si trova nella fase ferromagnetica, l'LSMO ha le caratteristiche di un half-metal, con polarizzazione all'energia di Fermi estremamente elevata.

In un esperimento pump-probe, gli elettroni sono eccitati otticamente da un impulso infrarosso molto intenso. L'arrivo dell'impulso di probe permette di seguire il rilassamento magnetico del sistema. Normalmente, vengono distinti tre reservoir in cui l'energia può essere immagazzinata: quello dell'energia cinetica degli elettroni, quello dello spin e quello del reticolo. In un normale metallo ferromagnetico, gli elettroni eccitati dal pump cedono rapidamente l'energia al sistema di spin, riducendo l'ordine magnetico molto rapidamente attraverso processi di spin-flip. Il sistema rilassa poi lentamente, cedendo energia al reticolo, con l'eccitazione di fononi. In un half-metal, i processi di scattering con spin-flip non sono possibili, in quanto non esistono stati con spin opposto appena al di sopra dell' energia di Fermi. Il collasso dell'ordine magnetico, quindi, avviene su scale temporali molto più lunghe, in quanto gli spin vengono disordinati solo dalla relativamente debole interazione fra spin e fononi.

L'esperimento time-resolved svolto durante questa tesi mirava dunque ad esplorare questo tipo di processi nell'LSMO, in particolare su film sottili LSMO(40nm)/STO(001) tramite l'uso della tecnica del time-resolved MOKE. Dopo una caratterizzazione con misure XPS, XAS, XMCD ed XRD di un campione cresciuto per MBE presso il laboratorio

della linea APE-NFFA, che ne ha dimostrato l'ottima cristallinità, omogeneità e carattere magnetico, le misure risolte in tempo sono state svolte presso l'Università di Regensburg con la collaborazione del Prof. C. Back, del Dott. S. Günther e della Dott. R. Ciprian. Da un iniziale studio della riflettività dei film, si è potuto osservare che l'onda di shock generata dall'improvviso riscaldamento locale della superficie del campione, si smorza lentamente, dando modo alla vibrazione di percorrere diverse volte lo spessore del film rimbalzando tra la superficie libera e l'interfaccia con il substrato. Questo ha permesso di dare una stima della velocità del suono nel sistema. Passando allo studio della dinamica di magnetizzazione, si sono esplorate due scale: una sui tempi brevi (0-7 ps) e una sui tempi lunghi (0-1.5 ns). Nelle misure a risoluzione temporale più elevata si è potuta identificare una dinamica complessa, che è stata divisa in tre fasi: una rapida riduzione del segnale magnetico (completata in circa 300 fs) è seguita da un recupero parziale (completato in circa 2 ps), che porta ad un equilibrio intermedio della durata di circa 2-3 ps. Sulle scale temporali più lunghe si è potuto osservare invece il summenzionato processo di demagnetizzazione lenta tipica degli half-metals. Mentre quest'ultimo è stato precedentemente osservato e discusso, la parte strutturata a tre componenti non risulta essere stata esplorata precedentemente. Per spiegare i risultati ottenuti, serviranno quindi altre misure e una analisi di tipo simulativo-computazionale. Si sono inoltre misurate le curve di demagnetizzazione al variare della temperatura del campione, al fine di gettare le basi di una analisi più ampia e approfondita, in cui possa essere esplorato il comportamento alla transizione di fase.

Concludendo, l'apparato di ULTRASPIN è pronto per iniziare ad esplicare il suo vero potenziale: la end-station, con tutta la sua strumentazione, è operativa, e il Vectorial Mott detector è pronto per essere testato con sorgenti impulsate. Sono inoltre state sviluppate le competenze per creare e studiare sistemi dotati di interessanti peculiarità nella polarizzazione della struttura a bande, aprendo così il ventaglio delle prospettive per i futuri utilizzi di questo straordinario strumento.

Part I

Electron spin polarimetry

Chapter 1

The road to polarimetry

Participating to research in the field of spin polarimetry means being surrounded by the legacy and the enthusiasm of little less than a century of exploration. Electron's spin is one of the most intimate and elusive characteristics of this elementary particle, and its study attracted a continued attention from the very first incongruences in the Old Quantum theory in the 1920 until now, when the new science of spintronics is succeeding in achieving an high level of control on it. It is therefore interesting to briefly summarize the the path which has brought to the modern technique of spin polarimetry, trying to point out the most important ideas that have strongly affected its development. In the following chapter the discovery of the spin, which has triggered the interest in spin polarimetry, is shortly outlined. Both the theoretical and first indirect evidences through the Stern-Gerlach experiment are mentioned. Furthermore, the first difficulties in the measurement of the electron's spin are exposed: the impossibility of a Stern-Gerlach experiment for electrons is discussed. Finally, it is shown how the deeper insight of the Dirac equation hints at new experimental methods.

1.1 The discovery of spin

> *It was a little over fifty years ago that George Uhlenbeck and I introduced the concept of spin. It is therefore not surprising that most young physicists do not know that spin had to be introduced.[...]*
>
> *- S. Goudsmith, 1978*

In the 1920's the Old Quantum Theory had achieved its highest point: the Bohr-Sommerfeld model could describe the energy position of elemental atoms' spectral lines under the only hypothesis that the orbiting electron's angular momentum was quantized[1].

[1] As a general reference for the development of quantum mechanics from its origins, it is possible to use [29]. For a much deeper insight on the topics related to condensed matter physics, see [30]. For the discussion that inspired the one exposed here, and that has a much broader spectrum, see [3].

N. Bohr had started formulating a model for the Hydrogen atom in which the electron was restricted to move in circular orbits of a well defined radius (and of well defined energy); the idea was further refined by A. Sommerfeld, which brought it to a more clear formal expression. Nowadays, as is known, the angular momentum is expressed in the subsequent form:

$$|\mathbf{L}| = \hbar\sqrt{l(l+1)} \tag{1.1}$$

where l is a non-negative integer, the *Orbital quantum number*, and $\hbar = 6.62606957 \times 10^{-34} \quad m^2 \cdot kg/s$ is the Planck constant. The *space quantization rule*, requires that the value of a component of $\mathbf{L}$ along one axis of reference (normally z is used) is an integer multiple of $\hbar$:

$$L_z = m_L\hbar \tag{1.2}$$

where m_L is the *Magnetic quantum number* and can assume values between $-l$ and l.

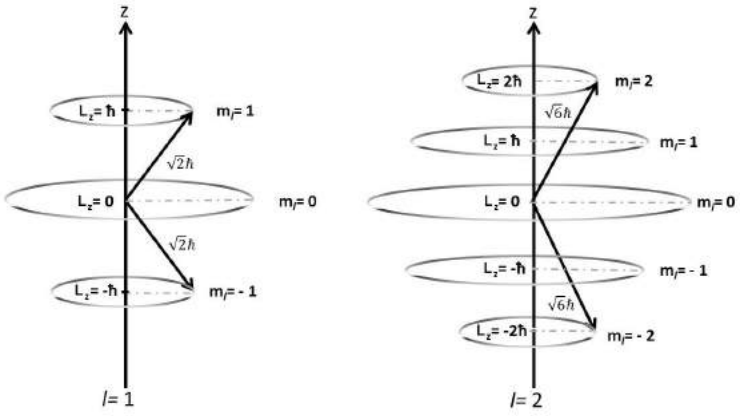

Figure 1.1. *Scheme expressing the concept of space quantization for two values of* $|\mathbf{L}|$ *corresponding to two different orbital quantum numbers.*

Nevertheless, no intrinsic explanation was given of why this restriction had to be used, and angular momentum quantization was considered an abstract rule deprived of a real physical meaning[2].

1.1.1 The Stern-Gerlach experiment

A new insight was given by an experiment, whose results were published in 1922, performed by O. Stern and W. Gerlach [32], which was specifically designed to demonstrate the quantization of angular momentum. Stern considered that, being the electron an electrically charged particle, its motion along an orbit can be considered as a current on a wire loop. This is the prototypical system in which a magnetic momentum is generated: if a charged particle of mass m_e possesses an angular momentum $\mathbf{L}$, it also has a magnetic

[2]This opinion is expressed in a particularly clear way by Max Born in his autobiography: *"I thought always that [space] quantization was a kind of symbolic expression for something that you didn't understand". [31].*

momentum **M**. Then if Bohr theory was true, also electron's magnetic momentum was quantized and could be written as:

$$\mathbf{M} = \mu_B \cdot \frac{\mathbf{L}}{\hbar} \tag{1.3}$$

where

$$\mu_B = \frac{e\hbar}{2m_e} = 9.27400949(80) \times 10^{-24} \quad J/T \tag{1.4}$$

is the Bohr magneton.

Stern hypothesis was that if a *neutral* particle (like an atom) has a non-zero **M** and is sent through a highly inhomogeneous magnetic field, it should be deflected from a straight line path proportionally to the amplitude and the direction of **M**. With the help of Gerlach, he realized a set-up in which a beam of neutral Ag atoms was sent in the gap of a magnet, whose poles were conveniently shaped. At the end of the magnet, the atoms would impinge on a photographic plate, which would register their position. A scheme of this experiment is shown in picture 1.2.

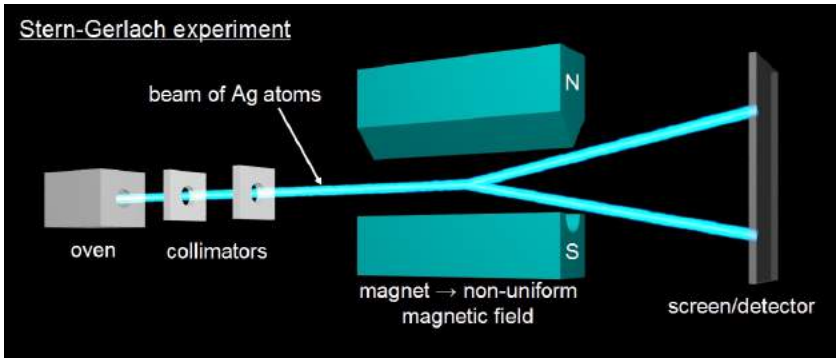

Figure 1.2. *Scheme of a Stern-Gerlach apparatus.*

The two scientists believed that, if Bohr theory was true, they would have observed a twofold splitting of the Ag beam, while, if the classical theory was true, they would have observed a continuous distribution of atoms. The idea of a twofold splitting was derived from a misconception: the Bohr-Sommerfeld model predicted that silver atoms would have an angular momentum corresponding to an orbital quantum number $l = 1$, which was thought to have two possible states corresponding to $m_L = 1, -1$. As can be easily seen in the modern formulas and Fig. 1.1, in modern quantum mechanics, $l = 1$ yields three possible states corresponding to $m_L = 1, 0, -1$. Furthermore, it is now known that the only electron that could contribute to the angular momentum of Ag is in a $l = 0$ state.

The result of the experiment can now appear surprising, because Stern and Gerlach observed exactly what they expected: when the magnetic field was applied, the straight-line profile of the Ag beam would split in two curved parts. The postcard with which the result was communicated is shown in picture 1.3.

While at that time it appeared to be the confirmation of the extremely counter-intuitive concept (the space quantization), we now know that the Stern-Gerlach Experiment (SGE)

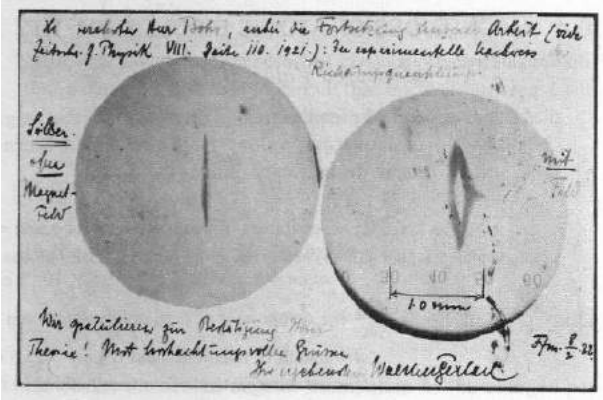

Figure 1.3. *The postcard sent to Bohr, dated Feb. 8, 1922.*

was on the brink of a new revolution: the discovery of electron's intrinsic angular momentum, or, in short, the spin.

1.1.2 Theoretical discovery: Uhlenbeck and Goudsmith

Despite this apparent success, some difficulties were still troubling the Bohr Model. For example, the discovery made by Zeeman[3] in the late 1890's that the emission lines of elemental gases split in doublets when the atoms were immersed in intense magnetic fields (the *anomalous Zeeman effect*). Many groups of theoreticians were competing on giving a solid explanation of this effect. In Leiden, the group of P. Ehrenfest, and in particular Samuel Goudsmith, understood that the anomalous lines could be described by formulas using quantum numbers which could assume only two values. At the same time, Goudsmith realized that the same quantum numbers he was using had properties very close to the ones hypothesised by Pauli in his paper on the exclusion principle[4].

Working together with G. Uhlenbeck, they rapidly realized that these two conclusions were connected and implied a more deep result: the electron had a fourth[5], intrinsic degree of freedom which could be coupled to the magnetic field. Uhlenbeck natural reaction was to identify it as a rotation of the electron around its own axis, generating another magnetic momentum:

> *"When the day came I [S. Goudsmith] had to tell Uhlenbeck about the Pauli principle - of course using my own quantum numbers - then he said to me: «But don't you see what this implies? It means that there is a fourth degree of freedom for the electron. It means that the electron has a spin, that it*

[3]Pieter Zeeman had started investigating the effects of magnetic field on light sources as an expansion of his research on magnetic effects on light upon reflection (i.e. MOKE, a phenomenon, and subsequently a technique, which will be used and described in the following.

[4]Published in the early 1925, the Pauli exlusion principle states that "two electrons in an atom cannot have the same set of quantum numbers", but, to account for the fact that *two* electrons were observed with the same known set of quantum number, he had to introduce a new, binary quantum number.

[5]Supplementary to the three degrees of freedom due to the motion in the three dimensions of space.

rotates.» "[6]

This intuitive interpretation, derived from the deep knowledge of classical mechanics that Uhlenbeck had, was anyway flawed as they immediately learnt. When the idea was submitted to Lorentz, he noticed that if a spinning charge with the classical radius of the electron had such magnetic momentum, it should have rotated so fast that its surface would have been moving at a speed higher than that of light. Despite this problem, they published a paper in 1925 on *Naturewissenschaften* [33], and one in 1926 on *Nature* [34], with a more complete analysis of the implications of the spin on the spectral analysis, and with an endorsement of Bohr. The spin was officially discovered.

Nowadays, this fourth degree of freedom is interpreted as a purely quantistic property and the electron is not (according to the knowledge to date) a particle with a finite size, much less a spherically shaped object. The name spin has remained, however, denoting its historical origin. Being an intrinsic angular momentum, it is subjected to the same quantization rules as the orbital angular momentum:

$$|\mathbf{S}| = \hbar\sqrt{s(s+1)} \tag{1.5}$$

where s is the *spin quantum nuber* and

$$S_z = m_s\hbar \tag{1.6}$$

where m_s is the *spin projection quantum number* and can range from $-s$ to s in integer steps.

The rule for possible s values is anyway different from those for l values. It can be demonstrated that very general angular momentum commutation relations allow only for integer or half-integer quantum numbers. But while l is associated with the position of a particle on an orbit and must satisfy De Broglie's condition[7] restricting its values to be integer; on the other hand, spin is not correlated to spatial coordinates, and can assume also half integer values. The electron, for example, has $s = 1/2$ and its projection can have only two values: $S_z = +\hbar/2$ (or "up") or $S_z = -\hbar/2$ (or "down"), as pictured in Fig. 1.4.

Another relevant difference is that for an elementary particle the value of s is fixed and cannot be changed by excitation: leptons and quarks have $s = 1/2$, photons, gluons and weak bosons have $s = 1$ while the newly discovered Higgs Boson appears to have $s = 0$. Actually, having integer or half-integer spin quantum number has also been shown[8] to define two different statistical behaviours when the particles are considered in ensambles, the very important result called *the spin-statistic theorem.*

[6] From Goudsmith on the discovery of electron.

[7] In 1924, Louis de Broglie published his PhD thesis [35], in which he studied the implications of the wave-particle duality, treating electrons as waves. This led to the condition that an electron moving along a stationary orbit must be represented by a standing wave. In order to support a standing wave, the length of the orbit must be an integer multiple of the wavelength: this condition forces the orbits to be quantized, and the orbital quantum number to be integer.

[8] The first formulation of this idea was made several years later, in 1939 by Markus Fierz, and later more formally demonstrated by Pauli.

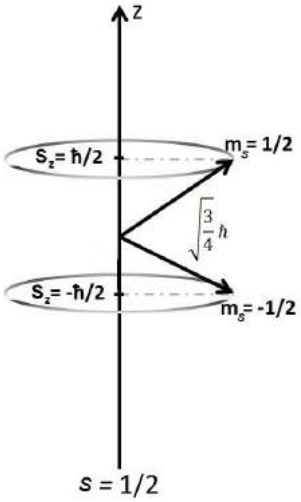

Figure 1.4. *Scheme of the intrinsic momentum quantization.*

In an atom, where each electron has both an orbital momentum and an intrinsic momentum, they add up, defining the resulting *total angular momentum*:

$$\mathbf{J} = \hbar\sqrt{j(j+1)} \tag{1.7}$$

and

$$J_z = m_j\hbar \tag{1.8}$$

where m_j can take values from $-j$ to j in integer steps. The sum rules are that, for a single electron[9]

$$m_j = m_L + m_s \tag{1.9}$$

and

$$|l - s| \leq j \leq l + s \tag{1.10}$$

which completely define the possible values of j. The magnetic momentum of an atom with only one electron is then:

$$\mathbf{M} = \frac{\mu_B}{\hbar} \cdot \mathbf{J} = \frac{\mu_B}{\hbar} \cdot (\mathbf{L} + g_s\mathbf{S}) \tag{1.11}$$

where g_s is the *gyromagnetic factor* and is used because the intrinsic angular momentum has, in general, to be weighted differently from $\mathbf{L}$ in the calculation of $\mathbf{M}$. For the electron $g_s \approx 2$, giving:

$$\mathbf{M} = \frac{\mu_B}{\hbar} \cdot (\mathbf{L} + 2\mathbf{S}) \tag{1.12}$$

[9] In an atom with many electrons the situation is more complicated: one can add $\mathbf{L}$ and $\mathbf{S}$ for each electron and then add all the resulting $\mathbf{J}$ (*jj-coupling*), or add all the $\mathbf{L}$ of different electrons, add all the $\mathbf{S}$ and finally calculate the total $\mathbf{J}$ (*LS-coupling*). Depending on which angular momenta interact more strongly, calculations can be easier choosing the right path: the former is used for heavy atoms ($Z > 40$) and the latter for light atoms ($Z < 40$).

The last result can explain clearly the apparent absurd of the SGE: in the Ag atom there are many electrons (47), but only one can contribute to the angular momentum[10]. This electron, anyway, happens to be in a $l = 0$ state, so the formula for the magnetic momentum yields:

$$\mathbf{M} = \frac{\mu_B}{\hbar} \cdot 2\mathbf{S} = \pm\mu_B \tag{1.13}$$

What Stern and Gerlach observed in their experiment was then the effect of the spin on the magnetic momentum of the atom and not, as was believed, the quantization of $\mathbf{L}$.

From the experimental point of view, Uhlenbeck and Goudsmith's idea sparked the desire of a more deep and powerful investigation: the question arose if it was possible to observe and measure the spin of a free electron. The SGE is, in fact, a rather indirect method of observing the spin effects and the whole momenta summation construction, especially considering the need for the gyromagnetic factor[11], must have looked again like a complex way to get around some phenomenon not yet understood[12]. This is the first question which pointed towards the measurement of spin of electrons. A whole branch of physics called *spin polarimetry* was at its dawn: it would unfold across many fields, such as nuclear, high energy and condensed matter physics, giving fundamental contributions to each one of them and giving an irreplaceable instrument of insight in complex phenomena.

1.2 A deeper understanding

> *But electrons do not move in clear-cut orbits [...], they dance [...]. They perform stately waltzes, weave curvaceous tangos, jitter in spasmodic quicksteps, and rock to frenetic rhythms. They are waves dancing to a choreography different for each kind of atom.*
>
> *- E. R. Harrison, 2003*

Before proceeding further, it is necessary to define accurately the most important concepts connected to spin measurement. In the experiments considered here analysis of spin

[10] The others are in closed shells, and their momenta cancel out completely, giving no contribution in the fundamental state.

[11] Parameters such as the gyromagnetic factor can really hide some deeper physics: a very pertinent example is the neutron, whose unexplainable variation of the g_s factor between the bound and free state lead to understand that it is a composite particle. Even for the same electron the calculation of the gyromagnetic factor up to the 9th decimal cipher and its consistence with experimental data were a success achieved by quantum field theory only when renormalization was fully developed.

[12] Many actually did not believe it, and the *Naturewissenschaften* paper encountered a rather cold reception by the community. For example, the very creator of the exclusion principle, W. Pauli, was so sceptical about it that he turned down one of his students, R. Kronig, who believed in the spinning electron more than a year before Uhlenbeck and Goudsmith's publication.

is not performed on a single electron[13], but on an *ensemble of electrons*[14]: what is measured is not a single spin state (up or down), but the *spin polarization* of the ensemble[15].

> *"An ensemble of electrons is said to be [spin] polarized if [...] there exists a direction [i.e. one quantization axis] for which the two possible spin states are not equally populated.[...] If all spins have the same direction one has the extreme case of a totally polarized ensemble of electrons [...]. If not all, but only a majority of the spins has the same direction, the ensemble is called partially polarized."*[16]

Polarization is then related to the unbalance between the number of electrons in the up-state (up-state population) and the number of electrons in the down-state (down-state population), where up and down are defined with respect to one arbitrary axis. In the three-dimensional space is then possible to define three independent quantization axes and polarization is normally treated as a three-dimensional vector $\mathbf{P}$, whose components (P_x, P_y, P_z) are the percent difference between the up-state population and the down-state population defined (in the same order) with respect to the quantization axes (x, y, z). It is important to remark that, while the single spin states are only two, and the spin state of a particle can be represented by a two components vector (the *spinor*), the polarization, an ensemble property, is a three components vector.

The first attempts to directly measure the spin of a free electron were made following the lines of the Stern-Gerlach Experiment, trying to send electrons through the gaps of a magnet and to observe a splitting. Unfortunately, this idea immediately lead to a halt, as it is mathematically impossible to obtain any result from an experiment of this kind. The mathematical proof is given in an extremely clear way in [37]; here, for the sake of readability, only a hint of it will be given. In a SGE apparatus, the beam of electrons has to pass through the gaps of the Gerlach magnet: here the external magnetic field $\mathbf{B}$ will have two main components B_y and B_z, as depicted in the cross section of Fig. 1.5.

The component B_z generates the force that tends to split the beam and to separate up-spins and down-spins, due to the interaction of the intrinsic dipole with the magnetic field.

$$F_z = \pm\mu_B \frac{\partial B_z}{\partial z} \tag{1.14}$$

Electron is, however, a charged particle and is subjected also to the Lorentz force due to its motion in a field:

$$\mathbf{F} = e(\mathbf{E} + \mathbf{v} \times \mathbf{B}) \tag{1.15}$$

Therefore there will be a not homogeneous force along the y direction caused by B_z. This component does not interfere with the measurement, since it can only shift electrons to the right-hand side of the picture, not affecting the distribution on the z direction.

[13] Although measurement of a single electron's spin is possible, see for example [36], it has to be performed using the most sophisticated forms of confinement at the nanoscale, and is beyond the scope of this thesis.

[14] Ensamble is used here as a statistical term. It denotes a set of identical particles whose energy and number is known (*microcanonical ensamble*).

[15] Most of the times, the ensemble is in the form of a well defined beam, with all electrons having their momenta as uniform as possible.

[16] [37].

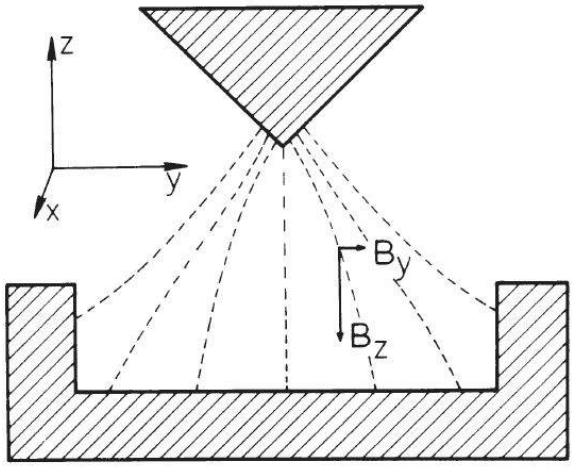

Figure 1.5. *Scheme of the magnetic field in a Gerlach magnet. From [37].*

The insurmountable obstacle is instead posed by the variability of B_y. Even in a thought experiment we have to consider a not infinitely narrow beam, because elementary particles are subjected to the uncertainty principle. This means that, even omitting the experimental difficulties, there will always be a distribution of particles in the y direction, and B_y will create a component of the Lorentz force that will deflect electron in the z direction. This will affect the detection, because the traces will be no longer horizontal lines, but skewed. Another point that should be taken into account is that the uncertainty relation exists also for the z direction, creating a broadening of the lines in stripes, schematically shown in Fig. 1.6.

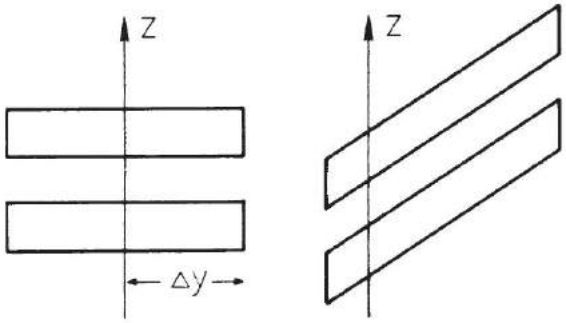

Figure 1.6. *Position of the traces for neutral (left) and charged particles (right). From [37].*

It can then be shown that this tilting is so strong, and the splitting is so small, that it is not possible to resolve the two stripes by any means in any direction. The realization of a real spin polarimeter had to wait for the development of more profound theoretical knowledge of spin-related effects in the interaction of electron with solids.

1.2.1 Dirac equation

Theoretical research on the description of elementary particles proceeded extremely quickly, with a turbulent evolution in those years. In 1924 De Broglie obtained the first results from the wave-particle duality, between 1925 and 1926 Erwin Schrödinger formulated the first dynamical wave equation describing the behaviour of non-relativistic particles. Almost simultaneously Werner Heisenberg, Max Born and Pascual Jordan developed matrix mechanics. In less than a year, however, the scientists had already moved one step ahead, trying to find an equation to describe relativistic particles, with the results of Oskar Klein and Walter Gordon in 1926 and Paul A. M. Dirac in 1928.

Dirac equation was built with the precise aim of describing the motion of a free electron in the frame of the special relativity, with the further restriction that it should be only of the first order in the time derivatives (and consequently, for Lorentz covariance, also space). This condition was originated from the previous results of Klein-Gordon, which built a second order equation that could describe the integer-spin particles, but had some serious interpretative issues, since in some cases it could give rise to absurdly negative probability solutions. The use of solely first derivatives guaranteed that Dirac equation could not have negative probabilities, but forced him to work with non-scalar quantities, describing the wave-function of an electron as a four-components vector (the *Dirac spinor* or *Bispinor*).

Dirac looked for an equation of the same form as the Schrödinger equation, but proposed an Hamiltonian (for the free electron) of the form:

$$\hat{H} = c\,(\boldsymbol{\alpha}\cdot\hat{\mathbf{p}}) + \beta m_e c^2 \tag{1.16}$$

using three parameters $(\alpha_x, \alpha_y, \alpha_z)$ and β which had to satisfy the conditions:

$$\alpha_i^2 = 1, \qquad \beta^2 = 1, \tag{1.17}$$

$$\alpha_i\beta + \beta\alpha_i = 0 \tag{1.18}$$

$$\alpha_i\alpha_j + \alpha_j\alpha_i = 0 \qquad (i \neq j) \tag{1.19}$$

in order to have free wave solutions with the same structure of Klein-Gordon's free waves. It is immediately clear from the second expression that simple numbers (or even complex ones) can not satisfy this conditions. The simplest assumption is that β and *each* α_i are 4×4 matrices. The Dirac equation is then:

$$i\hbar\frac{\partial\Psi(\mathbf{x},t)}{\partial t} = c\,(\boldsymbol{\alpha}\cdot\hat{\mathbf{p}})\Psi(\mathbf{x},t) + \beta m_e c^2\Psi(\mathbf{x},t) \tag{1.20}$$

where $\Psi(\mathbf{x},t)$ is a four-components bispinor:

$$\Psi(\mathbf{x},t) = \begin{pmatrix} \Psi_1(\mathbf{x},t) \\ \Psi_2(\mathbf{x},t) \\ \Psi_3(\mathbf{x},t) \\ \Psi_4(\mathbf{x},t) \end{pmatrix} \tag{1.21}$$

The free-electron solutions can be written as:

$$\Psi(\mathbf{x}, t) = u(\mathbf{p})e^{i(\mathbf{p}\cdot\mathbf{r}-Et)/\hbar} \tag{1.22}$$

where $u(\mathbf{p})$ is also a bispinor satisfying:

$$c\,(\boldsymbol{\alpha}\cdot\hat{\mathbf{p}})u(\mathbf{p}) + \beta m_e c^2 u(\mathbf{p}) = Eu(\mathbf{p}) \tag{1.23}$$

with E energy of the free electron. One of the many extraordinary successes of this equation is that the intrinsic angular momentum emerges naturally from the geometrical properties of the object used to represent the electron's wave-function. In fact it can be shown that applying a rotation to a bispinor solution of the Dirac equation, two quantities remain unchanged: the orbital angular momentum, and an intrinsic angular momentum, the spin. This means that Dirac's equation and the bispinor construction have caught a picture of electrons' behaviour far deeper than the previous one and, furthermore, have proven far more insightful than expected.

The solution to the problem of the spin detection is now only one step ahead: having finally achieved a deeper understanding, it is now necessary to conveniently describe how it interacts with matter. If a spin-dependent behaviour is to be found in some electron-matter interaction process, it can then be used to realize a polarimeter.

Chapter 2

Spin polarimetry

In this chapter the scattering processes that have some spin dependence are explained. Particular attention is given to the characteristics of each process that make it useful for the realization of a spin detector. Initially the use of some terms about scattering is focussed. Then a picture of the spin-orbit interaction is given, explaining the classical analogue of the process from which spin-orbit potential arises. Next, high energy Mott scattering and the way in which it can be used to measure polarization are discussed. Following the chronological evolution, low energy scattering and low energy coherent scattering (Spin Polarized-LEED) are examined. Finally, exchange interaction is introduced and very low energy coherent scattering (VLEED) from ferromagnets is described as a spin-resolving process.

2.1 Scattering nomenclature

The main process of interaction of a particle with matter is scattering. Under this term is collected the whole set of phenomena in which a particle can be considered to interact with another particle or an external potential in three steps:

- the scatterer starts in an initial, non-interacting state whose parameters are known (at the best allowed by uncertainty principle);
- the scatterer interacts with the scattering centre;
- the scatterer is diffused in a final state again non-interacting, which is observed after a long time.

As stated before, the ensembles of electrons considered for spin-polarization are most of the times in the form of a beam: for this reason, scattering will be the most common and interesting process in the following.

Being such a large class of processes, many different classifications exist. The most important ones are associated with the final state characteristics, because they can be observed experimentally and give insight in the characteristics of the interaction. The

properties of a scattered electron that can be observed are: energy, momentum (or wave-vector) and spin[1]. When an electron approaches the target, it can[2] be deflected by some angle (*scattering angle*). This means that the momenta of the incoming and outgoing electron define a plane which contains both and an angle ϑ is present between them. It is clear that a large ϑ implies a strong interaction with the target: generally scattering is divided in *small-angle scattering* ($\vartheta < 90°$) and *large-angle scattering* ($\vartheta > 90°$). In both cases the incoming electron can be simply deflected, without any change in its kinetic energy (*elastic scattering*); or loose part of its energy in creating an excitation (collective or atomic) of the target (*inelastic scattering*). It understandable that elastic scattering will still carry important information about the initial state of the scatterer, while in inelastic scattering much more details of the target are involved. Finally, one speaks of *spin-conserving scattering* if the spin of the electrons is unchanged, and of *spin-flip scattering* in the opposite case. In the following, a short discussion of the processes that can give an insight on the initial spin state will be given. The focus will then be on elastic, spin-conserving large angle scattering processes, in which the initial spin state determines the number of electrons deflected at a certain angle.

2.2 Spin-Orbit interaction

The first to give a formulation of scattering theory for relativistic electrons was Sir Neville Mott in 1929 [3]. He represented the initial and final states with the free-electron solutions of the Dirac equation, while, as interaction potential, he used the one generated by a simple, infinitely heavy coulombian charge. This potential ($\varphi(\mathbf{r})$) is spherically symmetric ($\varphi(\mathbf{r}) = \varphi(r)$) and, if generated by a charge $q = Ze$ composed by Z elementary charges, it can be written as:

$$\varphi(\mathbf{r}) = \frac{Ze}{4\pi\varepsilon_0 r} \tag{2.1}$$

This choice was made not only for the sake of simplicity, but also because, if a relativistic electron impinges on a heavy atom, the dominant interaction is between the scatterer and the positive charge of the nucleus: the electrons bound to the atom are hardly "seen" by the high energy particle, and the recoil of the atom (more than 20 000 times heavier) is negligible. In particular, the range in which all assumption of Mott theory are valid is for initial energies of the scattering electron ranging from some 10 keV to less than 500 keV. The upper limit is set because to study polarization and the spin projections discussed above, the electron must not be ultrarelativistic, i.e. its kinetic energy must be less than its rest energy ($m_e c^2 \approx 500\ keV$). In ultrarelativistic scattering only the projection of spin in the direction of motion (*elicity*) is conserved.

In the non-ultrarelativistic regime the relevant components of the Dirac bispinor (1.21) are only two, and is therefore possible to use a simpler two components (spinorial) repre-

[1] This further clarifies the reason of the interest in measuring the electron's spin: it contains one third of the information that can be extracted from analysis of scattering processes.

[2] It is mandatory to express possibility here, because in some conditions, for example a beam of high-energy electrons impinging on a thin free-standing film of metal, most of the scatterers do not interact at all, and are not even deflected from the initial path.

[3] [38].

sentation of the wavefunction. If electromagnetic interaction (2.1) is plugged into Dirac equation (1.20), and the non-ultrarelativistic approximations are applied, the following expression is obtained:

$$\left[\frac{1}{2m_e}\left(\mathbf{p}-\frac{e}{c}\mathbf{A}\right)^2+e\varphi-\frac{e\hbar}{2mc}\boldsymbol{\sigma}\cdot\mathbf{B}+i\frac{e\hbar}{4m^2c^2}\mathbf{E}\cdot\mathbf{p}-\frac{e\hbar}{4m^2c^2}\boldsymbol{\sigma}\cdot(\mathbf{E}\times\mathbf{p})\right]\Psi=E\Psi \quad (2.2)$$

where $\boldsymbol{\sigma}$ is a three-components vector of 2×2 matrices $(\sigma_x,\sigma_y,\sigma_z)$, the Pauli matrices. The vector of Pauli matrices connects the three-dimensional space of the potential with the two dimensional space of the spin states, substantially representing the spin projection in the three orthogonal spatial directions. In quantum mechanical terms, each σ_i is the observable corresponding to the spin along the i-th coordinate axis of the three dimensional space. The terms appearing in the last equation can now be connected with precise physical processes:

- The first term, $\frac{1}{2m_e}\left(\mathbf{p}-\frac{e}{c}\mathbf{A}\right)^2$ describes the kinetic energy of the particle, which is modified from the simple $\frac{\mathbf{p}^2}{2m_e}$ by the presence of the vector potential $\mathbf{A}$.
- The second term is the electrostatic potential.
- The third term describes the interaction of the intrinsic magnetic momentum $\mathbf{M}_s$ with an external magnetic field.
- The fourth term represents a relativistic correction to the energy and has no classical analogy.
- The fifth term is the spin-orbit (SO) interaction. In the electron frame of reference, in fact, the nucleus is moving and generating a magnetic field $\mathbf{B}_n$, which can interact with $\mathbf{M}_s$.

As this last term shows, again an interesting point concerning the spin falls out naturally from the Dirac equation. Fortunately, the spin-orbit term has also a clear classical interpretation that helps to understand it more deeply. $\mathbf{B}_n$ is given combining the expression:

$$\mathbf{B}_n=-\frac{\mathbf{v}}{c}\times\mathbf{E} \quad (2.3)$$

with the expression of $\mathbf{E}$, which can be induced from $\mathbf{E}=-\nabla\varphi(r)$, and in the present case is:

$$\mathbf{E}(\mathbf{r})=-\frac{Ze}{4\pi\varepsilon_0 r^3}\mathbf{r} \quad (2.4)$$

then B_n is related to the *orbital* angular momentum ($\mathbf{L}=\mathbf{r}\times\mathbf{p}$):

$$\mathbf{B}_n=\frac{Ze}{4\pi c\varepsilon_0 r^3}\mathbf{v}\times\mathbf{r}=-\frac{Ze}{4\pi mc\varepsilon_0 r^3}\mathbf{L} \quad (2.5)$$

This magnetic field interacts in the usual way with $\mathbf{M}_s(V_{SO} = -\mathbf{M}_s \cdot \mathbf{B}_n)$. The intrinsic magnetic moment can be written in terms of S as seen before in eq. 1.11, thereby obtaining[4]

$$V_{so} = \frac{Zeg_s}{16\pi m^2 c^2 \varepsilon_0 r^3} \mathbf{L} \cdot \mathbf{S} \tag{2.6}$$

Once determined a relevant spin-dependent interaction, it is then necessary to understand how it affects the scattering of electrons.

2.3 High energy scattering with spin-orbit interaction

The scattering theory in the presence of spin-orbit interaction is a rather long and complicated mathematical procedure and, for readability, it discussion is omitted[5]. A classical qualitative picture can anyway be given[6]. When the electron approaches the target, the vector $\mathbf{v}$ and $\mathbf{r}$ lay in the scattering plane, to which the resulting $\mathbf{B}_n$ is orthogonal. $\mathbf{B}_n$ defines also the direction of the quantization axis for the spin of the electron: the M_s interacting with $\mathbf{B}_n$ can be parallel or anti-parallel to it. In the following, only processes in which the electron will be elastically deflected at large angles ($\vartheta \geq 90°$).

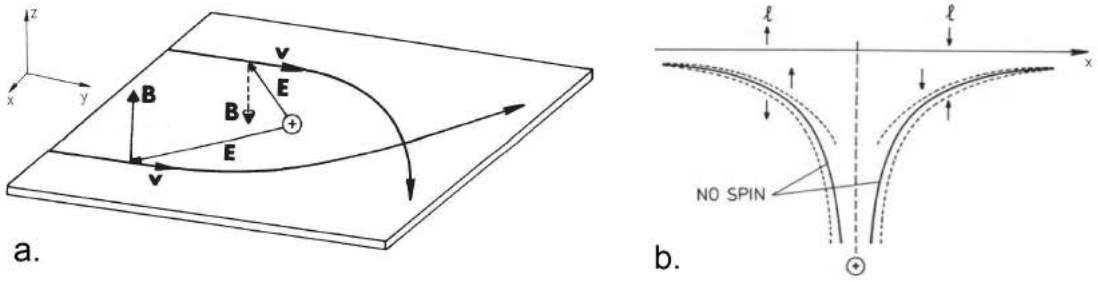

Figure 2.1. *a. Scheme of the vectors involved in Mott scattering. The* $\bigoplus$ *represents the nucleus, the vectors labelled with* $\mathbf{v}$ *indicate the velocities of two possible incoming electrons. The vectors labelled with* $\mathbf{B}$ *show the direction of the induced field, while the vectors labelled with* $\mathbf{E}$ *display the electric field generated by the nucleus. b. The spin-orbit potential as seen by spin up, spin down (dashed lines) and spinless particles (solid line) impinging on the two sides (corresponding to a positive or negative angular momentum) of a nucleus. Adapted from [37].*

An electron moving along the y direction, as shown in Fig. 2.1 a, can pass on the right or on the left of the nucleus, thus having an orbital angular momentum directed along

[4] A further 1/2 factor has to be included to account for Thomas precession [3].

[5] It can anyway be found, with an extremely precise and relatively simple formalism in [37]. The way in which Mott first obtained it, and that is used in [37], is the partial wave method, implemented with the density matrix formalism to obtain the statistical properties. In this way, an infinite series that exactly expresses the phase shifts can be obtained. However, closed forms for the series cannot be obtained and the last step of calculation of cross sections must rely on numerical evaluations or approximation formulas. Spin asymmetry can also be derived from the scattering from an external potential in the second Born approximation using quantum field theory, as is done in [39].

[6] This picture is possible because at these energies electron's wavelength is much smaller than the atomic radius and it is therefore possible to think to the interacting particles as point-like objects. When lower energies will be discussed, classical analogies will hold no more.

z and respectively upwards or downwards. This generates a small positive shift in the effective potential for up-spin electrons arriving on the left and down-spins arriving on the right. Viceversa, a small negative shift will be created for down-spins arriving on the left and up-spins arriving on the right as shown in Fig. 2.1 b. The effective nuclear potential will therefore result more attractive for up-spins on the right and for down-spins on the left. Interacting more strongly, they are more likely to be deflected at large angles. As shown in Fig. 2.1 a, up-spins will then have a slightly higher probability of being deflected to the left and down-spins to the right.

Up to this point, the discussion was referred to a single electron, and the next step is to extend it to the ensemble (the beam), which will create a link with polarization. The main tool in this description is the *differential cross section*, which gives the number of particles being deflected in a certain infinitesimal interval of solid angles ($[\Omega, \Omega + d\Omega]$) per unit time, per unit flux of incoming particles and per unit number of scattering centres. The full theory of Mott scattering demonstrates that, in the range of energies considered, the differential cross section can be written as:

$$\left(\frac{d\sigma}{d\Omega}\right)_{Mott} = I(\vartheta)\left[1 + S(\vartheta)\mathbf{P}\cdot\hat{\mathbf{n}}\right] \tag{2.7}$$

where:

- $I(\vartheta)$ is the spin-averaged cross-section, cancelling out the effects of spin[7];
- $\mathbf{P}$ is the polarization vector of the incident beam;
- $S(\vartheta)$ is a function, called *Sherman function*, dependent on the angle of deflection, that expresses the efficiency with which the scattering process selects the spin[8] (see Fig. 2.2);
- $\hat{\mathbf{n}}$ is a unit vector, normal to the plane depicted in Fig. 2.1 a, defining which component of the polarization is relevant. It must be stressed here that $\hat{\mathbf{n}}$ has opposite signs if opposite angles are considered: if the deflection angle is $90° \leq \vartheta \leq 180°$ (deflection to the left), then it is along z and upwards in Fig. 2.1 a; if $180° \leq \vartheta \leq 270°$(deflection to the right), it is still along z, but downwards.

If a partially polarized beam (with non-vanishing components of $\mathbf{P}$ in the direction of $\hat{\mathbf{n}}$) impinges with a sufficient energy on a heavy atom target, then, the number of electrons scattered on the right and on the left will be different, as illustrated in Fig. 2.2.

Now it is possible to understand the core process used in Mott polarimetry: if two ideal[9] identical detectors are positioned at opposite angles with respect to the primary beam, for example one at $\vartheta = 120°$ (left detector) and one at $\vartheta = 120°$ (right detector), they define a scattering plane. If the detectors are able to count only elastically scattered electrons, the right detector will measure a number of signals N_r per unit time and the

[7] It can also be used to define the deflected intensity of a perfectly unpolarized beam [40].

[8] The Sherman function is obviously also dependent on the scattering energy and on the atomic number of the target atom.

[9] Here with "ideal" it is meant that they have an infinitesimal solid angle of acceptance ($d\Omega$).

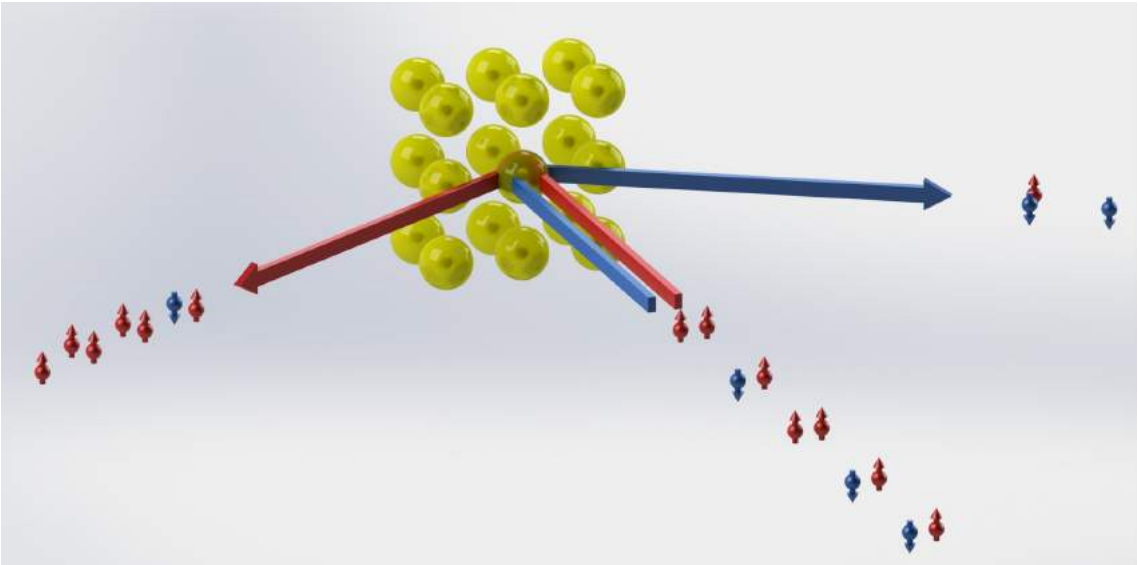

Figure 2.2. *Simplified picture of Mott scattering. As it can be observed, the unbalance in the number of of up and down spins in the primary beam is transformed in different numbers of electrons deflected to the left and to the right. Some electrons with down (up) spin are however deflected to the left (right), as the efficiency (the Shermann function) is generally less than* 100%.

left N_l. These two numbers are connected with the polarization component perpendicular to the scattering plane:

$$N_l = I(\vartheta)[1 + S(\vartheta)P_\perp] \tag{2.8}$$

$$N_r = I(-\vartheta)[1 - S(-\vartheta)P_\perp] = I(\vartheta)[1 - S(\vartheta)P_\perp] \tag{2.9}$$

The last equality holds because both $I(\vartheta)$ and $S(\vartheta)$ are, for the spherically symmetrical potential used, even functions. It can then be defined the *asymmetry function*:

$$A(\vartheta) = \frac{N_l - N_r}{N_l + N_r} \tag{2.10}$$

and, substituting eq. 2.8 and eq. 2.9:

$$A(\vartheta) = \frac{I(\vartheta)[1 + S(\vartheta)P_\perp] - I(\vartheta)[1 + S(\vartheta)P_\perp]}{I(\vartheta)[1 + S(\vartheta)P_\perp] + I(\vartheta)[1 + S(\vartheta)P_\perp]} = S(\vartheta)P_\perp \tag{2.11}$$

Therefore, measuring $A(\vartheta)$, it is possible to evaluate the component of the polarization of the primary beam normal to the plane of the detectors:

$$P_\perp = \frac{1}{S(\vartheta)} A(\vartheta) \tag{2.12}$$

From this expression is clear that in the realization of an instrument the geometry, the energy of the primary beam and the scattering target must be accurately selected in order to achieve the highest $S(\vartheta)$: in this way, the experimental uncertainty in the value of $A(\vartheta)$ will give an error in the value of $P_\perp$ as small as possible. Simultaneously, the highest

possible value of $I(\vartheta)$ should be achieved[10]: even though it is not evident in eq. 2.12, the relative statistical error (assuming Poisson distribution statistics) on N_r and N_l is proportional to $1/\sqrt{N}$ and is thus reduced if $I(\vartheta)$ is bigger[11].

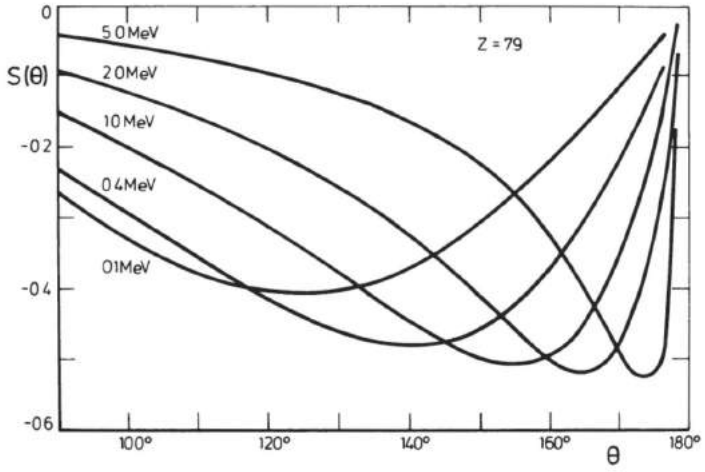

Figure 2.3. *Shermann function $S(\vartheta)$ for scattering by Au at various energies. From [37].*

A smaller statistical error can improve significantly the performance of a detector (in terms of time required to obtain data with a good signal-noise ratio), in particular in the case of the measurement of asymmetry, which is proportional a small difference between the right and left signal, meaning that the noise is the same as in N_l or N_r, but the signal is much less[12]. This last point is expressed by a quantity, called *figure of merit* (FOM) which roughly quantifies the performance of a spin detector, and is defined as:

$$\varepsilon = \left(\frac{I}{I_0}\right) S_{eff}^2 \tag{2.13}$$

where I_0 is the beam intensity entering the polarimeter, I is the total scattered intensity measured by the detectors $(N_l + N_r)$ and S_{eff} is the effective Sherman function[13] of the detector. As it will be discussed in the next chapters, state of the art polarimeters based on high-energy spin orbit scattering can achieve $\varepsilon = 4 \times 10^{-4}$, manly due to the low value of the ratio I/I_0: the cross section of such large angle deflections required to efficiently select spin is extremely low.

It is very important to observe that, from eq. 2.12, one limit of spin-orbit scattering arises: the component of the polarization in the direction of the incoming beam can not

[10]This combined requirement is, also from the theoretical point of view, a rather demanding one. As Kessler [37] notes, in fact, the difference in the differential cross sections for up and down-spins is very small and therefore it will have the maximum relative weight when the total differential cross section is minimum. This means that the maxima in the Sherman function will be found in correspondence of minima of the total differential cross section, as it is particularly evident in Fig. 2.4.

[11]For a more formal discussion, see Appendix I.

[12]$N_l - N_r$ can be, in a typical case, two order of magnitude smaller than N_l or N_r.

[13]While the Sherman function is calculated for an ideal scattering experiment, in a real detector other factors can arise that further reduce the efficiency of spin selection: contamination of the target, multiple elastic scattering, finite angular acceptance of the detectors, etc.

be measured. Independently of the orientation of the scattering plane, indeed, $\mathbf{v}$ is by definition laying on it and therefore its projection on the normal to the plane is identically zero. Many ways have been used to determine the longitudinal component of polarization, and one of them will be reviewed in the next chapter.

The first polarimeters to be realized, and to work effectively, were based on this process. In 1942, Shull et al. [41], working with extraordinarily low counts (the total electron count of the whole experiment was around 300 000 counts), could measure a real asymmetry. The spin-polarization of the free electron had been measured. Since then, the interest in the measure of electron's spin has never stopped to attract the attention of physics research: measuring the fourth degree of freedom of electrons can give valuable informations, that can range from study of nuclear reactions to the understanding of magnetism in condensed matter. The work on this kind of detectors has therefore been uninterrupted up to now, deepening the knowledge of all the processes and the technological solutions needed to increase the performance to a level unequalized by most of the instruments that can today be seen in a normal laboratory. Mott detectors are still the best-known and most stable polarimeters to date.

2.4 Low energy scattering with spin-orbit interaction

Mott detectors' relatively low efficiency has, anyway, triggered a strong effort to realize higher performance systems, and, in many cases, the radically innovative path of using different processes was chosen. The main aim of the research of further spin dependent scattering processes was the reduction of the scattering energy. High energies have two disadvantages: they are inconvenient to implement, because they require bulky high voltage systems and they reduce the FOM, because $I(\vartheta)$ is small.

The first attempts focused on simply reducing the energy of the primary beam. It was shown in many experiments [42] that significant asymmetries could be detected down to few hundreds eV. It is obvious that the hypotheses for the mathematical discussion of Mott scattering hold no more at these energies. The asymmetry in this process emerges because the DeBroglie wavelength of the electrons becomes comparable with the dimensions of the whole atom, so the scatterer now does not interact like a classical point like charge with the nucleus, but as a wave with the entire atom. A wave-like behaviour means that the scattered intensity will present interference patterns: the effect of the spin-orbit potential will be the creation of slightly different effective paths for electrons of opposite spin direction on the left and on the right. The differential elastic scattering cross section then displays an oscillatory behaviour as a function of ϑ and is sensitive to spin due to the presence of V_{SO} in the Hamiltonian. An example of such kind of measurements is shown in Fig. 2.4.

The theory necessary to account of such low energy scattering is anyway extremely complicated, and most of it is performed through numerical calculations [14] Also lowering the energy of scattering has some downsides, anyway:

[14] Low energy electrons are much more sensitive to the details of the whole atomic potential, for this reason more sophisticated models must be used. One example is the self consistent Hartree potential, which anyway requires the use of computers from the very first steps of the calculation [37].

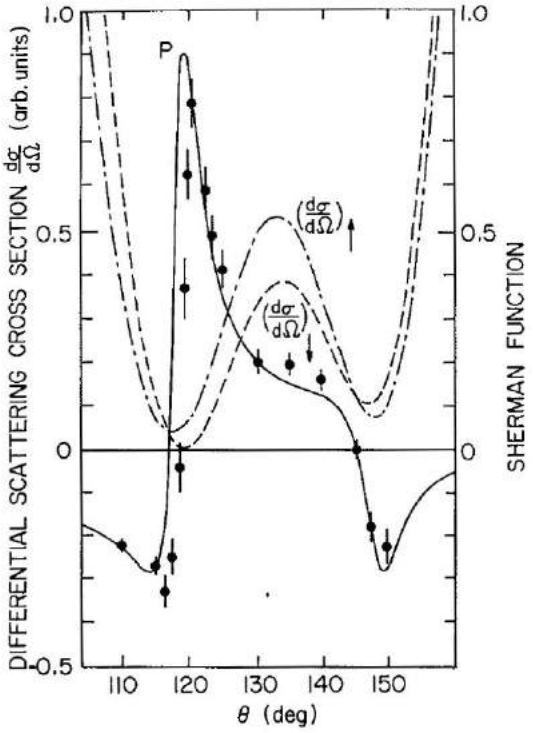

Figure 2.4. *Dashed curves: calculated elastic differential scattering cross sections for spin-up and spin-down electrons incident at 300 eV on Hg atoms. Solid curve: calculated $S(\vartheta)$. Dots: measured $S(\vartheta)$. From [40].*

> *"[...] the extrema with values of $|S|$ near 1 are extremely narrow [...]. Accordingly, $|S| \approx 1$ can be realized experimentally only if one works with very good angular resolution, which again means a reduction of intensity."*[15]

Furthermore, the scattered intensity and asymmetry become more sensitive to the contamination of the target.

This processes led to the construction of some prototypical polarimeters based on low energy scattering from mercury vapours or on amorphous films of gold continuously renovated by evaporation [40]. The difficulty in handling the targets, however, prevented the diffusion of such systems, but the attention on low energy spin-orbit scattering did not vanish, as other ideas emerged.

2.4.1 Spin Polarized Low Energy Electron Diffraction

If the primary energy is further decreased, the DeBroglie wavelength can become comparable with the inter-atomic distance, and if the position of atom on the surface is periodic (i.e. the target is a crystal), the resulting process is Low Energy Electron Diffraction (LEED). The interference between electrons' wave-functions is now not only due to the

[15] [37].

single atom's potential characteristics, but also to the effect of all other scattering centres. This means that the backscattered intensity is not a slowly varying function of the angle ϑ, but has sharp peaks corresponding to secondary beams. The number of spots that appear in the pattern is dependent on the primary energy: each spot enters constructive or destructive conditions as the energy varies. The curve of the intensity of a secondary beam as a function of its energy is the so-called *I-V curve* of which the lower panel in Fig. 2.5 is a very special case. As a general trend, however, the higher is the primary energy, the higher is the number of possible spots[16]. The spin-orbit effects are still present, but the formation of beams helps to focus much more intensity in the detectors:

> *"If one selects a diffraction maximum that occurs at such an angle, one has combined the high intensity of the diffraction peak with the high polarization of the scattered beam. In doing this the magic rule that high values of polarization are always associated with low scattering intensities [...] will be broken. [...] with low-energy electron diffraction, however, high intensity maxima can also be obtained at large angles where there are high polarization values."* [17]

This process is normally called *Spin Polarized Low Energy Electron Diffraction* (SPLEED), where the difference in intensity of opposing LEED spots are used to calculate asymmetry. In Fig. 2.5 the characteristics of the central reflected beam are shown. It is possible to observe that between 100 eV and 105 eV of energy of the primary beam, is present a sufficiently broad interval of energies in which both the asymmetry and the intensity are relatively high.

The theoretical modelling of this process is even more complicate than the previous one, because in this case the Dirac equation must be solved accounting of the whole crystal potential. A very important effort has been made by R. Feder and his group in this direction, which gave very good results when confronted with experimental data [43].

Despite the similarities with Mott scattering processes, the SPLEED has some relevant differences, due to the solid-state effects that determine the formation of reflected beams. First, the component of the polarization vector which is measured is not determined by the ingoing and outgoing beams, but by the crystal symmetry: a relevant parameter, which changes significantly the asymmetry, is the azimuthal angle (the angle describing the rotation of crystallographic axes around the axis of the primary beam). Furthermore, asymmetry is very sensitive not only to contamination[18] but also to geometrical distortions of the lattice at the surface. It has been shown that a contraction of 10% of the top-layer spacing with respect to the bulk distance can completely reverse asymmetry [37].

On this process are based the so-called *SPLEED detectors* patented by J. Kirschner group in 1979, which uses the diffracted beams from a tungsten crystal. This kind of machines have been developed to achieve a good efficiency, with $FOM \approx 1.6 \times 10^{-4}$ and are active competitors of Mott detectors in routine laboratory use.

[16] The actual number depends on the I-V curve of each individual spot.
[17] [37].
[18] In particular, hydrogen residual gas is particularly destructive for tungsten-based systems, as shown by [44] and [45].

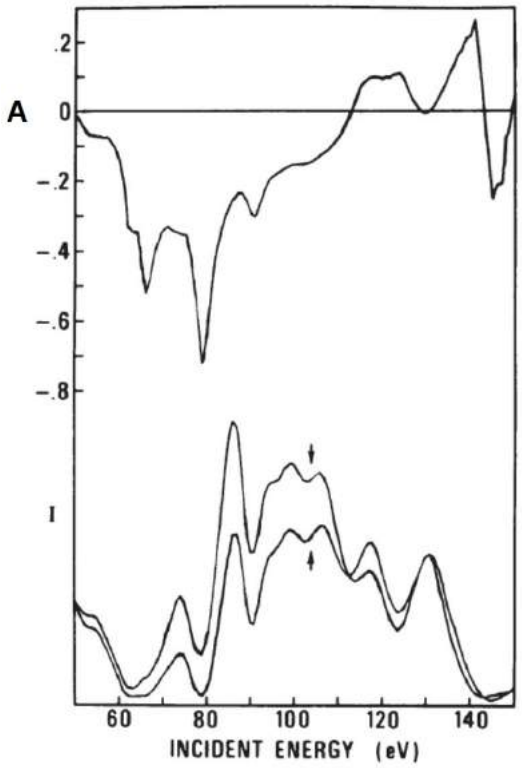

Figure 2.5. *Lower panel: scattered intensities in the central (00) LEED beam measured as a function of energy normalized to a* 100% *primary beam. Upper panel: The measured asymmetry. From [37].*

2.5 Exchange interaction

A more radical approach to the increasing of the efficiency is to choose a completely different spin-dependent process. Up to now, the interaction of electrons with a different particle (atom's nucleus) has been considered as a core mechanism, but as has been mentioned before, when electrons impinge on a solid they can interact (and they mainly do if the energy is low enough) also with target's electrons. It is therefore interesting to study what kinds of electro-electron processes can have some spin dependence.

When the interaction between two electrons is considered, the *symmetrization postulate* must be accounted. Elementary particles, such as electrons, are completely defined by their mass, charge and spin. Since all electrons have exactly the same value of these, they are said to be identical. This means that processes such as the ones shown in Fig. 2.6, if the scattering is elastic, cannot be distinguished in any way. In fact, the quantum mechanical description, considers them as happening simultaneously as a quantum superposition.

The fact that electrons are identical particles has some extremely relevant consequences in the description of the system. The two electrons' wave-function:

$$|\Psi(\mathbf{x_1}, \mathbf{x_2})\rangle \tag{2.14}$$

must account for the fact that if electron 1 is switched with electron 2, all the quantum mechanical observables are identical. The wave-function can have only two definite

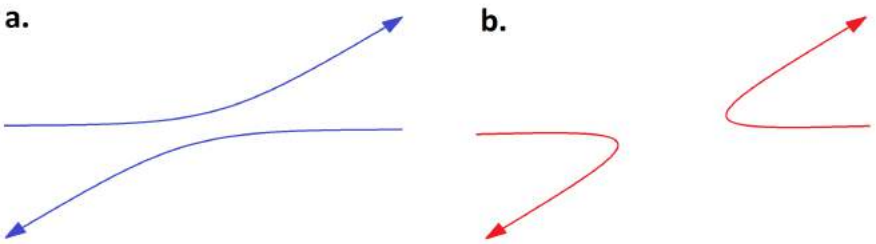

Figure 2.6. *Two indistinguishable electron-electron scattering processes.*

behaviours:

$$|\Psi(\mathbf{x_2}, \mathbf{x_1})\rangle = |\Psi(\mathbf{x_1}, \mathbf{x_2})\rangle \qquad \textit{symmetrical} \tag{2.15}$$

$$|\Psi(\mathbf{x_2}, \mathbf{x_1})\rangle = -|\Psi(\mathbf{x_1}, \mathbf{x_2})\rangle \qquad \textit{antisymmetrical} \tag{2.16}$$

The empirical observation that no mixed behaviours can occur is the *symmetrization postulate*. It can be shown that this is associated with the statistical behaviour of the particles (*bosonic* or *fermionic*) and this, in turn, can be related with their spin. Particles with half-integer spin are fermions and their wave-function must be antisymmetric with respect to particle index permutation. In building the two-particle wave-function by multiplication of the single-particle wave-functions of electron 1 ($|1\rangle$) and electron 2 ($|2\rangle$), the two combinations of definite symmetry must be considered: the symmetric state

$$|\Psi(\mathbf{x_1}, \mathbf{x_2})\rangle = \frac{1}{\sqrt{2}}(|1\rangle\,|2\rangle + |2\rangle\,|1\rangle) \tag{2.17}$$

and the antisymmetric one

$$|\Psi(\mathbf{x_1}, \mathbf{x_2})\rangle = \frac{1}{\sqrt{2}}(|1\rangle\,|2\rangle - |2\rangle\,|1\rangle) \tag{2.18}$$

and the last should be chosen to describe the fermionic behaviour. But $|\Psi(\mathbf{x_1}, \mathbf{x_2})\rangle$ can also be split in the product of two terms: one is the spatially dependent wavefunction and the second is a spin function independent of the spatial coordinates.

$$|\Psi(\mathbf{x_1}, \mathbf{x_2})\rangle = \phi(\mathbf{x_1}, \mathbf{x_2})\chi(m_{s1}, m_{s2}) \tag{2.19}$$

The antisymmetric requirement then demands that if $\phi(\mathbf{x_1}, \mathbf{x_2})$ is symmetric then $\chi(m_{s1}, m_{s2})$ must be antisymmetric and vice versa. If one uses the symbolic notation: $|\uparrow\uparrow\rangle = \chi(1/2, 1/2)$, $|\uparrow\downarrow\rangle = \chi(1/2, -1/2)$, $|\downarrow\uparrow\rangle = \chi(-1/2, 1/2)$ and $|\downarrow\downarrow\rangle = \chi(-1/2, -1/2)$; then the symmetric forms of χ are

$$\chi_t = \begin{cases} |\uparrow\uparrow\rangle \\ \dfrac{1}{\sqrt{2}}(|\uparrow\downarrow\rangle + |\downarrow\uparrow\rangle) \\ |\downarrow\downarrow\rangle \end{cases} \tag{2.20}$$

and are the triplet states. The only possible antisymmetric form is

$$\chi_s = \frac{1}{\sqrt{2}}(|\uparrow\downarrow\rangle - |\downarrow\uparrow\rangle) \tag{2.21}$$

i.e. the singlet state. The total spin operator, defined as $\mathbf{S}_{tot} = \mathbf{S}_1 + \mathbf{S}_2$, yields a total spin quantum number $s = 1$ for the triplet states and $s = 0$ for the singlet state.

The antisymmetry of the wave-functions has relevant effects in electron-electron scattering. From standard scattering theory, the stationary diffusion spatial wave-function has the asymptotic form:

$$\Phi(\mathbf{x}_1, \mathbf{x}_2) = e^{i\mathbf{k}\cdot\mathbf{x}} + f(\vartheta)\frac{e^{i\mathbf{k}\cdot\mathbf{x}}}{r} \tag{2.22}$$

where $f(\vartheta)$ is the *scattering amplitude*, ϑ is again the scattering angle, $\mathbf{k} = \mathbf{k}_1 - \mathbf{k}_2$ is the exchanged wave-vector and $\mathbf{x} = \mathbf{x}_1 - \mathbf{x}_2$ is the relative position, while r is the relative distance. This expression substantially states that the spatial wavefunction will be given by an incoming beam described as a plane wave in the first term, and the spherical outgoing scattered wave, modulated by the function $f(\vartheta)$. In the scattering amplitude all the details of the effective interaction are enclosed. The symmetrization of this function yields:

$$\Phi(\mathbf{x}_1, \mathbf{x}_2) = e^{i\mathbf{k}\cdot\mathbf{x}} + e^{-i\mathbf{k}\cdot\mathbf{x}} + [f(\vartheta) + f(-\vartheta)]\frac{e^{i\mathbf{k}\cdot\mathbf{x}}}{r} \tag{2.23}$$

for the singlet singlet state and

$$\Phi(\mathbf{x}_1, \mathbf{x}_2) = e^{i\mathbf{k}\cdot\mathbf{x}} - e^{-i\mathbf{k}\cdot\mathbf{x}} + [f(\vartheta) - f(\pi - \vartheta)]\frac{e^{i\mathbf{k}\cdot\mathbf{x}}}{r} \tag{2.24}$$

for the triplet state. The differential cross section is then given by the squared modulus of the scattering amplitude:

$$\frac{d\sigma}{d\Omega} = |f(\vartheta) \pm f(\pi - \vartheta)|^2 = |f(\vartheta)|^2 + |f(\pi - \vartheta)|^2 \pm 2\mathfrak{Re}[f^*(\vartheta)f(\pi - \vartheta)] \tag{2.25}$$

Therefore again the cross section depends on the spin state[19] (singlet or triplet) of the incoming and target electrons as shown in Fig. 2.7.

To have a significant dominance of this scattering process over the others, it is necessary that the incoming beam impinges on a high number of electrons with the same spin. The convenient condition is then realized with solid state targets made of transition metal

[19]The way chosen to show this is the quickest and is again lacking of formal rigour. This problem can be approached in many ways: for example, one can study the problem of electron-electron interaction in a mean field approach (Hartree-Fock method). Inserting a simple Hamiltonian $H_{1,2} = e^2/r$ allows to calculate different energies for triplet and singlet state, obtaining a final expression of the energy which is dependent on the spins of the two electrons:

$$E = K_{1,2} - \frac{1}{2}J_{1,2} - 2J_{1,2}\ \mathbf{S}_1 \cdot \mathbf{S}_2 \tag{2.26}$$

with

$$K_{1,2} = \int \phi_1^*(\mathbf{x}_1)\phi_2^*(\mathbf{x}_2)H_{1,2}\phi_1(\mathbf{x}_1)\phi_2(\mathbf{x}_2)d\mathbf{x}_1 d\mathbf{x}_2 \tag{2.27}$$

and

$$J_{1,2} = \int \phi_1^*(\mathbf{x}_1)\phi_2^*(\mathbf{x}_2)H_{1,2}\phi_1(\mathbf{x}_2)\phi_2(\mathbf{x}_1)d\mathbf{x}_1 d\mathbf{x}_2 \tag{2.28}$$

$J_{1,2}$ is the *exchange integral*. It can then be found an *exchange potential* $V_{ex} \propto \mathbf{S}_1 \cdot \mathbf{S}_2$, and scattering theory can be developed considering its effect.

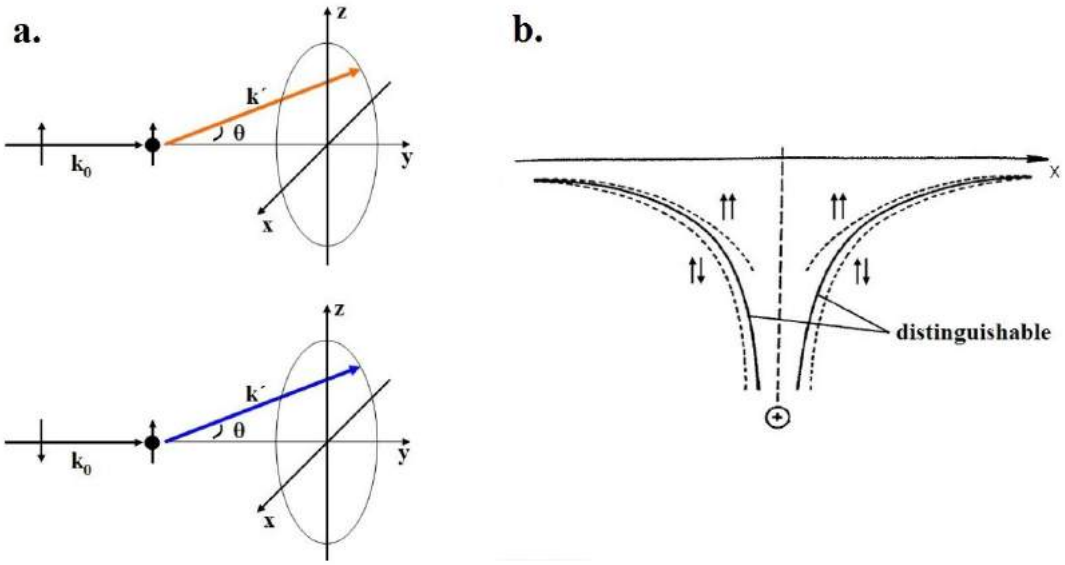

Figure 2.7. *a. Vectors involved in exchange potential. b. Scheme of the exchange potential. Diagram built in analogy with Fig. 2.1 panel b. The dashed curves represent the potential for a spin singlet (↑↓) state and for a spin triplet (↑↑) state. The solid line represents the Coulomb interaction potential of distinguishable particles (for spin-0 particles or neglecting the spin orbit effect). Adapted from [3].*

atoms. Transition metals are used both because are relatively light atoms, thus minimizing the spin-orbit interaction (which is now undesired and it will soon be explained why) and because they possess a high number of electrons with the same spin in the outermost atomic shell. For this last property, together with exchange coupling (see note 19) throughout the solid, Fe, Co and Ni are macroscopically magnetic.

Applying an external magnetic field, the spins will orientate in the field direction, and if the field is removed they will remain in this condition (*remanence magnetization*). It is thus possible to send electrons on the solid in absence of the external magnetic field (which would disturb the trajectories through the Lorentz force), let them interact mainly with the exchange potential and then count their number. If the remanence magnetization is reversed, and the electrons are again counted, it is possible to observe an asymmetry as shown in Fig. 2.8.

Mathematical formalism can be built on analogy with spin-orbit scattering. The differential cross-section (see eq. 2.7) can be written as:

$$\left(\frac{d\sigma}{d\Omega}\right)_{ex} = I(\vartheta)\left[1 + S^{(ex)}(\vartheta)\mathbf{P}\cdot\hat{\mathbf{m}}\right] \tag{2.29}$$

where again $I(\vartheta)$ is the cross-section in absence of the exchange coupling and is independent of incident spin or surface magnetization, $\mathbf{P}$ is the primary beam polarization, but $\hat{\mathbf{m}}$ is a unit vector representing the direction of the target's magnetization, not any more correlated with the scattering plane. Normalized asymmetry (see eq. 2.10) can also be

written as:

$$A_{ex} = \frac{I_{m\uparrow} - I_{m\downarrow}}{I_{m\uparrow} + I_{m\downarrow}} \tag{2.30}$$

where $I_{m\uparrow}$ is the intensity measured with magnetization in the "up" direction and $I_{m\uparrow}$ is measured with magnetization in the "down" direction. Through the cross section in eq. 2.29 it is possible to find:

$$P_m = \frac{1}{S_{eff}^{(ex)}} A_{ex} \tag{2.31}$$

where P_m is the component of polarization in the magnetization direction and $S_{eff}^{(ex)}$ represents the effective Shermann function of the system. The exchange polarimeter is therefore sensitive to the polarization component along the target magnetization axis. Again, as in spin-orbit scattering, the polarization can normally be measured only in two directions normal to the primary beam propagation direction, because the targets are realized by thin films of metal, whose magnetization can lay only in the plane of the film.

Despite the close similarities, spin-orbit and exchange scattering have significant differences. While in spin-orbit scattering there is an intrinsic left-right asymmetry arising from the geometry of scattering, in exchange potential only relative spin orientation is relevant, therefore only an up-down (referred to the magnetization of the target) exists. Indeed, considering the difference between b. panels of Fig. 2.1 and 2.7 it is evident that while the exchange potential is symmetric with respect to the inversion of the x coordinate (left-right inversion), the spin orbit one is not. The spin-orbit interaction is also independent of the magnetization of the target, therefore it is considered as a spurious asymmetry, that can rigidly shift the zero of the exchange measurement. Spin-orbit effect can be anyway be evaluated through a target calibration procedure[20] and then removed from the measurement. These differences are extremely important because they effect the design of detectors based on such processes in a very deep way, making them efficient in different conditions with respect to spin-orbit based systems.

2.5.1 Very Low Energy Electron Diffraction

Exchange scattering polarimetry has been tentatively realized with many different geometries and designs ranging from high energy Møller scattering to transmission through a Fe thin film. However the most efficient and easily achievable way is again to reduce the energy and use the focusing power of diffraction. As the path followed for the SPLEED by Kirschner had demonstrated, in effect, the interference processes involved in the formation of the LEED pattern are much more sensitive to small corrections to the Coulomb potential such as exchange or spin-orbit scattering and, at the same time, the higher backscattering probability and the collimation of outgoing beams increase the ratio (I/I_0).

But now it is possible to go even further: the exchange potential in principle needs only diffraction one spot, and asymmetry sequentially measured reversing the magnetization of the target crystal. It is therefore possible to use only the (00)-beam, which is the specular reflection of the primary and has the highest intensity of the whole LEED pattern. Clearly,

[20] [3].

the scattering geometry has to be adjusted with respect to the normal incidence design considered up to now, thus giving the scheme depicted in Fig. 2.8.

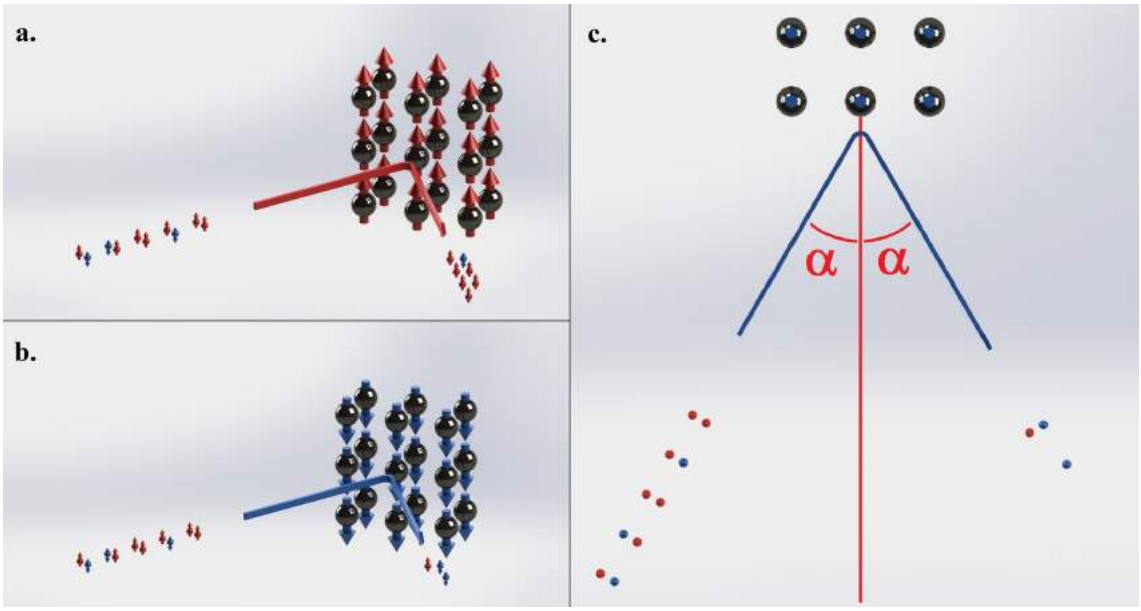

Figure 2.8. *Cartoon picture of exchange scattering. a. The configuration for the measurement of up-spins: the atoms are magnetized in the up direction and the scattered beam contains mainly up-spins. b. Configuration for the measurement of the down-spins: target magnetization is reversed and the scattered beam contains mainly down-spins. c. Top view of panel b. showing the incidence and reflection angle* α.

The primary beam is sent off-normal with the respect to the surface of the crystal of an angle α, so that the reflected electrons' momenta will also make an angle α with the normal, but in the opposite direction, thus making the (00) beam distinguishable and physically measurable. Furthermore, if one is interested only in the (00) reflection, it is possible to reduce the energy until no other beams are present in the LEED pattern, so that all the intensity coming from elastic processes is focussed in this spot. This happens at energies as low as 5-20 eV and this asymmetry, together with high reflectivities, was used in early works to realize spin-polarimeters based on reflection from Fe(100)[21], obtaining spectacular[22] FOM $\approx 1 \times 10^{-2}$.

At such low energy, anyway, the electrons are subject to many interactions, and the description is not as simple as the previous paragraphs suggested. For example, the crossing of the target's surface potential barrier is extremely important in the formation of the asymmetry signal and, as in the SPLEED, the contamination of the surface can reduce the signal until it vanishes. A solution has however been found by Bertacco and Ciccacci [49], which discovered that if Fe is covered by a monoatomic layer of oxygen adsorbed on the surface in a well-ordered fashion (Fe-O(1x1)p surface *passivation*), asymmetry is not

[21] [46], [47], [48].

[22] To relate correctly the FOM of exchange-based polarimeters with the one of spin-orbit-based it is necessary to divide by a factor of two the former (which measures serially the up and down signal in one detector), because the latter acquires simultaneously the left and right channels.

reduced (or eventually enhanced), but the system is much less sensitive to contamination[23]. Furthermore, the whole band-structure of the solid is involved in the process. In fact a qualitative picture can be used to describe the process, based on Fig. 2.9.

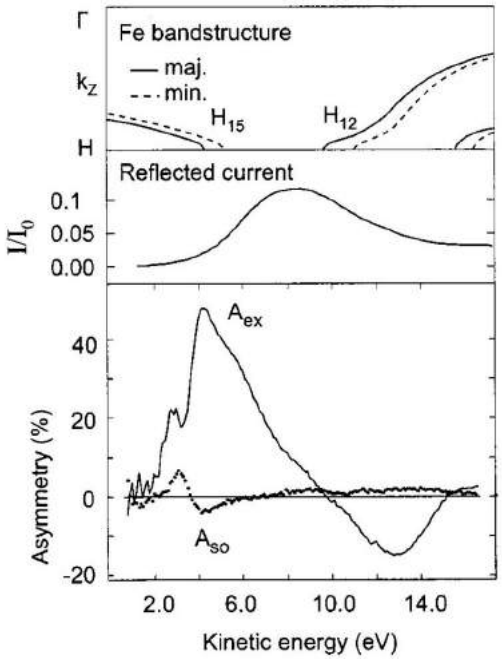

Figure 2.9. *Top panel: bandstructure of Fe-O(1x1)p. Central panel: reflectivity as a function of energy expressed as the ratio I/I_0. Bottom panel: Asymmetry due to exchange as a function of energy. The smaller (but still present) asymmetry due to spin-orbit is also shown. From [49].*

The reflectivity of a surface, in fact, depends strongly on the empty-states band-structure of the solid: as can intuitively be guessed, if an electron has an energy corresponding to a solution of the wave equation in the solid, it will very easily enter in the crystal and propagate inside it (i.e. it will be absorbed); on the contrary, if the energy of the electron corresponds to a gap in the band-structure, solutions for the electron propagating in the solid do not exist, and it will be strongly reflected from the surface. As it can be seen from the first panel in Fig. 2.9, displaying the empty states of Fe(100) surface covered with a single layer of oxygen, the band-structure of this system has a gap between 5 and 10 eV. In the middle panel it is shown that the reflectivity radically increases in this interval, giving a very high value of I/I_0.

Exchange potential has an effect also in the band-structure, as it reduces of few eV the band for electrons aligned with the magnetization (*majority electrons*) and increases that of the ones in the opposite direction (*minority electrons*) thus the gap is spin-dependent and, if one chooses an appropriate primary energy (around 5-6 eV), one of the spin states of the primary beam (the one anti-parallel to the magnetization) will be able to enter the solid and be absorbed, but the other will be strongly deflected (the one parallel to

[23] As the construction of a target with this structure will be one of the experiments of this thesis, it will be described more accurately in the following.

the magnetization). Reversing the magnetization, it will thus be possible to measure an asymmetry associated with the polarization of the primary beam, as shown in the last panel of Fig. 2.9. While this is far from a complete quantitative explanation, it is anyway able to explain why Iron is normally chosen as a target: it has the largest splitting of the band-edge (2.5 eV) of the three ferromagnetic transition-metals.

Chapter 3

Modern spin detectors

In this chapter, a review of the most recent spin detectors will be given. Particular attention will be dedicated to systems carrying the legacy of the long-standing research described in the last chapter; and, at the same time, to the machines built to achieve high temporal and energy resolution, in close similarity with the Ultraspin project. The advantages and disadvantages of each detector from the point of view of the project's aim will be described, and the final choice of a classical Mott detector will be justified.

3.1 High energy detectors

The most diffused detectors for the measurement of spin-polarization are based on high energy spin-orbit scattering. From the first measurement realized by Shull et al. [41], this kind of systems have undergone a very long and challenging process of development. Working with very small signals, any progress is obtained at the price of an extremely delicate synthesis. New modifications should improve the operation reducing as little as possible the effect of the results achieved previously.

The gross scheme is identical for all systems: the electrons to be analysed are collected by a system of electrostatic lenses that organizes a well focused beam, then enter an acceleration stage, which brings them to the scattering energy. Only electrostatic lenses are used in this systems because the polarization vector is extremely sensitive to magnetic fields and the information that it contains can easily be destroyed by magnetic lenses.

Electrons are then sent on the target, backscattered at 120°[1] and detected by electron counters. A significant difference arises, however, in the potential at which the detectors are held: if the detectors are at the same potential of the target foil, the electrons travel from the target in a field free environment and one speaks of **Classical Mott detector**; if, on the other hand, the detectors are at the ground potential (or close to it), and electrons travel in a decelerating field, the system is called **Retarding-potential Mott detector**. A short discussion of the most recent advancements in these two categories will be given in the following.

[1] In this position, the highest asymmetry is achieved, as can be noticed from Fig. 3.1.

3.1.1 Compact Classical Mott

This kind of polarimeters was developed in its most recent version by the Surface Magnetism Group of V. N. Petrov and coworkers [50]. This group realized a system that is called *Compact Mott detector*, of which a cross section is shown if Fig. 4.5. The system operates at 40 keV of primary energy, a significant reduction with respect to the previous systems, which used a higher energy of 100 keV[2]. The acceleration is generated by two concentric hemispherical electrodes with a very small aperture in the direction of the target, normally constituted by a heavy element characterized by a large spin-orbit. This configuration has proven to be the most effective in collimating the high energy beam on the target thus making this system extremely stable with respect to small shifts of the beam [51]. A polycrystalline gold film is chosen because it is highly resistant to contamination of the surface. Heavier targets made of Thorium have been used in other cases (see sect. 5.1.2), and have been shown to have a higher asymmetry (about 20-30 % higher [40]), but were not chosen for this machine because they are more reactive and require periodic cleaning: this, together with the inconvenience added by radiation safety rules, makes less convenient the implementation in a laboratory.

The reduction of the energy was achieved thanks to a series of very important factors: firstly, it was observed that the Shermann function of gold is reduced only of a 12% when the primary energy goes from 120 keV to 50 keV [3] as shown in Fig. 3.1.

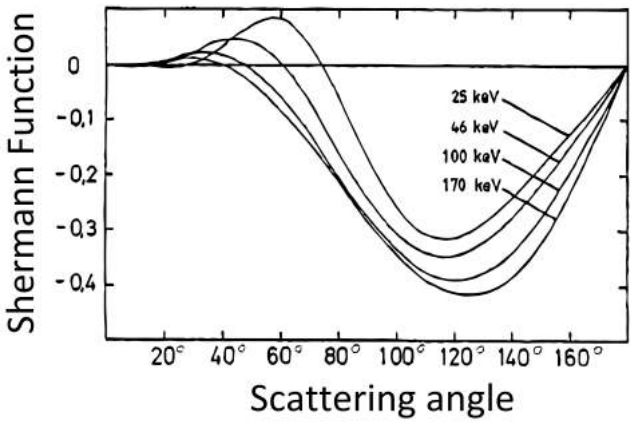

Figure 3.1. *The Shermann function of gold at energies between 170 and 25 keV. From [51].*

The reduction of S_{eff} is anyhow more severe, but can be compensated by a reduction of the thickness of the target. The lower the thickness, in fact, the closer the S_{eff} is to the theoretical Shermann function, because the multiple scattering events are suppressed. However, mechanical stability and the reduction of the reflected beam set a limit to the

[2] As is evident in Fig. 3.1, for the 100 keV scattering, the Shermann function is larger, and thus the signal-noise ratio is higher. For this reason, old polarimeters, featuring less efficient detectors, were forced to work in this regime, having to face significant safety challenges for high voltage.

[3] This is discussed in [51] and [52], in which the results of theoretical works (like the ones shown in Fig. 3.1) are shown and further corroborated by accurate experimental measurements.

thinning procedure. The Surface Magnetism Group managed to build relatively robust gold target films on Formvar[4] with a thickness of 80 nm.

Secondly, the efficiency of the system is further improved by the fact that four channels are acquired: four detectors are mounted in a cross configuration and thus able to measure the two asymmetries associated to the two accessible independent components of the polarization, as shown in Fig. 3.2.

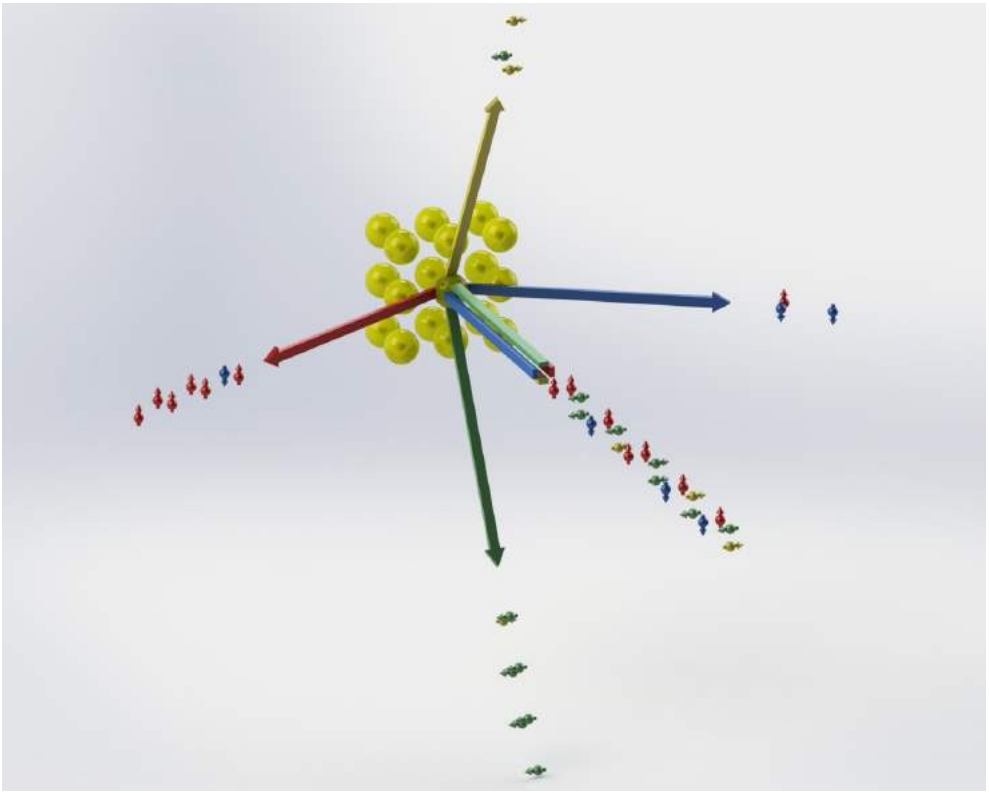

Figure 3.2. *Simplified picture of simultaneous measurement of the two transversal component of polarization. The asymmetry between green and yellow arrows is associated with the component of* **P** *in the horizontal direction, while the one between red and blue arrows is connected with the vertical component.*

Finally, a significant improvement was obtained by the implementation of very high level electron detectors and preamplifying electronics, able to deliver very clean signals and thus to work with uncompromising signal to noise ratio even in regimes in which S_{eff} is smaller. It is worth describing in deeper detail these elements because they differ significantly from the channeltron or microchannel plate (MCP) assembly, typical of standard electron counters for spin-integrated electron spectroscopy.

[4]Formvar is a kind of polyvinyl resin that is able to sustain very thin free-standing films. It also has a very high transparency to electrons, so that the background of electrons backscattered by the substrate is extremely low. This resin was designed for TEM applications.

Electron detectors

The scattered beam is collected and measured by four Passivated Implanted Planar Silicon detectors. To describe them it is probably best to follow the steps of the construction process (described for the firs time in [53]), while observing Fig. 3.3. These detectors are constituted by wafers of n-doped Silicon which is first exposed to oxygen to create a thick and rugged insulating layer (*passivation*). In the area which is meant to be sensitive to electrons (a circle of about 1 cm diameter) the oxide is removed by photolitography, both on the top layer and on the bottom. The bottom side is then n-doped by implantation of arsenic ions, while the top layer is p-doped by implantation of boron. This allows to have a pn-junction with extremely abrupt transition from the p side to the n side. To the junction is then applied a strong reversed potential (50-90 V), which creates a depletion region.

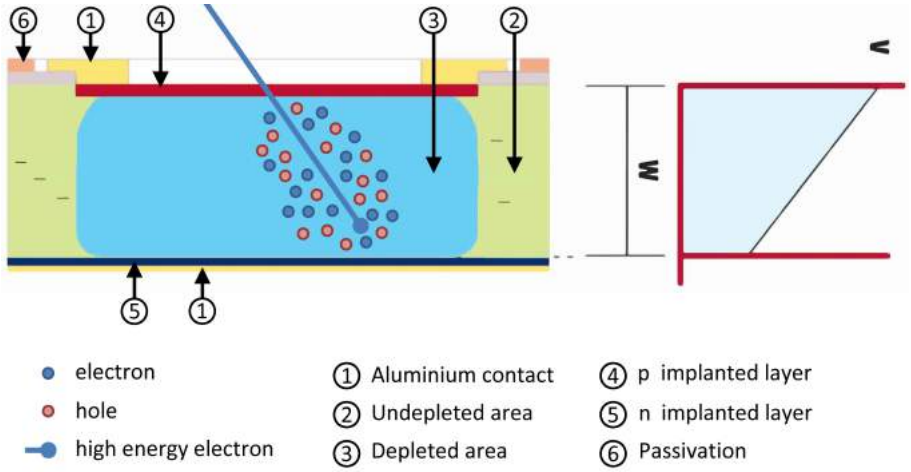

Figure 3.3. *Cross sectional scheme of a PIPS detector. The graph on the side shows the voltage (**V**) across the wafer thickness (**W**). Some electron-hole pairs generated by the arrival of a high energy electron are shown. The holes will flow to the bottom contact, and electrons to the top.*

When a charged energetic particle enters the junction from the top side, it loses energy by creation of electron-hole pairs. In the configuration used in this case, the thickness of the depletion region is larger than the stopping length of the particle in the material, so that the particle loses all its energy in the depletion region (from the signal, it will then be possible to retrieve information about the total energy of the particle). The electrons and the holes are then separated by the electric field present in the depletion zone and collected by the opposite electrodes. A charge sensitive preamplifier is then able to convert the charge pulse in an analogic voltage signal. Fortunately, the energy required to excite a pair is almost independent of the incoming particle's energy, so the height of the charge pulse is proportional to its energy.

This energy resolution comes at a price, however: PIPS are relatively slow particle detectors. Considering signal formation as a function of time, indeed, it will be clear from the dynamics described above that the charge pulse can be relatively sharp[5] (i.e. the *rise*

[5] As shown in [54], depending on the detailed structure of the PIPS, the Full Width at Half Maximum

time is short), but the detector will restore its original state in a rather long time (i.e. the *recovery time* is long). This is because the electrical behaviour of the system, with its thin implanted layers and thick depletion zone, closely resembles that of a condensator, which is rapidly (and only partially) discharged by the incoming charge pulse, but is slowly recharged according to the usual exponential recharge law[6]. If two electrons enter in the PIPS separated by a time interval smaller than the recovery time, they will be counted as one, and the signal will be altered. Therefore the PIPS detector must be operated at relatively low rates of incoming particles, i. e. less than a million per second.

It is also clear that the only sensitive region of this detectors is the depletion region: if a pair is generated in the p-doped part, where the field is vanishing, it recombines giving no charge signal. Therefore the thickness of the p-doped part (also called *dead layer*) is extremely important in terms of performance of measurement of energy: this is true in particular for electrons in the range of energies 1-10 keV which lose energy easily in the matter, and thus are very likeable of wasting a significant part of their energy in the dead layer. For this reason the PIPS detector brought a revolution in the field of the low-energy particle detectors, reducing the dead layer to a thickness under 50 nm and allowing for depletion regions four orders of magnitude bigger, around 300 μm. The passivation, reducing the leakage current to very low values even in high bias condition, further reduces the presence of noise.

The combination of all these characteristics allowed to achieve higher resolutions in the measurement of energy, which in turn means higher capability of discriminating the elastically scattered electrons in the present application. The ability of the detector to evaluate internally the energy of the particles is indeed vital for the working of this machine: without the possibility of applying retarding fields there is no other way in which the elastic electrons could be selected over the unpolarized background.

High voltage design and detector structure

PIPS detectors must be held at the same potential of the inner electrode to let the electrons drift in a field free space, and this creates some complicated issues. These problems are, however, assessed in a very efficient way, managing to reduce the spatial obstruction typical of high voltage systems. The main difficulties arising are two:

- the read-out and preamplification electronics (in direct electrical contact with the detectors) is supplied by a normal DC current, but its reference potential should be a 40-50 keV fixed potential and not the normal ground,
- the electronics output is also floating at 40-50 keV, so a way must be found to decouple it from the bias potential.

of the charge pulse can range between some hundred picosecond to some nanoseconds.

[6]There is then a characteristic time $\tau = RC$ where R is the resistance with which the detector sees the bias supply and C is the capacitance of the PIPS. The resulting τ depends strongly on the details of the detector design and on its connection with the bias power supply: in the particular application of Compact Mott detectors, it is around some microseconds, because safeguard of components against high voltage requires high values of resistance. Other uses of PIPS, however, can push total time resolution down to few nanoseconds [54].

The first problem has been solved through the development of a specifically designed power supply, provided with two output cables, both at a controllable high voltage bias from ground. Between the two cables the power supply is able to generate an alternate current (5 V peak-to-peak). This is then converted by a rectifier in a DC current once it reaches the floating electronics. It must be observed, anyway, that this solution is not the best possible considering the highly demanding application. The propagation of the supply current in alternated form through the cables (however shielded), in fact, exposes it to any kind of harmonic noise which can have significant effects on the sensitive preamplifying circuitry. Other solutions are possible and have been attempted, as it will be discussed in the following. The output signal problem is, instead, solved by converting it in a light pulse which is sent to the data acquisition computer through optical fibres. The fibres, being made of insulator (glass or plastic) completely decouple the signal from high voltage.

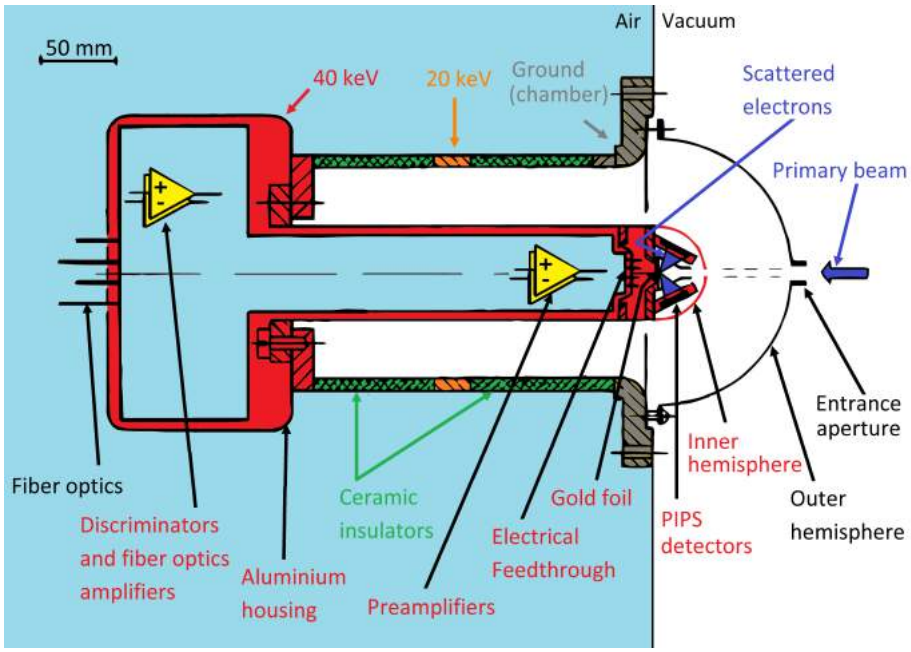

Figure 3.4. *Cross sectional scheme of a Compact Mott detector. The colour code helps to understand the different potentials in the system. In red are marked the parts floating at 40-50 keV. In orange is displayed the intermediate ring at 20 keV. The parts connected to the chamber ground are coloured yellow. The insulating ceramics are displayed in green. Adapted from [50].*

The detectors are placed inside the inner spherical electrode, facing the gold foil, and receive the scattered beam. They are positioned so that the angle of scattering is $\vartheta = 120°$ with respect to the centre of the detector, but they are placed very close to the target so that their collection angle is around 48° and the ratio I/I_0 is improved as much as possible. The signal is then sent through a uhv-feedthrough to the high-voltage air-side. This is constituted by an aluminium box with the shape of a T: in the vertical part is contained the preamplifying electronics. This section acts as a linear charge-to-voltage amplifier, that receives a bunch of charges (<20 fC) and converts it in a easily measurable analogic voltage pulse of proportional height. It is composed by four independent identical circuits, that amplify simultaneously the signals coming from the PIPS detectors.

The signal is then sent in the horizontal part of the T where the four discriminators are housed: these are the elements that allow only signals from elastically scattered electrons to pass and be counted in the data acquisition computer. Thanks to the fact that the intensity of the charge pulse (and consequently, after preamplification of the voltage peak) is proportional to the energy of the scattered electron, it is sufficient to let pass only pulses higher than a certain threshold and to block the others. A low threshold implies that electrons suffering severe energy losses are accepted, thus increasing the number of counted signals, but deteriorating the signal-noise ratio of the asymmetry (S_{eff} is reduced). On the other hand, increasing the threshold selects more and more strictly elastic electrons, enhances the asymmetry, but reduces I/I_0, lengthening the time required to reduce the statistical noise. Obviously, a compromise must be found, adapting to the experimental conditions: the discrimination threshold can indeed be controlled manually by a potentiometer[7].

The selected signals are then sent in electrical-to-optical converters in which the optical fibres can be plugged through a standard connector. The signal is then carried away from the high voltage region through the fibres. A general purpose board with mating optical-to-electrical converters is then able to count the light pulses from each one of the four channels in a controlled time window. Through computer analysis is then possible to calculate the asymmetry and finally (after calibration) the polarization of the primary beam.

In the horizontal part of the T-shaped aluminium box is also plugged the connector of the high voltage power supply, and immediately after it are positioned the rectifiers that convert the AC current from the supply in the DC alimentation current for all the electronics systems in the high voltage region. The aluminium T is welded on two rings of very thick ceramics insulators which are in turn welded on a CF 100 flange that can normally be bolted to a UHV chamber. This part is mechanically delicate, because the whole weight of electronics and aluminium box is leaning on the brittle ceramics, and in particular on the welding with metal. The two rings of insulator are separated by a copper ring, connected with two very high resistance ohmic resistors to the aluminium box and to the chamber (ground). The two resistors work as a voltage divider, keeping the copper ring at one half of the voltage of the aluminium box, thus reducing the voltage drop at the edges of the insulator and reducing the risk of dangerous sparking. The detector is normally shielded with a metallic cylinder connected to ground and covered with a cap that allows only optical fibres and power supply cables to sort out. The whole system, despite its complexity, is fitted in a volume of less than 0.2 m^3 including the metallic shield (i.e. a cylinder of 30 cm height and 20 cm diameter).

Recent applications

The compact classical Mott system developed by the Surface Magnetism Group is now considered one of the most reliable systems of spin detection. Further development of this kind of machines can now be more focused on further improvements of the detectors:

[7] Obviously, for high voltage handling safety, the potentiometers con be moved using a very long plastic bar that insulates the operator from the high voltage.

Petrov and coworkers have already realized a new machine with much faster detector response by substituting PIPS with NaI scintillators cascaded with channeltrons [55] and a system able to perform coincidence measurements to study entangled states in condensed matter [56].

Being coupled with an unprecedented reduction of the bulk dimensions, it has been applied in many extremely high level research machines: one example for all is the COPHEE (COmplete PHotoEmission Experiment) endstation, built at SLS by a collaboration between the APE beamline team (Elettra Sincrotrone Trieste) and the group of J. Osterwalder from University of Zürich, Irchel. In that machine, all the possible information that can be extracted from an electron is measured: the energy, the in-plane momentum and the spin. When the electrons are photoemitted, they are collected by a system of electrostatic cylindrical lenses (Einzel lenses), which send them in an hemispherical analyser.

An hemispherical analyser is constituted by two concentric hemispherical electrodes in which, by electrostatic deflection, electrons are selected in energy so that only an extremely narrow interval of energies (depending on the model characteristics, $\Delta E \approx 1.8meV$ can be achieved) around the chosen one can propagate beyond a pair of controllable exit slits. The central energy can be regulated by changing the voltage of the two hemispherical electrodes, while the resolution is increased (again at the expense of statistics) by reducing the slits' aperture. The normal procedure to acquire a spin integrated spectrum is to scan the central energies continuously, measuring with a channeltron or MCP the number of electrons transmitted out of the exit slits at each value of E.

In COPHEE, instead, energy-selected electrons are picked up by another electrostatic deflector lens and sent in the polarimeter. Here two orthogonal Motts are used (with an electrostatic switch lens that passes the beam from one to the other) to measure all the three components of the spin-polarization[8]. Electrostatic lenses are used at any point of the system because they allow to modify electrons' trajectories without affecting the spin state, that, just as an angular momentum, keeps its orientation in the laboratory coordinate frame during the flight. The in plane components of the electrons' momentum are scanned by varying the angular position of the sample surface with respect to the analyser position. This system was able to perform very important measurements both on magnetic and on non-magnetic samples as, for example, the spin-resolved fermi surface mapping of gold, with the resolution of the spin-orbit split dispersion of the surface states (Rashba splitting) [10]. It must be considered, anyway, that selecting only a narrow energy window in the ensemble of electrons reduces the I_0 entering in the detector and thus reduces the FOM of the energy and spin analyser considered as a whole, thus increasing the time demand of accurate measurements.

Compact classical Mott detectors have been also applied very recently in time-resolved measurements. This kind of experiments consists in applying the pump-probe photoemission technique described in Introduction with spin-resolution. Several effects are expected to be observable in such new research field. One fundamental process, anyway, characterizes the first observations: as in the optical measurements (TR-MOKE), the spin polarized signals (in particular the ones arising from exchange interaction in the solid) are rapidly

[8]This assembling, named *Compact Classical Mott Vectorial Polarimeter* will be descibed in greater detail.

quenched. After the quenching, relaxation phenomena follow, with different behaviours depending on the material.

Two of these systems are now efficiently working: one in the laboratories of the University of Regensburg (professor's Christian Back chair) and one, realized by the group of Y. Acremann from ETH Zürich. As shown in Fig. 3.5 a. the Regensburg system uses as a source a frequency quadrupled Ti:sapphire laser, and the analysis of spin is performed by a single Mott detector without a real energy filtering[9]. Acremann's system, on the other hand, uses a Ti:sapphire laser only as a pump, and a FEL pulse as a probe; furthermore, the electrons are selected in energy by an hemispherical analyser before entering the Compact Classical Mott detector.

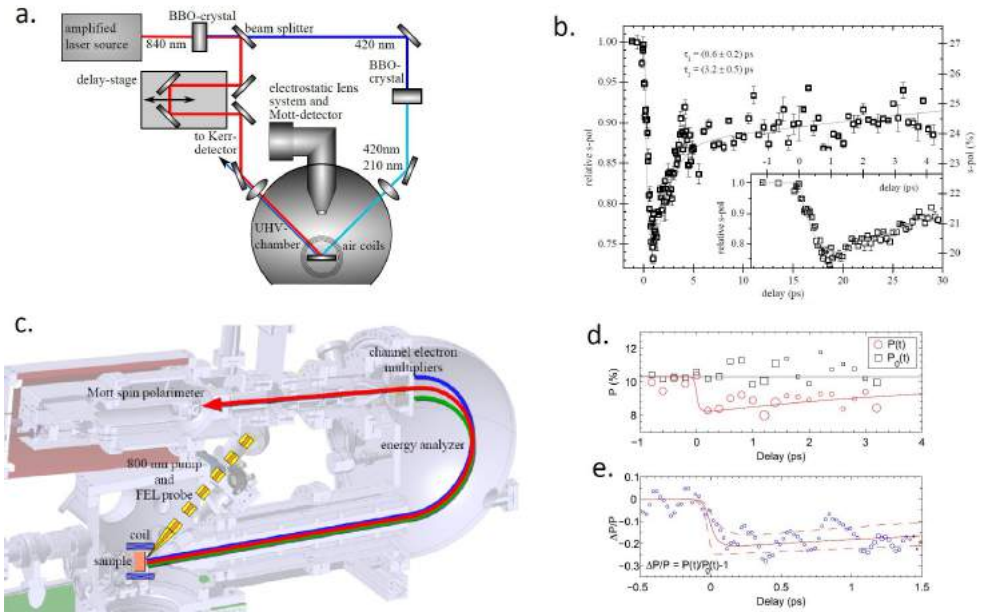

Figure 3.5. *a. Block diagram of the system realized in Regensburg. The pulsed laser light is emitted at 840 nm. The beam is then split, and one part (pump) is sent to a controllable delay line, while the other (probe) is frequency quadrupled by two BBO crystals. The two beams are then focussed on the sample. The electrons are then collected by the electrostatic lenses and measured in the Mott detector (not explicitly shown). From [57] b. The results of a measurement with the system in a: the quenching generated by the pump pulse and the successive recovery are displayed as a function of time delay in this 13 hours long measurement on a Fe/W(110) sample. On the left ordinate is shown the relative polarization, used to estimate the variation with respect to the equilibrium one. On the right ordinate, absolute polarization. From [57]. c. Diagram of the system built by Acremann group. The pump (from a Ti:Sapphire laser) and the probe (from FEL emission) enter in the chamber from a 45° angle. Electrons are then collected by electrostatic lenses, energy-selected and then sent to a Mott detector. d. Absolute polarization as a function of time of photoelectrons from a Fe/W(001) sample measured with this system. The open squares and the black line show the values measured in absence of pump pulse. e. Relative polarization as a function of time. The red line is a fitting with combinations of exponential functions. From [58].*

A confrontation of the results in Fig. 3.5 b. d. and e. which are measurements of the quenching of polarization generated by the pump pulse in the same system (Fe/W(110)),

[9]The 90° bend of the electron optics hinted in Fig. 3.5 a. can be used to implement a rough band-pass type selection of low energy electrons.

shows in a clear way the importance of the FOM maximization. In the Acremann system the presence of an hemispherical analyser, combined with the limited time-window of a FEL beamtime, resulted in a less defined curve. However these two systems differ for much deeper characteristics than an hemispherical analyzer: the handling of the signal generated in the PIPS by the short bunches of electrons generated by a pulsed source is completely different, and in both cases, being of fundamental importance in the realization of Ultraspin project, it will be discussed again in the following.

3.1.2 Retarding Grid Mott

Another interesting system is the so-called Retarding Grid Mott detector, or mini-Mott detector (or also Rice-type Mott detector, because the best-performing design was developed and patented by F. B. Dunning and its group at Rice University). A cross section of the system can be seen in Fig. 3.6. The primary electron beam enters in the polarimeter passing through an aperture and a grid close to ground potential, is energy selected by a system of retarding grids, and sent through the acceleration system. A first Einzel lens accelerates it to about 1.7 keV and sends it through a collimating aperture, and a second operates a slight deceleration to 1 keV to remove secondary electrons from the aperture's metal. The beam then enters the central electrode, held at 25 keV, which has roughly the shape of a cone and is isolated through a thick piece of Macor insulator. When the accelerated electrons reach the base of the cone, they meet a Thorium or Gold target and are scattered. Four scattered beams are extracted through apertures in the side of the cone. At this point the main difference with respect to Classical detectors emerges, as the particles are strongly decelerated in two stages: first by a focussing electrode held at 1.5 keV, and then by a retarding grid which is kept at 800 V. Four channeltrons, biased at the same potential of the grid, can measure the two asymmetries corresponding to the two in-plane components of the polarization.

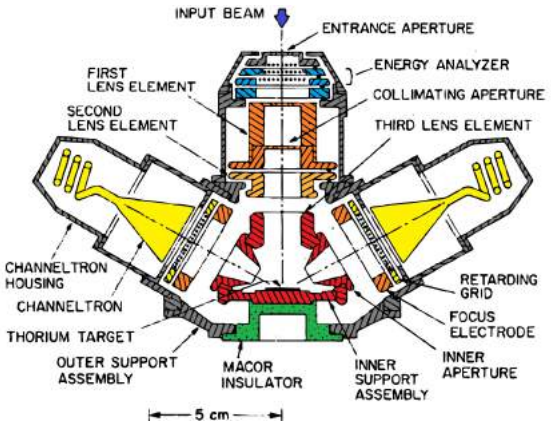

Figure 3.6. *Cross-sectional scheme of a Retarding Grid Mott detector. The potentials are again colour-coded for clarity. In grey are the parts close to, or exactly at ground potential; in yellow the ones at 800 V, in light orange at 1keV, in orange at 1.5-1.7 keV, in red at 20-25 keV. The retarding grid analyser, in which the potentials can be changed widely, is in light blue, and the Macor insulator in green. From [59].*

The most striking difference of this system from the classical Mott detector is the

presence of a retarding field between the target and the electron counters, which has some very far-reaching implications. In particular, the requirements are much less stringent on the detection system: it does not need to be energy selective, because the potential of the retarding grid deflects inelastically scattered electrons, and, being much closer to ground potential, does not need special arrangements for readout and signal extraction. The energy interval of the electrons to be counted can be widened by increasing the potential of the last retarding grid, or tightened by reducing it. The electrons are measured as charge pulses generated by the avalanche process on the walls of the channeltron or of a microchannel plate (MCP)[10], preamplified and counted via a standard data acquisition system. This contributes to make of this system a very convenient apparatus, which can easily be implemented in a UHV system.

These advantages, anyhow, come at a price: it was demonstrated[11] that the signal in a mini-Mott detector is strongly dependent on the beam alignment and the asymmetry can be changed up to 10% by slight movements of the primary beam on the sample (of the order of one mm). This is not a problem when the system is used with sources of proved spatial stability, like synchrotrons, UV or X-ray lamps or lasers. FEL or HHG sources, however do not possess such strong stabilities, and measurements with this system can be strongly distorted by spurious signals.

Recent applications

Rice-type Mott detectors are widely applied to spin detection in many high-performance machines: they are often used after a large acceptance hemispherical analyser to perform spin and angle resolved photoelectron spectroscopy (SARPES or SPARPES); in particular in [62] an extremely high resolution was demonstrated. A particularly interesting machine, achieving high temporal resolution thanks to the acquisition speed of MCP, features a retarding grid Mott detector at the end of a Time-Of-Flight spectrometer [63].

A Time-Of-Flight electron spectrometer (TOF) is a system that uses the time of arrival at the detector to measure electrons' energy. In fact if electrons starting all at the same instant are let to drift through a field free space for a well defined distance, their time of arrival at the detector has an inverse quadratic dependence on their energy. Then if one uses a very short pulse to excite photoemitted electrons, and if the complete process of detection of a number of incoming particles is fast enough (i.e. the detector has a sufficiently high time resolution), it is possible to simply let electron drift in a lens system with a significantly long field-free region and measure the intensity of the electron flux as a function of time. It is then possible to build the XPS spectrum by simple calculation, transforming the time abscissa in a energy axis.

The advantages of this kind of spectrometer for time and spin resolved photoelectron spectroscopy are many: firstly the requirement of a short excitation pulse, that can be a limit in other experiments, is intrinsic in the technique considered here, i.e. ultrafast

[10] In particular, microchannel plates can be used as very fast (the typical total time resolution is less than 100 ps) [3].

[11] First by a systematic confrontation with a Compact Classical Mott [60] and later by observations of the same Rice university group [61].

spectroscopy. Secondly, a TOF spectrometer is the only one which is able to discriminate electron energies without eliminating part of the intensity: a crucial advantage for the cascading with an intensity-hungry Mott detector. Thirdly, if implemented with position-resolved detectors, TOFs can achieve angular resolution, again without reducing the measured intensity. Finally, the resolution of the system is not linear, but improves for low energy electrons[12]. This is an advantage, because, most ultrafast lightsources are in the UV-soft X-rays range and excite relatively slow electrons. The machines realized by combination of a TOF and a Mott detector, therefore, can achieve a very high efficiency and resolution if combined with a pulsed, stable source and are starting to be used in particular with synchrotrons or ultrafast lasers with FHG.

3.2 Low energy detectors

A new wave of spin detectors is arising which uses scattering at low energy, following from the great improvement of the surface preparation techniques, combined with the development of powerful theoretical methods for the analysis of coherent scattering in solids. In these very recent years, the renovated interest in spin detection and the refinement of the procedures are starting to produce new machines with very high performances.

These systems can again be divided in the two categories discussed above: machines based on spin-orbit processes (**SPLEED**) and on exchange processes (**VLEED**). A short discussion of the most recent advancements in these two categories will be given in the following.

3.2.1 SPLEED detector

The most recent SPLEED detector are based on a rather simple scheme, shown in Fig. 3.7 a: a suite of Einzel lenses prepares the electron beam extracted from the sample. The scheme of this optics is cylindrical, with the purpose of collimating, aligning and adjusting to the correct final scattering energy the beam, while avoiding as much as possible the loss of electrons. The striking difference that can be noticed in Fig. 3.7 c. is that the voltages used here are almost two order of magnitude lower than the ones used for Mott detectors. Once collimated, the beam of electrons enters the scattering chamber, where a crystal of tungsten (cut so that the (001) surface is exposed) is positioned on a manipulator which allows for accurate positioning with translational and rotational movements. In particular the asymmetry signal is very sensitive to the two angles of rotation around the surface normal (ϕ) and around the intersection between the scattering plane and the surface (ϑ).

The beam, with an energy of 103.5 eV, impinges on the surface and is diffracted. The diffraction pattern that is generated is represented in Fig. 3.7 b. After long experimental

[12]The concept is very straightforward, because the time resolution of the detector is always the same, but low energy electrons are much slower and thus their time of arrival can be determined with higher relative precision:

$$\Delta E = 2\frac{E}{t}\Delta t$$

If the energy (E) decreases, the arrival time t increases, while the time resolution (Δt) is constant, thus making the energy resolution ΔE smaller and smaller.

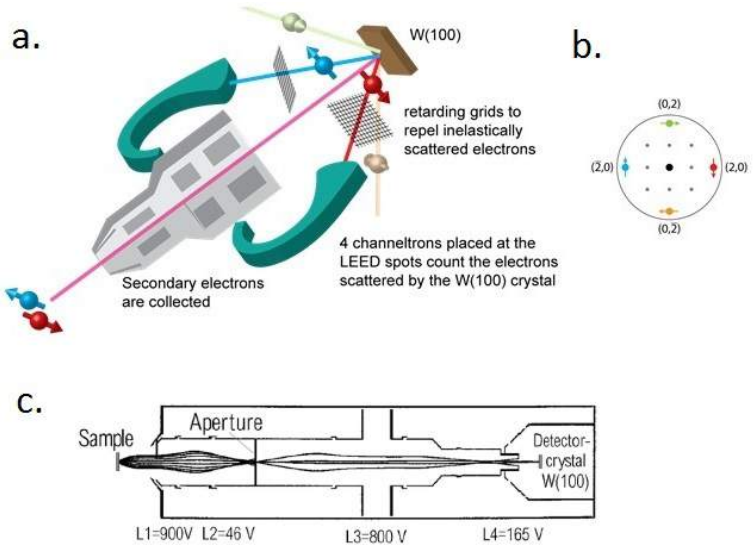

Figure 3.7. *a. General scheme of the SPLEED detector use. b. Diagram of the LEED pattern of W(001) with the spots used for asymmetry detection highlighted by different colors. The polarization along the vertical axis can be measured using the red and blue spot, while the one along the horizontal axis can be obtained from the green and orange spots. c. Scheme of the input lenses with the typical applied voltages. a. and b. from Mainz University SEMPA, c. from [45].*

and theoretical research it was concluded that the spots of the (20) family (i.e. the ones with different colours in Fig. 3.7 b.) are the most suited to evaluate the asymmetry because they are less sensitive to surface contamination [45]: four apertures covered with fine grids are then positioned in the shield that surrounds the scattering area, and electron passing through them are then counted by four channeltrons. This system is then able to measure the two components of polarization that lay in the plane of scattering, while it is needed a rotation of the sample to measure the third. The typical FOM is of $\approx 1.6 \times 10^{-4}$, but with a Shermann function slightly higher than classical Mott ($S_{eff} \approx 0.27$).

The great reduction of voltages with relatively small reduction of FOM comes at a price, however. The tungsten surface has to be prepared very accurately because W(001) can have many different reconstructions depending on the preparation procedure, and this effects the asymmetry signal [37], but, furthermore, it has to be cleaned and refreshed very often. The SPLEED system commercialized by Focus Gmbh, for example, requires performing complicated sequences of four different cleaning procedures[13] every two hours to keep the target clean. The residual gases, present even in a very performing UHV chamber (with base pressure in the 10^{-11} range), and in particular hydrogen, have indeed a strong effect on the S_{eff} rapidly deteriorating the asymmetry signal. For this reason, even in the presence of constant polarization from the sample, the measured value changes of more than 30% with time, varying non-linearly except in the range of 80 to 200 minutes after the cleaning procedure, as shown in Fig. 3.8.

[13]These cleaning procedures are, however, by themselves relatively simple, requiring only heating of the crystal at very high temperatures in various atmospheres (vacuum or oxygen) and for different times.

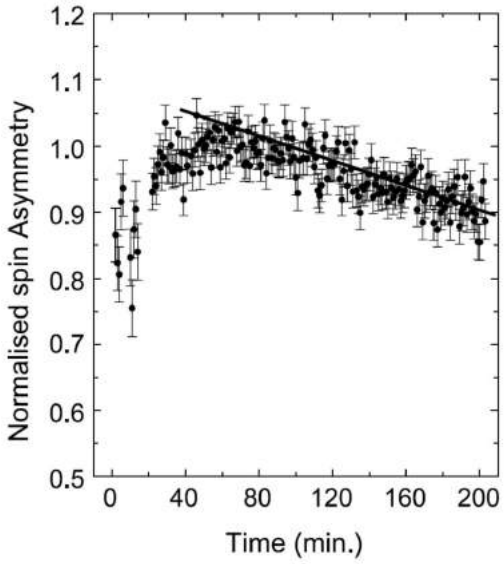

Figure 3.8. *Measurement of the beam with constant polarization with a SPLEED detector. Time zero corresponds to the end of the cleaning cycle. The non-linear behaviour seen in the first 80 minutes is due to the cooling of the surface, which can even change structurally during this period. After 200 min, instead, the gases start to saturate the surface, again deviating the asymmetry trend from linearity. From [45].*

In the linearity range it is thus possible to weight each point with the Sherman function that the detector has at the moment of measurement, but it is clear that performing quantitative spin analysis in the presence of further external difficulties (instabilities of the source, contamination of the samples etc.), or simply measuring very small signals (which require high statistics and therefore long measurements) can become very difficult. Furthermore, the need of cleaning procedures means that the sample must be kept in an independent chamber, which can be isolated from the sample environment through a gate valve, in which the target temperature can be changed and controlled doses of gases can be fluxed. The need of an independent chamber with its own pumping system increases the volume that a SPLEED detector occupies on the air side, so that the reduction in the mechanical obstruction between this and a Compact Classical Mott detector is rather slight (0.17 m^3 to 0.2 m^3).

Very recently, however, the SPLEED technique has witnessed a new impulse, because in the general trend of detectors improvement towards parallel acquisition also spin detectors are included. The direction is towards the realization of two dimensional maps in a single step of measurement, using position-sensitive detectors, like MCPs or pixel-detectors. The LEED-based scattering processes are advantaged in this situation, because they can use the mirror reflection from the (00) beam which has very small intensity losses and geometrical distortions. A very recent application is therefore in microscopy, where the Kirschner and Schönense group have built a system able to realize spin-resolved real-space images of domain walls in magnetic materials [64]. The apparatus is able to resolve electrons' energy, momentum and spin[14], and can be operated with an ultrafast laser to achieve

[14]The asymmetry is, in this case, not trivially observed, because only one beam is measured and the

temporal resolution. The difficulties generated by the contamination of the W crystal surface remain, however, and very recently the group is trying to move to new and less reactive targets using Iridium (001) [65] or pseudomorphic Au on Ir (001) [66].

3.2.2 VLEED detector

The scheme of a VLEED spin detector is rather simple, as can be seen in Fig. 3.9. In its most essential design, the electrons are focussed and accelerated (or decelerated) to the correct energy by a small set of lenses, sent on a magnetized target of crystalline Fe, which is positioned slightly off-normal, and reflected in a channeltron. As shown in Fig. 2.9, there are two main working points where the asymmetry is significant, one at 6 eV and one at 13.5 eV. Both are used, depending on the different design of the detector[15]. The magnetization of the target is then reversed and the measurement is repeated: if the intensity has not changed during the magnetization reversal process, an asymmetry due to the polarization of the beam can be measured.

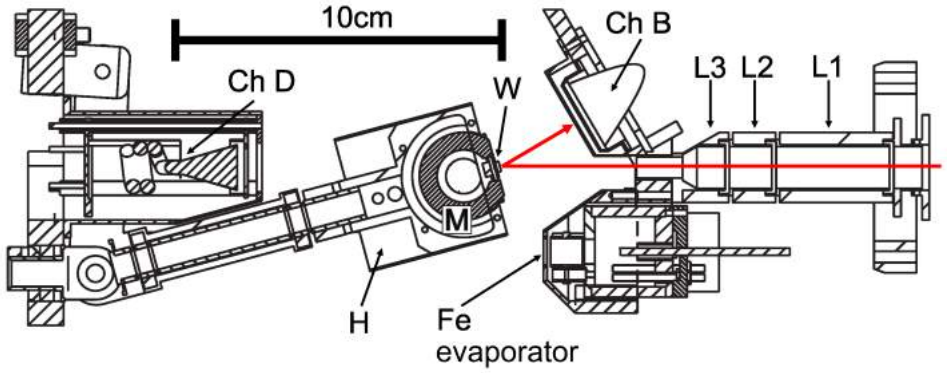

Figure 3.9. *Scheme of a VLEED system with W substrate. The red arrow represents the trajectory of the primary electrons. L1, L2, L3 are the lenses that prepare the primary beam for scattering. W indicates the substrate on which the Fe film is evaporated. M labels the magnetizing coil with ferrite core, and H the sample holder with heating filament. The channeltron for spin-resolved measurements is Ch. B while spin integrated detection can be realized with Ch. D when H is moved in front of the Fe evaporator. The whole system is surrounded by a shield that protects it from external magnetic fields. From [67].*

The reflecting target is positioned on a manipulator, which must be equipped with at least one coil which can magnetize it in opposite directions. In the system displayed here only one coil with a ferrite core is present, but in many other applications four [3] or six [68] Helmoltz coils have been used. The first apparatus of this kind was realized and operated

target crystal is not rotated during measurements. As explained in [64], it can be achieved through a careful analysis of the images obtained at two different scattering energies, and weighting the data with a generalization of eq. 2.12 for continuously varying incidence angles and for the combination of different scattering energies (and thus different S_{eff}).

[15] In particular in [67] the higher energy side is preferred because it enables the use of some form of energy filtering before counting in the channeltron. A system of grids acts as a high pass filter, selecting electrons with energies in the range 10-13.5 eV which have higher polarization, thus further enhancing the FOM, and obtaining a smaller dependence on the surface contamination.

successfully by Kisker group in 1989, and was based on thin films of Fe grown on Ag(001) [46]. Despite the good results obtained by this group [47], with observed FOM much higher than Mott detectors, the high reactivity of Fe surface was a significant obstacle. The target films, indeed, became contaminated very quickly even in good pressure conditions[16] deteriorating the measurement of asymmetry, but could not be cleaned as quickly as the W surface of SPLEED machines and had to be grown again.

A revolution came when the Fe(001)-p(1x1)O target was discovered by Bertacco and Ciccacci in 1998 [49]. It consists of a Fe film with a relatively high thickness (100 nm) grown on a substrate of MgO(001), whose free surface is covered by a single atomic layer of oxygen[17] in an ordered fashion: the two dimensional lattice of oxygen atoms has the same unit cell as the Fe surface, and each atom is positioned in a hollow site [**?**]. This oxidation saturates the chemical reactivity of Fe (*passivation*), making its surface much more inert and stable, while at the same time the bandstructure of the surface is modified so that the asymmetry in the reflected beam is not only maintained, but also slightly enhanced with respect to the clean Fe [69]. Bertacco and Ciccacci immediately realized the implications of their discovery for the realization of spin detectors, stating it explicitly in their paper. This definitely brought exchange polarimetry to be competitive with the other techniques.

Modern VLEED polarimeters like the one shown in Fig. 3.9, therefore, possess a small preparation chamber in which Fe can be evaporated on the substrate, and the oxygen treatment can be performed. The FOM that can be obtained by such systems with a freshly prepared target is $\approx 6 \times 10^{-3}$, one order of magnitude higher than Classical Mott. However, even if the chemical reactivity of the surface is saturated, residual gases from the chamber can still be adsorbed by physisorption and contaminate the surface: the asymmetry deteriorates anyway, but on a scale of several weeks[18]: at that point one needs to re-prepare the target. If a MgO substrate and a sufficient thickness of Fe are used, it is possible to refresh the surface by flash annealing in vacuum or in oxygen atmosphere [70]. However, after some of these procedures it is necessary to change the target, and a new substrate must be inserted from air. A small preparation chamber and transfer system have then to be connected with the scattering chamber without breaking UHV.

It is also possible to use a Tungsten substrate and lower thickness (anyway larger than 40 ML). This system is not stable against heat treatment[19], but it is possible to remove all the Fe from the substrate trough sequences of high temperature heating and oxygen exposure, and to reuse the same W crystal for many target depositions. Therefore, each time the FOM deteriorates a new film is grown, but there is no need to insert any substrate from air, and the preparation chamber can have much smaller dimensions and pumping system. This is the design illustrated in Fig. 3.9: the tungsten crystal is fixed on a

[16] [46] reports some hours in low 10^{-10} mbar.

[17] The realization of a target of this kind is one of the experimental works that will be discussed in this thesis, so a more precise discussion of the methods and a deeper physical insight on this structure is demanded to the appropriate chapter.

[18] The safest assumption that can be found in literature is of two weeks [67] but the range extends up to more than one month [68]. Needless to say, this solution pushes the working time of the detector well beyond a critical time period, i.e. the duration of the longest acceptable single measurement (which can be of the order of days in highly automated machines).

[19] If heated, the evaporated film disintegrates in μm-sized crystallites with a 1 ML Fe carpet underneath, as it would happen in a Stranski-Krastanov growth [67].

manipulator that can rotate in the plane of the page, switching from the measurement position to the preparation position, in front of the Fe evaporator. The crystal is then cleaned by heating with a filament wired behind it on the manipulator, and a new film is deposited by the evaporator. A second channeltron allows to perform spin-integrated measurements while the target is in preparation.

Recent applications

The VLEED detector is best used after an energy analyser, because it requires very precise energy of the primary beam to achieve high efficiency. In other applications, such as measurement of the polarization of secondary electrons without energy analysis, high energy detectors are best suited. Thus, may applications were realized in which this system was implemented after an hemispherical analyser (as in [68] and [70]) or a TOF system (as in [3]), following the aforementioned trend of parallel acquisition.

The system described in [68] and schematically shown in Fig. 3.10, for example, consists of a state-of-the-art spectrometer (VG Scienta R4000) and a single channel VLEED detector. This hemispherical analyser is a large-radius (200 mm) system, with a wide acceptance angle, able to image at once on the exit aperture the electrons momenta in one transverse direction included in a range of $\pm 15°$. Along the other direction the energies of the photoelectrons are dispersed, thus creating a two dimensional plot that gives insight in the bandstructure of the solid. This is registered positioning an MCP detector in the exit aperture followed by a phosphor screen and a CCD camera: this allows to acquire simultaneously a high number of curves, thus reducing the measurement time. The value of energy that is in the centre of the exit aperture can be scanned by changing the potential of the hemispheres in an interval going from 0,2 to 1500 eV with a $\Delta E < 1.8meV$, and, as a unique feature of Scienta analysers, the second transverse component of photoelectrons can be scanned by changing the potentials in the first input lenses.

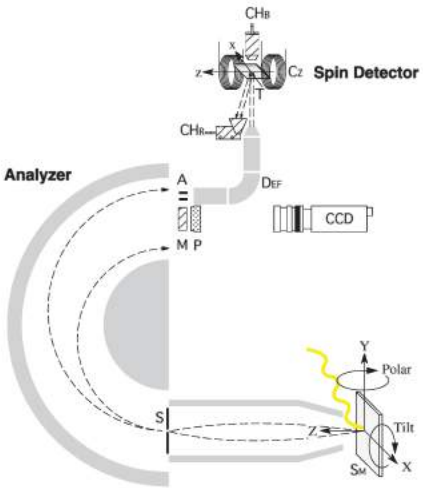

Figure 3.10. *Scheme of a SARPES system with VLEED detector from [68]. Details in text.*

In the system described in [68], called ESPRESSO (Efficient SPin REsolved Spec-

troScopy Observation) machine, the 2D photoelectron detector (MCP + Phosphor screen + CCD) has reduced dimensions, and does not cover the full extension of the exit aperture. On its side in the energy dispersion direction is, instead, positioned an aperture which leads to a 90° deflector and then to a VLEED detector. This detector is based on Fe(001)-p(1x1)O structure on MgO substrates, and the film is magnetized by three coils that can orient the magnetization in all the three independent direction of space, thus allowing, with six measurements for each point, to determine the three components of polarization. By scanning the central energy on the MCP detector, one thus changes also the energy of electrons that enter in the polarimeter and can measure spin-resolved photoemission spectra. If the aperture leading to the spin detector is small enough in both directions, one can also choose a precise take-off angle, thus resolving also the transverse momentum of the electrons observed. This system is installed at the multi-mode undulator beamline BL-9B of Hiroshima Synchrotron Radiation Center and thus has access to a third generation synchrotron ligtsource, but is also equipped with He and Xe discharge lamps for offline measurement.

The staff of APE beamline is working on the implementation of a system similar to this, based on a Scienta D80 spectrometer, in substitution of a spin integrated Scienta SES2002. The spin integrated part is already operating since march 2014 and has demonstrated outstanding performance in several beamtimes. Part of the work of this thesis, that will be described below, was the realization of a target to implement spin resolution in this system, and in particular to find an efficient recipe in the beamline sample preparation chamber, that could be later replicated in the independent target preparation chamber connected to the analyser.

This system is based on continuous intensity sources and, while the spin integrated measurement benefits of the advantages of parallel acquisition, the spin resolved measurements are still based on a single channel acquisition mode, an heavily rely on intensity stability. Moving to pulsed sources, like FHG Ti:Sapphire lasers, it is possible to use TOF energy filtering and thus to scale up spin resolved measurements to faster acquisition.

A system of this type has been realized by the group of A. Lanzara at University of California Berkeley in close connection with the Advanced Light Source facility [3]. This system features two separated TOF detectors, which share part of the electrostatic lenses, as shown in Fig. 3.11, and are separated by a 90° electrostatic deflector. The first one, which can be reached by electrons propagating on a straight path, is spin integrated.

The electrons photoemitted by a sharp laser pulse of few femtoseconds drift in the electrostatic lenses assembly spreading in a time interval of few hundred nanoseconds. When they reach the detector, they meet a MCP stack which amplifies the charge pulse of about 10^6 times, while keeping a very sharp temporal resolution. The charge pulse is then collected by an anode and sent to the preamplifying and timing electronics: the ultimate total timing resolution is around 70 ps, enough to register with high resolution the photoelectron spectrum. The electrons arriving in a software controllable time-interval are then counted, and a raw spectrum is obtained in a single-shot. The obtained data must then be deconvoluted from the free propagation law of electrons and then the ordinate must be mapped on an absolute energy axis. For this reason, TOF technique requires that at least one peak of the spectrum is used as an energy reference.

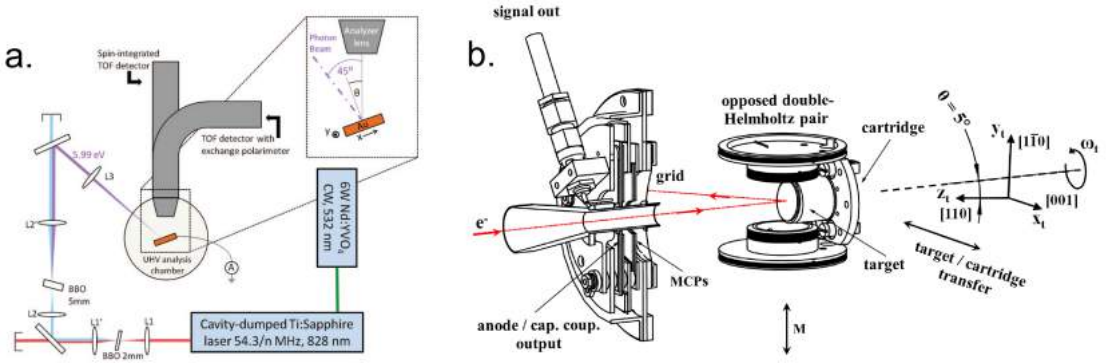

Figure 3.11. *Scheme of a SARPES system with VLEED detector and TOF spectrometer. a. Block scheme showing also the frequency multiplied laser source and a magnification of the sample area. b. Scheme of the detector assembly for VLEED measurements. From [3].*

If the deflector electrodes are activated, instead, the electrons are sent to a VLEED detector. The deflector also acts as a band-pass filter restricting the energy interval of the transmitted electrons to $\approx 1eV$. This ensures that the energy spread of the electrons will not be so big that part of the intensity will fall out of the regime with high scattering asymmetry. It must be observed, anyhow, that the FHG laser used as source provides 6 eV photons and, considering that the work function of most metals is around 5 eV, the full spectrum is generally in the accepted energy interval. The spin-resolved detector is similar to the spin integrated one, but, before entering the detector, electrons are reflected from a ferromagnetic target[20], magnetized by four Helmoltz coils along the two in-plane directions.

The difficulty here is of the geometrical kind, because the polarization is higher if the reflection angle (α in Fig. 2.8) is smaller than 10°. This has been solved by realizing a ring detector: the MCP stack is shaped in the form of a ring with a hole in the centre, through which the primary beam can pass. The sensitive part of the MCP is facing the ferromagnet surface and the primary beam is scattered onto it trough a 5° reflection. In this way, the full spin-polarized spectrum can be acquired in a single shot[21], and in two shots one can obtain the polarization throughout the whole range of energies. The angle of emission, and thus the in-plane momenta, can be selected by rotating the sample with the manipulator. With this system, the measurement of spin and angle resolved measurements can be performed, and the realization of a study of the Au spin-polarized surface state took not longer than two hours [72]. By small modifications of the optical scheme of the source laser it is also possible to achieve temporal resolution, using the pump-and-probe technique.

[20]The group in UCB normally uses Co thin films grown on W(110) without any passivation, because they provide higher FOM up to 2×10^{-2} (thanks to an enhancement of spin-polarization due to QW states that are also exchange-split in a ferromagnet). The lifetime of the target is anyway shortened to a few days [71].

[21]It must be stressed, however, that for applications with higher photon energies (as for example a synchrotron with only few bunches in the accumulation ring, or a FEL), more shots are required, because the band-pass filter cuts off parts of the spectrum.

It is interesting to observe that both these state-of-the-art systems have been designed in order to be used with very stable sources such as synchrotrons, lamps or lasers: this is because the VLEED method is extremely advantageous only if the intensity is constant between the two magnetization phases, because by using only one beam it becomes completely "blind" to the other components. In the opposite case, when the source intensity varies strongly, this enters in the noise of the measurement without any filtering, thus increasing the measurement time until this effects have been averaged out. A variation of 10% in the shot-to-shot intensity (which would be an extraordinary achievement for a FEL facility) pushes back a FOM of 2×10^{-3} to 2×10^{-4}, the value typical of a Mott detector.

3.3 Conclusion and detector choice

Stability and reliability have been chosen over the higher efficiencies for the Ultraspin project. In particular, seen that the application is the measurement of energy integrated secondary electrons with a FEL lightsource, so that the primary beam has a rather wide spread of energies and very significant shot-to-shot intensity variations (many tens percent [23]), the Compact Classical Mott detector meets more tightly the required specifications.

A Compact Classical Vectorial Mott is, indeed, able to measure the three spatial components of the polarization vector without ever loosing the control on the intensity behaviour: even if two separate acquisitions are required to characterize the full spatial description of $\mathbf{P}$, there is one redundant component common to the two measurements which can be used for normalization. The intensity variation thus does not enter in as noise in a Mott spin polarimeter. Also the typical beam-position variations do not effect significantly this system: the positional stability of Mott detectors is so efficient that it is possible (and it will be shown further on in this thesis) to perform measurements of hysteresis by polarized secondary-electron emission, when the emitted low-energy beam is deflected very strongly by the applied field. Furthermore, a broad interval of energies of the photoelectrons can be accepted and is scattered with approximately the same S_{eff}, thus allowing for a full energy-integrated sensitivity. Finally, Mott detectors are best suited for the use in complicated and long experiments: the absence of preparation requirements for the target and the definition once-for-all of most of the electronic lenses allow for a stable and extremely long operation without the need of man intervention, allowing for high statistic and time-consuming experiments to be done in a fully automated way.

The use of such detector will enable to work with any kind of unstable ultrafast source (both in the sense of spatial position of the beam and of the shot-to-shot intensity) at the reasonable cost of slightly longer measurements, and will give the possibility to obtain trustful quantitative results in absolute polarization analysis.

Part II

Development and implementation of an independent UHV station

Chapter 4

ULTRASPIN experimental apparatus

The ULTRASPIN apparatus is designed to be a very compact but versatile endstation that can be moved easily and be connected to different ultrafast photon sources. The design is therefore essential and consists of two independent spherically-shaped vacuum chambers, lying on the same horizontal plane. One is dedicated to the sample preparation and the second to the spin polarization analysis. They are mounted on aluminium frames that position the centres at 1.3 m from the ground[1]. The two chambers are pumped independently by means of magnetically levitated turbomolecular pumps, but are connected by a straight tube with a gate valve: a long horizontal travel arm allows the samples to pass from to the other. Each chamber is provided with a load lock for sample fast entry and a vertical manipulator with four degrees of freedom (it can be moved linearly in the three dimensions of space and by rotation around the vertical axis) and features several instruments. The whole apparatus is designed to be highly automatized and is controlled by a PC station close to the chambers. In this chapter the whole system in its most recent configuration will be described in detail.

4.1 Analysis chamber

The analysis chamber constitutes the central part of the ULTRASPIN apparatus, where the ultrafast spin polarization measurements will be performed. This kind of experiments, despite the effort for the maximization of the efficiency, is expected to require long integration times: the chamber is then designed to allow the realization of parallel measurements as much as possible or anyway to keep to a minimum the manipulation procedures. The shape is spherical (with a 30 mm diameter), with a unique focal point (the centre) for all the instruments pointing inwards. This will allow, in the future, to implement further optical or electronic techniques (MOKE or TR-MOKE, XAS in fluorescence or total electron yield) simultaneously to photoelectron spectroscopy.

[1]For the technical drawings used for the construction of the chamber, see Appendix B, Tab. I-IV.

This choice is important not only for the reduction of the time-consumption of an experiment: the performance of photoemission techniques is at present difficult and uncertain[2], and the optical measurements are a necessary complement. For example, they can be used to disambiguate if an unexpected signal is effectively coming from a sample, or if it is spurious, originated by electron detector's inappropriate operation. Furthermore, optical methods (in particular for magnetic measurements) have a much broader literature, and can provide solid foundations to the successive explanation of photoelectric signals. Finally, the polarization measurement (particularly when polarization is small) gives a distinct and recognizable signal only after few minutes: this is a particularly relevant downside in the initial phases of the experiments, when "coarse" and quick measurements are needed to understand which areas of the sample are the best suited for the analysis[3]. An efficient measurement routine would then consist in locating the "best-spots" in the sample rapidly with a secondary technique, and then performing high integration time measurements in that positions. These advantages are obtained only if measurements can be performed simultaneously and without changing the position of the sample.

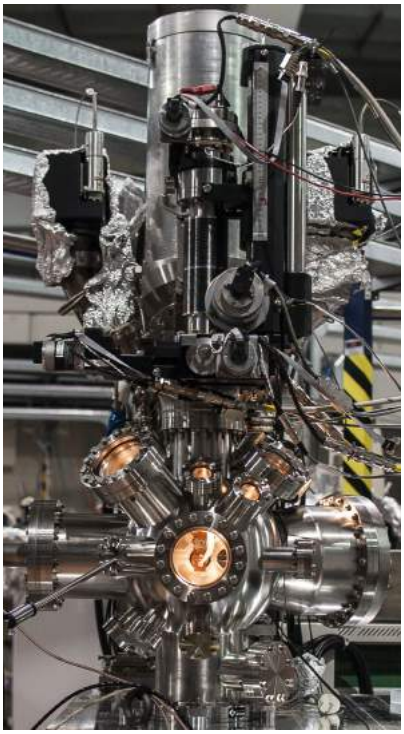

Figure 4.1. *Photography of the main chamber front. It is possible to see the head of the manipulator inside from the front viewport. Over the chamber the manipulator assembly can be observed, with four stepper motors. The body and lenses of Mott polarimeter are aligned with the manipulator column, but the safety cylindrical case and the ion pumps are visible.*

On the spherical body a high number of flanges (25) is placed, to allow for a great flexibility in the disposition of instruments. In particular the ports are disposed on the equatorial plane (parallel to ground) pointing towards the centre (approximately one every 45°). Only one of them is off-centre, since it is dedicated to the sample transfer from and towards the preparation chamber. On this plane, several ports are present[4]: a CF 200 flange[5], where a time of flight detector (whose develoment is a work in progress

[2]It is natural for a new technique: the troubleshooting and noise elimination routines are not yet consolidated.

[3]Normally, if one has a simple homogeneous sample, the surface is explored to maximize a signal that is observable anywhere. On the other hand, if the sample is highly sophisticated, such as the microlithographed devices used for *in-operando* measurements, it is possible that not the best, but the only interesting signal is originated from a very small portion of the sample area.

[4]If a clear picture of the disposition of ports is desired, see Appendix B, Tab. VI, the numeration of the ports in the text and in the drawing is coherent.

[5]Port 7.

thanks to the collaboration with Roma III) is expected to be assembled, a CF 150[6] and a CF 100[7], designed to allow easy UHV connection to other apparatuses. On the opposite side to the one shown in Fig. 4.1, three CF 40 flanges[8] are designed to be possible inlet for the light beam, giving a high flexibility also on the angle between the primary beam and the instruments. For the work of this thesis, an electron gun was connected to the central inlet flange, and provided the source of excitation for the commissioning of the machine.

On the parallel planes at $+45°$ (over the eq. plane) and $-45°$ (under the eq. plane) other small flanges are also placed with angles of $45°$ between each other. A CF 100 port[9] is placed on the $+45°$ parallel exactly over the central beam inlet[10]: on this the Mott detector is mounted. The spin detector is the instrument on which a significant part of the work described here was concentrated and will be described in sect. 4.3. On the vertical axis a long tube terminating with a CF 150 flange is directed downwards for pumping (with lateral ports for vacuum gauges), and a CF 100 tube is directed upwards for the manipulator stage flange.

The chamber is completely realized in μ-metal[11] to screen the enclosed experimental volume from magnetic fields. Electron spectroscopies, and in particular spin-resolved, are very sensitive to external magnetic fields because the trajectories of low energy photoelectrons can be distorted and the spin can precess in the external fields blurring the momentum and spin resolution. Thanks to the use of 5 mm thick μ-metal walls, a residual magnetic field of less than $2 \times 10^{-7}\ T$ was measured in the centre of the chamber with a Hall probe.

The system is pumped by high throughput turbomolecular pump followed by a Scroll-type oil-free rotary pump. The output of the Scroll pump is connected through a hose to Elettra's system of management of exhaust gases. The chamber was baked-out several times during the commissioning, up to temperatures of $200\ °C$, achieving a base pressure of $2 \times 10^{-10}\ mbar$ despite the absence of third stage pumping (such as getter, ion or cryo pumps), that is anyway scheduled to be implemented soon[12].

4.1.1 Manipulator

The manipulator of the analysis chamber is controlled by the four stepper motors visible in Fig. 4.1. The two lower ones control the motion of a VG Scienta XY table, i. e. a system of two metal plates that can slide one on the other in two directions without breaking the vacuum. In Fig. 4.1, the Y direction is perpendicular to the plane of the page (with negative values moving towards the reader and positive moving into the page), while X

[6] Port 3.
[7] Port 5.
[8] Ports 1, 2, 8.
[9] Port 9.
[10] Port 1.
[11] μ-metal, or mu-metal, is an alloy with extremely high magnetic permeability, with approximate composition 77% nickel, 16% iron, 5% copper and 2% chromium or molybdenum. It is used in several applications for screening from magnetic fields.
[12] In the form of a NEXTorr-500, a non-evaporable getter (NEG) pump combined with a small ion pump, a system that has already proven very efficient in the preparation chamber. For the principle of operation of the NEG pump, it is possible to refer to this link.

is in the plane (with positive values going to the right and negative to the left). The motion range is $\pm 10\ mm$ with sub-micrometre resolution in both directions. The bigger central motor controls the vertical movement (Z), enabled by the long bellow visible in Fig. 4.1 and the VG Scienta vertical travel system. The motion range is $0 - 300\ mm$ with sub-micrometre precision. Finally the fourth motor, on the top, generates a rotatory motion around the vertical axis (ϑ coordinate): a VG Scienta differentially pumped rotary platform allows 360° rotation with 0.05° resolution.

The manipulator employed for the work of this thesis is only temporary in the plan of ULTRASPIN development and, even in that period, it underwent several modifications, following the improvement of all the other parts. While the final manipulator is expected to be implemented with a cryostat, the present system is simpler: on the in-vacuum side a CF 63 flange, is welded a polished steel rod, 30 cm long, whose lower cylindrical face has a threaded hole. On this, the manipulator head is secured firmly with a screw. The in-air side of the top flange features two smaller ports (CF 16) for the electrical feedthrough (for a total of 8 available pins). The head of the manipulator is a block of copper with the shape of a Γ, whose short arm is screwed to the steel rod, while the long, vertical arm (visible in Fig. 4.2) is carved to allow a compact organization of the electrical connections. Here are hosted the sample housing, a magnet and a switch.

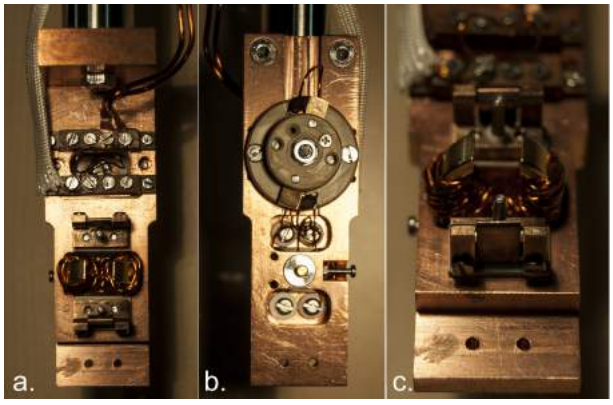

Figure 4.2. *a. Front view of the head of the manipulator. b. Rear view. c. Detail with a close-up of the magnet.*

The standard of sample holders[13] used for the ULTRASPIN chambers is coherent with the one of APE beamline, the Ferrovac SHB standard based on pins distanced 16.5 mm and on forks with 12 mm gap between their tines. The sample housing is formed by two pins sticking out of the vertical plane of two separated "chairs". Two strong metallic clips are instead positioned on the horizontal plane: when the sample holder is position, the two pins enter in the two external holes and the clips lock the holder in a stable position. The two "chairs" are electrically isolated between each other and independent wires carry the connection to the air-side. On the electrical path of the lower contact, a in-vacuum switch is placed, which can be operated with wobblestick's fork by rotating

[13]The samples, by themselves cannot be manipulated easily, as they come in very different shapes. Before putting them inside a UHV chamber, they are placed on a sample holder, in this case a metallic parallelepiped with holes at 16.5 and 12 mm distance on each of the four lateral faces (see Fig. 5.3).

the plastic circle visible in Fig. 4.2 b. This switch was always kept closed for the work described in this thesis, and is the result of the transitory character of the manipulator set-up: the disposition described here has a great abundance of feedthrough pins (more than needed), but future ones, with more complicated electrical schemes or geometrical design, will require to reduce the number of wires by the use of this component directly inside the chamber. The presence of two electrically independent ends in the sample holder allow for the application of electric fields, currents or the construction of complex electrical circuits on the sample, as will be described in Chap. 5. In a simpler design, both ends can be electrically connected and grounded through a picoamperometer, thus registering the photoejected current simultaneously to photoemission measurements.

In the gap between the two "chairs" a coil of copper thin wire covered by kapton[14] is wrapped around (in 90 loops) an horseshoe-shaped iron core coated with gold to prevent oxidation and out-gassing in vacuum. By sending a current in the coil it is possible to control the field between the poles of the horseshoe: the intensity of field generated has been tested in air between $\pm 200 A/m$, obtained with maximum currents of $1A$; but in vacuum it is possible to achieve up to $5A$ for short times without the risk of overheating, thus ranging in $\pm 1000 A/m$, a field sufficient to reverse most of the soft magnetic samples. The choice of this magnet is not the most diffused one between spin-resolved spectroscopy set-ups: most of the time, Helmoltz coil with no core are used, because they have lower residual stray fields. However, geometrical considerations (Helmoltz coils are in general much bigger and are built with a great amount of insulator that, if not screened, can charge and generate sparks in the chamber), performance needs (Helmoltz coils generate much smaller fields unless very bulky assemblies are used), and thin film properties (thin films, combined with the horseshoe geometry, generate very small stray fields) brought to the realization of this option. The two coil ends are brought to the air side by independent pins. This circuit is driven by a bipolar power supply (Kepco BOP 20-20ML) that allows to control with high accuracy and reproducibility the magnetic field on the sample. The complete electrical scheme (including the unused 4-pin connector) is shown in Fig. 4.3.

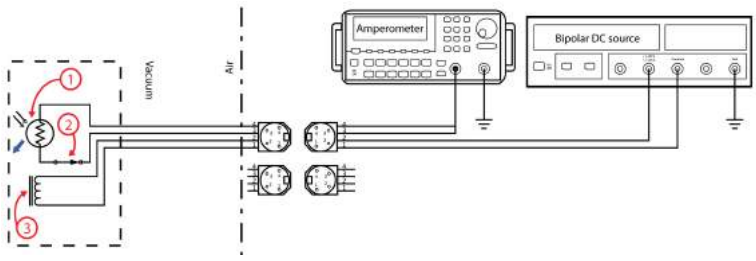

Figure 4.3. *Electrical scheme of the manipulator in its final form. 1. Sample drawn as a resistive element with a flux of photons (or electrons) impinging. Electrons photoemitted generate an outgoing current represented by the blue arrow. 2. Switch (closed). 3. Coil with iron core.*

Despite this is the most recent configuration achieved by the chamber, most of the experiments described here have been performed on a slightly different set-up, while the commissioning was still proceeding. The differences with respect to the situation described

[14]Kapton is a polyimide film with advanced properties: it is a good electrical insulator, UHV compatible and able to withstand a wide range of temperatures.

here will be discussed in the sections relative to the single experiments, when they will be needed to understand the experimental procedure.

4.2 Sample preparation Chamber

The sample preparation chamber, shown in Fig. 4.4, has a shape very similar to that of analysis chamber: a sphere, with a 30 cm diameter, with two vertical ports (upward for the vertical manipulator, downward for pumping), a set of flanges in the equatorial plane, and two more sets in the $+45°$ and $-45°$ parallel planes. The chamber is in high quality steel with an internal polished finishing to enhance the UHV performance.

In particular, one CF 150 in the equatorial plane is designed to host a large Auger-LEED system. Next to it, the mass spectrometer is mounted on a spacer tube, to avoid protruding of the hot filament in the chamber. Moving in clockwise direction, this is followed by the long linear translator for sample transfer to the analysis chamber, featuring a four-spaces revolving carousel. The following flange is occupied by a wobblestick, used to load and unload the linear travel. A small load-lock chamber is connected to the next flange and separated from the preparation chamber by a gate valve. In the equatorial plane is also present an annealing stage, provided with two pins, with which high voltage can be applied to the sample holder, and a filament: using the sample holder as the target anode of the beam of electrons extracted from the filament, it is possible to heat the samples up to several thousands degrees. This is also a temporary apparatus that will be substituted by an high temperature annealing stage on the manipulator.

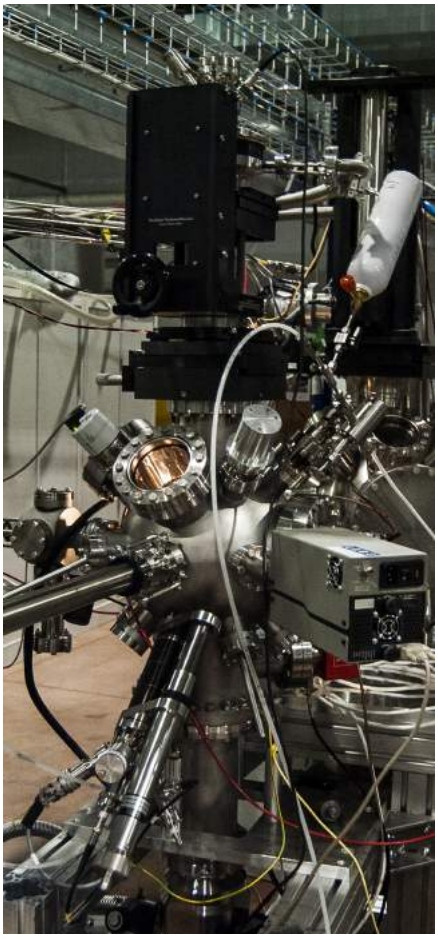

Figure 4.4. *Photography of the preparation chamber as appears from the control desk.*

In the set of flanges on the $+45°$ parallel plane, a sputter gun is mounted (top right in Fig. 4.4), with a lateral gas inlet flange controlled by a gate valve. The small bottle of high-purity Argon gas visible in Fig. 4.4 supplies the sputtering system. The design of the gas delivery tubing is such that the replacement of the bottle, or the substitution with another gas can be performed efficiently and rapidly. The sputter gun is pointing to the centre of the chamber and thus sputtering

can be performed directly on the manipulator, and the geometry can be controlled (it is possible to realize grazing incidence as well as low-angle incidence sputtering).

In the set of flanges on the $-45°$ parallel plane, instead, a high performance e-beam evaporator (FOCUS EFM-3 Omicron Gmbh) is mounted after a micrometric linear travel system (bottom left in Fig. 4.4). The core of the evaporator consists in a circle-shaped filament that operated as a cathode, while the anode is formed by a rod of the material to be evaporated (*evaporant*) or a crucible containing small amounts of the substance. When a high voltage is applied between the cathode and the anode, an electron beam current is established that heats the evaporant up to the sublimation point. With heating, the vapour tension at the surface is rapidly increased, and a flux of free atoms starts to flow from the material. The shape of the emitted flux of atoms is almost spherical in the case of a rod, much more directional with the use of a crucible, but needs anyway to be further collimated. A system of apertures[15] allows to obtain a small-diameter (few mm) beam, that can be abruptly interrupted with the use of a mechanical shutter. In this evaporator, the filament is fixed and the crucible or rod can be moved with a small linear translator to obtain the optimal configuration.

This assembly is surrounded by a cooling shroud, so that the heat used to evaporate does not diffuse to large metallic parts (such as the metal rods forming the frame that sustains the evaporator, the chamber itself, etc.) that could degas and deteriorate vacuum or to delicate parts that could be permanently damaged by high-temperature heating. In the cooling shroud, a closed serpentine tube allows to flow water in order to actively remove the heat: when in operation, this system allows to evaporate in a temperature range from several hundreds to few thousands degrees without detectable changes in the pressure of the chamber. A large linear travel stage is used to place the evaporator at a suitable distance from the centre of the chamber, so that the beam diameter becomes sufficiently large to cover the whole substrate (more than 5 mm).

The manipulator of this chamber is also similar to the one of the analysis chamber, with four axis motion in the X,Y and Z direction plus rotation (with a doubly differentially pumped stage) around the vertical axis ϑ. The motion stages are, however, not motorized and are controlled with lower resolution (hundreds of microns). The head of the manipulator has also similar features to to the analysis chamber, with separate electrical contacts for the upper and lower sample pins, both independently brought to air-side, but, instead of the electromagnet, this manipulator features a heating filament and a thermocouple so that samples' annealing in a few hundred degrees range can be performed directly on the manipulator, with a rather accurate control on temperature.

The differential pumping stages of both manipulators and the clearing tube for the sputtering gas line are all pumped by the same membrane pump that is able to maintain $5\ 10^{-3}\ mbar$ in the whole medium vacuum circuit. The load lock chamber is now pumped

[15] In this particular model of evaporator not only apertures are present in the path of the beam. The atomic beam generated by an evaporator, in fact, is not perfectly neutral: a fraction of the atoms (that depends on the geometry and on the evaporant characteristics) is ionized. This is addressed in two ways: a *flux monitor* is formed by an electrode that measures the flux of ions in the beam, proportional to the total flux (enabling to approximately evaluate the output stream of the evaporator), while after it an *ion suppressor lens* is used to deflect ionized atoms, that, if deposited on the sample can constitute centres for the formation of defects.

with a roll-in cart system, with a turbo and a membrane pump, but the implementation of a dedicated small turbo to be connected with the whole medium vacuum circuit is already in schedule. The preparation chamber is pumped by a turbomolecular pump backed by the same rotary pump used for the analysis chamber. The choice of using a unique primary for both UHV chambers was made for the sake of compactness of the whole apparatus. However, it was noticed that this introduces a small cross talking between the two chambers when the pressure in one of them is increased rapidly (in case of controlled flow of gases, or degassing of a bulky element) while the other is at its base pressure. A system of valves was then designed to isolate the chambers, so that short increases in the pressure in one chamber do not affect the vacuum in the other. The preparation chamber is also pumped by a NEG pump combined with a small ion pump (NEXTorr-500), that pushed further the vacuum performance: the pressure, after few weeks in high vacuum ($10^{-8} mbar$) and only one effective bake-out, reached 2 $10^{-10} mbar$, and is expected to improve with successive bake-outs and longer exposure to UHV of the internal surfaces.

All the electronics used to control the instruments in ULTRASPIN chambers is collected in a single rack (except for the power supplies of Mott detector's electron optics that are in an independent small rack), which also hosts the computer dedicated to data acquisition and automation control. Monitor and keyboard are on a control desk, that is positioned close to the preparation chamber. On the control desk is placed also a second computer, dedicated to data analysis and connected to ELETTRA network.

4.3 Spin detector

As explained in Chap. 3, the polarimeter chosen for this application is a Vectorial Mott detector, whose principle of operation is described in Sect. 3.1.1. The instrument, in order to achieve a full three dimensional analysis of the polarization vector, is formed by two Mott detectors disposed orthogonally. In this apparatus[16] one detector (*Mott-1*) is parallel to sample's surface normal, i.e. horizontally, and the other is vertical (*Mott-2*), as can be seen in Fig. 4.5. The beam of electrons extracted from the sample is sent to one Mott or the other by a system of 10 electrostatic lenses (*electron beam switch*), two of which can be reversed in polarity to rapidly change the path of electrons.

The upper part of the instrument is located in an independently pumped[17] vacuum chamber that is closed by a gate valve. This small chamber (*Mott chamber*) is necessary to decouple the pressure in the Mott chamber from the rest of the UHV system: while an experimental chamber undergoes several ventings (at least one per year) for the Mott detectors is better to keep the excursions in air pressure to a minimum, because the thin free-standing gold targets can be ruined by the pressure differences created by pumping, or contaminated by humidity. Bake out of such delicate systems is also a very long procedure because low temperatures must be used. The Mott chamber is held in position by a fixed

[16] Differently from the COPHEE endstation, which has non-right angles between the sample normal and the detectors [10].

[17] Two ion pumps, placed at the end of curved tubes to reduce the electronic noise in the detectors, guarantee a maximum pressure of about 10^{-9} *mbar* even when the chamber is completely surrounded by air.

frame placed on a movable platform: its position can be controlled with micrometric precision by the use of screws, so that when it is connected to analysis chamber no stress is applied on the junction elements. The frame is planned to be changed with a newer one that can be seen in App. B Tab. 4, that will enable, in combination with a bellow, to move the detector closer or further to the centre of the analysis chamber.

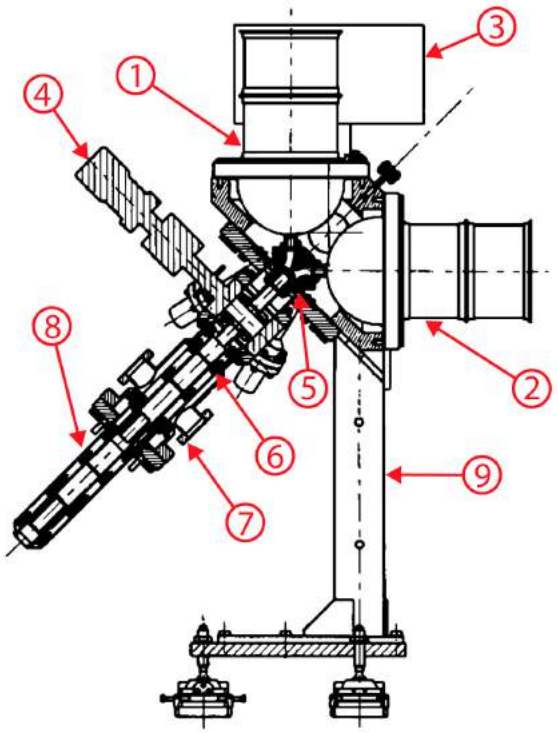

Figure 4.5. *Cross section of the vectorial Mott detector. 1. Vertical Mott detector (or Mott-2) 2. Horizontal Mott detector (or Mott-1) 3. Ion pump 4. Gate Valve 5. Set of lenses after the valve (electron beam switch) 6. Set of lenses before the valve (electron transport lenses) 7. Transport lenses external jacket, with four ports for lenses feedthrough 8. Mott detector "nose", covered by a μ-metal shield 9. Detector's frame.*

Electrons are brought to the Mott chamber by a system of 7 lenses that have the task of collecting electrons and organizing their trajectories in a well defined beam (*electron beam transport*). This element can be divided in two parts: one, closer to the Mott chamber, that is in the physical space between the analysis chamber and the Mott chamber, and is surrounded by a jacket that creates the UHV connection between the two chambers; and the second (the *"nose"*) which is inside the analysis chamber and is surrounded only by a μ-metal shield. The last part is the one reaching close to the sample and collecting the electrons emitted from the surface. In the first part the contacts for the lenses are brought to the the air-side by four feedthrough ports, with high voltage (SHV) connectors. A dedicated rack is connected to them, with 20 independent high voltage power supplies, that allows for a complete control of the lenses as independent parameters. The potentials of the lenses discussed below will then be all referred to the ground potential.

The polarization vector components, thanks to the simple geometry realized in this experiment, are straightforwardly extracted from the four asymmetries observed in the

detectors, according to the diagram of Fig. 4.6.

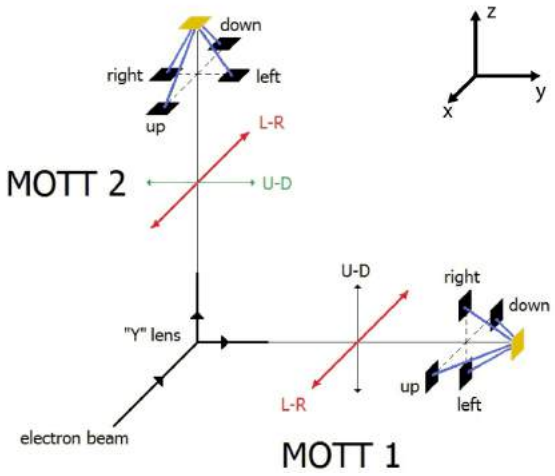

Figure 4.6. *Labelling of the detectors and of the detected asymmetries. Details in text.*

The apparatus uses a tricky notation. If one considers the sample frame of reference, the three Cartesian axes are: X (in the surface plane and horizontal), Y (coincident with the sample normal) and Z (in the surface plane and vertical). For Mott-1 this translates in two accessible asymmetries: an asymmetry that corresponds to the vertical component of **P** (P_z) being *up* or *down* and that is read by the two PIPS disposed in the horizontal plane. The PIPS output channels, however, *are labelled for the polarization component that they measure and not for the position that they have.* So the *up-down* channels of Mott-1 measure the P_z component of **P**, while the *left-right* channels measure P_x. In Mott-2 the same labelling of Mott-1 is reported with a rigid rotation of 90°, so that the *left-right* asymmetry determines again the P_x component, while *up-down* asymmetry for Mott-2 assesses the P_y component.

4.3.1 Electron optics

A relevant part of the commissioning of an electron analyser consists in setting up the electron optics to achieve the performance required to conveniently operate the instrument. For this reason, continued attention was dedicated to careful optimization of the lenses system and to a deep understanding of the behaviour of the electron beam. The electron optics is entirely formed by electrostatic lenses, formed by a sequence of aluminium elements (mainly of cylindrical shape) separated from each other by insulating rings of aluminium oxide. As hinted above, in sect. 4.3, the lenses are divided in two separate suites by the valve, the aforementioned electron transport lenses and electron beam switch.

The electron transport suite is composed by five cylindrical lenses, one dipolar lens and one quadrupolar lens, as shown in Fig. 4.7. The lenses will be described following the stream of the electrons moving towards the Mott detector. Lens 1 is dedicated to the collection of the electrons emitted by the surface, while lens 2 is the quadrupolar element that has the leading role in optimizing the geometry of the beam to obtain a periaxial

propagation of the particles. In this two lenses, most of the beam formation takes place: the counts in the detectors are therefore very sensitive to the configuration of this two lenses and, each time a sample is changed they have to be slightly refocussed to obtain an optimal configuration.

The next five lenses, instead, have the role of gradually accelerating the beam while maintaining the highest possible acceptance (i.e. losing the smallest number of particles). This is achieved by a sequence of focussing and defocusing regions, that allow to obtain a beam of relatively high energy (few thousands volts) in correspondence of the last lens (lens 7). The high energy is required in this point, because the electron beam has to "jump over" the region at grounded potential created by the valve, without being affected in its parameters.

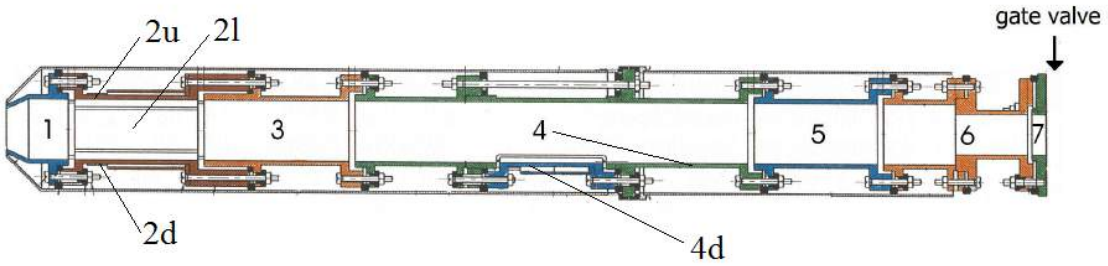

Figure 4.7. *The electron transport lens suite. The labels reproduce the original names that are used to refer to each lens in the apparatus.*

Once the potential step has been overcome, the beam enters the switch system of lenses, pictured in Fig. 4.8. Here, electrons are picked up by two cylindrical lenses (INC and IN), that further accelerate and inject them in the real switch element, formed by two parallel plates (SwU and SwD) with asymmetrical potential that deflect electrons upward or downward. Their voltage can be quickly reversed by an electronic element hosted in the same rack of the HV power supplies. The body (B) elements regulate the access of the beam to a new section, formed by two elements, the central deflector (CD) and the side deflectors (SdD and SdU).

In the deflector, the trajectories are bent in a smooth curve, completing the path that brings the beam, until this point propagating at a 45° angle from the sample surface, to be parallel or orthogonal to it. The deflected electrons pass then through the lateral wall, held at the same potential of the body (thus again B), are further accelerated and selected by the small-aperture cylindrical exit lens (E) and finally sent in the Mott detectors.

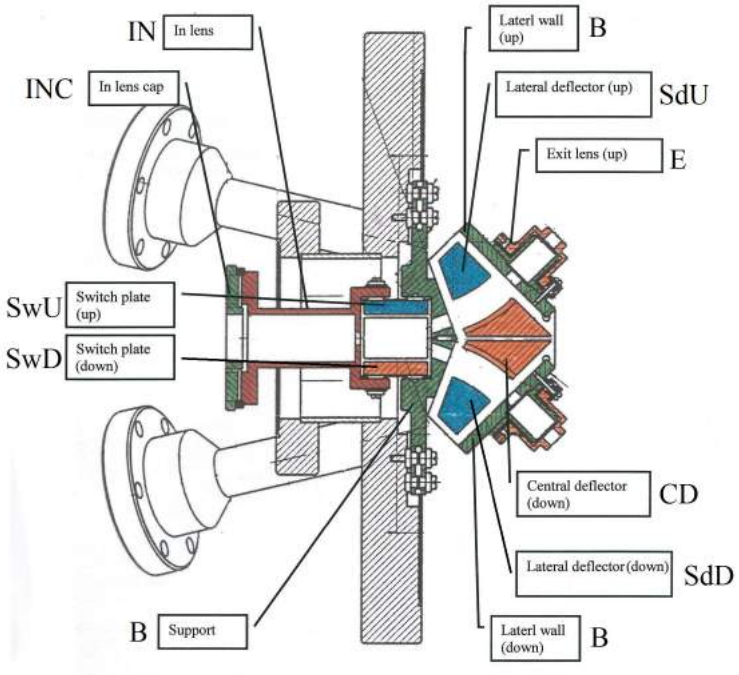

Figure 4.8. *The electron beam switch lenses suite. The framed labels show the extended name, related to each electrode task or geometrical shape. Next to them, the abbreviation used on the apparatus and in tables.*

The work performed on such system of lenses aimed at achieving several objectives simultaneously:

- Maximum transmittance. As discussed in Part I and in Appendix A, the main strategy to reduce the uncertainty in Mott polarization measurements is to detect a high number of electrons. For this reason, the highest number possible of electrons emitted from the sample must be delivered to the spin-detectors.

- Minimum disturbance of the trajectories. The polarization of a beam is very easily destroyed or distorted by strong bending of the particles' paths. Furthermore, if internal metallic parts are hit by the beam, they can generate unpolarized secondary electrons that reduce the polarization signal.

- Partial energy filtering. Despite the fact that the system does not possess energy resolution, it is possible to design the lenses voltages to obtain significant transmittance in a precise part of the spectrum. As hinted in the Introduction, the only broad region with a high spin polarization is the very low-energy region in the spectra of magnetic materials. It is then possible to improve the signal-noise ratio by letting only electron from this region of energies to reach the detector.

- Flexibility. The instrument will have to adapt to different sources with pulsed or continuous operation, high or low intensities. For this reason, not a single configura-

tion of the electron optics has to be elaborated, but a full set of them, able to meet the different needs of each experiment.

The implementation of such stringent condition on a very complicated system (more than twenty independently variable parameters) may appear as a formidable task. However, with the combination of computational instrumentation, patience, experience and skill of the team that I had the chance to be in, most of these points have been fulfilled. In the next two sections, a summary will be given of how this relevant part of the commissioning was performed. The first difficulty was of hardware nature: at the first switch on of the lenses, the power supply of electrode four indicated that the element was grounded. The whole electron beam transport system of lenses had to be dismounted, cleaned and repaired. This operation set the apparatus back to regular operation, and the real optimization of the voltage settings could be performed.

Optimization

The first phase of lenses optimization was carried out with the use of the software SIMION 7 [73]. This program is designed specifically for simulation of charged particles trajectories in arrays of macroscopic potentials, even with complex three dimensional geometry. The fundamental elements of SIMION 7 are three: a simple CAD software, used to design the array of lenses, a solver for the electrostatic equation that is able to determine the electric field at each node of a three dimensional grid and a solver for the equations of motion of the particles in the calculated field.

The drawing of the array of lenses is realized only once for each instrument, when the operation has to be designed the first time: for this reason, the drawings were already available and did not need further elaboration. Once the drawings are loaded in SIMION 7, the workflow proceeds as follows:

- An independent panel must be opened to set the potentials of each lens element. When this panel is closed, the electrostatic solver is launched, and the static fields are calculated.
- Another panel has to be opened to set up the initial conditions and the characteristics of the particles: initial energy, initial direction of motion, charge, mass. Particles can be divided in several sets containing each a defined number of particles whose initial conditions can be changed in a automatic step-by-step fashion.
- When the initial conditions are set, it is possible to return to the drawing panel, where it is possible to start the trajectory calculator, that displays in real time the paths of electrons in the lenses graph.

The result is shown in a 3D projection. The CAD allows then to separate elements, to cut and represent them bidimensionally to obtain the desired view. As an example, a typical test run for the transport lens array projected in the vertical plane is shown in Fig. 4.9.

Thanks to this computational instrument it is possible to elaborate the lenses settings to achieve the desired performance trying several configurations very quickly, while having the

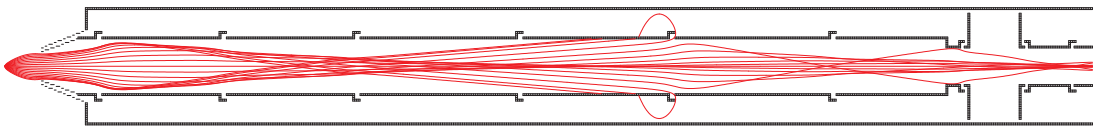

Figure 4.9. *A typical run for the electron beam transport lenses of ULTRASPIN apparatus. In this case, a non optimal transmittance is observed, because the initial energies of the particles are higher than the desired passing values.*

possibility to observe the trajectories. The general indications mentioned above (gradual acceleration, focussing and defocussing sequences, the high energy at the valve jump and the smooth bends) could then be translated in a set of tables of potentials that could be implemented on the machine. The simulations' result, however, is not expected to be immediately the best configuration for the effective operation of the machine: many effects, arising from sources unaccounted for, can modify the outcome. Furthermore, the final criterion to obtain maximum transmittance is to obtain the highest count rate at the detectors in the real system, and therefore the results of computational calculations have to be considered as a method to individuate a point in the space of parameters close to the desired one, so that it is possible to achieve the latter with small (and more easily manageable) variations from the former.

The commissioning of the machine is following a gradual schedule, moving from the static operation to the dynamical one in steps that aim to gain the maximum advantage without losing the relevance of the results obtained before. As a first step, the first lenses configurations had to be studied in continuous mode using an electron gun as a source. For the sake of machine testing, an electron gun is much better than a synchrotron, an X-ray tube or a laser, because provides a primary beam in a very wide range of intensities and energies, and is not subject to schedule in the use. As a second step, it was planned to transition to dynamical regime with a table-top laser, such as a FHG or HHG system. These would bring the instrumentation to cope with very low intensities, rather high repetition rates, and very low energies of the photoemitted electrons. Finally, a beamtime with a FEL source is expected to finally bring the apparatus to operate in its definitive regime: with relatively low repetition rates, but with high intensity per each pulse. At each step, electron optics is expected to need attention in order to achieve the optimal working point. However, the transition to step two requires both the ultrafast source and the electronics for pulsed measurements to be ready, i.e. the commissioning of two highly sophisticated systems, and the time covered by the work of this thesis was dedicated to the full development of step one.

Using the secondary electron emitted from a metallic surface, the tables of potentials obtained from the simulations were tested and optimized to reach the maximum transmittance and minimum disturbance of the trajectories. It must be noted that a very small variations from the computational results were needed, an indication that the lenses are close to ideal conditions. The gun was used with a very low emission current (in the range of few nA), as the obtained transmittance is very high and higher currents would

have saturated the detectors[18]. With the use of a magnetic sample (the details of this experiment will be described in Chap. 5), then, the electron optics was optimized further in order to maximize the polarization signal.

While performing these tasks, however, attention was dedicated also on the ease of use of the apparatus: the machine was brought in condition of starting to work almost immediately after switch-on[19] and of operating with extremely long-lived stability[20]. These precautions are absolutely necessary in a machine such as the Mott detector, because the reduction of uncertainty on polarization requires long integration times (particularly if the polarization is small): measurements of several hours are not uncommon, and it is necessary that instrument does not introduce long dead times and does not ruin a very long measurement by suddenly dropping out of the initial configuration. The realization of stability required a very time consuming routine, but once realized it is expected to significantly improve the performance of the machine.

From the synthesis of all these necessities, an optimal configuration was finally achieved. The values of the potentials are given in Tab. 4.1.

To have a visual check of the final configuration, the potentials obtained on the machine were inserted back in SIMION, and the trajectories were calculated for the entire assembly of lenses both in the case of 5 eV electrons (4.10 a.) and in the case of 100 eV particles (4.10 b.). Since the accuracy of the simulation resulted to be high in the first implementation, this description is expected to be faithful to the real electrons' paths.

El. label	Volt. [V]	El. label	Volt.	El. label	Volt.	El. label	Volt.
1	125	3	250	7	1750	SwD	2054
2u	98	4	650	INC	344.5	SdD,SdU	2119
2d	98	4ud	650	IN	2925	CD	1625
2l	100	5	138	SwR	793	E,B	650
2r	102	6	388	SwU	1209		

Table 4.1. *Best set of potentials for the electron optics.*

Observing the picture, it is clear that the desired results have been attained: the trajectories are smooth, and the transmittance is maximum in an interval of energies going from 0 eV to 50 eV. Flexibility is at reach, because once such an efficient setting has been found, a rigid multiplication of it gives a good starting point for realizing a new one. However, all the requirements for different regimes of operation will be met only when other sources will be implemented. Moreover, quick switch-on of the machine and very high stability were obtained.

[18] As will be explained in Sect. 4.3.2, in the static regime detectors must be operated with much smaller intensities than the dynamical one.

[19] Small adjustments are still needed, but mainly arising from the fact that an electron gun, when working at such low currents, requires some warm-up time before achieving good and stable operation.

[20] The aim was the realization of a system that, after switch on, is able to maintain unaltered all the parameters involved in the measurement, such as the intensity of the source and the counts in the detectors for many hours or days.

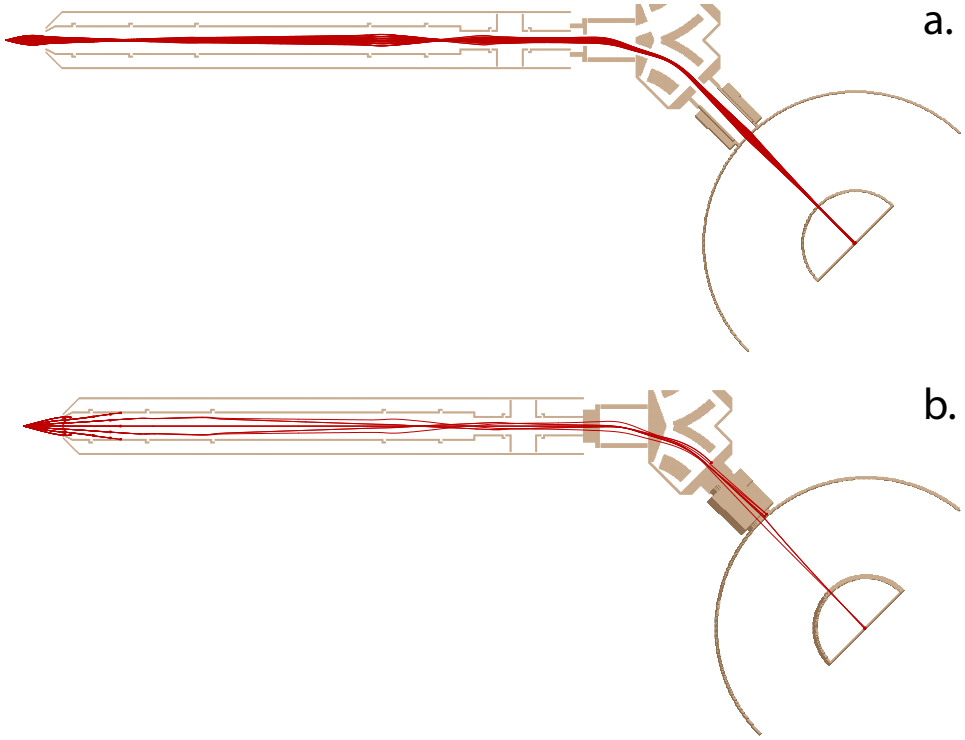

Figure 4.10. *a. Trajectories (red) of 5 eV electrons in Mott electrostatic lenses (brown). The initial conditions were distributed in an angular spread of* 30° *in both the vertical and horizontal direction. a. Trajectories (red) of 100 eV electrons, with the same angular spread. As can be seen, the trasmittance is reduced significantly.*

4.3.2 Readout Electronics

The data acquisition chain described in Sect. 3.1.1, is designed to operate in continuous mode, with a constant stream of electrons of a rather low intensity, so that the number of electrons reaching the detector in a second is of few 10^5. This means that 10 μs pass on average between an electron and the next. If two electrons are closer (from 1 μs to hundreds of ns) the signal will be distorted, because the charge pulse of the first will influence the one of the second (*saturation*[21]), if the electrons are much closer (tens of nanoseconds and less), the electronics with discriminators will not be able to separate the pulses and will count only one electron (*multi-hit event*). Furthermore, this will appear with a high intensity signal, thus being read as a high energy electron, even though the two electrons that have actually generated the signal have a low energy and are not carrying information on polarization.

When stepping to the time resolved regime, instead, the apparatus has to cope with

[21]The saturation regime for the detector used in ULTRASPIN is around 150 kcps (kilocounts per second), as was discussed in [74], and observed frequently during the work described in this thesis. Beyond this minimum saturation threshold, the response of each detector is dependent on the single PIPS characteristics, such as number of defects, slight variations in size, etc. The asymmetry signal therefore can not be trusted any more beyond these count rates.

extremely short pulses (of a typical duration of tens to hundreds of nanoseconds depending on the length and the velocity of drift in the lens system) which contain a high number of electrons, separated by intervals (from milliseconds to microseconds, depending on the repetition rate of the laser) with no particles incoming. It is clear that the aforementioned electronics can not be used straightforwardly, because during a single pulse particle fluxes as high as 10^{12} electrons per second and thus would deeply saturate the acquisition system. It is therefore not possible to obtain an asymmetry signal in these conditions. To overcome this problem, the whole electron counting system must be rethought. It is useful to report here the relevant characteristics of the two main blocks (detectors and electronics) as described in Sect. 3.1.1:

- PIPS detectors have a fast rise time (around few hundreds of ps), but a long recovery time (hundreds of ns to μs), and, for each particle entering the detector, they generate a pulse of charges i.e. a small current burst.
- The electronics integrates the burst of current to give the total charge of the pulse, and then discriminates the signal, letting pass only pulses higher than a selectable value. These procedures are performed at the usual electronics time-scale of few μs.

The first solution that could circumvent this difficulty has been developed at University of Regensburg by the group of Prof. C. Back. Using as a source a FHG table-top laser, they reduced the intensity of the source so that the number of electrons is very low and the detectors are kept outside of the saturation regime. This is simply achieved by keeping the count rate smaller than the repetition rate of the laser, meaning that one electron per pulse (or less i.e. one electron every few pulses) is detected. This ensures that distortion of the signal due to saturation is avoided, but does not strike out the effect of multi-hit events. The latter can be anyway accounted with an analysis of the signal. A plot of the measured polarization as a function of the intensity (and therefore the count rate in the PIPS) is shown in Fig. 4.11.

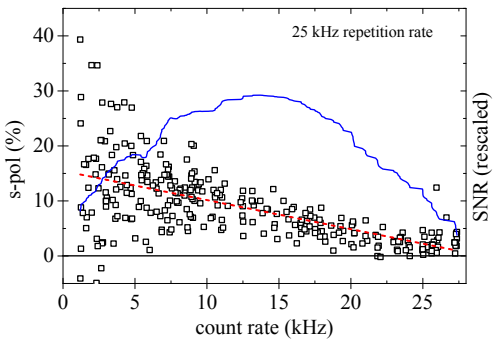

Figure 4.11. *The polarization signal of Fe/W(110) in the secondary electrons yield as a function of the intensity of the source (expressed in terms of the count rate at the detector). Each open square (measured polarization) is the result of acquisition for the same time. The number of squares for each count rate is identical. The red dashed line is a linear fitting of the polarization data. The blue line is a plot of the signal-noise ratio (SNR) as a function of the count rate. From [57].*

It is evident from the picture that it is possible to drive the system to a configuration such that the detectors register much less than one electron per pulse (left end of Fig. 4.11): this gives a high polarization signal, because the asymmetry is not disturbed by the presence of multi-hit events. In this configuration, however, the SNR is not optimal because the asymmetry is large, but intensity is very low and therefore also noise is very large. It is more efficient to move to higher count rates, (approximately in the centre of Fig. 4.11, i.e. again to about 100-150 kcps) in this case the noise will be much smaller, but multi-hit events will reduce the measured polarization signal. However this reduction is a constant factor and, if the detector is calibrated and operated at the same count rate, it can be included in S_{eff}, giving the correct polarization values. This method is appealing because it does not require a deep modification of the electronics, but it is clearly not suited for FEL applications, where the repetition rate is very low and the intensity is very high. Furthermore, as only one electron per pulse is counted, a large amount of information contained in the characteristics of the pulse is lost.

The second approach is based on a result obtained by Y. Acremann and coworkers (ETH Zürich), that were able to show that if a high intensity pulse of electrons is sent on a PIPS detector, the *shape* of the output pulse is a magnification of the input one. If the acquisition chain is then changed to register the detailed shape of the incoming current pulse (instead of integrating it to give a charge signal), the whole distribution of intensity can be studied. This design exploits cleverly the time windows given by a PIPS detector: the time-shape of the electron bunch is well reproduced thanks to the fast rise time of the PIPS, and the initial state is recovered when the whole bunch is passed, i.e. while waiting for the next pulse, thus matching the recovery time with the dark intervals due to the repetition rate.

In Fig. 4.12 the difference between the static acquisition chain (a.) and the one for time-resolved measurements (b.) are sketched: while in the first case the signal is immediately converted in a number (through charge conversion and discrimination) and the asymmetry is then calculated according to eq. 2.10 between two numbers, in the second case the whole distribution of intensities as a function of time is recorded in each detector, and delivered to the acquisition PC. These curves can then be manipulated as desired, by calculating the asymmetry at each instant and obtaining the time-distribution of polarization in the pulse, or by integrating each pulse and calculating asymmetry again with eq. 2.10.

The former method yields a great interest because in the time-distribution of the intensity the energy spectrum (or at least a part of it) of the sample is somewhat encoded. The electron bunch photogenerated at the surface is in fact spread along the time axis by the time of flight in the electron lenses. This method implemented on a Compact Classical Mott detector holds the potential to produce four spin-resolved XPS spectra for each single FEL pulse. This is an exciting possibility that could produce a very powerful instrument for the study of spin polarization. However, the extraction of this information may reveal to be very difficult, or even impossible, as the electron bunch scatters with the gold foil before reaching the detectors, and it might turn out to be very difficult to extract only the contribution of the elastically scattered electrons. This anyway opens up a very interesting field of technological development of this kind of detectors, where a lot of work can be done.

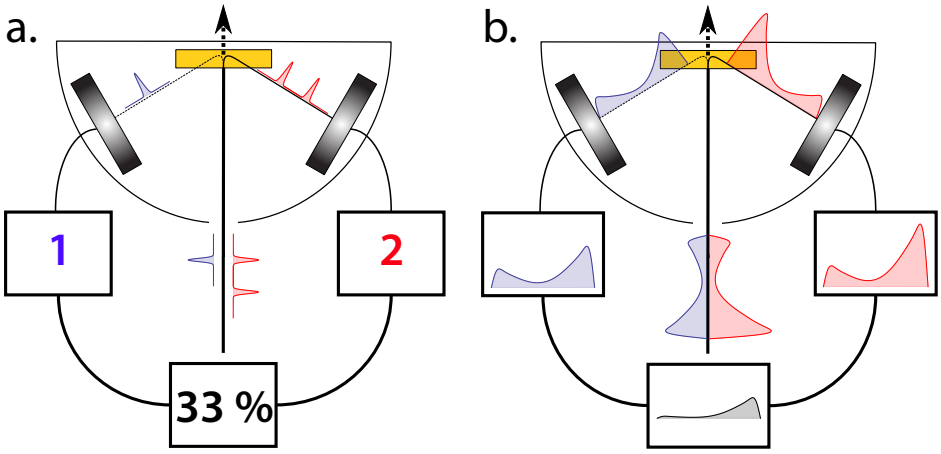

Figure 4.12. *a. Continuous operation. A steady stream of electrons enters the detector, is split in the two spin-filtered beams that are sent in the electron counters. The electronics immediately converts them in numbers, that, in a PC, allow to calculate polarization. b. Pulsed operation. The pulse reaches the detector and is split in two spin-filtered bunches that are sent to the detectors. The new electronics design acquires instant by instant the incoming current. The two curves are received by a PC that allows to manipulate data and calculate the polarization of the pulse conserving its time structure.*

It is not only for the energy resolution perspectives, however, that this configuration is preferable to the previous one. Indeed, it allows to retrieve a signal from all the electrons reaching the detector, thus giving a high statistics on the polarization measurement for each pulse. It is therefore much better suited for a applications with FEL sources. Furthermore this design of electronics can also reproduce the operation of the old one, and therefore the implementation of such system enables also to let the system work with continuous sources or high repetition rate pulsed systems.

For the reasons described above, the second approach was chosen for the upgrade of ULTRASPIN acquisition chain, and a new electronics was developed by the group of Laboratory of Instrumentation and Detectors at Elettra Synchrotron, led by Dott. G. Cautero. Following the scheme in Fig. 4.13, a short description of the main elements can be given.

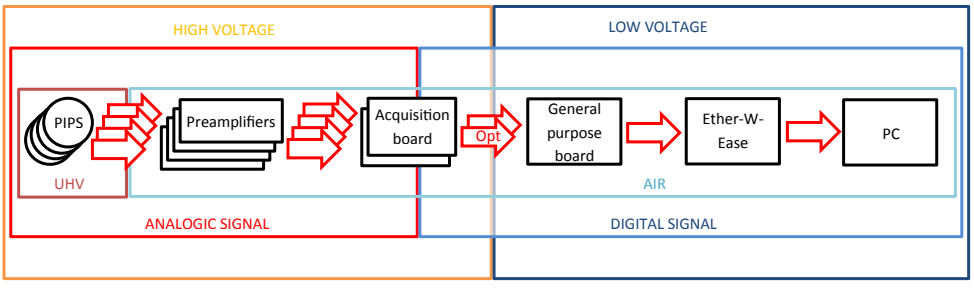

Figure 4.13. *Block diagram of the new electronics for ULTRASPIN. From [75].*

The first part of the electronics is, as the old on was, floating at a high voltage and

physically mounted on the detector assembly. The analog signal generated by the four PIPS is picked up by four *preamplifying boards*. Here, the signal is amplified by two cascaded amplification stages, separated by an attenuator: this system allows to control the dynamic range of the preamplifiers in a very large interval, in order to adapt to the different intensities that each application entails. The preamplifiers are supplied by a network that creates a strong decoupling from external noise. The amplified analog signal is then sent to two data *acquisition boards*. Each of these features two very high sampling frequency *analog-to-digital converters* (ADC) combined with a buffer: these two elements, controlled by a logic unit, allow to translate the input pulse current in a digital output with high temporal detail. Each acquisition board then sends its output to a *transduction board*, where the digital electric signals are converted into optical ones, sent through the optical fibres and decoupled from high voltage. From this point on the electronics elements work close to ground potential and are in a rack mount case. A second transduction board receives the signals from the fibres and sends them to the *general purpose board* which constitutes the real "intelligent" core of the system, where the huge fluxes of information are administered. The general purpose board sends the signals to a *Ether-W-Ease board*, which encodes the data in the TCP/IP protocol and sends them to the PC.

It is obvious that such a high flux of data cannot be withstand with continuous acquisition: for this reason, the inverse path for the signals must also be possible, and the electronics will start to record data only when effectively interesting information is arriving from the PIPS. This "triggering" is organized on two levels. The first is provided by the experimenter, which starts the measurement from the control software of the PC, sending a command that is delivered to the general purpose board which sets the components upstream in a "listening configuration". At this point the second (and more properly called so) *trigger* is needed to start acquisition: the electronics described here allows for two alternative kinds of such a signal.

- When the system is operated with a pulsed source (FEL or table-top laser), the same source provides a trigger when the pulse is delivered. After it, the pulse shapes are acquired and saved for a user-defined time window.
- When the system is used with a continuous source (synchrotron, X-ray tube or electron gun), it starts measuring when the experimenter's signal arrives, but dumps the data of a bunch once it starts to measure the next. Before dumping the data, however, the logic unit calculates its intensity, and, if it is higher than a user-defined threshold, it creates a "virtual trigger". After it, the system starts to increment a counter each time the threshold is overcome again until the whole pre-set time-window is passed. At this point the numeric data are sent to the PC.

The second method recreates the mode of operation of the previous electronics, thus giving an extraordinary flexibility to the system.

Finally, with the reconstruction of the electronics system, chance was taken to improve the power distribution system and the delivery of the supply current to the high voltage electronics, also bettering the heat removal from the electronics. This tasks were realized by a system of plastic bars an tubes, rather long and thick, and thus able to withstand

voltage differences of more than 100 kV. The supply current is delivered by a brushless motor (on the low voltage side), that spins a plastic bar. This is in turn mechanically linked with a second brushless motor (on the high voltage side), that is used as a dynamo, generating the required power. A dedicated board transforms the motor's output in a 22 V DC current, cleaning it from noise. A hollow tube with a fan on the low voltage side, allows to extract hot air, avoiding overheating of electronics[22]. A photography in Fig. 4.14 of the system on a benchmark shows the details of the element that is mounted on the detector.

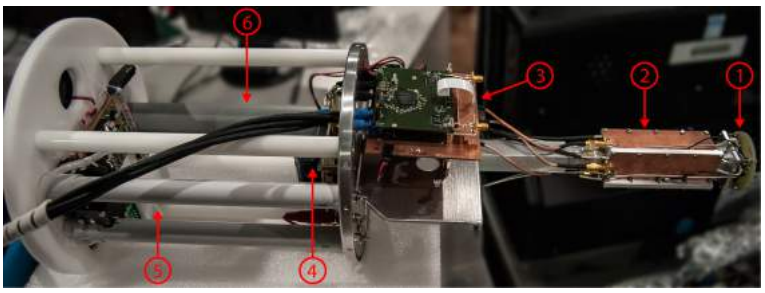

Figure 4.14. *1. Connector. 2. Preamplification boards. 3. Acquisition and Transduction to optical signal boards. 4. High voltage electronics supply current generator. 5. Brushless motor. 6. Fan for heat extraction.*

[22]This was a serious issue in the previous electronics scheme, because when the system was operating it was closed in a high voltage safety cylinder that blocked air circulation. Long measurements were then affected by a slow build up of counts in the detectors, due to the increasing thermal noise.

Chapter 5

First polarization measurements

During the commissioning of the instruments the first polarization measurements were started rather early, in order to optimize the operation of the spin detector. For this task, experiments of secondary electron yield magnetometry were performed. The plan was to measure the polarization of the secondary electrons emitted by a magnetic sample under continuous excitation by an electron gun (1300 eV unpolarized primary electrons), selecting the low-energy end of the spectrum as discussed in 4.3.1. In the following chapter, a short description of the experiments performed will be given.

The inelastic mean free path[1] (IMFP) of electrons in a magnetic material is strongly spin dependent, due to the exchange interaction that shifts the bandstructure above and below the Fermi energy, and to the spin dependence of the low-energy collective magnetic excitations [76]. This has an important effect on the phase (number 2 in the three step model exposed in Introduction) of electron emission in which the particles reach the surface by being transported through the solid. In particular, as this phase is extremely important in the formation of the spectrum background, the effect is relevant in the energy region where the background is larger and where the electrons having undergone the highest number of inelastic collisions are concentrated. For these reasons, the low-energy end (5-50 eV) of the secondary electrons spectrum of magnetic materials is highly polarized and the polarization is proportional to the magnetization of the material (because it is mainly generated by exchange-related interactions). This can be exploited as an analysis instrument in two ways:

- it can be used to develop a highly surface sensitive magnetometry technique, thanks to the low escape depth of the electrons, that can study, when complemented with bulk-sensitive techniques, the details of the magnetic behaviour of the surface.
- it can be applied to the study of the same IMFP in solids. This is a particularly interesting field of research, as it is strongly correlated to the transport in magnetic materials, and in particular to spin relaxation[2], of great interest for the spintronic

[1] The inelastic mean free path is the average distance that an electron can travel in a solid between two successive inelastic collisions.

[2] Spin relaxation is used here to indicate the class of processes that tend to reduce the polarization of an ensamble that travels in the solid.

research community and also for the ultrafast magnetism, as the dynamics of spin-relaxation processes is under active debate.

The set-up used for this work, limited by the needs of the commissioning procedure, with the use of a unpolarized primary electron gun and an energy integrated spin-detector, can be applied mainly as a highly surface sensitive magnetometer, but with the use of a tunable photon source this apparatus can be used (and in fact was originally designed and used for this application) to realize X-ray Absorption Spectroscopy measurements with resolution of the spin polarization of the quantum yield [11], a technique that can assess both the applications listed above with element specificity.

The planned experiment required to record the full hysteresis cycle of the sample. Measuring magnetic materials with an electron-out technique is always difficult, because the magnetic fields present in the space are often strong enough to bend the trajectories of electrons, changing the number of electrons able to enter in the lenses or, in particular for low energy electrons, driving them back to the surface, where they are adsorbed by the sample. In particular for the measurement of hysteresis loops, when an external magnetic field is applied, this effect can assume significant proportions, thus severely affecting the signal[3]. It is therefore necessary, in order to realize such kind of measurements, to minimize the external magnetic fields in two ways:

- The *stray fields* must be kept to a minimum. Indeed, when a magnetic material is magnetized and the external field is removed, it is left in a state of *remanent magnetization*. In this condition, the sample possesses a macroscopic magnetization vector, directed in on well-defined direction. This implies that the sample can be treated as a macroscopic magnetic dipole, with a north and a south pole: a magnetic dipole field (stray field) will therefore be present in the free space around the sample, whose field lines will go from the north pole of the sample to the south. For samples of macroscopic thickness, this fields can be a serious issue and geometric stratagems have to be used. With thin or ultra-thin films, instead, stray fields are generally very small, and do not require special attention.

- The *external field* applied to the sample in order to run the hysteresis loop must extend as little as possible in the free space: this can be achieved by minimizing the gaps between high permeability materials in the field application geometry.

Luckily, the long-standing research on spin-resolved secondary electron spectroscopy has established an efficient method to solve this problem, i.e. the use of *picture-frame* samples: the material to be analysed is geometrically realized in a rectangular shape with a hole (also rectangular) in the centre, so that the field lines of the magnetization field can be closed inside the material, and the external stray fields are kept to a minimum (for a scheme of a picture-frame sample, see Fig. 5.3). Furthermore, these samples are not magnetized by an external electromagnet, but simply by a coil wound around one of the arms: sending a current in such a cable, the induced field is generated directly in the material under study, and thus no external fields are generated in the free space.

[3]For this reason, magnetic materials are normally measured with spectroscopic techniques when in remanence state.

5.1 Sample structure

A sample of that type was realized specifically for ULTRASPIN experimental apparatus, with the intent of creating a reference system, able to be operated even in commissioning conditions, i.e. when parts of the machine are missing. In particular, it was designed to require a very simple preparation procedure, to be able to be magnetized (and run hysteresis loops) even without an external magnet and, obviously, to fit onto a sample holder compatible with ULTRASPIN manipulator. The most important choice in this sense was the selection of the sample material, which had to be easy to prepare for spectroscopic measurements, simply machinable and a very soft magnet, with a high polarization of the secondary electrons. The material that was finally selected is magnetic amorphous metal, also called metallic glass.

5.1.1 Amorphous Metal

Amorphous Metal is a term used to define a large class of alloys produced by rapid solidification of the melt ($10^5 - 10^6$ K/s) so that the crystalline structure of the solid does not have the time to form[4], and a solid metal with with the atomic order typical of glass materials is formed. The creation of a system in which atoms are connected by a metallic bond, but without a crystalline orders, yields a significant number of advantages, that can be applied in several fields: high strength, high hardness, high corrosion and wear resistance, high reflection ratio and good soft magnetic behaviour are only few of them [77]. The glassy structure relaxes also several restrictions on the stoichiometry of the alloys, that can be engineered in a much broader range of values, collecting a very large number of elements in a single material. Furthermore, if such system are slowly annealed, they start to recrystallize, forming nanocrystals [77]: controlling the size, shape and magnetic anisotropy of this crystal formation, it is possible to tune material behaviour on an even larger interval of values and properties.

In particular, some classes of such alloys, based on the presence of large amounts of magnetic transition metals (especially Co, Fe and Ni), together with metalloids Si and B (which are necessary for the glass formation and the stabilization of the structure), are especially suited for soft magnetic applications. To be a good soft magnet, a material must have a very low magnetic coercivity, i.e. the external field required for reversing magnetization must be as small as possible. Amorphous metal alloys allow to achieve coercive fields as small as 0.1 A/m, yielding at the same time very high saturation (and, in some cases also remanence) polarization. They are therefore suited for electrical energy generation and distribution whit high efficiency, and in particular for very high frequency applications.

For the creation of a picture-frame sample, an amorphous metal alloy is very well suited: the lack of crystalline order and the ribbon shaped geometry allow to manipulate it easily (it can be cut with a knife or scissors), allowing to realize the complex geometrical

[4] In the most common production technique, the metal melt contained in a large crucible is poured on a cooled spinning (at 100 km/h) disk, that "freezes" it in less than a millisecond. The high thermal quench required to obtain amorphous materials limits the shape to thin (50 μm) ribbons, of few millimiters width.

shape. Furthermore, the preparation for spectroscopic measurements of the surface can be limited only to sputter etching, while annealing procedures are not needed, as there is no structure to be recovered. Finally, soft magnetic behaviour enables to magnetize it even with a very small coil mounted on the sample. The alloy of choice was the Co-based $Co_{72.5}Ni_{12}Fe_{9.1}B_{5.5}Si_{0.4}Mn_{0.5}$.

Before the realization of the sample, the metallic glass alloy was characterized with the realization of a *hysteresigraph* [78]: the amorphous metal ribbon was rolled in a cylindrical shape and two windings of electrical cable were wrapped around it. One of the windings (*primary*, with 45 loops) was then connected to an AC power supply through a shunt resistance (50 Ω), while the second (*secondary*, with 40 loops) was connected in series with an itegrating RC circuit. A scheme is shown in Fig. 5.1.

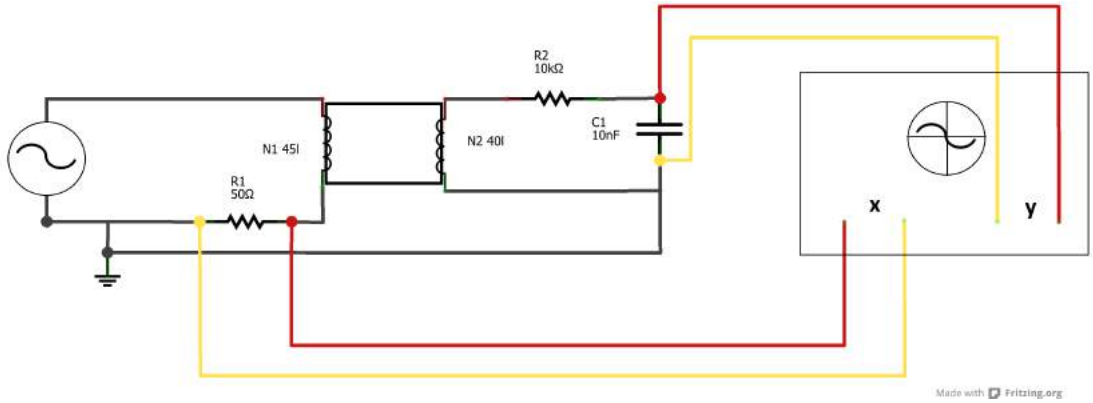

Figure 5.1. *Scheme of the circuit used to characterize the metallic glass alloy used for the picture-frame sample.*

Evaluating the current in the primary winding through a voltage measurement at the ends of the shunt resistor, it is possible to calculate the magnetic field H generated in the metallic glass with the simple expression:

$$H = \frac{N_p I_p}{l} = \frac{N_p V_p}{l R_1} \tag{5.1}$$

where N_p is the number of loops of the primary circuit, V_p the measured voltage, l the circumference of the metal glass ring and R_1 the resistance of the shunt resistor (I_p, the current in the primary circuit is therefore obtained from the ohmic law as the voltage drop at the ends of the resistor). The voltage output of the integrating circuit connected to the secondary winding is, instead, proportional to the magnetic flux density B, trough the expression:

$$B = -\frac{R_2 C}{N_s A} V_s \tag{5.2}$$

The hysteresis curve of the magnetization versus the applied magnetic field can be immediately visualized if the secondary circuit output is inverted ($V_s = -V_{out}$) and the two signals are fed into the x-y plot functionality of an oscilloscope. The magnetization can then be calculated as:

$$M = \frac{B}{\mu_0} - H = \frac{R_2 C}{N_s A \mu_0} V_{out} - \frac{N_p V_p}{l R_1} \tag{5.3}$$

The hysteresis cycle in Fig. 5.2 was obtained with this method, at an AC frequency of 22 kHz and with 13 Volts as a peak-to-peak amplitude. As it can be observed, the hysteresis loop has a low coercive field (23 A/m, or 0.29 Oe), and a high magnetization saturation. The shape of the loop is not squared, due to the lack of the magnetocrystalline anisotropy that stiffens the motion of the magnetization vector.

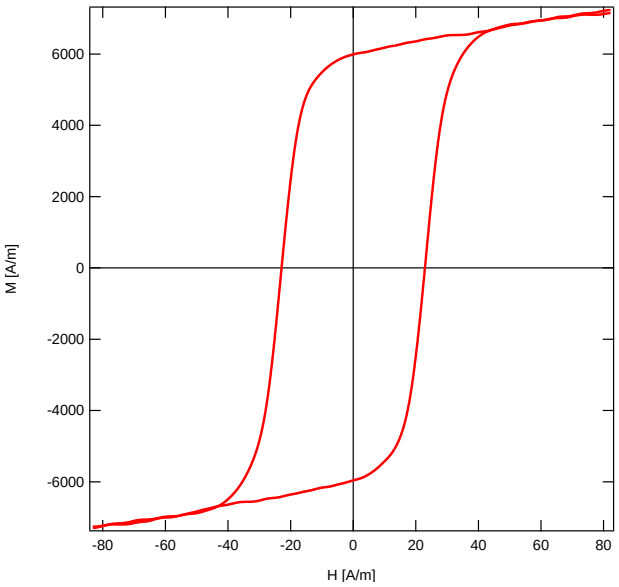

Figure 5.2. *The hysteresis registered with the hysteresigraph circuit.*

The construction of the sample required a rather accurate planning and the preparatory drawings are shown in Fig. 5.3. The exploded view (Fig. 5.3 c.) can help to understand the structure, while the two projections allow for a overall inspection. The basic element is a sample holder with two electrically isolated ends: two Molybdenum blocks (3) are held together by a Al_2O_3 block (2) to which they are screwed (1). This sample holder is used for the development of sophisticated samples and for in-operando measurements also in other apparatuses of the beamline. On the two Molybdenum blocks, two spacers of equal thickness are placed, one (4) of Tantalum and glued with conductive paste, and the other of Al_2O_3 (5) and glued with epoxy. In this way, one side of the sample will always be grounded, to avoid charging due to electron emission, while on the other side it will be possible to control the path of the current.

The ribbon of amorphous metal is too thin and flexible to sustain itself and the weight of the components that are mounted onto it, so a thick Tantalum frame has been realized (6) on which the picture-frame of amorphous metal (7) is glued with conductive paste. Around the side of the picture frame which is leaning out, a 10 loop coil of kapton-insulated wire was wrapped (8). The electrical contact of the two ends of the coil with the Mo blocks of the sample holder was ensured by a twofold action: after removal of the kapton from a short tract, they were spot-welded to the blocks with a thin Ta stripes (10) and were glued to the blocks with conductive paste (9). Finally, a thin tantalum sheet (11) was positioned above the coil and spot-welded to the Ta picture-frame (6), in order to avoid that the kapton surface, exposed to electrons emitted from the sample, could be charged.

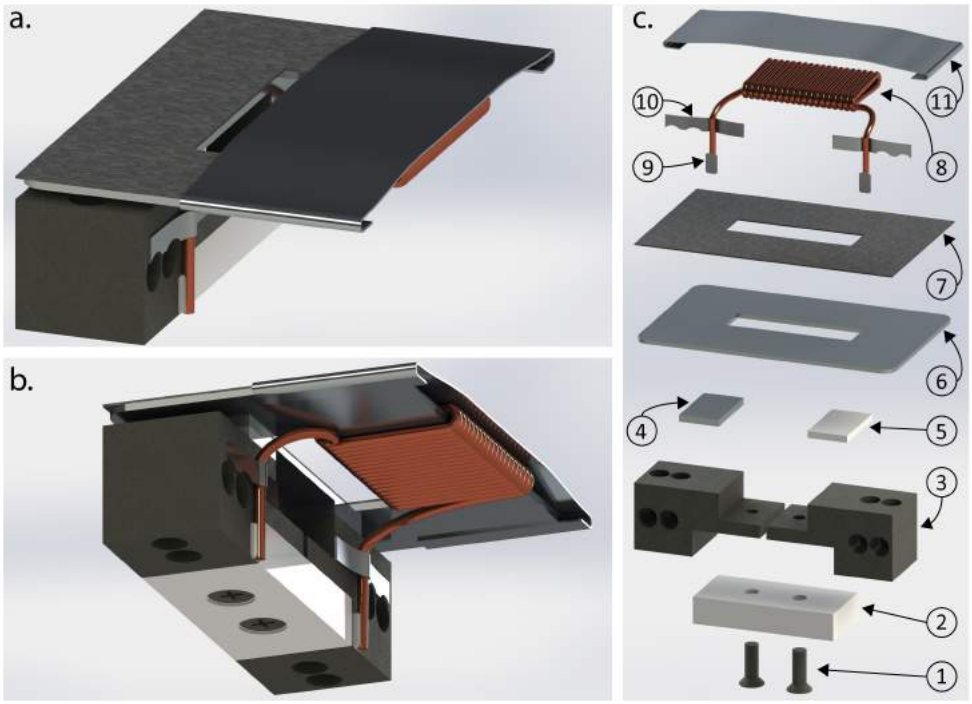

Figure 5.3. *a. Three dimensional projection of the sample from above. b. Three dimensional projection of the sample from below. c. Exploded view, details in text. For scale, it must be considered that the short side of (7) is 12.5 mm.*

With this design, it was possible to send current trough the coil that was hosted on-sample and, at the same time, to keep the amorphous metal sheet always electrically grounded.

5.2 Spin polarization measurements

With this sample, the first spin-resolved measurements were performed. As a matter of fact, the experimental phase of the optimization of the lenses discussed in 4.3.1 proceeded in two phases: in the first, the characteristics of an unpolarized beam were optimized (obtaining high trasmittance, temporal stability etc.), in the second, the signal-noise ratio of the polarization signal was improved. This second task was performed acting coherently on the full setting of the electron optics to shift the window of pass energies until the best polarization measurements were obtained. The configuration achieved in such a way has proven the best ever since, and also the very first measurements from thin films have given encouraging results.

5.2.1 Hysteresis loop

A typical hysteresis measurement realized with the set-up described above is shown in Fig. 5.4. The sample was prepared with several sputtering cycles of one hour, and kept in a the

main chamber in a base pressure of 5×10^{-10} *mbar*. No deterioration of the polarization was detected on time-scales shorter than a day.

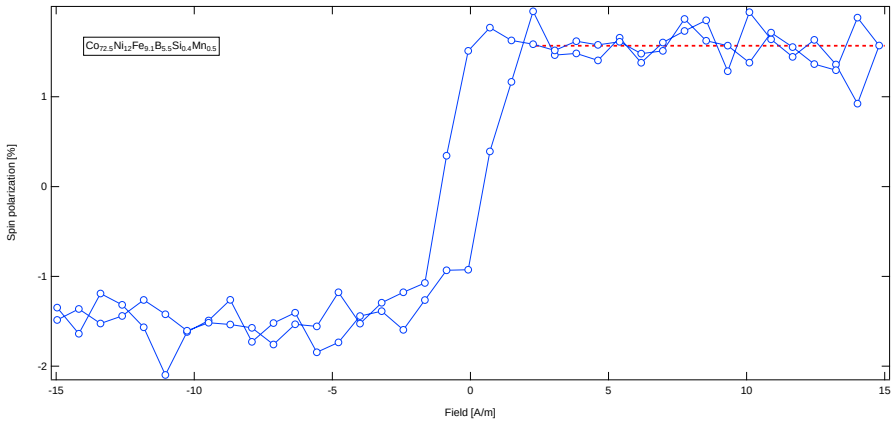

Figure 5.4. *Hysteresis measurement of* $Co_{72.5}Ni_{12}Fe_{9.1}B_{5.5}Si_{0.4}Mn_{0.5}$ *amorphous alloy. The red dashed line shows the average value of the saturation region.*

The measurement was realized with a primary electron beam of 1300 eV of energy and an emission current of 10 nA. In this configuration, the counts in Mott detectors were around 120 kcps, just below the saturation threshold. The software that controls the apparatus enables to control the current in the coil (by driving the bipolar power supply), and to simultaneously register the four channels of each Mott detector. A specifically developed routine calculates in real time the asymmetries, that are displayed on screen and allow to quickly check the quality of the signal. The software saves the single channels, the asymmetries and the coil current in a single file. Several hysteresis loops can be acquired serially and saved in a unique file, allowing for long unmanned operation. An Igor routine with graphical interface has been developed and can be used to rapidly convert the long output file in a single hysteresis loop averaged over the single curves: in the process, the coil current is also converted in the applied magnetic field H and the asymmetry in the percentage spin polarization[5].

The measurement shown here is obtained from a 20 loops run, lasted little more than an hour. The result is very significant, if one considers that the measured polarization is only about $\pm 1.5\%$. This unexpected smallness of the signal can probably be attributed to the roughness of the amorphous metal strip: measurements on polished materials, as well as preliminary studies on thin films, have yielded much higher values. Also the resulting coercive field is strikingly lower than the one in Fig. 5.2: this can be taken as an evidence of the profound difference between the bulk and the surface for what concerns magnetic behaviour. In fact, while the hysteresigraphic method is inherently bulk sensitive, the

[5]The applied magnetic field was calculated with eq. 5.1, where the current in the primary was already known as the current supplied (and measured) by the source. The polarization is instead calculated from the asymmetry as in eq. 2.10, dividing by a Shermann function $S_{eff} = 0.1$, and then converted to percentage. The value of the Shermann function had to be guessed from the characteristic of twin apparatuses, because the detectors of ULTRASPIN were not calibrated. However, a self calibration procedure is possible ([79], [50]), and is scheduled to be performed soon. The value chosen for the analysis of these data is rather conservative, and higher values may result from calibration.

detection volume of spin polarimetry is strongly limited to the surface. It is possible, for example, that the numerous sputtering cycles have altered the stoichiometry of the sample (as the sputtering yield is different for each element) and thus the magnetic properties have been modified[6]. Another possibility is that the lower coercive field is originated from smaller size of domains at the surface: the lower ratio between the volume and the boundary area, allows the domains to yield a smaller energy density, and thus to be reversed with lower external fields.

A very remarkable result can be obtained by the observation of the two flat regions that appear on the hysteresis once the magnetization saturation is reached:

- Firstly, they are extremely flat, and show no bending at higher fields. This is a feature that can be taken as a conclusive demonstration that stray fields have been removed efficiently from the free space around the sample. Typically, hystereses recorded with electron spectroscopy techniques show severe decrease of the signal when moving towards higher fields, as the electrons spiral back to the surface due to the Lorentz force. Here, no sign of such process is evident. Wider scans, reaching up 1 kA/m showed that magnetic field effects start to set in at fields higher than 400 A/m.

- Secondly, the analysis of the the noise can easily be performed. In these regions it is possible assume that the original polarization signal is a constant, and thus it is possible to evaluate its average (shown in Fig. 5.4 as a red dashed line) and standard deviation. For the saturation obtained with the positive field, this procedure yields:

$$P = (1.6 \pm 0.2)\% \tag{5.4}$$

  the standard deviation defines, in this case, the uncertainty on polarization. If one considers the absolute uncertainty, i. e. $\Delta P = 0.002$, it is possible to observe that this is purely of statistical origin, as can be obtained from eq. A.9, by considering that for each point the acquisition time was of 3 s, and that 20 loops were measured:

$$\Delta P_{stat} = \frac{1}{\sqrt{(N_r + N_l) \cdot S_e f f^2}} \approx \frac{1}{\sqrt{2 \cdot 120000 \cdot 3 \cdot 20 \cdot (0.1)^2}} \approx 0.0026 \tag{5.5}$$

  Thus the measurement uncertainty is even slightly smaller than the calculated statistical one. This is probably due to the fact that the real Shermann function is slightly larger than assumed.

It is therefore possible to conclude that the commissioning of the machine has been completed in the continuous mode, and that the apparatus is now able to perform measurements of even very small polarizations with a rather high precision, and the results are affected only by statistical uncertainty.

[6] As discussed above the coercive field can be changed significantly by variations of the chemical composition.

Part III

Experiments

Chapter 6

Experimental techniques

In the following chapter, the most important techniques employed in the experiments that will be discussed in the following will be revised. The discussion is restricted to the methods less commonly applied in laboratories, highlighting the peculiar traits of the measurements performed. In the first section, the basics of the MOKE technique are sketched, focussing on the relevant characteristics for its experimental implementation. The application of MOKE technique to time-resolved pump and probe experiments is then explained, and the most relevant details of the set-up used (hosted in the laboratories of Regensburg Universty) are outlined. In the next two sections, the X-ray absorption measurements are discussed in their physical meaning and application, while the synchrotron-based XPS technique is revised pointing out the most important differences with the picture of the technique that emerges throughout the previous parts of this thesis. Finally, the layout of the beamline on which electron-spectroscopy measurements were made is shortly explained.

6.1 Optical magnetic measurements

The Magneto-Optical Kerr Effect (MOKE) is a phenomenon of variation of light polarization upon reflection from a magnetic system. As long as it is based on a reflection process, it is relatively sensitive to the surface, especially when used on metals with an elevated conductivity, where the skin-depth is of few tens of nm. It is therefore not surprising that MOKE has become, since 1985, the pivotal element of a measurement technique employed in surface magnetism, named SMOKE (Surface Magneto-Optical Kerr Effect). Nowadays, owing to the simplicity of realization and the efficiency of the technique, the SMOKE set-ups are very diffused and even used in advanced applications such as Time-Resolved MOKE, that will be discussed in the next sections.

In the study of the MOKE technique, the experimental geometry is extremely important. The direction of application of the magnetic field **H** (and thus the component of the magnetization which is externally driven by the experimenter) with respect to the light incidence plane and the surface of the sample defines three different measurement geometries, shown in Fig. 6.1.

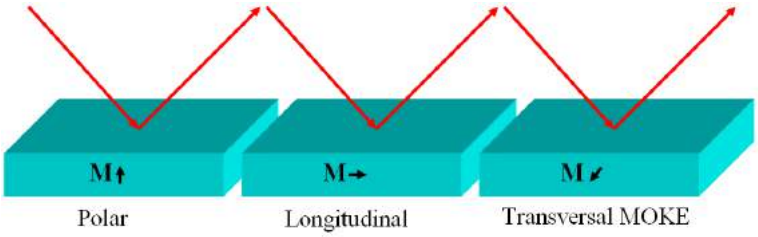

Figure 6.1. *The polar, longitudinal and transverse MOKE measurement configurations.*

- *Longitudinal* geometry when **H** is lying in the the sample's surface plane and in the light incidence plane.
- *Transverse* geometry when **H** is in the sample's surface plane, but orthogonal to the light incidence plane.
- *Polar* geometry when **H** is in the light incidence plane, but orthogonal to sample surface.

As in the experiments discussed in the next chapters only longitudinal configuration has been used, the discussion will be restricted to this geometry. From the theoretical point of view, it is possible to give a relatively simple description of the process in terms of the Fresnel coefficients [80].

Classically, when an electromagnetic field interacts with a solid, the response of the material is determined by a 3x3 tensor, the *dielectric tensor*, ϵ_{ij}, that can be rewritten as the sum of a symmetrical term and an anti-symmetrical term. The magnetic response is enclosed in the anti-symmetrical term, as the external field generates a breaking of the time-reversal symmetry. If one considers:

$$\tilde{\epsilon} = \epsilon \begin{pmatrix} 1 & iQ_z & -iQ_y \\ -iQ_z & 1 & iQ_x \\ iQ_y & -iQ_x & 1 \end{pmatrix}$$

in which the symmetrical part is simply given as a multiplication factor[1] (ϵ), while the anti-symmetrical part is represented in the matrix form. The normal modes in the medium are therefore circularly polarized waves with *different* refraction index:

- $n_L = \sqrt{\epsilon}(1 - \frac{1}{2}\mathbf{Q} \cdot \hat{k})$ for the left circularly polarized light
- $n_R = \sqrt{\epsilon}(1 + \frac{1}{2}\mathbf{Q} \cdot \hat{k})$ for the right circularly polarized light

$\mathbf{Q} \equiv (Q_x, Q_y, Q_z)$ is called Voight vector, and and enables to map on a vector the tensorial anti-symmetrical structure of the dielectric tensor, while $\hat{k}$ indicates the direction of propagation of the light in the medium. If a linearly polarized beam is refracted through the

[1]This corresponds to assuming an isotropic response of the material to external electric fields.

medium, it excites both the circularly polarized modes (a linear polarization can be considered as a combination of two circularly polarized waves), but each mode has a different phase velocity, and therefore the polarization plane of the outgoing beam will be rotated. This process is called *Faraday rotation*. In fact also the absorption of the two modes is slightly different, and, as one of the two components is less attenuated than the other, the outgoing polarization is not any more perfectly linear, but it acquires a small ellipticity (*Faraday ellipticity*). The dissimilarity between the two modes has repercussions also on the the boundary conditions at the interface, and it is thus possible to observe these two processes in reflection, called *Kerr rotation* and *Kerr ellipticity* respectively. The two acquired phases are thus represented with two angles, one real (ϕ') associated to the phase velocity, and one imaginary (ϕ''), associated with the absorption. These two numbers are usually collected in a unique complex number, called *Kerr angle*:

$$\tilde{\phi} = \phi' + i\phi'' \tag{6.1}$$

(ϕ') e *Kerr ellipticity* (ϕ'').

A this point another important distinction must be made, i.e. the difference between s and p polarization. If the linearly polarized light has an electric vector perpendicular to the incidence plane, it is called *s-polarized*, while if it is parallel, the term *p-polarized* is used. Therefore, the polarization state of a beam incident on the surface can be written as:

$$P_i = \begin{pmatrix} E_s^i \\ E_p^i \end{pmatrix} \tag{6.2}$$

and, under the Fresnel optics assumptions it is possible to write that the reflected beam is given by:

$$P_r = \begin{pmatrix} E_s^r \\ E_p^r \end{pmatrix} = \begin{pmatrix} r_{ss}E_s^i + r_{sp}E_p^i \\ r_{ps}E_s^i + r_{pp}E_p^i \end{pmatrix} \tag{6.3}$$

where the r coefficients are called Fresnel coefficients and describe how each component of the incident polarization contributes to the reflected polarization. These coefficients hold the information about the magnetization of the sample, as their linear combinations depend on the components of the magnetization vector. The Kerr angles for s or p incident polarization are calculated as:

$$\tilde{\phi}_s = \phi'_s + i\phi''_s = \frac{r_{ps}}{r_{ss}} \qquad \tilde{\phi}_p = \phi'_p + i\phi''_p = \frac{r_{sp}}{r_{pp}} \tag{6.4}$$

Thus selecting the polarization of the incident beam, the one of the reflected beam and measuring the intensity of the latter, it is thus possible to evaluate the three components of magnetization. The MOKE is an effect at the first order in the magnetization.

6.1.1 Time-Resolved MOKE

As discussed above, the resulting complex Kerr angle can be written as a linear combination of terms proportional to the magnetization components:

$$\tilde{\phi} = G_0 + \sum_i K_i m_i = \tilde{\phi}_s + \tilde{\phi}_a \tag{6.5}$$

where G_0 is a term independent on magnetization, m_i are the magnetization components, and K_i are the coefficients that can be extracted from the linear combination of the r coefficients and are called *effective Fresnel coefficients*. The index i runs on the spatial coordinates (x, y, z). The last term of Eq. 6.5 shows that the Kerr angle can be divided in two parts, one symmetric with respect to magnetization reversal ($\tilde{\phi}_s$) and one anti-symmetric ($\tilde{\phi}_a$). In measurements where magnetization is reversed allows to evaluate $\tilde{\phi}_a$, as the difference yields $\tilde{\phi}(\mathbf{M}) - \tilde{\phi}(-\mathbf{M}) = 2\tilde{\phi}_a$. If the time evolution of the magnetization is now considered, as it will be assessed in the pump-probe configuration, its relationship with the Kerr angle must be considered. The discussion follows closely the one in [81].

As observed in **??** the total rotation can be written as a functional expression:

$$\tilde{\phi}(t) = \Phi[\mathbf{M}(\mathbf{t}, t)] \tag{6.6}$$

which can be guessed to yield:

$$\Phi[\mathbf{M}(\mathbf{t}, t] = G_0(t) + \sum_i K_i(t) m_i(t) \tag{6.7}$$

If a weak perturbation regime can be assumed (i.e. the magnetization is varied slightly with respect to its equilibrium value, and so do the effective Fresnel coefficients), it is then possible to linearise, and if the magnetization direction does not change and one magnetization component is dominant in determining $\tilde{\phi}(t)$, then:

$$\tilde{\phi}(t) = \Delta G(t) + F(0)\Delta m(t) + \Delta F(t) m(0) \tag{6.8}$$

Where F is a linear combination of K_i. This shows that TR-MOKE signal arises from two processes: the variation of the magnetization ($\Delta M(t)$) and the variation of the Fresnel coefficients ($\Delta G(t)$ and $\Delta F(t)$). If the Fresnel coefficients do not vary significantly in time, it is then possible to write:

$$\tilde{\phi}(t) = F(0)\Delta m(t) \tag{6.9}$$

And to obtain by normalization the direct relation:

$$\frac{\tilde{\phi}(t)}{\tilde{\phi}(0)} = \frac{\Delta m(t)}{\Delta m(0)} \tag{6.10}$$

6.1.2 Set-up

The time-resolved MOKE measurements are performed with the pump probe method. In this section the TR-MOKE set-up in the laboratories of the University of Regensburg will be discussed, as shown in Fig. 6.2. An ultrafast laser system generates a beam with a high repetition rate (up to 250 kHz) and short pulse duration (60 fs) and an elevated intensity, at a wavelength of 800nm (1.5 eV). The pulse is then split in two parts, the pump and the probe. The pump is sent on the delay line, though an optical chopper, and then impinges normally on the sample. The probe is frequency doubled by a BBO crystal, sent trough a polariser, and reaches the surface. Here, it is reflected, passes through a second polariser and finally reaches a photodiode, where it is absorbed and detected. The photodiode and

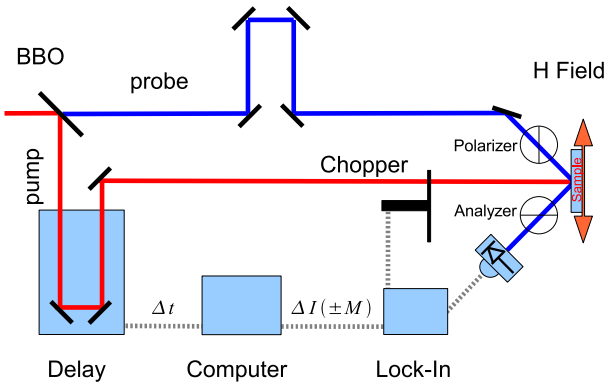

Figure 6.2. *Scheme of the set-up used for time-resolved MOKE measurements.*

the chopper are connected to a lock-in amplifier, that allows to amplify the signal greatly removing a significant part of the noise. The intensity variations are then registered by the computer that controls the delay line, allowing to measure the curves of $\Delta m(t)$ as a function of Δt.

The system uses the crossed polariser configuration to detect the Kerr rotation angle, meaning that the beam is completely polarized vertically before reaching the sample, and then passes through an almost horizontally oriented polariser. In this way, the signal is almost extinct, but small variations in the polarisation have a large signal-noise ratio. In particular if the first polariser is set at an angle $\alpha_1 = 90°$ and the second at $\alpha_2 \approx 0°$, the outgoing intensity can be evaluated as:

$$I(t) = R(\alpha_2^2 + 2\alpha_2\phi'(t)) \tag{6.11}$$

where $R = |r_{ss}(t)|^2$ is the square modulus of the Fresnel coefficient related to the reflection of the s-wave in the s-wave as indicated above, and is also time dependent. The induced intensity variation can be written as:

$$\Delta I(t) = \alpha_2^2 \Delta R(t) + 2R(0)\alpha_2 \Delta\phi'(t) \tag{6.12}$$

this enables to evaluate both the reflectivity change and the real Kerr rotation angle, as if the intensities with opposite magnetization are evaluated one has:

$$I(t, m) - I(t, -m) = 4R(0)\alpha_2 \Delta\phi'(t) \tag{6.13}$$

while, when summing:

$$I(t, m) + I(t, -m) = 2\alpha_2^2 \Delta R(t) \tag{6.14}$$

6.2 Photoelectron spectroscopy measurements

6.2.1 XAS and XMCD

The spectroscopies in which the momentum and spin of the photons (the initial states) are varied and emitted electrons are simply counted, are a branch of the absorption spectroscopies (X-ray Absorption Spectroscopy, or XAS). These techniques evaluate the coefficient of absorption of X-rays as a function of their energy, angle of incidence and polarization. Each element, indeed, possesses particular thresholds (*absorption edges*) of energies at which it absorbs strongly the X-ray radiation, because it excites electronic transitions from the core-levels. The shape of the absorption edge is very peculiar for each element and shows dependence from its chemical (oxidation state) and physical (magnetization, electrical polarization, temperature, strain state) environment of the probed atom, due to the fact that the initial states are core levels, while the final states are the empty states above the Fermi energy. If the study is restricted to the photon energies very close to the absorption edge (50-100 eV) the technique (Near Edge X-ray Absorption Fine Structure, or NEXAFS) is sensitive to atom's physical state and chemical bonding. If the range is extended to many hundreds or thousands of eV beyond the edge the technique (Extended X-ray Absorption Fine Structure, or EXAFS) is sensitive to the collective excitations of the system and to the short range order in the solid.

One of the channels by which the solid relaxes the energy absorbed is the emission of electrons[2]. These electrons can be counted by grounding the sample through a picoamperometer, or by an electron counter without energy filtering, in the so-called Total Electron Yield. The main difficulty in this measurements is the source: a high brilliance, high energy resolution and high collimation photon beam is required. The only system that can perform such demanding task is a synchrotron, and in particular, thanks to the development of third generation light sources making use of undulator radiation, it is now possible to perform routinely these measurements with a very high efficiency.

In a typical XAS measurement, the incident photon energy is scanned in small steps, stating from a value smaller than the binding energy of the core-level in study and increasing it. When the photon energy approaches the binding energy, a resonant absorption condition is achieved, and the material shows a sharp increase of the absorption signal. In Fig. 6.3 are shown the peaks due to the excitation of 2p peaks of transition metals.

The double peaks (L_3 and L_2) are due to the spin-orbit splitting of the 2p level in $2p_{3/2}$ and $2p_{1/2}$ respectively, which are promoted to the conduction 3d band (l+1 transitions), while the step-like background shown in inset is due to 2p to 4s transitions, whose intensity is much lower due to the different density of states of the 4s band. These edges are of high interest because they have large cross-sections and large spin orbit splitting, allowing to separate efficiently the multiplet. Normally, the different multiplicity of the $2p_{3/2}$ and $2p_{1/2}$ levels leads to a 2:1 ratio in the intensities. However, the physical and chemical state of the sample can strongly modify the lineshape. In particular, the magnetic state of the sample, combined with circular polarization of the incoming photon beam give rise to

[2]At the side of this de-excitation channel, another very important exists, which is the emission of photons. It also can be detected and is called Fluorescence Yeld (FY).

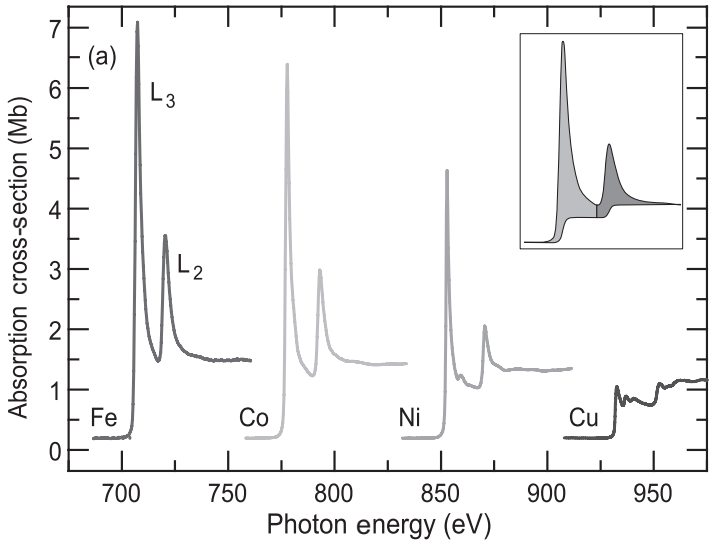

Figure 6.3. *Typical absorption spectra of transition metals. From [12].*

X-ray Circular Magnetic Dichroism (XMCD) i.e. the observation of variations in the XAS intensity (also called white-line) in magnetic materials when the magnetization is varied in the direction of the photon momentum, or alternatively, if the photon polarization is reversed and the magnetization is fixed.

XMCD can be schematically described in a simple one-electron two step model, shown in Fig. 6.4, in which the simplifying (but often adequate) assumption that the spin-orbit effect can be considered only for the core-levels.

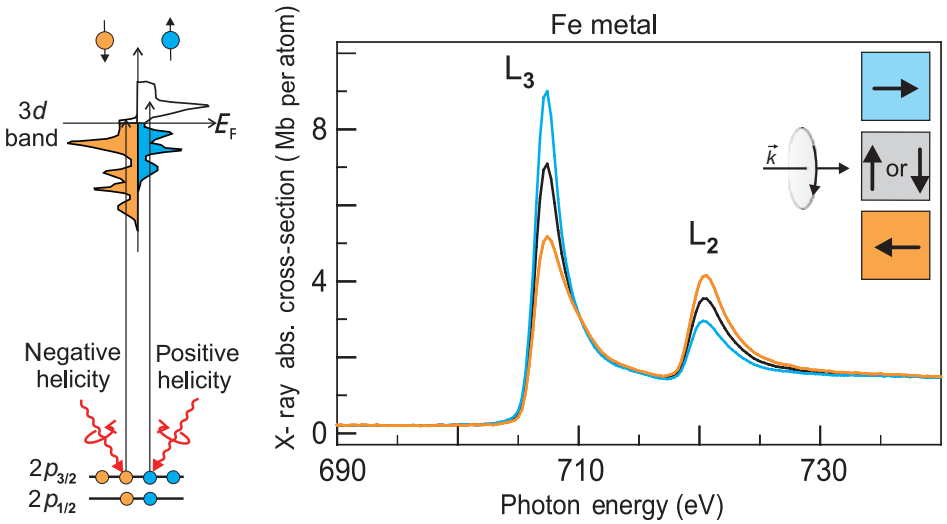

Figure 6.4. *The XMCD effect for the L-edge absorption in Fe metal. From [12].*

In the first step, the photon is adsorbed and a core hole is created. If one uses the

dipole approximation for radiation-matter interaction, the selection rules on the quantum numbers require a transfer of angular momentum from the photon to the electron. The spin-orbit interaction, however, allows for part of the angular momentum of the photon to be transferred to the spin degree of freedom. For this reason, the excited electrons are spin-polarized. If the light is right circularly polarized, 62.5 % of up-spin electrons are excited from the L_3 edge (+ 25 % spin polarization), and 25 % from L_2 (- 50 % spin polarization); vice versa, if left circularly polarized light is used 37.5 % spin-up electrons are excited from L_3 (- 25 % spin polarization), while 75 % from L_2 (- 50 % spin polarization). It can be noted that the spin polarization a the two edges are opposite in sign, as expected from the opposite spin-orbit coupling.

In the second step, electrons are injected into the final states, the exchange-split 3d bands, which have a different DOS for up- and down-spin states. This gives to the signal the dependence on the magnetization direction. For example, if magnetization is *down*, the down-spin 3d band will have a lower energy, and its DOS above the Fermi energy will be reduced. If the polarization of photons is positive, the L_3 edge will be enhanced and the L_2 reduced. If the magnetization is reversed, the intensities also are reversed. Vice versa for the negative polarization case (in Fig. 6.4).

Considering the description given above, it can be understood how an XMCD spectrum is measured. The XAS spectra for the two opposite magnetization directions are acquired and subtracted. The resulting spectrum is then normalized to the intensity of the XAS signal by dividing with the maximum intensity of L_3 peak, and is then scaled to account for the angle of incidence ($1/cos(\vartheta)$) and the percentage of circular polarization of the incoming beam.

The XMCD technique in TEY constitutes then a method for probing the magnetism at the surface by probing the spin polarization of the empty states above the Fermi energy. As a further, extremely relevant feature, it can be performed on buried surfaces and it possesses element specificity. A set of sum rules allows also to calculate the orbital and spin moment of the atoms [12].

6.2.2 XPS

The physical principles at the basis of the XPS technique have been discussed widely throughout this thesis. For this reason, the discussion here will be limited to the experimental routine and to differences introduced by the use of synchrotron radiation. The normal procedure in XPS spectroscopy is to measure a survey scan and to individuate the peaks of interest, in order to dedicate long, high definition and statistics measurements to single interesting peaks.

The use of synchrotron radiation allows to change continuously the energy of the primary photon beam. This has two very important effects that give to the experimenter new tools for solid state analysis:

- It allows to increment the photoionization cross section of an element. If one moves the energy of the primary photon energy closer to the binding energy of the level under study, one can have a signal up to tens or hundreds of times higher than when the system is excited with X-ray tube radiation.

- Secondly, it is possible to tune the probing depth of the technique. The electrons observed in XPS, in fact, have a inelastic mean free-path that depends strongly from their energy, according to the curve in Fig. 6.6. If one then chooses the primary energy so that the peaks of interest are measured at the desired kinetic energy, it is possible to achieve extreme surface sensitivity, restricting the signal to come from depths of few Å.

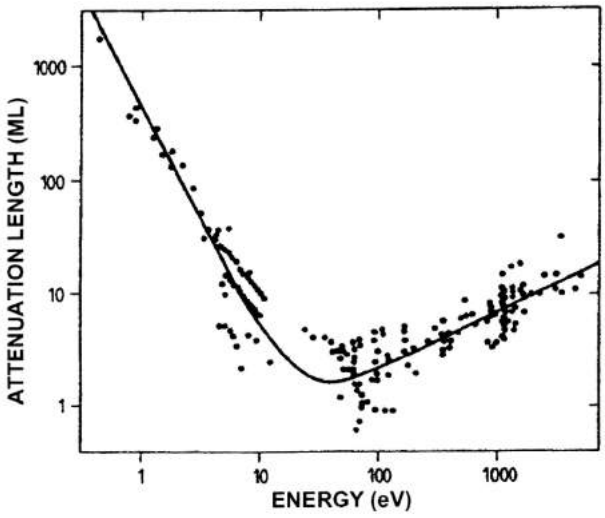

Figure 6.5. *The universal curve of the escape depth of electrons as a function of energy.*

The XPS technique with synchrotron radiation is thus a more adaptable technique, that allows to control several fundamental parameters of an experiment enabling to perform characterization of materials with deeper understanding of the involved mechanisms.

6.2.3 APE beamline

The spectroscopic measurements were performed at Advanced Photoelectric Effect beamline [82], at Sincrotrone Elettra, Trieste. The beamline receives two independent radiation beams produced by two independent APPLE-II undulators, set in a zig-zag geometry forming an angle of 2 mrad. The two beams, in the range of energies from 10-100 eV and 100-2000 eV are deflected by silicon mirrors and sent towards two independent branchlines, respectively APE Low Energy (LE) and APE High Energy (HE). The radiation is monochromatized and refocused by silicon mirror stages.

The XPS, XAS and XMCD measurements were performed in the High energy chamber, which features a highly sophisticated manipulator, with the possibility of applying electrical and magnetic fields, to cool down samples to cryogenic temperatures, and to measure efficiently the small currents characteristic of XAS and XMCD in TEY. An electron spectrometer is mounted on the same horizontal plane of the incomong beam, but at an angle of 45° from it.

Samples were prepared in the sample preparation chamber, an indipendent UHV system that features a great variety of instruments: between them, several UHV e-beam evapo-

rators, a sputter gun, a Vectorial MOKE system, a LEED system and several annealing stages.

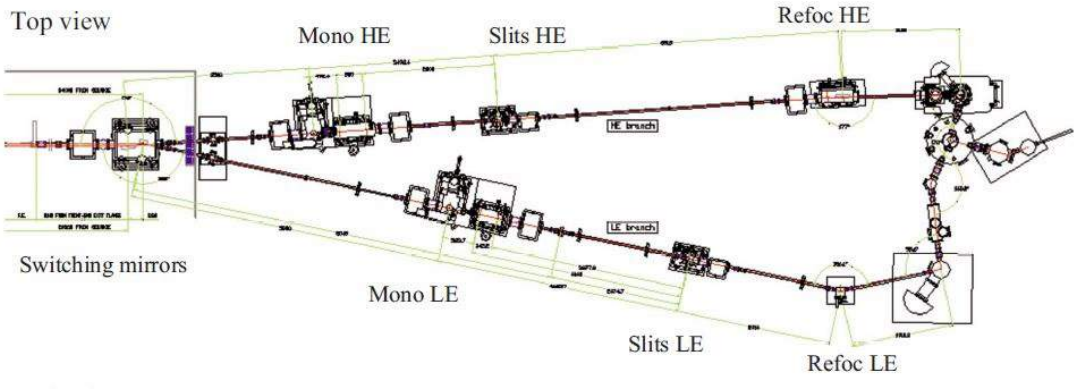

Figure 6.6. *A top view of the beamline layout. From [82].*

Chapter 7

VLEED target sample: Fe(001)-p(1x1)O

In the following chapter, the growth and characterization of a highly spin polarized surface will be described. The system chosen for this experiment is a film of Fe (001), 100 nm thick, grown on a MgO substrate. On its surface, it is chemisorbed a single layer of oxygen atoms that are arranged in an ordered fashion: the bidimensional lattice of oxygen atoms follows the square pattern of the underlying Fe (001) surface with one atom per cell in the so-called $p(1 \times 1)$ *phase* (see Fig. 7.1 c.).

The structure of the system is the object of several investigations, ranging from LEED experiments to first principle calculations, with results that were not always in agreement between each other. Recent measurements, performed with surface x-ray diffraction [83] and spin-resolved scanning tunnelling spectroscopy [69], have produced influential high-precision results, that allow for an accurate description of the structure. As shown in Fig. 7.1 a. the oxygen atoms are placed in the fourfold symmetrical hollow sites of the lattice, protruding from the surface for a small distance, $d_{(O-Fe)} = 0.48$ Å. The underlying Fe layers are relaxed outwards: the interlayer distance between the outermost layer of oxygen (1) and the next one (2) is $d_{(12)} = 1.66$ Å, a 16% increase with respect to the bulk value, 1.43 Å. The deeper layers have no difference in spacing within the error bars (0.03 Å). In Fig. 7.1 b. the structure of an oxygen rich phase, with degraded structural order, is shown for contrast showing a much deeper penetration of oxygen in the Fe crystal. The charge density map derived from scanning tunnelling microscopy data and shown in Fig. 7.1 c. shows the top view of the surface, with the ordered square pattern of oxygen and Fe atoms. As it can be noticed, a slightly larger protrusion of the oxygen atoms is measured, that is anyway very close to the value obtained from X-ray diffraction data.

The interest in such system arises from the relevant qualities of the Fe surface. The clean iron surface possesses a rather large exchange splitting of both the occupied states close to the Fermi energy and the empty states above it, generated not only by the magnetic properties of bulk Fe, but also from the reduced atomic coordination[1]. In particular, as

[1]Due to the strong symmetry reduction generated by the breaking of the translational symmetry, the bands are split in surface states that can have a strong spin character. Between these, for example a

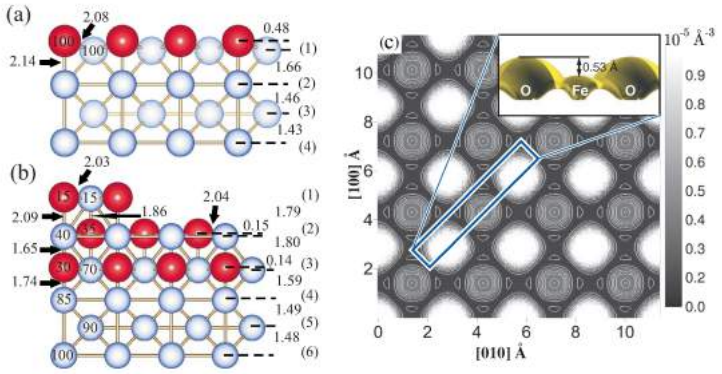

Figure 7.1. *a. Structural scheme of a cross section of the Fe(001)-p(1 × 1)O surface. The red and light blue spheres represent the oxygen and Fe atoms respectively. The distances are in Å and the numbers in parenthesis indicate the layers, while the numbers inside the spheres represent the occupancy factors in percent of 1 ML. b. The same diagram for samples where the ordered oxygen pattern was not created. From [83]. c. Bidimensional map of the charge density at the Fermi level calculated in vacuum about 4 Å above the surface. The bright areas show the positions of oxygen atoms, while the dark ones the Fe sites. Inset: equal density contour of the charge density of* $7 \times 10^{-5} e\text{Å}^{-3}$ *calculated on the (110) plane. From [69].*

discussed in Sect. 3.2.2, an exchange-dependent band gap is present between 4 eV and 10 eV above the Fermi energy as shown in Fig. 2.9, that is the core feature allowing the operation of VLEED detectors. Iron surfaces, however, are of high interest also for another vast class of applications i.e. the realization of spintronic devices. As electronics is starting to encode information in the spin polarization of the electron currents, indeed, the need for surfaces which show radically different behaviour with respect to the spin states of low-energy electrons increases. Most of the contacts used to generate, absorb or inject spin-polarized currents in spintronics devices are based on Fe surfaces, often interfaced with insulating oxide materials.

However, the clean Fe surface deteriorates very quickly, as iron is very reactive. The uncontrolled accumulation of oxygen and other contaminants destroys the spin properties of the surface. This is a problem for both the outlined applications, as a detector's target has to operate for long times without degrading its performance (and even in the highest vacuum systems a small flow of residual atmospheric gases, including oxygen, is present), while in spintronic applications the oxidation of the Fe surface can significantly modify the contact behaviour[2]. For these reasons, the attention was focused on researching developing and testing of adsorption of gases that could make the surface less chemically reactive (passivation), and at the same time preserve the surface spin properties of the system. In the late 1990's the realization of the Fe(001)-p(1x1)O surface [49] finally set a very important result: a passivation procedure was found that was reproducible and renewable[3], that yielded the aforementioned ordinate crystalline structure and that modified the spin

particularly evident $d_{3z^2-r^2}$ structure is highly spin-minority polarized, as observed in several inverse photoemission experiments, and is considered as a criterion for the realization of a clean Fe (001) surface.

[2]In particular, the behaviour of Fe/oxide magnetic tunnel junctions is dramatically influenced by the presence of an oxidized surface, also resulting in an opposite sign of the spin polarization [69].

[3]If a Fe(001)-p(1x1)O surface appears to have degraded properties, it is possible to refresh them by a

character of the system by enhancing the surface spin polarization[4]. After it, a range of application was explored, ranging from the realization of VLEED detectors with high efficiency and stability [70], to the development of new interfaces for magnetic tunnel junctions [85].

The staff of APE beamline is now upgrading the Low-energy endstation, that features an advanced ARPES experimental station, with a new wide acceptance and parallel acquisition electron detector, the Scienta D80, that is provided by the manufacturer with the option for the implementation of a spin detector. The conceptual design is similar to the one described in 3.2.2, with a reduction of the size of the parallel acquisition system (from a 80 mm diameter MCP to a 40 mm diameter), for the simultaneous channelling of part of the electrons to spin-resolved vectorial detectors. However, Scienta presents the possibility of implementing vectorial spin resolution only with two orthogonal Rice-type Mott detectors, while, as discussed above, the highest efficiency for continuous and constant intensity measurements is realized with VLEED systems. A different design was thus chosen, implementing a VLEED detector which now starts to operate efficiently in spin integrated mode. One of the activities during my thesis was to develop a suitable procedure for the realization of the Fe(001)-p(1x1)O target. The stability of polarization at the surface makes it also a very attractive sample for the commissioning of the Mott detector: if the surface is able to generate a beam of photoemitted electrons with constant and large polarization for long times, it can be used to perform an accurate self-calibration of the detector, a particularly long procedure on whose result the systematic error of Mott detector measurements is strongly dependent[5].

7.1 Growth

The growth procedure[6], mainly described in [49] is based on the use of a polished MgO substrate. On this, Fe can be evaporated by MBE with an epitaxial relation

$$\text{Fe}[100](001)||\text{MgO}[110](001)$$

This means that the Fe body-centred-cubic unit cell grows with a rotation of 45° with respect to the rock-salt unit cell of MgO, leading to a very low lattice mismatch between 2% and 4 %. The Fe film must be rather thick, i.e. $t \geq 100nm$, for several reasons:

short annealing in oxygen or in vacuum.

[4]Both the density of the empty and filled states are modified. Oxygen forms p bondig states below the Fe d bands, located around 5.5 eV below the Fermi energy. The strong hybridization between O p and Fe d states induces a moment on the oxygen that has been calculated in $0.23\mu_B$. The antibonding states of oxygen, instead, are about 3 eV above the Fermi level. The bonding of these levels with the Fe bands shifts the Fe d states in both spin channels away from the Fermi energy, boosting the Fe magnetic moment to a calculated value of $3.23\mu_B$ and inducing al large spin polarization at the Fermi energy [69]. In the absorption process, however, the minority d_{z^2} surface state is quenched. Moreover, a further feature emerges at higher energies (3.8 eV), very close to the edge of the gap presented in Fig. 2.9, that has been identified as the image-potential surface state of the Fe(001)-p(1x1)O surface, indicating that the surface reflectivity is enhanced [84].

[5]See App. A.

[6]The growth procedure was performed in APE beamline sample preparation chamber (called Kerr chamber). Here a LEED system was used, allowing to analyse the crystallinity, epitaxy and possible surface reconstruction during each step of the growth.

1. The MgO surface is exposed to the air, and, despite the fact that repeated cycles of cleaning procedures are applied, it shows the presence of contaminants, in particular carbon. The C atoms trapped at the interface between MgO and Fe can then diffuse to the surface when the annealing procedures needed to optimize the crystal structure are performed. If the film is thick enough, the lattice structure is recovered before the contaminants can reach the surface.

2. Thin films of Fe on MgO are known to produce a very discontinuous coverage when heated to temperatures higher than 600 K [86]. A high temperature rapid heating is needed to desorb the excess oxygen during the last phases of preparation, and the film must maintain its integrity.

An annealing must then be performed to recover a highly ordered crystal structure. Subsequently, the surface must then be exposed to a pure oxygen flux. On this point the recipes published in literature differ widely, ranging from 0.6 L[7] to 30 L. As pointed out in [83], this is probably due to the fact that the adsorption of atoms on the surface proceeds in three phases: at very low fluxes (up to 3 L) the gas undergoes dissociative chemisorption, at intermediate fluxes (3 to 20 L) the oxygen adatoms are incorporated in the topmost layers of the surface, and at higher fluxes the oxide formation sets in. The transition between these phases is not sharp, and this explains the variety of values. However, a rapid annealing to 900 K removes the excess oxygen and leads to the ordered and oxygen saturated Fe(001)-p(1x1)O surface, and thus the most used procedure consists in overdosing up to 30 L and subsequently flash annealing to order the surface.

The growth of a film of such an elevated thickness is a rather difficult task with common evaporator for MBE: at the typical maximum rate of 1-2 Å/min, a 17-8 hours evaporation must be performed, in which the evaporator is constantly kept at full power. The first trial phases were then performed on lower thickness samples, on which the MgO surface cleaning procedure and the Fe epitaxial growth were tested. The procedure to obtain a clean and ordered surface of MgO was established as the following:

- *Substrate shaping in air.* The substrates were obtained from 1x1x1 cm cubes of high purity crystalline MgO provided by the manufacturer with one epi-polished[8] face. The cubes were cleaved in air to obtain crystal with a 5x5 mm polished face and the lowest thickness possible (less than one mm). The substrates were then placed on a sample holder and mechanically ensured on it by spot-welded Tantalum stripes.

- *Sputter etching.* A single sputtering cycle was performed for 20 min with 1 keV Argon atoms (the pressure in the chamber after the injection of Ar was $1 \times 10^{-6} mbar$).

- *Low temperature annealing.* A 2h low temperature annealing was performed at about 600 K to desorb the impurities deriving from air exposure of the crystal. In particular, water must be desorbed because MgO is hygroscopic.

[7] The Langmuir, unit of measurement of flux, is defined as $1\ L = 10^{-6}\ Torr\ s$.

[8] Epi-polished is a term used to indicate the fact that the mechanical polishing has been performed with such a high precision that the surface is suited for epitaxial growth.

- *High temperature annealing.* A second annealing cycle of 2h was performed at a higher temperature, at 1050 K measured with pyrometer.

This procedure allowed to obtain the very sharp LEED pattern shown in Fig. 7.2 a. the

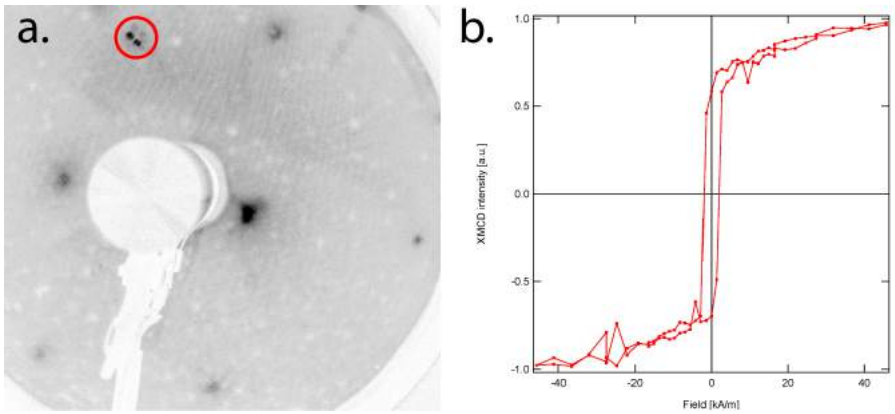

Figure 7.2. *a. LEED pattern of clean MgO after surface preparation procedure. The primary energy is 69 eV, the spot in the red circle is a flare due to the glass of the viewport (the picture was registered with an external camera). b. Hysteresis curve measured as a variation of the XMCD signal on the Fe(5nm)/MgO test samples.*

image shows the presence of a square lattice, in agreement with the rock-salt structure expected from MgO. While the central spot, close to the electron gun in the centre is clearly the (00) beam, it is possible that the spots visible in Fig. 7.2 a. are not the first order beams. This is due to the fact that at energies lower than 69 eV LEED measurements were not possible due to the charging of the insulating surface.

After the preparation of MgO surface, few low thickness test samples were grown, and after long 600 K annealing showed a sharp and homogeneous LEED. The fact that the expected epitaxial relation was attained was shown by the fact that the hysteresis curves measured with XMCD (Fig. 7.2 b.) showed a clear hard magnetization axis behaviour when the magnetic field was applied along the [010] direction of the sample. As it is known, indeed, the magnetic hard axes of a Fe crystal form 45° angles with the unit cell vectors: the appearance of a hard axis in the [010] direction of the substrate is in agreement with a rotation of the Fe lattice of 45° with respect to the one of MgO, confirming the good epitaxy of the growth. As mentioned above, it was not possible to passivate these surfaces, because even the short annealing needed to desorb excess oxygen fragments the film in separated islands.

A new film was then realized. The substrate was mounted this time rotated of 45°, so that the [110] direction of MgO was directed along the vertical, this enabled to have the easy magnetization axes of the Fe film on the horizontal and vertical direction. After the MgO cleaning procedure, a film of the full 100 nm thickness was grown with an 8 h evaporation at an effective 2 Å/min rate, as obtained by microbalance calibration. Subsequently, a 15 min annealing at 1000 K allowed to obtain the sharp LEED shown in Fig. 7.3 a. The observation of an easy axis hysteresis confirms that the pattern in Fig. 7.2 is identical to the one in 7.3, and not rotated of 45°, due to the fact that the former is

probably constituted by second order beams, while the latter is surely given by first order ones.

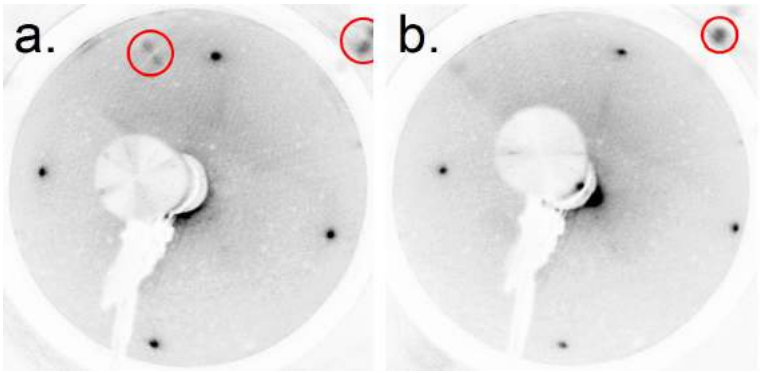

Figure 7.3. *a. LEED pattern of Fe surface after annealing. The primary energy is 58 eV. b. LEED pattern of Fe surface after passivation. The primary energy is 54 eV. the spots in the red circles are flares due to the glass of the viewport.*

Finally, the sample was passivated: it was heated to 450 K and was exposed to 5×10^{-8} mbar of spectroscopy-grade O_2 for 10 min. After the exposure, the sample was finally heated to 1000 K for 5 min to desorb the excess oxygen and to build the ordered pattern. The LEED pattern thus obtained is shown in Fig. 7.3. As it can be observed the pattern reproduces exactly the one of the clean Fe surface (the square pattern is slightly larger because the primary energy in is slightly lower), hinting at the fact the p(1x1)O ordered adsorbed layer was obtained.

7.2 Characterization

During the phases of the growth, measurements aimed at understanding the development of the structure were performed. In particular, XPS, XAS, XMCD and hysteresis loops were recorded at the most important phases of the growth. As the measurement chamber of APE-HE is isolated from the preparation chamber, the characterization routines were not done simultaneously to the growth. Furthermore, as it required a transfer of the sample[9], spectroscopic analysis was concentrated in the three relevant phases of the growth:

1. after the Fe deposition,
2. after the Fe film annealing,
3. after passivation (oxygen exposure and short annealing).

[9] A transfer of the sample, in particular with very reactive materials such as clean Fe, increases the possibility of contaminating the surface in an uncontrolled way.

unfortunately, the MgO surface could not be measured due to charging[10], and its quality was checked only with the LEED patterns shown above. The characterization followed identical steps: the photon energy of the undulator X-ray source was set to 850 eV (close to the maximum energy achievable by HE) and XPS scans were performed in order to observe the Fe 2p doublet and O 1s peak. Then the photon energy was changed to 480 eV to enhance the photoionization cross section of C 1s state (which increases the signal of a factor of 10 with respect to the one obtained from Mg K_α photon source) and to observe with higher definition the low energy range of the spectrum. Finally, XMCD and hysteresis loops were measured at the $L_{2,3}$ absorption edges of Fe. The duration of the synchotron beamtime shift dedicated to this phase was rather limited, and the statistics could not be very high. In Fig. 7.4 the survey scans at the two different photon energies mentioned above, in the initial and final phases of Fe surface processing are shown.

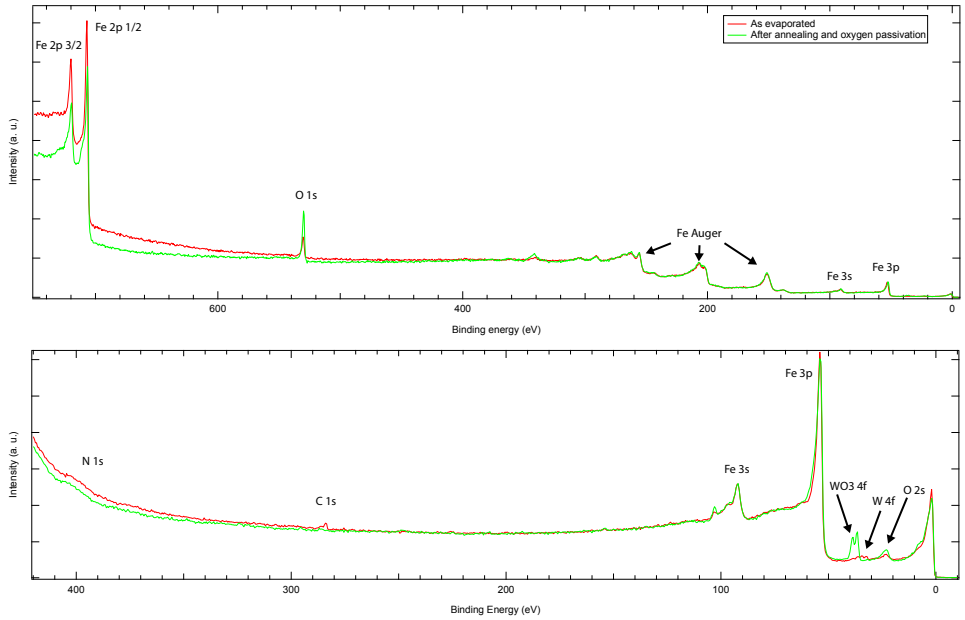

Figure 7.4. *a. Survey scan with 850 eV primary photon energy. b. Scan with 480 eV primary photon energy, aimed at enhancing the photoionization cross section of C 1s.*

The single peak graphs are shown if Fig. 7.5, as obtained after Shirley or linear background removal. The Carbon peak, studied at 480 eV shows that the as-grown film presents a small amount of carbon (as it can be seen in Fig. 7.4, the peak is barely detectable). The main structure is centred at 284 eV, that hints at the presence of free C adsorbed on the surface. During the annealing phase, C is oxidized forming Carbon di- and monoxide, that are thermally desorbed, leaving only small traces of CO and CO_2 on the passivated structure. The oxidation of C during the first annealing of the surface indicates that the small rise in pressure unavoidable when heating up to 1000 K may have already exposed

[10]While the Al window of X-ray tubes generates a small flux of electrons that reaches the sample and acts as a flood gun, compensating the positive charging due to photoemission, in a synchrotron X-rays come as an absolutely clean beam. For this reason the first MgO spectra showed up to 40 eV electrostatic shifts and deformed structures, and this characterization step was skipped.

the surface to a dose of oxygen.

However, the examination of the oxygen peak (measured at 850 eV) shows that the possible exposure to oxygen due to annealing was not sufficient to significantly increase the overall amount of oxygen (the peak is even slightly smaller), probably due to the fact that, as stated above, at low exposures (below 3 L) the oxygen is not incorporated in the surface layers[11]. The peak measured after passivation, instead, shows a clear increase, due the formation of the oxide layer.

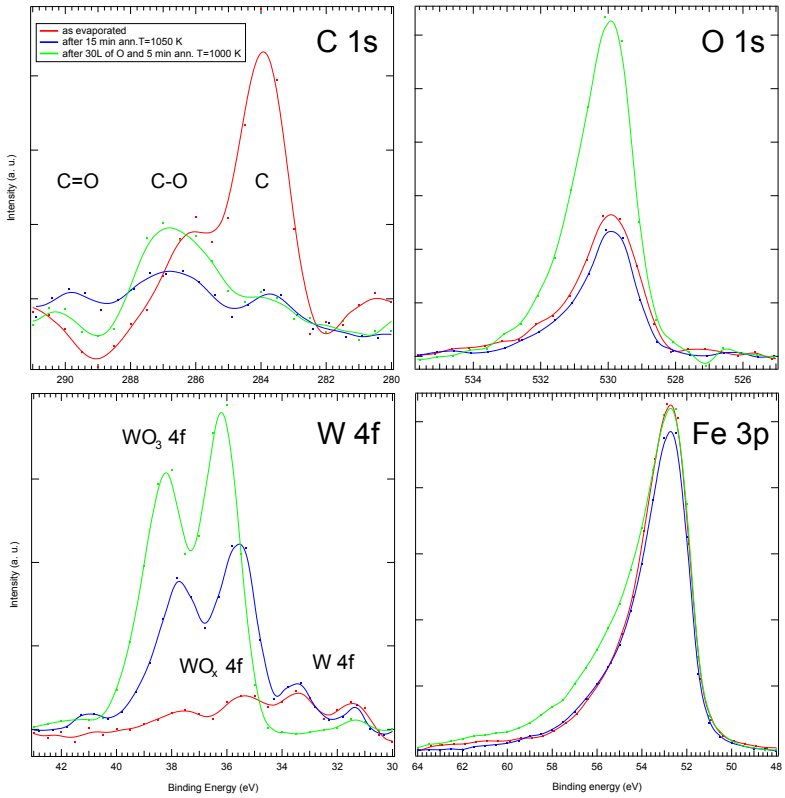

Figure 7.5. *Set of single peak scans. All the spectra shown here have been measured with primary photon energy of 480 eV, except for the O 1s which needed a higher energy of 850 eV.*

Following the disposition in clockwise direction, the Fe 3p peak can be observed: it shows that the chemical modifications discussed above are anyway confined to the extreme surface of the sample, as the shape of the Fe peak is not substantially changed by the procedure: a slight reduction of the intensity observable after the annealing is readily recovered after the passivation procedure. Moreover, in the last step the tail of the peak is slightly broadened due to the formation of the oxide layer, that generates a contribution from chemically shifted 3p peaks, a process that will be observed again and more clearly in Fe 2p peaks. The Fe 3p spectra of the clean iron surface (as deposited and after annealing) already display a tail towards the lower binding energy: this is not due to

[11]It is likely that the exposure was lower than 1 L, as the pressure never overcame the 10^{-10} mbar range, and even if the whole raise in pressure was given by solely oxygen, 10^{-9} Torr for 15 min make up for less than 1 L.

chemically shifted components but to the many-body energy-loss spectrum identified as Sunjic-Doniach lineshape that derives from excitations across the Fermi level (electron-hole pairs) and is a consequence of metallicity.

Finally, a last interesting feature is shown in the low-left panel. Indeed, the $4f_{7/2}$ and $4f_{5/2}$ peaks of Tungsten can be measured. In particular, the W 4f doublet can be observed both in its metallic form (at lower binding energies) and in its oxidized form (at higher binding energies). The evolution of the peak shape is rather notable: initially, only a small amount of W is present, suggesting that a contamination is present, possibly arising from the fact that the tungsten filament and crucible of the evaporator were heated at maximum power for very long time. After the first annealing the overall amount of W increases, possibly due to the emergence of W atoms that were previously locked into the bulk, and that could reach the surface thanks to the increased diffusion length during heating. The W is at that point for the main part oxidized. After the passivation and annealing, the W appears to increase further and to be completely oxidized. If one observes the edges of the oxidized W doublet, it is possible to notice that they tend to shift to the left: this may be due to the fact that during the first phases of the preparation very small amounts of oxygen were available, and the oxide is probably intermediate between WO_2 (chemical shift[12] 1-2 eV) and WO_3 (chemical shift[13] 4-5 eV); when the surface is exposed to oxygen, W is found completely in the WO_3 compound. A contribution to the shift of the peaks may also arise from the reduced coordination of W at the surface. It must be considered that, despite the fact that W contamination is evident, it is not large: in fact, the cross section of this element is very large at 480 eV (about 10 times larger than the already enhanced cross section of C 1s), thus the resulting signal is significant, but the amount of atoms is low.

The doublet of Fe 2p XPS peaks is shown in Fig. 7.6. After removal of a Shirley background, these doublet shows clearly the situation of the Fe outermost layers. In fact, the electrons originated from this binding energy range have a kinetic energy of 100-200 eV, and thus possess the shortest mean free path: the signal is then really originated from a volume reaching a depth of 5-10 Å below the surface. As it can be observed, the peak after evaporation has substantially the shape expected from clean Fe, while after the annealing and the passivation the 2p peaks chemically shifted of Fe-O set in. The feature at 715 eV of B.E. is a known satellite of the $2p_{3/2}$ peak of Fe on the Fe-O state. This result is in agreement with literature [85], and the shape of the peaks in this measurement hints at an even more defined Fe^{2+} character of the shoulder, with small contribution of the Fe^{3+}, sign that mainly the FeO oxide is formed, while no significant amounts of Fe_2O_3 are present.

Synchrotron-based XPS gives much more possibilities to the experimenter, but, possessing a continuously tunable range of photon energies, makes much more complicated the procedure of data analysis because most of the parameters of peak shape and intensity are different from the standardized ones, as most of the literature derives from X-ray tube-generated radiation. In order to achieve a good understanding of the structure of the sample, simulations were then performed with SESSA [87], allowing to obtain the shape,

[12] From NIST database.
[13] From NIST database.

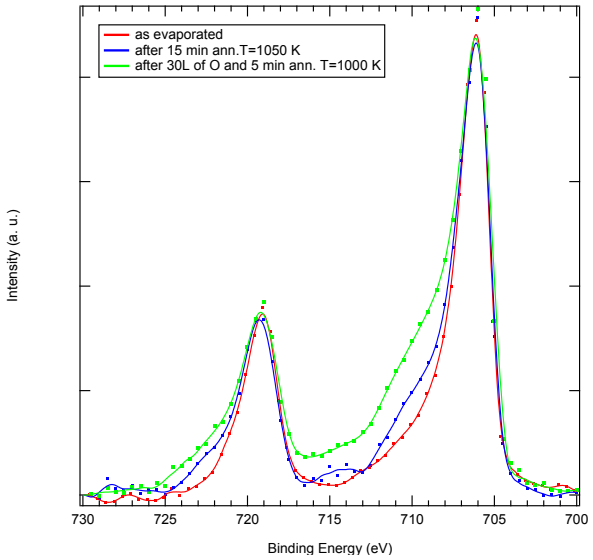

Figure 7.6. *The 2p peaks of Fe, measured with 850 eV primary photon energy. The peaks have been normalized to the height of the* $2p_{3/2}$ *peak to focus on the relative height of the shoulder structures.*

dispositions and relative intensities of the observed peaks. The primary photon energies can be given as a numerical input, together with the structure and chemical composition of the sample: the peak shapes and positions are then automatically extracted from databases and weighted accounting for as many aspects of the experiment as possible. The result of the simulation is shown in Fig. 7.7, confronted with the last survey scan measured at the end of the preparation procedure. Despite the different background, most

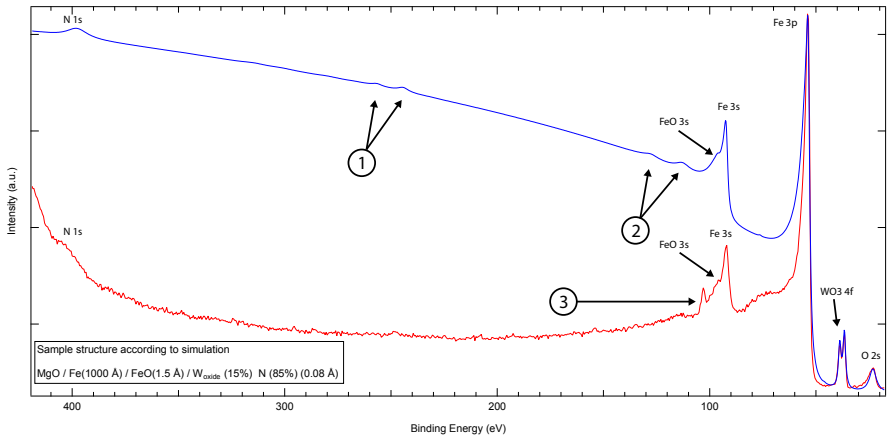

Figure 7.7. *Confrontation of the simulation (blue) with the survey scan of the last step of preparation. The features 1 and 2 are respectively XPS (4d) and Auger peaks of W (NNN) that are probably beyond detection. The satellite peak indicated with 3 is not reproduced, and may be a spurious effect.*

of the features are reproduced with the sample structure

$$\mathrm{MgO/Fe(1000\text{Å})/FeO(1.5\text{Å})/W_{oxide}(15\%)N(85\%)(0.08\text{Å})}$$

i.e with a FeO layer of the thickness expected (about the thickness of 1 ML of Fe) and a sub-ML coverage of contaminants containing N and a very small amount of W. C is present in amounts so small that in the survey scan is undetectable and was not included in the simulation. It is difficult to estimate the uncertainty on this values because of the different background, but the relative intensities of the features without a steep background as W 4f, O 2s and N 1s, together with the shape of the Fe 3s peak and its shoulder do not allow large variations (more than 5 on the last digit of each number) of the parameters without obtaining a spectrum visibly far from the measured one. In particular, it can surely be ruled out the possibility that the thickness of the FeO layer is larger than 2 Å and much less the 3-4 Å showed in Fig. 7.1 b. for the oxygen rich disordered phase.

Also XMCD spectra were recorded at the same steps of preparation and are shown in Fig. 7.8. It must be noted that XMCD measurements are extremely important for

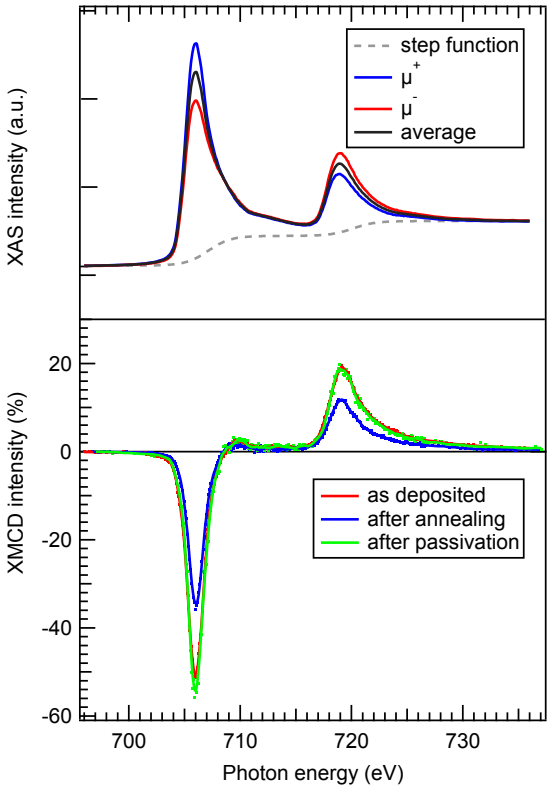

Figure 7.8. *On the upper panel, the absorption lineshape of Fe* $L_{2,3}$. *The curves for positive and negative magnetization of the film are shown in red and blue, respectively, while the average is shown in black. The dashed gray line shows the step function used to remove the background. In the lower panel, the percentage XMCD signal at the three steps of preparation.*

the experiment discussed here as the polarization of the unoccupied states just above the Fermi energy is assessed. This is the fundamental aim of the experiment: the polarization of the empty states few eV above the Fermi energy, necessary to create a VLEED target able to operate efficiently, must be preserved at the end of the passivation procedure. As is shown in Fig. 7.8, this is indeed the case, as the L_3 edge of the sample after evaporation

gives a maximum XMCD signal of -51 %, that is reduced after Fe annealing to -35 %, but is recovered, and even slightly increased to -56 % after passivation. However, the probing depth of the TEY measurements performed here is larger than the one of the XPS Fe 2p measurements, as electrons of all energies are counted for absorption. For this reason, no significant variations were observed in the XAS lineshape.

Finally, the magnetic behaviour of the film was studied through XMCD hystereses, shown in Fig. 7.9. These curves show the importance of the Fe annealing. The hysteresis

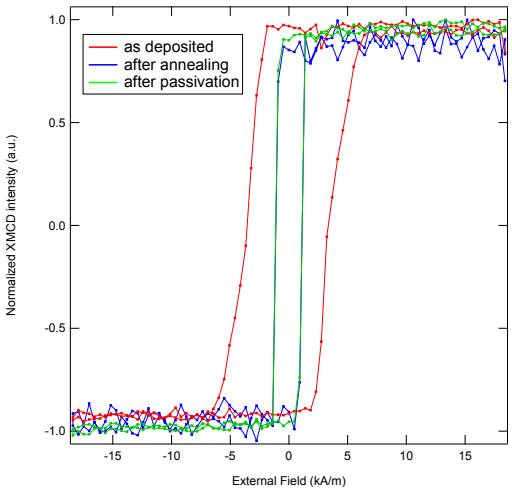

Figure 7.9. *Hystereses measured from XMCD signal. The field is applied along the [010] direction of the Fe lattice.*

of the as deposited sample, in fact, exhibits the characteristics of a multi-domain structure, as the switching of the magnetization vector goes through several intermediate steps, visible in the skewed lines that connect the two saturation regions. After the annealing, instead, the vertical inversion lines suggest that the magnetization rotates coherently and that the behaviour of the film is single-domain-like. Furthermore, the coercive field is reduced to give the typical soft-magnet characteristics of crystalline Fe. The hysteresis is now on the easy axis (no difference can be determined between saturation and remanence magnetization), as the substrate was rotated to achieve this condition. The passivation procedure does not alter significantly the magnetic behaviour.

7.3 Refreshing procedure

The Fe(001)-p(1x1)O surface is also refreshable, i.e. even after contamination, it can be recovered, giving the same spin-and magnetic characteristics. To test this ability, the sample was left for 4 weeks in the UHV chamber of APE-HE. After this period the sample was measured again, annealed in vacuum for 10 min at 900 K and was characterized. The survey scans measured at 480 eV are shown in Fig. 7.10.

As it can be noticed here and in Fig. 7.11 where the single peak scans are reported, a strong contamination of C probably in the form of Carbon dioxide is present, together

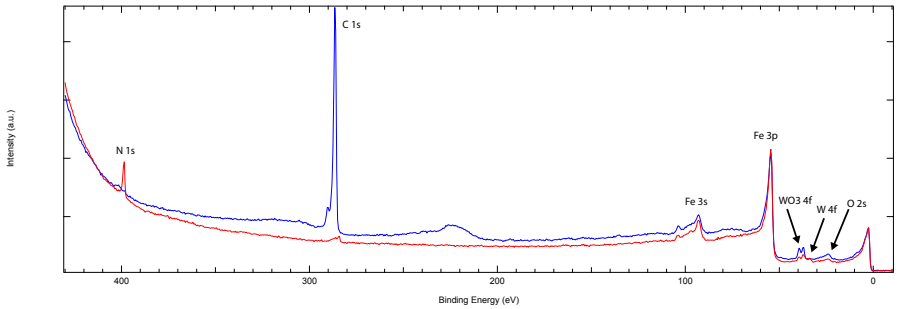

Figure 7.10. *Blue, survey scan after 4 weeks in UHV. Red, same, after 10 min annealing in UHV. The primary photon energy is 480 eV.*

with small amounts of Carbon monoxide. The annealing procedure is however extremely efficient in removing it, leaving only a small amount of free carbon on the surface.

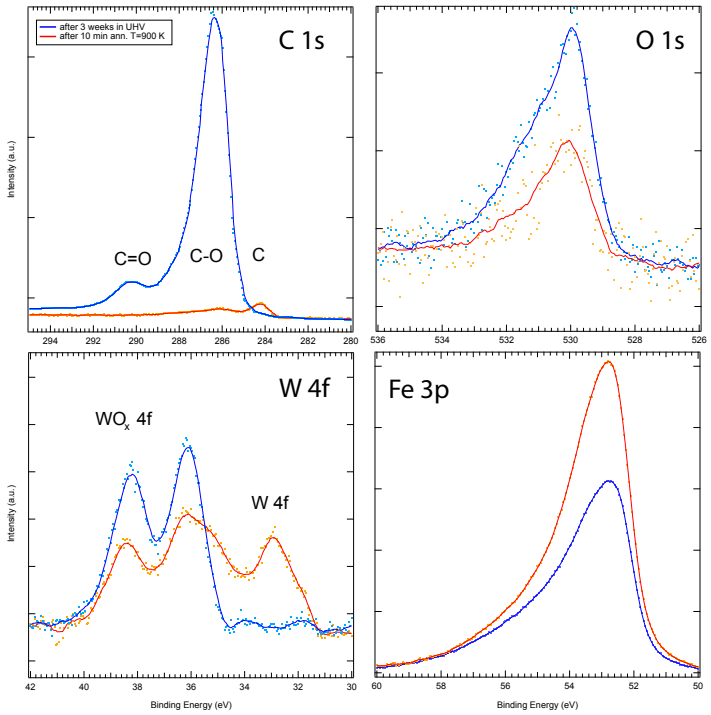

Figure 7.11. *Set of single peak scans. All the spectra shown here have been measured with primary photon energy of 480 eV, except for the O 1s which needed a higher energy of 850 eV.*

A contamination of N rises after annealing. This is possibly due to the fact that the preparation chamber was vented before the refreshing procedure, and, despite an accurate degassing had been performed, the Nitrogen washings might have left some traces on the annealing stages and filaments.

Following the clockwise direction used above, a picture emerges: while the contaminating layer is removed, and the signal of the underlying Fe increases in intensity significantly,

the oxygen is instead removed. The W quadruplet of peaks confirms this hypothesis, as part of the W oxide is reverted in metallic form. Also the Fe 2p peaks, in Fig. 7.12 show a significant increase of the signal, but the Fe-O shoulder is reduced.

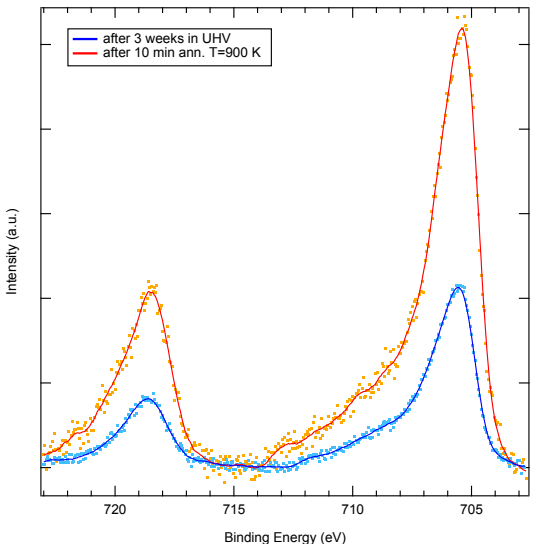

Figure 7.12. *The 2p peaks of Fe, measured with 850 eV primary photon energy. The peaks have been normalized with the same constant as in Fig. 7.11, to show the intensity increase of the Fe signal.*

The XMCD measurement after the annealing procedure produced a lineshape identical to the one shown in 7.8, but a slightly larger percentage XMCD signal, as shown in Fig. 7.13, reaching -59 % at the L_3 edge. This small increase is probably due to the fact that the characteristic of the beam may have been slightly different as in the accumulation ring the electrons were injected at 2.4 GeV during the last measurements and at 2.0 GeV during the first ones, so a different configuration of the undulator had to be used, possibly slightly varying the percentage of circular polarization of the beam.

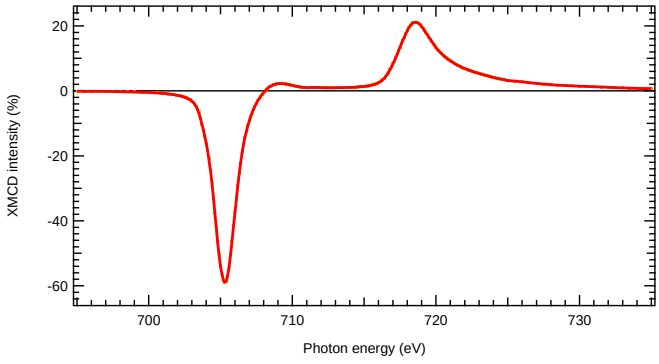

Figure 7.13. *Percentage XMCD signal from the Fe* $L_{2,3}$ *edges.*

Hysteresis cycles did not significantly differ from the ones in Fig. 7.9, neither before or after the refreshing procedure. Finally, a second simulation was performed, trying to reproduce the data of the final survey scan. A confrontation is shown in Fig. 7.14.

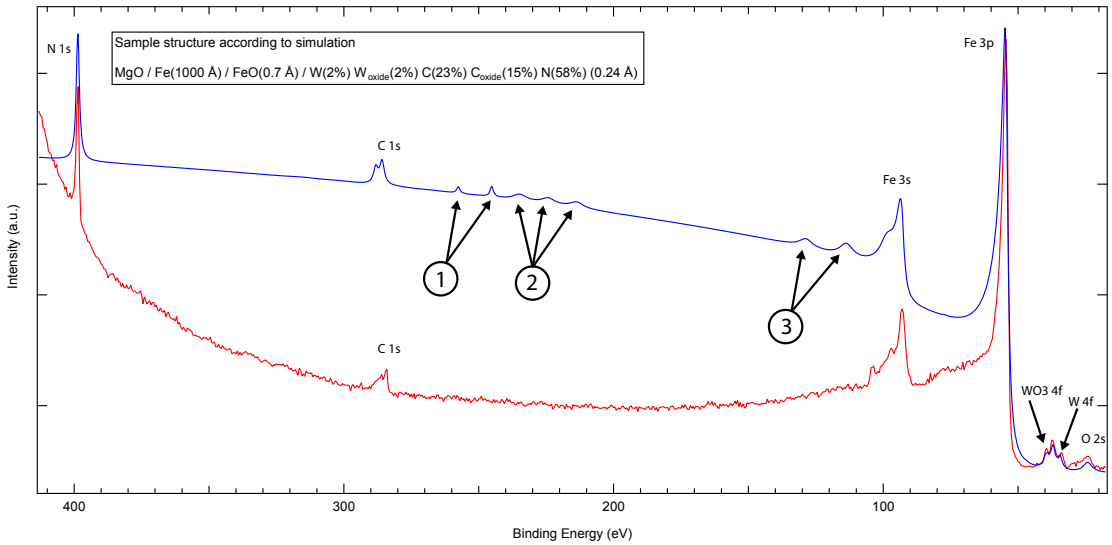

Figure 7.14. *Confrontation of the simulation (blue) with the survey scan of the final step of surface refreshing. The feature 1 is formed by undetectable 4d XPS peaks, feature 2 by Auger peaks of C (KLL) and feature 3 is again formed by W Auger peaks (NNN).*

The features are reproduced rather correctly with the structure

$$\mathrm{MgO/Fe(1000Å)/FeO(0.7Å)/W(2\%)W_{oxide}(2\%)C(23\%)C_{oxide}(15\%)N(58\%)(0.24Å)}$$

except for the features labelled with the circled numbers, whose width was probably underestimated by the software. The result of the simulation shows that the refreshing procedure reduces the contamination layer to a sub-ML thickness, that however is thicker than the one observed for the freshly prepared sample. On the other hand, the FeO layer thickness is reduced to less than a half. It is thus possible that the FeO layer coverage is not any more homogeneous and that in some zones the Fe surface is directly exposed. The performance of a surface refreshed with this procedure is then expected to deteriorate faster than the fresh Fe(001)-p(1x1)O. It is possible that the same procedure performed in an oxygen atmosphere can give better results as long as the homogeneity of the coverage is concerned.

Chapter 8

Characterization and ultrafast magnetization dynamics of $La_{0.67}Sr_{0.33}MnO_3$ thin films

The ULTRASPIN apparatus was designed to assess several scientific questions, as briefly hinted in the Introduction. In particular, its potential is in the fact that it will be able to explore the dynamics of solids with measurements directly based on the spin detection, generating a complementary point of view with respect to techniques that are based on indirect effects produced by spin-orbit interaction such as MOKE and XMCD. One of its possible applications is therefore in disentangling the aspects of the dynamics of highly correlated materials.

One of the most promising topics on this matter is the study of ultrafast magnetism in half-metallic ferromagnets. A half-metal is a solid whose band-structure is radically different for the spin-up and down state. In particular, if the densities of states for the two possible magnetic quantum numbers are considered separately, one of them (the minority state) has a gap at the Fermi energy. This means that the conduction electrons are completely spin polarized in the majority state, as in the solid do not exist empty energy levels for minority electrons close to the Fermi energy. Materials possessing this characteristics are of extreme interest in spintronic research, as they can constitute spin filters with close to 100% efficiency. Actually, a classification of half-metals has been developed [88] that includes also materials that do not have a perfect minority gap at the Fermi energy, but more generally systems in which the spin polarization at the Fermi energy is extremely high.

One interesting half-metallic system is $La_{1-x}Sr_xMnO_3$ (LSMO). It is a compound derived by doping the rare-earth manganite $LaMnO_3$ with Sr that is included substitutionally to La ions, acting as a hole donor. The crystal structure is called perovskitic and is displayed in Fig. 8.1. As it can be observed, both Mn^{3+} and Mn^{4+} ions are present in the structure separated by O atoms. This structure determines both transport properties and magnetism in LSMO. The electrons and the holes, generated by doping of the crystal, are in fact able to move into the material thanks to a sequence of hoppings between the Mn

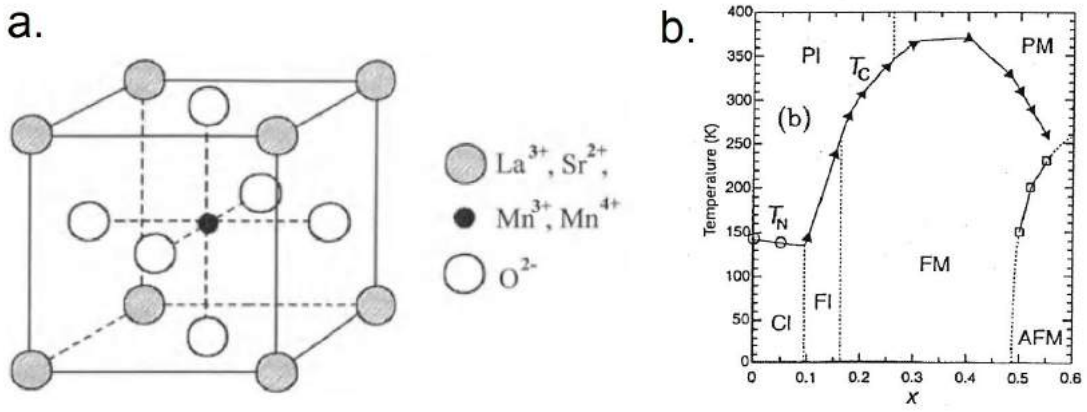

Figure 8.1. *a. Simplified scheme of LSMO unit cell structure. b. LSMO phase diagram as a function of the hole doping (x is the percentage atomic concentration). The phases are identified by abbreviations: CI is for Canted Insulator, FI for Ferromagnetic Insulator, PI for Paramagnetic Insulator, FM for Ferromagnetic Metal, PM for Paramgnetic Metal and AFM for Antiferromagnetic Metal. The lines indicate the expected critical temperatures, the markers the ones measured experimentally. From [89].*

3d bands and the oxygen orbitals. Due to the fact that the bands are differently occupied, hopping happens easily between Mn^{3+} and Mn^{4+} by crossing through a O 2p orbital. The hopping probability depends on the initial and final steps of the process and thus both on the spin state of the travelling electron and on the configuration of localized electrons on the ions. The free electrons in the material possess then different energy levels depending on the electronic configuration of the ions, and in high spin systems such as the 3d bands of Mn atoms, this is in turn dependent on the exchange interaction. The itinerant electrons will then be favoured in hopping from one site to the other if the Mn atoms have their spins aligned in a form of magnetic correlation called *double exchange ferromagnetism*[1].

This kind of magnetism presents an extremely wide number of applications: being intrinsically and strongly coupled with electrical transport, several complex behaviours are observed. For example, LSMO is one of the so-called Colossal Magnetoresistance Manganites, i.e. systems in which the resistivity changes greatly under the application of the magnetic field. Furthermore, the phase diagram of the compound (shown in Fig. 8.1 b.) as the Sr content is varied is very rich and displays a large number of phases that are seldom found in a unique system. In particular, at a low hole density, several exotic behaviours have been observed (ferromagnetic insulator, FI and spin-canted insulator, CI) and have raised a long standing effort to achieve a coherent theoretical interpretation: the single double exchange coupling is not sufficient to explain all the details and polaron effect, with Jahn-Teller distortion have been discovered to play a significant role. However, the discussion of the low hole density phases is beyond the scope of this thesis and will not be explored further. In the range 0.2-0.4 at.%, however, the system has a low-temperature ferromagnetic phase in which it shows a metallic behaviour, and an high temperature phase

[1]The ferromagnetic coupling is allowed thanks to the fact that itinerant electrons hop between Mn sites with differently occupied 3d bands. In the opposite case, the coupling would be antiferromagnetic. The exchange is called "double" because it arises both from the Coulomb exchange and from the itinerant exchange interaction due to the hopping of the free electrons.

in which it is a paramagnetic insulator (for $x < 0.3$ at.%) or a paramagnetic metal for ($x > 0.3$ at.%). At higher doping level the behaviour is that of an antiferromagnetic metal at low temperatures, changing to ferromagnetic and then to paramagnetic metal as the temperature is increased. At a doping of $x = 0.33$, the system reaches the paramagnetic metal phase at temperatures of about 350 K, well above room temperature, thus making it suitable for electronic application. Above the Curie temperature, when the correlation between the Mn ions is destroyed, $La_{0.67}Sr_{0.33}MnO_3$ resistivity increases drastically, as it could be expected from the double exchange model hinted above.

The most interesting feature for the experiments discussed below, however, is that $La_{0.67}Sr_{0.33}MnO_3$ has the behaviour of an half-metal, as was discussed in [90], upon observation of the spin-resolved XPS spectra of a 190 nm thick film of $La_{0.67}Sr_{0.33}MnO_3$ grown by pulsed laser deposition on a substrate of $SrTiO_3$[2]. The results are shown on Fig. 8.2 a, together with a scheme showing how, above the Curie temperature, not only the exchange splitting is removed, closing the minority gap, but also the density of states at the Fermi energy is strongly suppressed, accounting for the increased resistivity. However, the picture is actually not so simple as it may appear from the scheme below, as successive investigations recognized $La_{0.67}Sr_{0.33}MnO_3$ to be as a peculiar kind of half-metal, in which the polarization at the Fermi energy does not arise from a complete minority gap, but from the very different dispersion of the carriers for the different spin states. The minority spin particles have such a high effective mass that they barely contribute to transport (half-metal of type III_A)[3].

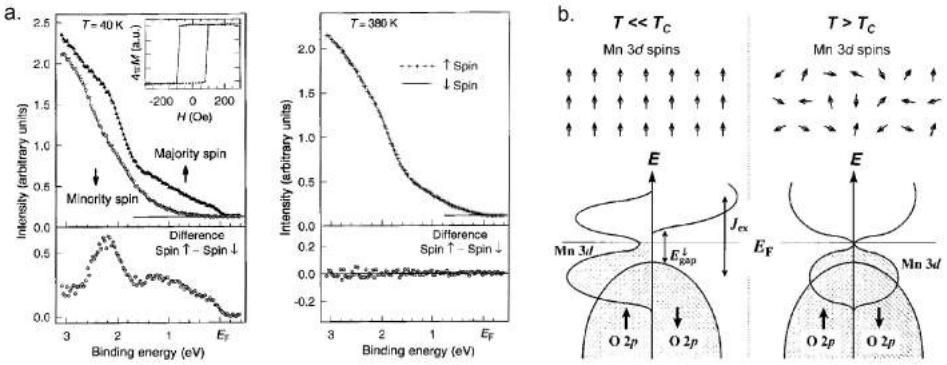

Figure 8.2. *a. Spin-resolved XPS measurements of LSMO valence band below and above the Curie temperature. b. Simplified picture showing the closing of the minority gap and the reduction of the density of states above the Curie temperature. From [90].*

The study of ultrafast response of half-metals was the object of a long standing work, which culminated in an extended survey on a vast range of materials [92]. The finding that is at the core of this exploration is closely related to the current understanding of laser induced demagnetization through the three temperature model. As illustrated in Fig. 8.3, when the laser pulse reaches a metallic ferromagnet, it is absorbed by the electrons, directly exciting their kinetic degree of freedom. The absorbed optical energy is rapidly

[2] $SrTiO_3$ is an oxide, also with perovskite crystal, that is used as a substrate for LSMO growth, as the it favours a good epitaxial growth of the cube on cube type, with low induced stress [91].

[3] [88].

transferred to the spin degree of freedom by spin-flip scattering processes[4] and then the two electronic energy reservoirs relax to the lattice through phonon scattering.

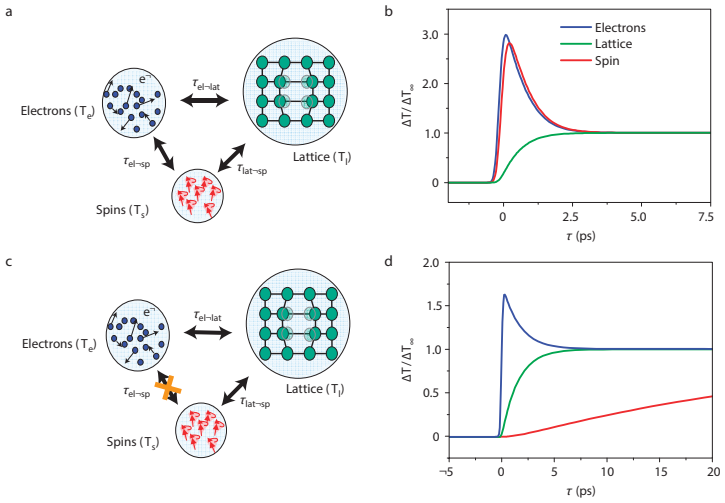

Figure 8.3. *a. Scheme of the interaction between the reservoirs in a magnetic metal. b. Numerical calculations for the temperatures of the three reservoirs for a ferromagnetic metal. c. Scheme of the interaction between the reservoirs in a half-metal. The relaxation of the electron reservoir directly in the spin reservoir is suppressed by the absence of spin-minority states. d. Same as b. but for a half-metal. Energy is transferred to the spin reservoir extremely slowly. From [92].*

In a half-metal, spin-flip processes have no final states, and close to 100 % spin polarized electrons are excited in the conduction band. The spin degree of freedom is then "frozen" until the lattice reservoir has been heated sufficiently to start transferring energy through the spin-lattice channel, a phenomenon that happens with much longer characteristic times. The long demagnetization time that characterizes half-ferromagnets has been also shown to be an efficient way to calculate the spin polarization of the electrons close to the Fermi energy.

As the study of half-ferromagnets progresses, a beneficial contribution can be given by alternative technique to the TR-MOKE used predominantly for these investigations. For this reason, the ultrafast demagnetization of LSMO can be an interesting topic for ULTRASPIN apparatus. While ULTRASPIN was in commissioning, trial experiments with a TR-MOKE set-up at the University of Regensburg were performed[5]. In the following sections, the characterization performed at APE beamline on LSMO samples and the time-resolved experiments will be described.

[4]The detailed mechanisms are under active debate in the ultrafast magnetism community.

[5]The ultrafast measurements were performed with Dr. Stefan Günther and Dr. R. Ciprian in the laboratories of the Lehrstuhl für Magnetismus und Magnetoelektronik at Fakultät für Physik at Universität Regensburg, under the supervision of Prof. C. Back.

8.1 Characterization

Several samples were made available by numerous laboratories. One LSMO[6](001)(40 nm)/STO(001) sample grown by MBE was provided by A. Petrov and B. Davidson of CNR-IOM (labelled TS-1). Two samples grown by PLD, one LSMO(001)(20 nm)/STO(001) (labelled BO-1) and one LSMO(001)(20 nm)/LSAT(001) (labelled BO-2) were provided by F. Borgatti, A. Dediu and I. Bergenti of CNR-ISMN. Two more samples grown by PLD, one LSMO(001)(20 nm)/STO(001) (labelled NA-1) and one LSMO(001)(3 nm)/STO(001) (labelled NA-2) were grown in the MODA system at CNR-SPIN (F. Miletto). However, static MOKE characterization on the Regensburg set-up showed that the signals retrieved from samples with thickness 20 nm was extremely small (BO-1) or non-existent (NA-1), due to the high transparency that good and epitaxial LSMO films have. No signal, for the same reasons, could be observed for NA-2[7]. BO-2 instead, showed unexpected behaviour with no obvious explanation as the magnetization did not decrease with time after the pulse, but increased instead. This is probably due to an interaction with the substrate as was not observed on films grown on STO. However, the comprehension of such behaviour was demanded to subsequent experiments, and most of the time-resolved measurements were concentrated on TS-1. For this reason, only data referring to this sample will be discussed in the following.

The system was characterized at APE beamline, firstly by XAS and XMCD measurement on the Mn $L_{2,3}$ edges. The results are shown in Fig. 8.4 a. and b. measured at room temperature. The XAS spectrum and XMCD showed that the system was magnetic at room temperature, as expected from the phase diagram shown above and from resistivity measurements.

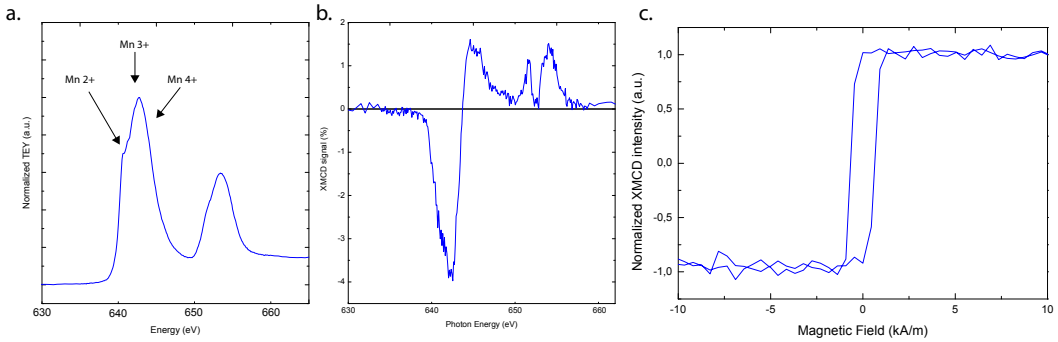

Figure 8.4. *a. XAS measurement at* $L_{2,3}$ *edges of Mn b. Corresponding XMCD signal c. Hysteresis loop measured with XMCD.*

The lineshape of both absorption lines and dichroism was found to be in agreement with literature of clean LSMO/STO structures, showing a very small contribution of Mn^{2+} ions

[6]From now on, LSMO will be used to indicate $La_{0.67}Sr_{0.33}MnO_3$.

[7]After the experiment MOKE measurements were performed with a MOKE set-up featuring a photoelastic modulator, in commissioning at APE beamline, that allowed to resolve smaller signals and thus to observe hysteresis loops also from the thinner films.

visible in the low photon energy shoulder of the L_3 peak[8]. It can be observed, that the percentage XMCD signal is much smaller, because LSMO is already very close to its Curie temperature at room temperature (RT) and its M(T) curve is already in its descendent phase (it will be extremely clear in Fig. 8.10). An hysteresis loop was also recorded showing a good coherence of magnetization momentum rotation and a very small coercive field of 711 A/m.

The quality of the film was also checked by XPS and XRD, shown in Fig. 8.5. The survey scan, measured at 800 eV photon energy, was acquired on the sample without any preparation, and displays no traces of contaminants other than C on the surface. A further

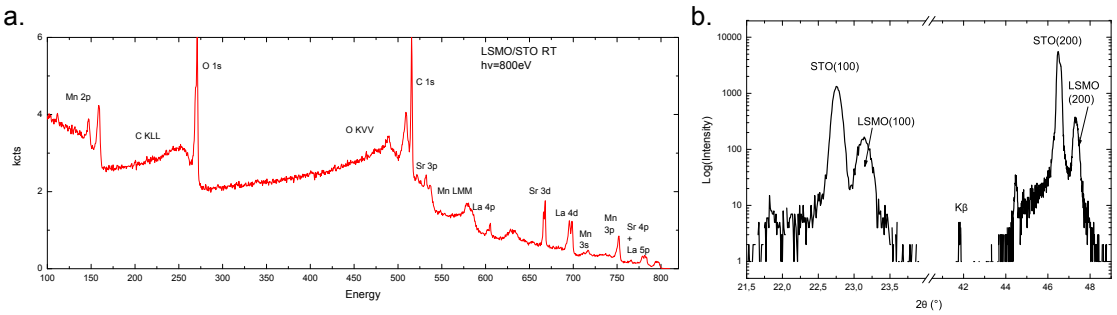

Figure 8.5. *a. XPS survey scan of LSMO/STO sample. b. XRD measurements performed with the ϑ-2ϑ method.*

characterization was performed after the time resolved with the use of X-ray diffraction. The measurements confirm the (100) epitaxial growth of the samples, showing moreover a good cristallinity. From the spectra no evidence of spurious phases can be detected.

8.2 Time-resolved measurements

The measurement procedure in the time-resolved pump probe experiment consisted always in two steps:

- Firstly, the set-up was configured in a continuous mode, blocking the optical path of the pump beam and registering only the probe Kerr rotation angle. Each time one parameter of the experiment was changed, a static hysteresis loop in the exact same conditions had to be measured. This is required in order to normalize the data.
- Secondly, the set up was configured in dynamical mode, by clearing the optical path of the pump beam and controlling the delay stage.

One of the static hystereses of the LSMO/STO sample acquired with the set-up is shown in Fig. 8.6. On the vertical axis, the signal after lock-in amplification is displayed. As it can be seen the ratio between the remanence and saturation magnetization is almost equal

[8]The presence of unwanted Mn^{2+} ions, due to a lack of oxygen at the surface, is discussed in [93] and can be recovered by oxygen annealing.

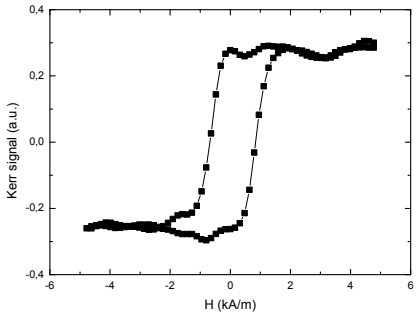

Figure 8.6. *Room temperature static-MOKE hysteresis of LSMO(40nm)/STO, used for normalization of the data sets.*

to one, in good agreement with the loop reported in Fig. 8.4 c. However, this loop differs significantly from the one measured with XMCD, as the coercive field is significantly larger. This can be explained considering that the depth sampled by MOKE (in particular on these films with high transparency), is much higher than the probing depth of TEY. The demagnetization curve, measured in remanence with opposite directions of magnetization, will then have to be divided by the total height of the associated hysteresis with the same set of experimental parameters to obtain a normalized plot of the time-evolution of magnetization.

Before stepping in the discussion of the details of the time resolved Kerr measurements, it is interesting to observe the reflectivity curve. If the two signals obtained from opposite magnetizations are summed instead of subtracted, it is possible to observe a signal proportional to the intensity of the reflected light, shown in Fig. 8.7.

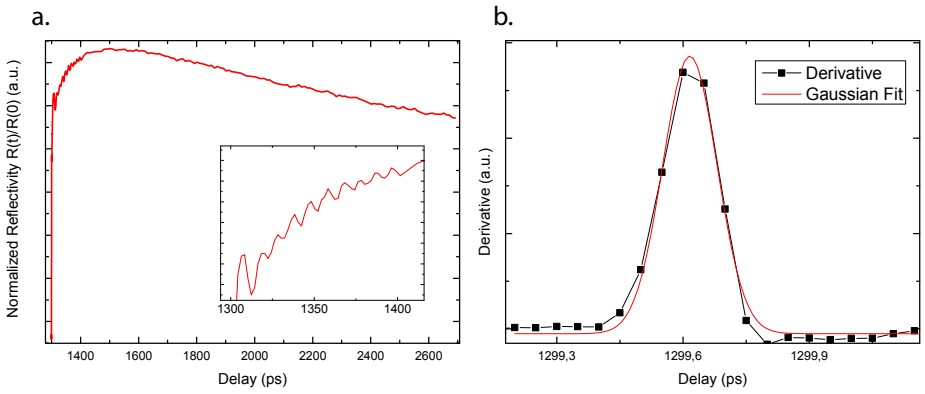

Figure 8.7. *a. Reflectivity of the LSMO sample as a function of pump-probe delay. Inset: Zoomed image on the short timescale after the pulse arrival. b. Derivative of the reflectivity curve used to characterize the pulse on sample.*

As it can be noticed in Fig. 8.7 a, the sharp increase of the reflectivity, due to the excitation of electrons to a high mobility state and recognizable as the coincidence instant of the pump and probe pulses, is not at the zero of the scale. This is because the time-

scale is actually derived as an encoded position of the mirrors on the delay line, and the coincidence between the pulses does not necessarily happen when the optical stage is in the zero position. It is thus necessary to characterize the beam. One of the quickest methods, based on the signal measured directly on the sample[9] is to calculate the derivative of the reflectivity curve and fit it with a Gaussian distribution, as shown in Fig. 8.7 b. This procedure led to set the zero position to $t = 1299.616 \pm 0.002$, that will be shown as zero in the graphs from now on. Furthermore, the fitting gave also information about the pulse duration, yielding a standard deviation of $\sigma_p = 64 \pm 2fs$.

An interesting feature can also be observed in inset of Fig. 8.7. The damped oscillation that can be observed superimposed to the large scale reflectivity curve is the effect of a coherent phonon observed in real time: the small variations of the reflectivity are, in fact originated by the shock-wave induced in the lattice by the absorption of the pump pulse. Owing to the high purity of the film, the damping of the phonon is rather small, allowing it to be reflected at the interface with STO and on the surface of LSMO, bouncing back and forth through the thickness of the film. Considering the period of such oscillation $T_{sh} = 10 \pm 2ps$, it is possible to give an estimate of the speed of sound in the material as $v_{ph} = 40nm/10ps = 4000m/s$. If a 10 % uncertainty is estimated on the thickness of the film, the measurement yields $v_{ph} = 4 \pm 1km/s$, in rough agreement with the data reported in literature for LSMO on STO [94]. The method sketched here can be used as the basis of accurate experiments that allow to explore in real time the behaviour of phonons [95].

As the magnetic relaxation of LSMO is expected to be very long, the dynamical curves were studied in two ranges: a short timescale (0-7 ps) and a long one (0-1.4 ns). A typical measurement is shown in Fig. 8.8. In these curves the demagnetization process appears

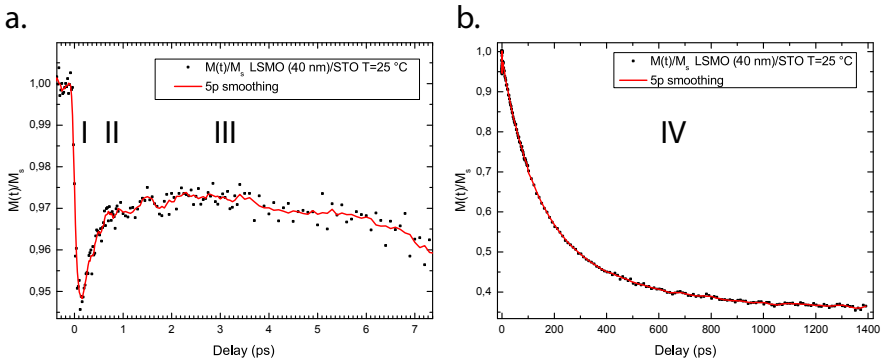

Figure 8.8. *a. Demagnetization curve of TS-1 sample at room temperature with 22 mW laser fluence, on a short time-scale. b. Demagnetization curve of TS-1 sample in the same conditions as a. on a long time-scale.*

to go through four different phases. The first one (I), completed in few hundreds of fs ($\approx 300\ fs$), is the ultrafast demagnetization due to the rapid increase of temperature of the electron kinetic reservoir. It appears to be anyhow slower than the quenching of a metallic ferromagnet, that is typically completed in half of the time ($\approx 150\ fs$). It must be noted

[9]Other method require the use of dedicated optical components, that anyway receive the beam after different optical paths.

that the initial quenching is very small, i. e. it is $\Delta M_{uf} = -5\%$ of the total magnetization before the pump pulse. After this, a fast partial recovery (II) sets in, and is completed in 2 ps, leading to a new meta-stable equilibrium (III). The partial recovery is even smaller than ΔM_{uf}, being: $\Delta M_{rec} = +2\%$. Finally, the metastable equilibrium collapses in the long time-scale phase (IV), that leads to a significant demagnetization reaching $\Delta M_{slow} = -63\%$ at the end of the explored time-scale, with no minimum detected. This process appears to be still ongoing after 1.5 ns. This is due to the aforementioned long time required for the optically pumped energy to relax into the spin reservoir, generated by the absence of spin-flip scattering processes. The low phonon damping observed in the reflectivity measurement suggests also that phonons interact weakly with other degrees of freedom in the solid, giving a small phonon coupling constant and thus contributing to elongate the relaxation time of the system.

While the long time-scale has been explored in other works [96], the ultrafast component has never been discussed thoroughly. To explain the underlying mechanisms, further measurements and computational simulations have to be performed. The long-time-scale component, instead, could be fit with a double exponential decay, and thus appears to emerge from two different processes, occurring at two different time-scales: one has characteristic time constant $\tau_1 = 128\ ps$, and the other appears to have longer characteristic times $\tau_1 = 408\ ps$. Also the explanation of such behaviour requires a deeper understanding of the system: for example the contribution of heat conduction in the STO substrate must be evaluated, as it can contribute in this time range.

The behaviour of the system was also studied when the fluence of the pump laser was varied, as shown in Fig. 8.9.

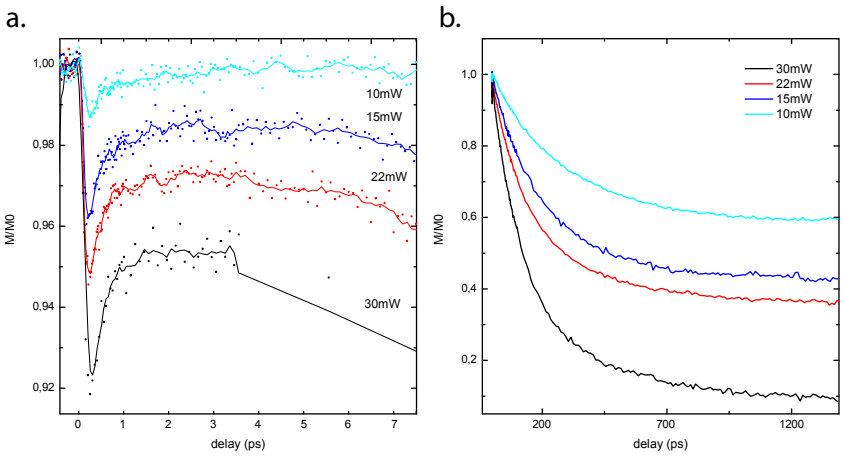

Figure 8.9. *a. Demagnetization curves for TS-1 sample as the laser fluence is varied on the short time-scale. b. Long time-scale.*

From these measurements, it was deduced that all the features, i.e. ΔM_{uf}, ΔM_{rec}, ΔM_{slow} scale linearly with the power deposited by the laser on the sample. In Fig. 8.9 b. it is possible to observe that the maximum laser fluence drives the sample to an almost

complete demagnetization, as the remaining magnetic signal at $t = 1400ps$ is less than 8% of the one observed for negative delays.

Finally, the behaviour of LSMO across its ferromagnetic-paramagnetic phase transition was studied. In Fig. 8.10 a. the SQUID magnetometry curves measured on TS-1 sample on a large interval of temperatures, showing the characteristics of a second order phase transition.

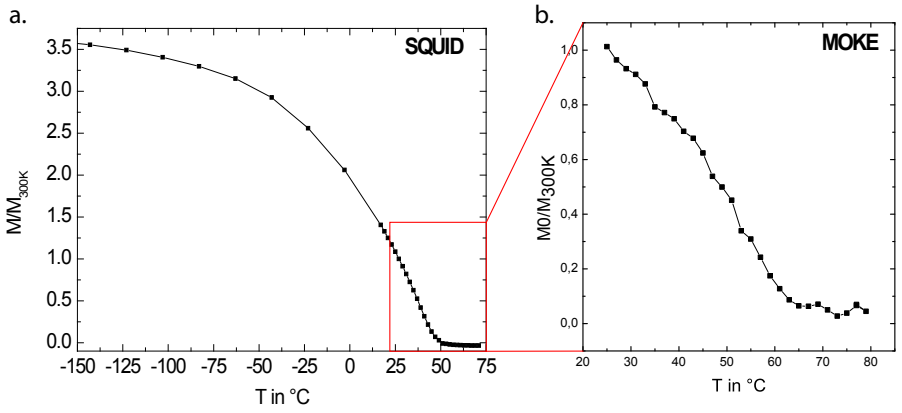

Figure 8.10. *a. SQUID magnetometry measurements of TS-1 sample in the temperature range from 120 K to 350 K. b. Normalized MOKE measurements of the 300 K to 350 K.*

In Fig. 8.10 b. the region explored with time-resolved MOKE experiments is displayed. The values shown here are the heights of hystereses measured for each value of temperature in the range achievable by a resistive heater positioned in thermal contact with the sample, normalized to the remanence magnetization at room temperature. Beyond 60°C no significant MOKE signal can be observed, and this established the Curie temperature to the best of the experimental resolution.

8.2.1 Complexity of data analysis due to cumulative thermal effects

The normalization of the curves as a function of the temperature, however, presents some challenges, as if one chooses to normalize each curve to one (i.e. to plot M(t, T)/M(0, T)), simply dividing each dynamical curve by the corresponding factor extracted from Fig. 8.10 b, the last measurements are excessively magnified. It is probably better to plot the un-normalized Kerr signal in 3D plots as a function of time and temperature. This is possible because the lock-in amplification used for all the curves is identical, so the relative amplitudes retain their physical meaning. The result is shown in Fig. 8.11.

Observing the curves presented in Fig 8.11 b, a clear behaviour is shown: as the magnetization saturation is reduced with the increasing temperature, the laser-induced quenching is reduced. In particular, the curves flatten on the long delay end and reach more rapidly a constant value, a sign that the complete demagnetization has been achieved. When the Curie temperature is overcome, the Kerr signal is practically constant. It is thus possible that the interpretation of these data is made difficult by two effects: the presence of a phase transition, that changes the static and dynamic behaviour between one curve

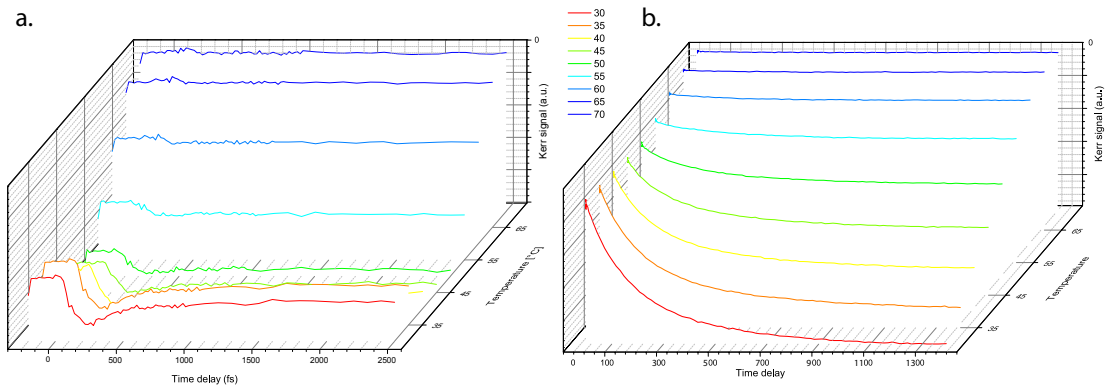

Figure 8.11. *a. Demagnetization curves of TS-1 as a function of temperature for the short time-scale b. Long time scans.*

and the other (not allowing for a simple confrontation of the curves), and the reduction of the magnetization saturation, that generates a complete demagnetization at some point in the temperature curve. For this reason, a much broader set of data, in particular with lower fluences, is needed.

Thermal drifts of the initial state in pump probe experiments

In Fig. 8.11 a, instead, the behaviour of short-timescales scans is shown. Firstly it must be noted that the system was calibrated by setting to zero the Kerr signal variation when the pump optical path was blocked. When the pump pulse is reaching the sample, the lattice is heated following the dynamics discussed above. However, seen the slow recovery time of this particular material, the overall temperature of the system does not go back to the initial value before the arrival of the successive light pulse. This leads to a situation, called DC heating, in which the film is slightly hotter when the pump pulse is switched on than in the moment of calibration. For this reason, the Kerr signal is negative even before the arrival of the pulse, as LSMO is already slightly demagnetized by continuous heating. When changing the temperature, this effects creates a slight shift of the initial temperature state of the sample with respect to the curve shown in Fig. 8.10: confirming this hypothesis, a close similarity between the derivative of M(T) and M(t<0, T) has been found.

Further measurements are needed to explore the behaviour of such a complex material, but several interesting points have been raised. Besides further accurate optical measurements, the understanding of the dynamics, in particular in the initial ultrafast phases may surely benefit from the different point of view offered by spin-resolved photoelectron measurements: it is for example possible to note that for the above reasons it is interesting to foresee experiments with higher photon energies, reducing the ratio of cross section of excitation of phonons and electronic excitations. Nevertheless, even with FEL pulses, disentangling thermal, electronic and magnetic excitations in time resolved experiments implies restoring the initial state in a controlled way.

Chapter 9

Conclusions and future perspectives

In the work discussed in this thesis, the commissioning of ULTRASPIN experimental end-station has been carried out. The experimental chambers, with all the featured instrumentation, were mounted and set to operation. A good UHV performance was obtained from the vacuum system. The central instrument of the set-up, a four-axial Mott polarimeter, was prepared for the realization of ultrafast time-resolved measurements by achieving an elevated efficiency, reliable operation and ease of use. The static performance of the detector was tested by spin-resolved secondary electron spectroscopy measurements on an amorphous metal picture-frame sample, showing that hystereses could be measured and that the polarization measurement noise was of purely statistical origin. Simultaneously to the static optimization of the detector, the development of a new data acquisition chain, able to match the large flux of information that can be collected in pulsed experiments, was performed.

The machine is now ready to enter step two of its commissioning, i.e. testing with a table-top ultrafast laser source. On a third step, it will finally be operated with a FEL light source, in the regime in which its characteristics are optimally exploited. This system holds promise to extract from materials a great amount of valuable information: in the best-possible scenario, the time-resolved Mott polarimeter will be able to acquire for each laser pulse four spin-resolved XPS spectra, with respect to two orthogonal quantization axes, and with energy resolution arising from the time-of-flight analysis. Moreover, the vectorial Mott set-up will enable to easily extend this extraordinary ability to spin-resolved measurements assessing each of the components of the polarization vector. This efficiency in the analysis of the final states will be conjugated with the ability to observe transient processes on an extremely short time-scale, thus giving in-depth information on the formation of equilibrium in spin systems. Furthermore, time resolved absorption spectroscopies will be applicable, both in total electron yield and with spin resolution of the quantum yield [**?**]. In the future of the ULTRASPIN end-station, however, also other advanced instruments are going to be tested: the feasibility studies of an angle resolved time-of-flight spectrometer, able to record a full angle resolved spectrum in a single pulse, are under way. These features will enable ULTRASPIN apparatus to become an highly

efficient system, giving access to several unexplored details of the structure of solids.

Tightly connected to the development of ULTRASPIN apparatus, experimental investigation of two highly spin-polarized systems was performed. A surface of Fe-p(1x1)O was realized, by growing a Fe film on an MgO substrate and creating an ordered pattern of adsorbed oxygen atoms. At each step of the growth the system was characterized and optimized to achieve the highest spectroscopic purity and crystalline order. Furthermore, the realization of an effective monolayer structure for oxygen was specifically addressed and confirmed. The resulting oxygen saturated surface has been found to have a lower chemical reactivity and a non-degraded (eventually slightly enhanced) spin polarization. The surface has furthermore been shown to be refreshable, i.e. the accumulated contaminants can be removed by a simple annealing. This has been verified by annealing in vacuum, but this procedure appeared to reduce the oxygen coverage. An oxygen annealing is then to be tested. The applications of interest of such system are several, ranging from the use as a high polarization reference sample, to the use as a contact element in spintronic heterostructures, to the realization of the target for the VLEED spin detector. This application in particular was the focus of the performed experiment, and the polarization of the low energy empty states above the Fermi level was specifically studied through the XMCD technique, holding promise of a good applicability of the developed system.

Time resolved MOKE measurements were also performed, in order to explore the range of possible applications of ULTRASPIN set-up. One of the potentialities of the system is that it can directly access the density of states of electrons in the matter, giving a complementary view to the optical techniques. For this reason, the first experiments are pointed at the study whose dynamical behaviour is deeply affected by spin-polarization of the band-structure close to the Fermi energy, i.e. half-metals. The compound of choice for these exploratory studies was $La_{0.67}Sr_{0.33}MnO_3$, a manganite whose magnetic coupling is dominated by double exchange interaction. In particular, this material was studied in the form of a film on a substrate, in the structure LSMO(001)(40 nm)/STO(001). After a characterization with spectroscopic techniques that confirmed the quality of the film, time resolved measurements have been performed: the dynamical behaviour of the manganite has been observed with unprecedented time resolution, showing features un-documented in the literature. The magnetization relaxation of the material was also studied as a function of sample temperature when crossing the phase transition. More extensive data, as well as computational simulations are what is needed to achieve a full understanding of such system in which several correlated effects take place.

In summary, ULTRASPIN is taxing on its take-off runway: the machine is set and ready to step in the time-resolved pulsed operation mode, while a few research directions are already starting to be explored, and awaiting for its contribution to shed a different light and achieve a deeper understanding on the dynamics of correlated electrons in solids.

Part IV

Appendices

Appendix A

Polarimeter efficiency

A.1 Error in polarization measurement

Using the definition of polarization presented in eq. 2.12, the uncertainty in its value can be written as:

$$P_\perp + \Delta P_\perp = \frac{A + \Delta A}{S_{eff} + \Delta S_{eff}} \tag{A.1}$$

it is possible to isolate $\Delta P_\perp$ using the propagation for independent errors and again eq. 2.12:

$$(\Delta P_\perp)^2 = \left(\frac{\Delta A}{S_{eff}}\right)^2 + \left(\frac{\Delta S_{eff}}{S_{eff}^2} A\right)^2 \tag{A.2}$$

$\Delta P_\perp$ has therefore two sources: a statistical one (related to ΔA), and a systematic one (caused by ΔS_{eff}). The systematic error is reduced during the calibration of the detector, when S_{eff} is measured as accurately as possible. However, it is very difficult to realize accurate measurements because of the intrinsic low statistics of both methods of calibration[1]. Once ΔS_{eff} is determined, anyway, it cannot be changed and does not effect significantly the measurement routine, as substitution of typical values show that even a 10% uncertainty on S_{eff} do not contribute significantly to $\Delta P_\perp$. For clarity of notation, in the following it will be neglected.

For what concerns ΔA, instead, it is possible to write, from eq. 2.10:

$$(\Delta A)^2 = \left(\frac{2N_r}{(N_r + N_l)^2}\right)^2 (\Delta N_l)^2 + \left(\frac{-2N_l}{(N_r + N_l)^2}\right)^2 (\Delta N_r)^2 \tag{A.3}$$

[1]The first method is *double scattering*, in which an high energy unpolarized electron beam is sent on a gold foil and the beam reflected at 120° is measured by Mott detector. This method requires very careful alignment, and the counts at the detectors drop by four orders of magnitude. The second method, called *energy acceptance reduction* consists in sending a polarized beam raising gradually the discrimination levels of the PIPS detectors: this allows to accept less and less electrons that have undergone inelastic interactions, giving a higher polarization signal. This can then be extrapolated to zero energy acceptance, i.e. to perfectly elastic electrons. A coefficient can be then found (and it will be the operational S_eff) that transforms the polarization in normal operation (lower discrimination levels) to the extrapolated, maximum one. When the discriminator levels are very high, however, counts are again very low.

and, assuming that the variances for N_r and N_l are determined by Poisson statistics ($\Delta N_i = \sqrt{N_i}$):

$$(\Delta A)^2 = \frac{4N_r N_l}{(N_r + N_l)^3} \tag{A.4}$$

but, from combining eq. 2.10 with eq. 2.12, one has:

$$P_\perp = \frac{1}{S_{eff}} \frac{N_l - N_r}{N_l + N_r} \tag{A.5}$$

and

$$1 - P_\perp^2 S_{eff}^2 = \frac{4N_r N_l}{(N_r + N_l)^2} \tag{A.6}$$

Therefore:

$$(\Delta A)^2 = \frac{1 - P_\perp^2 S_{eff}^2}{(N_r + N_l)} \tag{A.7}$$

which allows to express:

$$\Delta P = \sqrt{\frac{1}{(N_r + N_l)} \left(\frac{1}{S_{eff}^2} - P_\perp^2 \right)} \tag{A.8}$$

normally, S_{eff} is smaller than $P_\perp$, and is possible to write:

$$\Delta P = \sqrt{\frac{1}{(N_r + N_l) S_{eff}^2}} \tag{A.9}$$

now, considering eq. 2.13, it is possible to write:

$$\varepsilon = \left(\frac{I}{I_0} \right) S_{eff}^2 = \left(\frac{N_r + N_l}{N_0} \right) S_{eff}^2 \tag{A.10}$$

where N_0 is the number of electrons per unit time in the primary beam. Therefore, one has:

$$\Delta P = \frac{1}{\sqrt{N_0 \varepsilon}} \tag{A.11}$$

this shows that the figure of merit has a rigorous statistical origin. It can also be connected with the effective time requirement of a measurement. The relative error in a simple intensity measurement is only:

$$\frac{\Delta N_0}{N_0} = \frac{1}{\sqrt{N_0}} \tag{A.12}$$

while for polarization:

$$\frac{\Delta P_\perp}{P_\perp} = \frac{1}{\sqrt{P_\perp^2 N_0 \varepsilon}} \tag{A.13}$$

Thus, if one has the same primary beam current I_0 (or N_0) and wants to achieve the same relative error in polarization measurement as in intensity measurement, one needs to measure for $1/\sqrt{P_\perp^2 \varepsilon}$ times longer. With typical values of $\varepsilon \approx 10^{-4}$ and $P_\perp \approx 10^{-1} - 10^{-2}$

this means from 100 to 10000 times longer. Obviously, higher relative uncertainties are accepted, and measurements do not actually take so long times.

However, despite the fact that a general improvement of the FOM is desirable, an extremely high FOM must not be accepted blindly: if the ratio I/I_0 is increased too much (for example increasing the angular acceptance of electron counters), it will result in an overall higher FOM at the expense of S_{eff}. This leads to an eventual reduction of the statistical error but of an increase of the systematic one, because spurious instrumental asymmetries can then dominate the uncertainty. Systematic error cannot be reduced by longer measurements, thus making a precise, but not accurate machine. Therefore, in the confrontation of polarimeters, FOM is a useful value, but must be together with a high effective Shermann function.

A.2 Absolute error for pulsed sources of light

The absolute error in polarization measurement in the pulsed regime can be calculated as well. If one considers a single shot, the number of primary electrons is given by:

$$N_0 = N_{epp}(i) \tag{A.14}$$

where $N_{epp}(i)$ is the number of electrons generated by the i-th light pulse that reach the detector (electrons per primary pulse). It is possible[2] to assume that this is proportional to the intensity of the i-th light pulse. In a FEL the intensity of the shots follows a Gaussian distribution with significant variance [23], of the order of few tens percent. Averaging over a large number of pulses one will then have:

$$\frac{\sum_{i=1}^{N_p} N_{epp}(i)}{N_p} = \bar{N}_{epp} \tag{A.15}$$

With N_p number of counted pulses.

A.2.1 Pulsed regime for detectors with two electron counters

If a Mott detector is considered, it is possible to treat the single pulse in the same way as was done for a continuous flux of electrons, obtaining (by simple substitution of N_0 in A.11):

$$\Delta P(i) = \frac{1}{\sqrt{N_{epp}(i)\varepsilon_{Mott}}} \tag{A.16}$$

Then if one considers N_p pulses, one can average the polarizations obtained, weighting them with the errors expressed in eq. A.16 (they will be different, because each $N_{epp}(i)$ is

[2]The effects of space charge, that distort the proportionality between light intensity and electron yield, are neglected here.

different). Such result will have an uncertainty in the form:

$$\Delta P(N_p) = \frac{1}{\sqrt{\sum_{i=1}^{N_p} \frac{1}{\Delta P(i)^2}}} = \frac{1}{\sqrt{\sum_{i=1}^{N_p} N_{epp}(i)\varepsilon_{Mott}}} \tag{A.17}$$

this procedure is thus very efficient in handling the instabilities of the source, because the weighted average is a powerful statistical instrument that enables to take little account of polarization measurements coming from very low intensity shots that carry a very high uncertainty. The system, having a feedback on the total intensity of each single shot, can reconstruct what pulses carry a high statistics and thus little uncertainty and which ones have too low counts, and account them accordingly. If one forces the formalism slightly, it is possible to consider N_p so big that:

$$\sum_{i=1}^{N_p} N_{epp}(i) \approx N_p \bar{N}_{epp} \tag{A.18}$$

and to consider the asymptotic behaviour:

$$\Delta P(N_p) \rightsquigarrow \sqrt{\frac{1}{N_p \bar{N}_{epp} \varepsilon_m}} \tag{A.19}$$

Thus the uncertainty reduces with an inverse square-root trend as a function of the number of pulses with a coefficient. If one includes some typical numbers, such as $\varepsilon_m \approx 6 \times 10^{-4}$ and $\bar{N}_{epp} \approx 10^5$, the resulting coefficient can be calculated:

$$\Delta P(N_p) \rightsquigarrow \frac{0.129}{\sqrt{N_p}} \tag{A.20}$$

A.2.2 Pulsed regime for detectors with one electron counter

For the case of the one electron counter detectors a slightly different situation arises, and it is necessary to rethink the whole procedure in the light of the different measurement routine. The asymmetry for a VLEED polarimeter is given in 2.30 as[3]

$$A_{ex} = \frac{I_{m\uparrow} - I_{m\downarrow}}{I_{m\uparrow} + I_{m\downarrow}}$$

but a subtle point must be considered when passing to the (unstable) pulsed regime. The real asymmetry that one expects to measure, and that is actually proportional to polarization vector components, is:

$$A_{ex}^{th} = \frac{I_{epp}\sigma_{\uparrow} - I_{epp}\sigma_{\downarrow}}{I_{epp}\sigma_{\uparrow} + I_{epp}\sigma_{\downarrow}} \tag{A.21}$$

[3]In the following discussion, the letter I was chosen for the expressions related to one-electron counter detectors in order to avoid confusion with the Mott-detector expressions. However, I is always a number of electrons per unit time, just as N in the Mott detectors.

where I_{epp} is an ideal intensity of the pulse *identical* when electrons are scattering with the cross section $\sigma_\uparrow$ and $\sigma_\downarrow$. In the real measurement, however, the electrons for $\sigma_\uparrow$ and $\sigma_\downarrow$ are coming from different pulses, and their number is different. It is then necessary to write:

$$A_{ex}^{real}(i, i+1) = \frac{I_{m\uparrow}(i) - I_{m\downarrow}(i+1)}{I_{m\uparrow}(i) + I_{m\downarrow}(i+1)} \tag{A.22}$$

each of the I measurements will be affected by the usual counting statistics, with Poissonian distribution, so that:

$$I_{m\uparrow}(i) = (I_{epp}(i)\sigma_\uparrow) \pm \Delta I_{\uparrow stat}(i) \tag{A.23}$$

and

$$I_{m\downarrow}(i+1) = (I_{epp}(i+1)\sigma_\downarrow) \pm \Delta I_{\downarrow stat}(i+1) \tag{A.24}$$

if one wants to refer to the expected asymmetry, however, one must introduce a third error when computing the numerator and denominator, due to the fact that they can be shifted by variations of the intensity from shot to shot[4]

$$I_{m\uparrow}(i) - I_{m\downarrow}(i+1) = (I_{epp}(i)\sigma_\uparrow - I_{epp}(i)\sigma_\downarrow) \pm \Delta I_{2p} \tag{A.25}$$

then it is possible to recover the expected asymmetry and to estimate the errors:

$$A_{ex}(i, i+1) = \frac{I_{epp}(i)\sigma_\uparrow - I_{epp}(i)\sigma_\downarrow}{I_{epp}(i)\sigma_\uparrow + I_{epp}(i)\sigma_\downarrow} \pm \Delta A(i, i+1)$$

it is now possible to calculate the relative uncertainty:

$$\delta A(i, i+1) = \sqrt{\left(\frac{\Delta I_{\uparrow stat}(i)}{I_{m\uparrow}(i) - I_{m\downarrow}(i+1)}\right)^2 + \left(\frac{\Delta I_{\downarrow stat}(i+1)}{I_{m\uparrow}(i) - I_{m\downarrow}(i+1)}\right)^2 + \left(\frac{\Delta I_{2p}(i, i+1)}{I_{m\uparrow}(i) - I_{m\downarrow}(i+1)}\right)^2}$$

where the terms divided $I_{m\uparrow}(i) + I_{m\downarrow}(i+1)$ have been neglected. Considering Poisson statistics for the counting errors:

$$\delta A(i, i+1) = \sqrt{\frac{I_{m\uparrow}(i) + I_{m\downarrow}(i+1)}{[I_{m\uparrow}(i) - I_{m\downarrow}(i+1)]^2} + \left(\frac{\Delta I_{2p}}{I_{m\uparrow}(i) - I_{m\downarrow}(i+1)}\right)^2} \tag{A.26}$$

It is now possible to obtain the absolute error on asymmetry[5]

$$\Delta A(i, i+1) = A \cdot \delta A = \sqrt{\frac{1}{I_{m\uparrow}(i) + I_{m\downarrow}(i+1)} + \frac{\Delta I_{2p}^2}{[I_{m\uparrow}(i) + I_{m\downarrow}(i+1)]^2}} \tag{A.27}$$

[4] It must be noted that the errors are of a statistical nature. Despite the fact that now ΔI_{2p} is introduced as a difference between two precise pulses, if one wants to deal with it as an error on the intensity measurement, one must consider ΔI_{2p} as the variance of the distribution of the differences, just as one uses the variance of the Poissonian distribution centred at $I_{m\uparrow}(i)$ for $\Delta I_{\uparrow stat}(i)$ or at $I_{m\downarrow}(i+1)$ for $\Delta I_{\downarrow stat}(i+1)$.

[5] The same result can be obtained considering directly the absolute error and neglecting the uncertainty on the denominator of $A_{ex}(i, i+1)$.

and, dividing by the effective Shermann function S_{eff}, the absolute error on polarization:

$$\Delta P(i,i+1) = \frac{1}{S_{eff}\sqrt{I_{m\uparrow}(i) + I_{m\downarrow}(i+1)}}\sqrt{1 + \frac{\Delta I_{2p}^2}{I_{m\uparrow}(i) + I_{m\downarrow}(i+1)}} \tag{A.28}$$

it is then evident that an object very close to the uncertainty observed in Mott detectors is obtained by multiplication of the pre-factor with the first summand under the square root. A second term, arising from the instability of the source is now present and increases (there are only non-negative numbers) the error.

If several pulses are used, a weighted average can be performed again, yielding:

$$\Delta P(N_p) = \frac{1}{\sqrt{\sum\limits_{2i+1=1}^{N_p} \frac{S_{eff}^2(I_{m\uparrow}(i) + I_{m\downarrow}(i+1))}{1 + \frac{\Delta I_{2p}^2}{I_{m\uparrow}(i) + I_{m\downarrow}(i+1)}}}} \tag{A.29}$$

where the sum over the index $2i+1$ denotes the fact that only every two pulses a measurement is completed, therefore the number of measurements with N_p pulses will be $N_p/2$. Stepping again to a less strict formal rigour, in the limit of big N_p it is possible to consider:

$$\begin{gathered} S_{eff}^2\ (I_{m\uparrow}(i) + I_{m\downarrow}(i+1)) \rightsquigarrow S_{eff}^2\ (\bar{I}_{m\uparrow} + \bar{I}_{m\downarrow}) = 2\bar{I}_{epp}\ \varepsilon_v \\ \sum_{2i+1=1}^{N_p} \rightsquigarrow \frac{N_p}{2} = N_m \end{gathered} \tag{A.30}$$

Where $\bar{I}_{m\uparrow}$ and $\bar{I}_{m\downarrow}$ are the average pulse intensities measured in the two magnetization configurations, $\bar{I}_{epp}$ is the average number of electrons per pulse before the polarimeter, and ε_v is the FOM of the detector. N_m is the number of measurements, that for one electron counter detectors is different from the number of pulses (N_p).

To evaluate ΔI_{2p}^2 the discussion needs to be deepened slightly further. This uncertainty is generated by the fact that $I_{epp}(i)$ and $I_{epp}(i+1)$ are two successively and independently extracted variables from the same normal distribution.

$$\mathcal{P}(I_{epp}(i)) = \frac{1}{\sqrt{2\pi\sigma_{epp}^2}} e^{-\frac{(I_{epp}(i) - \bar{I}_{epp})^2}{2\sigma_{epp}^2}} \tag{A.31}$$

Where σ_{epp} is the variance in the distribution of number of primary electrons. This quantity can be traced back to the variance in the photon beam with: $\sigma_{ph} = \sigma_{epp}/\bar{I}_{epp}$ as the relationship between intensity and number of photoemitted electrons can be approximated to be linear in this range. To lighten the notation, it is better to define $I_{epp}(i) = x$ and

$I_{epp}(i+1) = y$. ΔI_{2p}^2 can therefore be calculated as:

$$\Delta I_{2p}^2 = \frac{\int_{-\infty}^{\infty}\int_{-\infty}^{\infty} (x\sigma_\uparrow - y\sigma_\downarrow)^2 \, e^{-\frac{(x-\bar{I}_{epp})^2}{2\sigma_{epp}^2}} \, e^{-\frac{(y-\bar{I}_{epp})^2}{2\sigma_{epp}^2}} \, \mathrm{d}x \, \mathrm{d}y}{\int_{-\infty}^{\infty}\int_{-\infty}^{\infty} e^{-\frac{(x-\bar{I}_{epp})^2}{2\sigma_{epp}^2}} \, e^{-\frac{(y-\bar{I}_{epp})^2}{2\sigma_{epp}^2}} \, \mathrm{d}x \, \mathrm{d}y} \tag{A.32}$$

giving:

$$\Delta I_{2p}^2 = \bar{I}_{epp}^2(\sigma_\uparrow - \sigma_\downarrow)^2 + \sigma_{epp}^2(\sigma_\uparrow^2 + \sigma_\downarrow^2) = \bar{I}_{epp}^2(\sigma_\uparrow^2 + \sigma_\downarrow^2)\left(\frac{(\sigma_\uparrow - \sigma_\downarrow)^2}{\sigma_\uparrow^2 + \sigma_\downarrow^2} + \sigma_{ph}^2\right) \tag{A.33}$$

where the aforementioned σ_{ph} has been inserted. The first summand in the last term is small, and can be neglected, giving:

$$\Delta I_{2p}^2 = \bar{I}_{epp}^2(\sigma_\uparrow^2 + \sigma_\downarrow^2)\sigma_{ph}^2 = (\bar{I}_{m\uparrow}^2 + \bar{I}_{m\downarrow}^2)\sigma_{ph}^2 \approx \frac{1}{2}(\bar{I}_{m\uparrow} + \bar{I}_{m\downarrow})^2\sigma_{ph}^2 \tag{A.34}$$

As $\bar{I}_{m\uparrow} \approx \bar{I}_{m\downarrow}$. By manipulating the first line of eq. A.30, it is possible to write:

$$\Delta I_{2p}^2 \approx \frac{2\,\bar{I}_{epp}^2\,\varepsilon_v^2}{S_{eff}^4}\,\sigma_{ph}^2 \tag{A.35}$$

It is then possible to obtain:

$$\Delta P(N_p) \rightsquigarrow \sqrt{\frac{2}{N_p\,2\,\bar{I}_{epp}\,\varepsilon_v}\cdot\left[1 + \frac{2\,\sigma_{ph}^2\,\bar{I}_{epp}^2\,\varepsilon_v^2}{2\,\bar{I}_{epp}\,\varepsilon_v\,S_{eff}^2}\right]} = \sqrt{\frac{1}{N_p}\cdot\left[\frac{1}{\bar{I}_{epp}\,\varepsilon_v} + \frac{\sigma_{ph}^2}{S_{eff}^2}\right]} \tag{A.36}$$

in the regime of large $\bar{I}_{epp}$, the first summand of the factor in square parenthesis is much smaller than the other. It is then possible to write:

$$\Delta P(N_p) \rightsquigarrow \sqrt{\frac{1}{N_p}}\cdot\frac{\sigma_{ph}}{S_{eff}} \tag{A.37}$$

and, substituting[6]:

$$\begin{aligned} S_{eff} &\approx 0.1 \\ \bar{I}_{epp} &\approx 10^5 \\ \sigma_{ph} &\approx 0.1 \end{aligned} \tag{A.38}$$

then one obtains:

$$\Delta P(N_p) \rightsquigarrow \frac{1}{\sqrt{N_p}} \tag{A.39}$$

[6]It should be noted that $\sigma_{ph} \approx 0.1$ is a rather generous estimate, based on the reported [23] performance of FERMI-1 seeded FEL in Elettra laboratory. Most SASE FELS operate with higher shot-to-shot fluctuations.

i.e. despite the lower FOM, the Mott detector has coefficient a factor of 10 smaller. This means that a repetition rate 100 times smaller is required to perform experiments with the same precision and the same duration, or that 100 times shorter experiments are required to Mott detectors at the same repetition rate. An example is plotted in Fig. A.1.

It is interesting to observe that the coefficient of the one electron detector is strongly dependent on σ_{ph}, and only weakly on $\bar{I}_{epp}$ (eq. A.36), while for Mott the situation is exactly opposite: the coefficient is determined mainly by $\bar{N}_{epp}$ and has no dependence on σ_{ph}. It is thus possible to conclude that Mott detector is better suited for FEL application[7], where the intensity is high, but oscillating strongly, while VLEED detector operate more efficiently with a table-top laser, i.e. with lower number of electrons per pulse, but a higher stability of the intensity of the photon beam. The detectors' performances are expected to match (if $\sigma_{ph} \approx 0.1$) when the average number of electrons per pulse is as low as 2×10^3, as obtained by equating eq. A.36 and eq. A.39 and solving for $\bar{N}_{epp}$ ($\bar{I}_{epp}$ and $\bar{N}_{epp}$ indicate the same quantity). For the three dimensional determination of the polarization vector with a pulsed source, Mott detectors are expected to outdo the VLEED apparatuses even more significantly, because the redundant component of the Mott detector allows to renormalise the asymmetries from each pulse, while the VLEED will have to acquire enough statistics to reduce the error arising from the combination of six independent measurements.

[7]The difference between the Mott detector and the one-electron detectors grows in favour of the former if the average number of electrons per pulse, and FEL can easily deliver more intensity to achieve $\bar{N}_{epp}$ much higher than the one used here. However, very recent experiments [**?**] have observed that above 10^5 electrons per pulse the space charge formed at the surface is sufficiently strong to distort the low energy (and high polarization) region of the spectrum, thus reducing the polarization signal. The compromise between reduction of the signal and reduction of the uncertainty will probably have to be addressed practically, depending on the aim of the experiment.

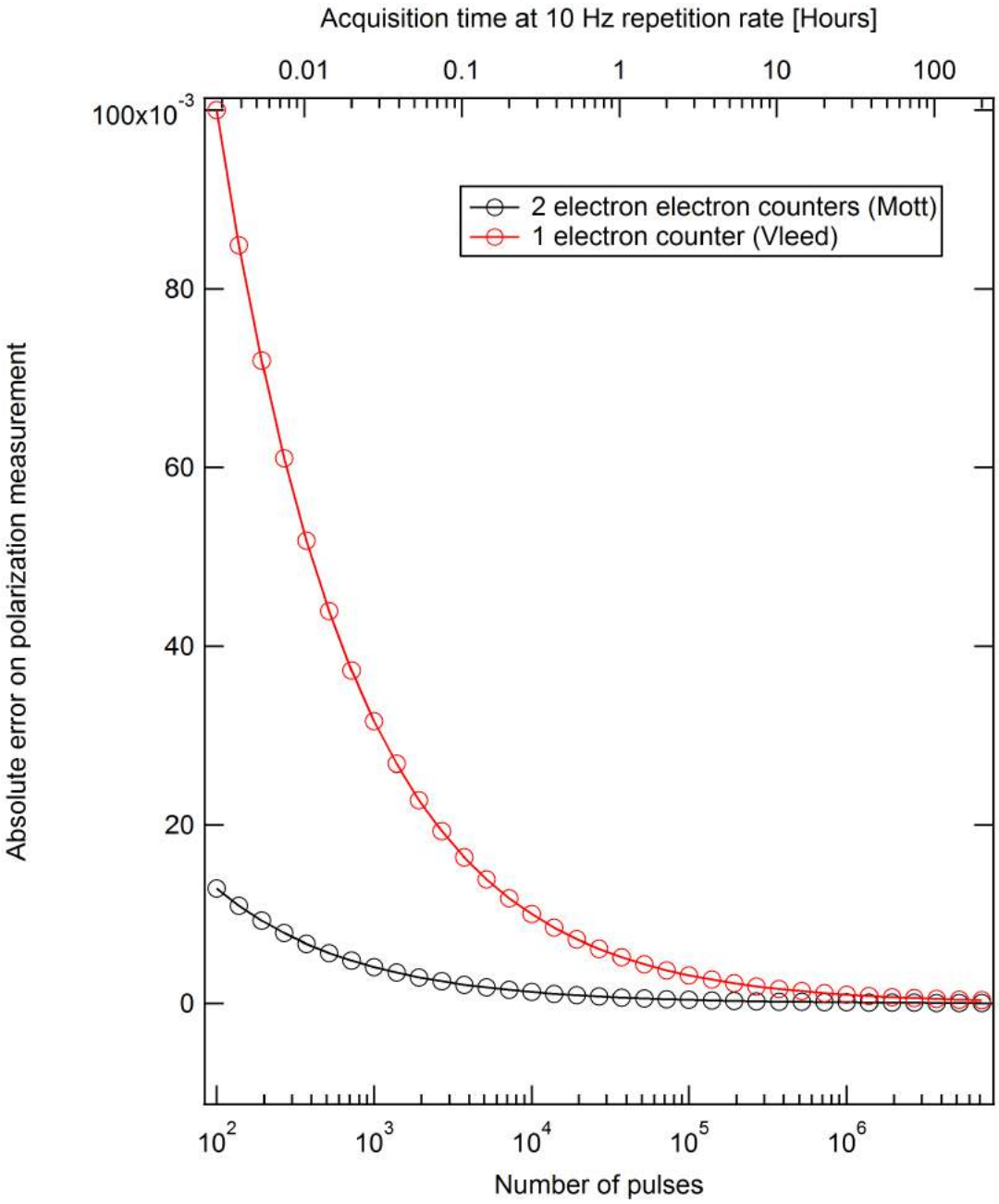

Figure A.1. *Plot of the absolute error as a function of the number of pulses in the limit of high statistics. On the top axis the time required to deliver the number of pulses in the lower axis at 10 Hz repetition rate.*

Appendix B

Drawings

The following drawings are reported by generous concession of A. De Luisa, Project Designer. Tab. 1 Represents a rendering of ULTRASPIN apparatus in isometric projection as it appears in its entirety (a.) and in sagittal section of the analysis chamber. In Tab. 2 front (a.) and back (b.) views are drawn. In Tab. 3 the side view is shown both of the complete machine (a.) and in the same sagittal section shown in Tab. 1. In Tab. 4 is presented the technical drawing used for the construction of ULTRASPIN, in both lateral views (a. and c.), in front view (b.) and top view (d.). Linear dimensions and angles are indicated in the quotes. Finally in Tab. 5 the detailed scheme of the analysis chamber, with complete labelling of the ports.

Tab. 1

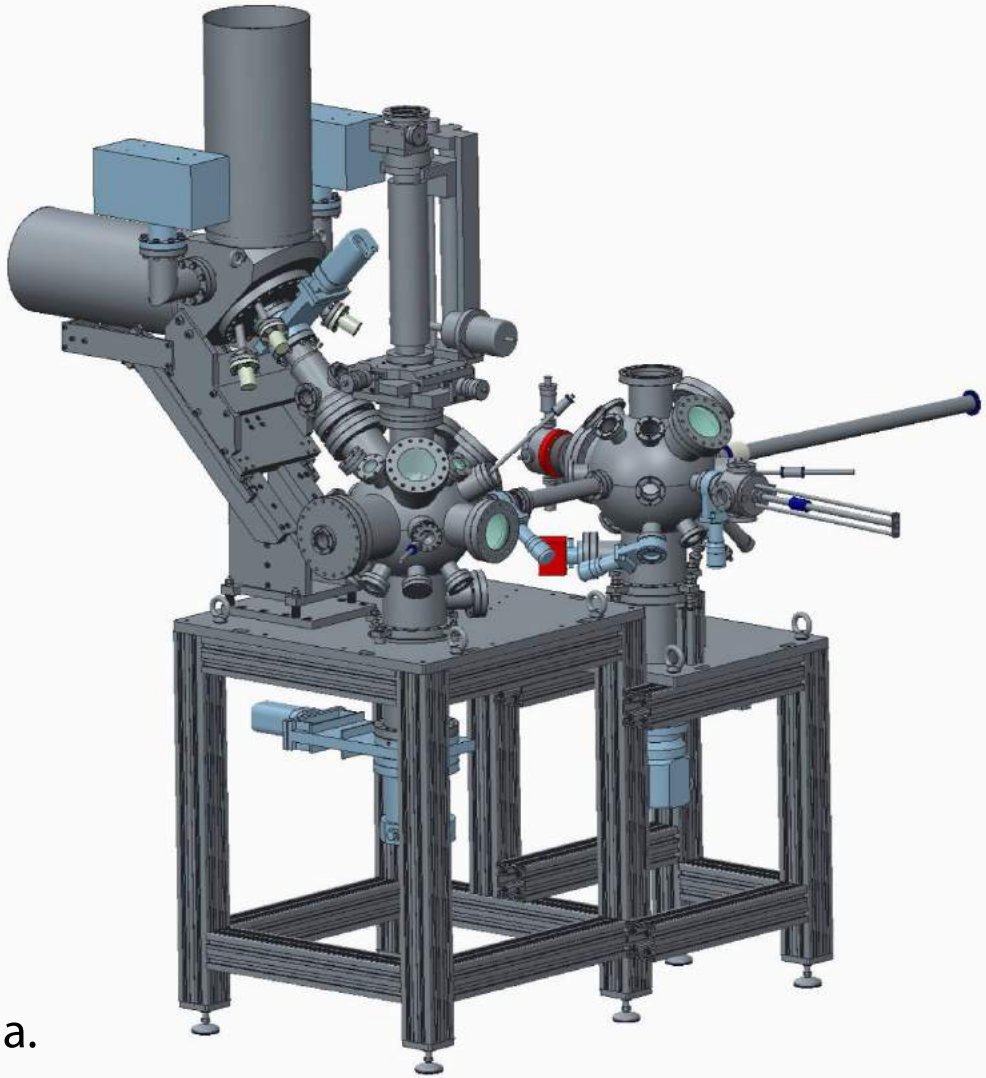

a.

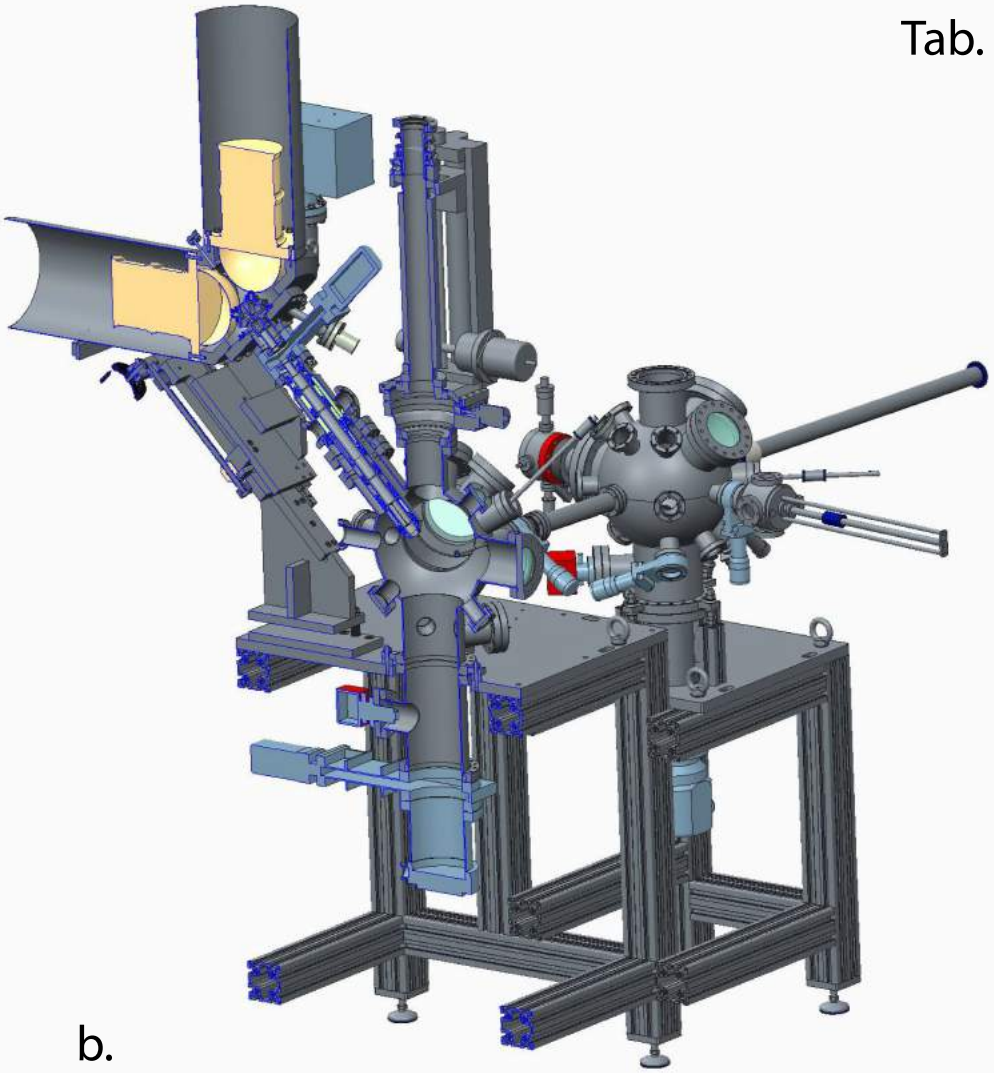

b.

Tab. 2

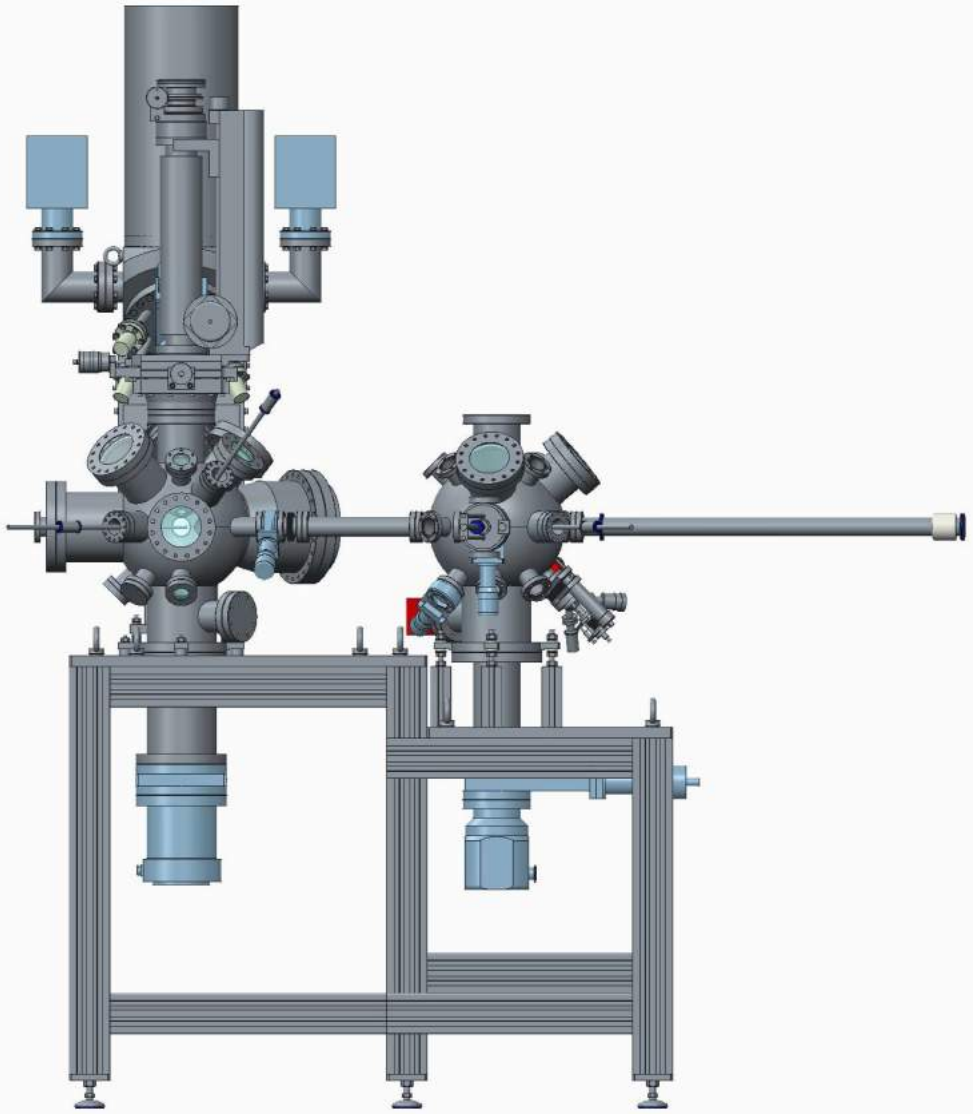

a.

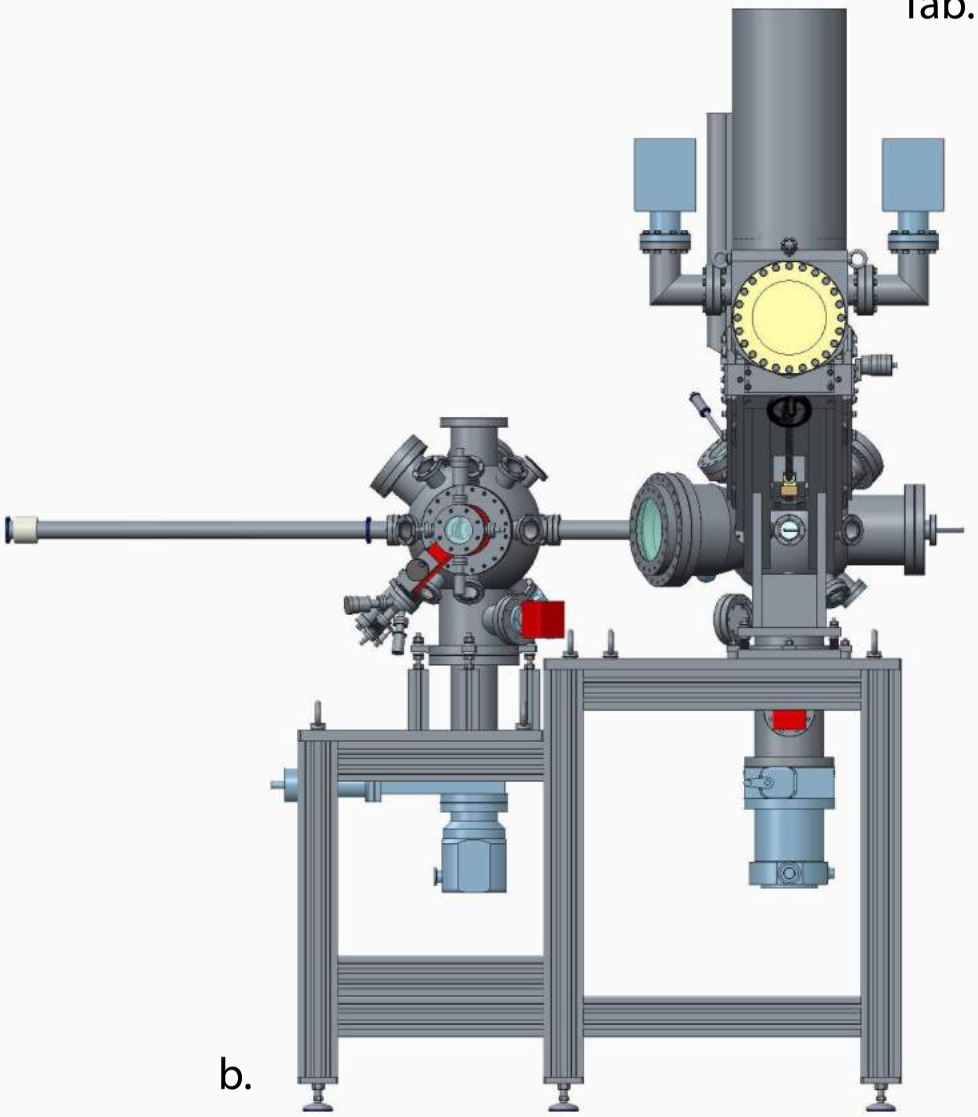

b.

Tab. 3

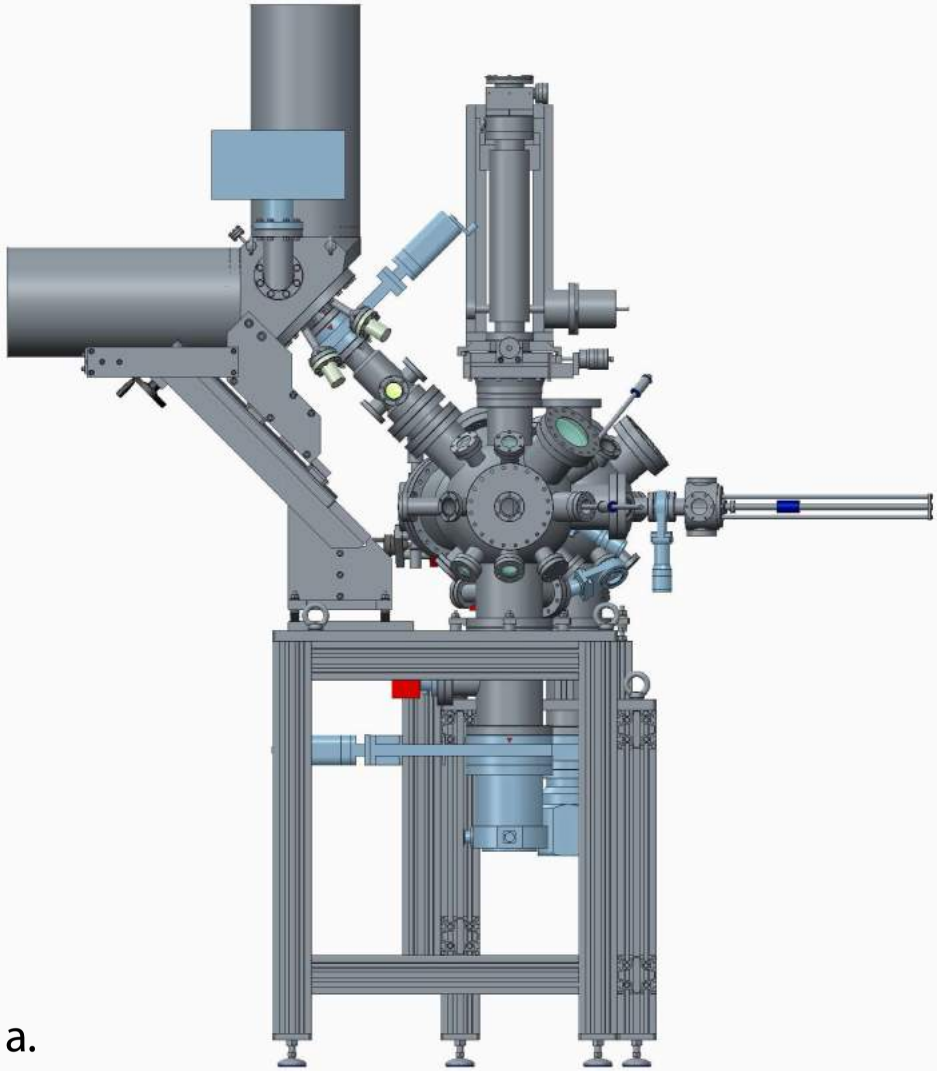

a.

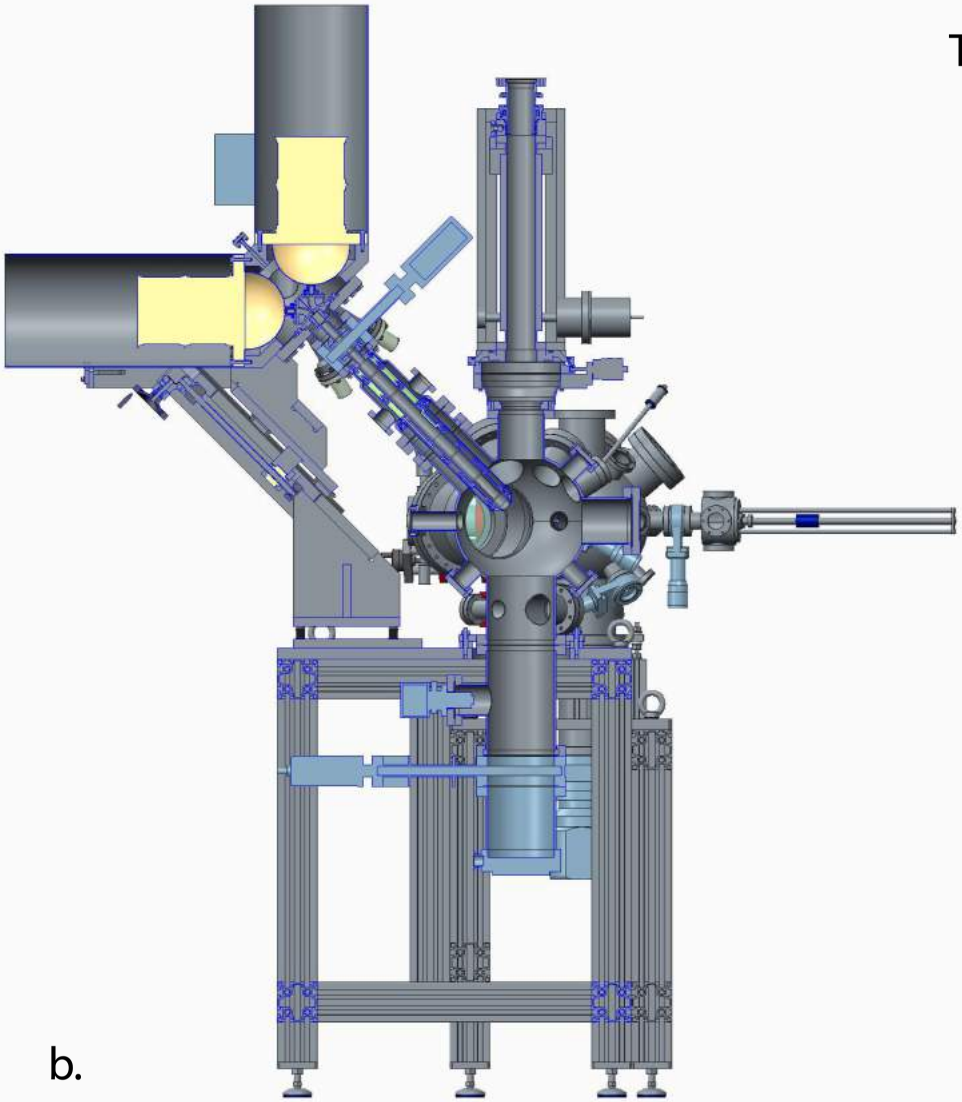

b.

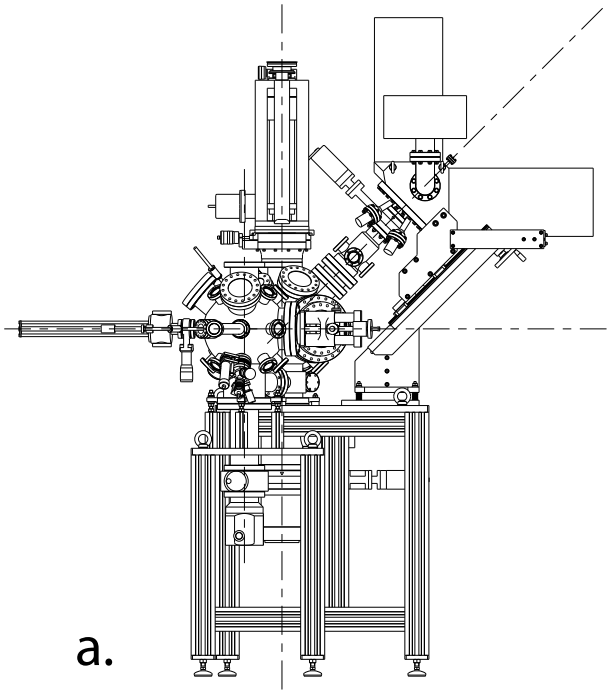

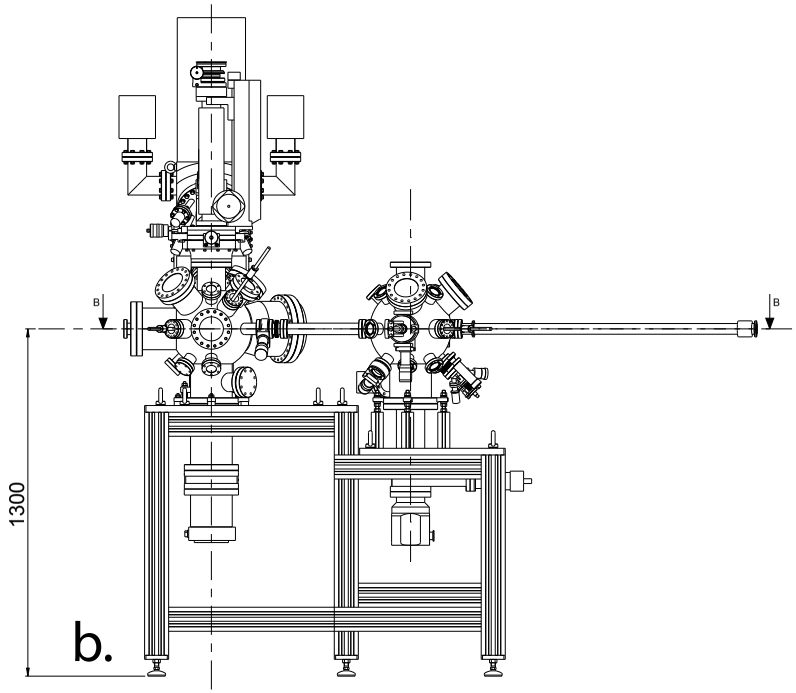

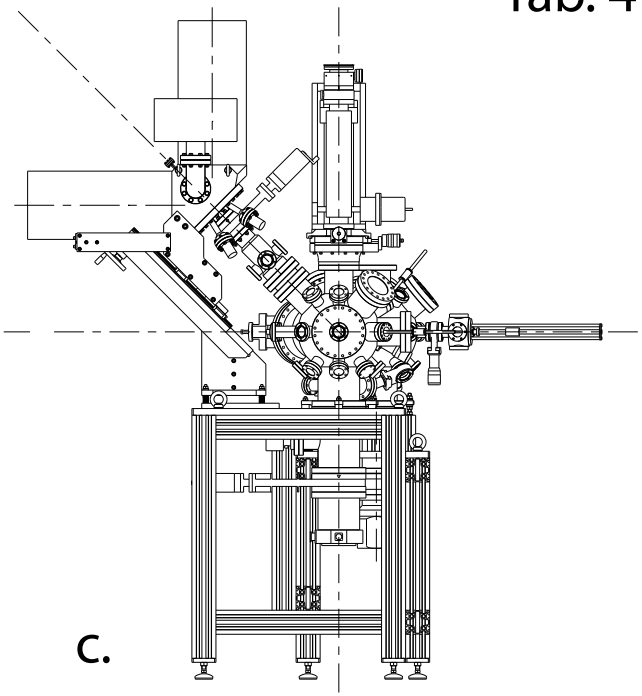

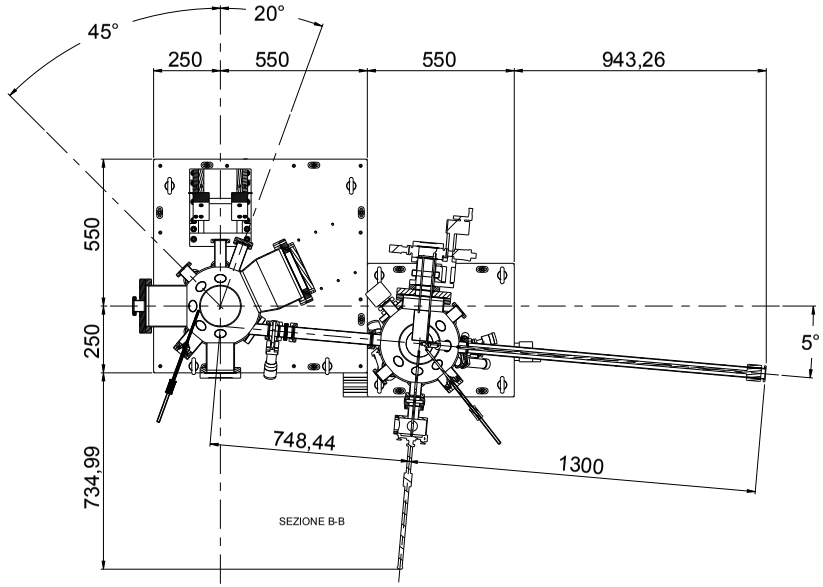

Tab. 4

General Tolerance / Tolleranza generale: UNI EN 22768/1 - M									⏥	0.4
Lenght and Diam. Lungh. e Diam.	0.00 6.00	6.00 30.0	30.0 120	120 315	315 1000	1000 2000	2000 4000	> 4000	○	0.4
								Angles Angoli	◎	0.25
Tolerance	±0.1	±0.2	±0.3	±0.5	±0.8	±1.2	±2.0	±3.0	—	0.2/100
PROG.	A. DE LUISA							±0.5°	//	0.2/100
MODEL.	A. DE LUISA								⊥	0.2/100
DIS.	A. DE LUISA						28-Nov-2013			

Not dim. Fillets Raggi non quotati	Not dim. Chamfers Smussi non quotati	Draft Angles Sformi gen.
R=1	0.5x45°	
REMOVE ALL PUNCHING BURRS AFTER MACHINING. ELIMINARE BAVE E SPIGOLI TAGLIENTI.		Gen. roughness Rugosita' gen. Ra 3.2

CNR - IOM

LABORATORIO TASC

MATERIALE

TRATTAMENTO

ULTRASPIN SYSTEM MAIN ASSEMBLY

A1

SCALA 1:10

Nr. DISEGNO 12260000

FOGLIO 1 DI 1

Pro/ENGINEER

Tab. 5

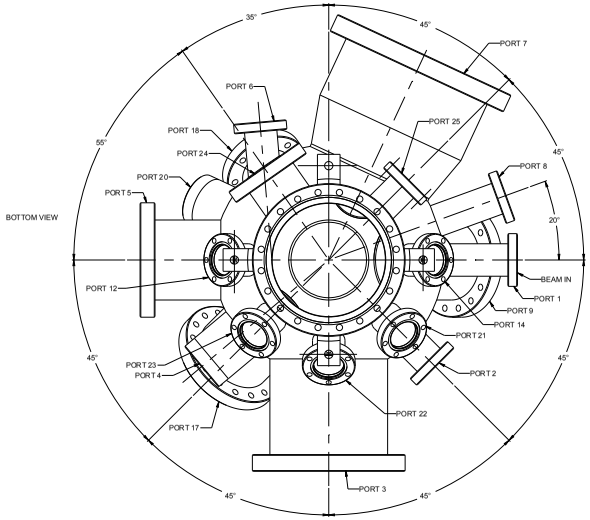

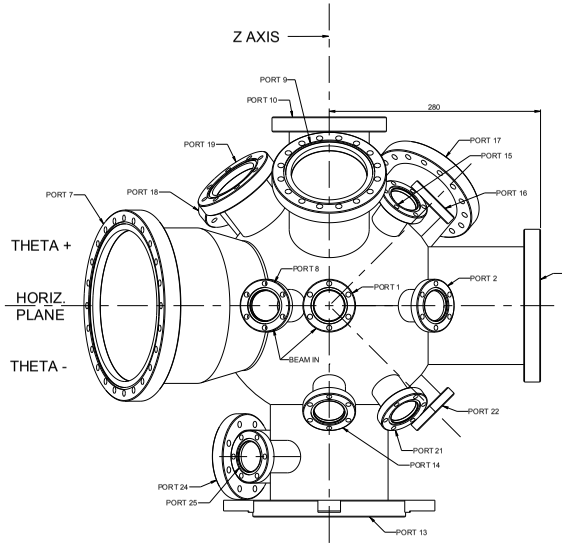

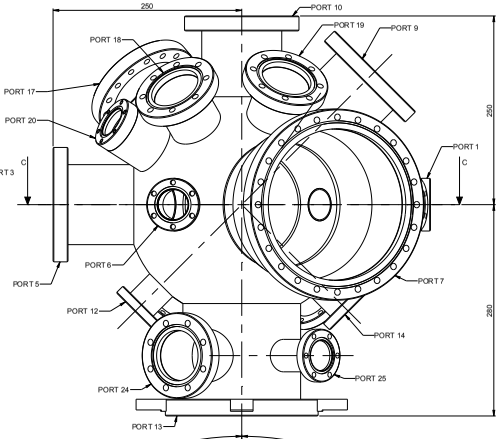

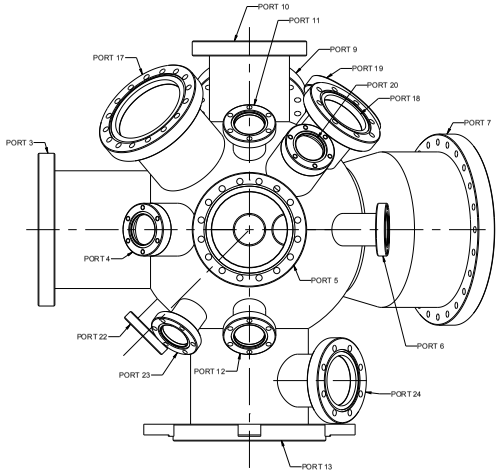

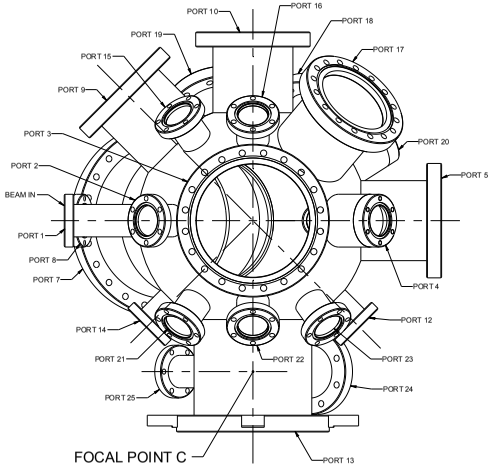

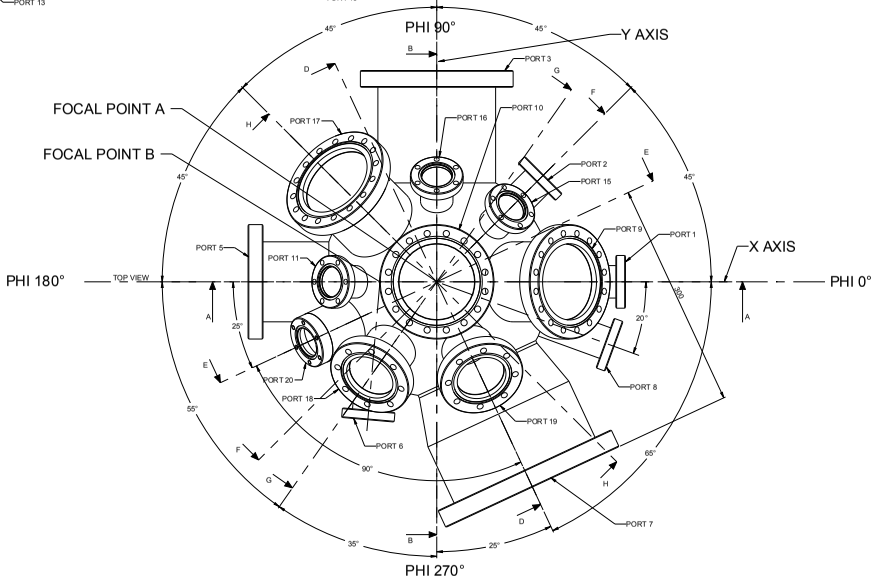

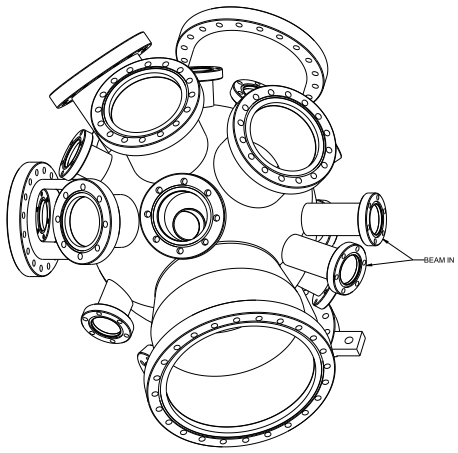

SCALA 2:5

NOTES:

- ALL FLANGES ARE EUROPEAN STYLE CF FLANGES.
- ALL TAPPED FLANGES HAVE METRIC THREAD.

P.OR.	N. DISEGNO	DENOMINAZIONE	Q.TA'	MATERIALE
23		CF 200 FIXED TUBE 206	1	AISI 316 LN
22		CF 150 FIXED TUBE 156	2	AISI 316 LN
21		CF 100 FIXED TUBE 106	4	AISI 316 LN
20		CF 63 FIXED	3	AISI 316 LN
19		CF 40 ROTATABLE	2	AISI 316 LN
18		CF 40 FIXED	11	AISI 316 LN
17		CF 38 SPECIAL	2	AISI 316 LN
16	122 60105-16	TUBE Ø43x1.5	1	PERMALLOY
15	122 60105-15	TUBE Ø43x1.5	1	PERMALLOY
14	122 60105-14	TUBE Ø169x3	1	PERMALLOY
13	122 60105-13	TUBE Ø70x2	2	PERMALLOY
12	122 60105-12	TUBE Ø70x2	2	PERMALLOY
11	122 60105-11	PLATE	4	AISI 316 LN
10	122 60105-10	TUBE Ø43x1.5	9	PERMALLOY
9	122 60105-09	CONICAL SHAPED TUBE	1	PERMALLOY
8	122 60105-08	TUBE Ø70x2	1	PERMALLOY
7	122 60105-07	TUBE Ø169x3	2	PERMALLOY
6	122 60105-06	TUBE Ø43x1.5	2	PERMALLOY
5	122 60105-05	TUBE Ø169x3	1	PERMALLOY
4	122 60105-04	TUBE Ø169x3	1	PERMALLOY
3	122 60105-03	TUBE Ø169x3	1	PERMALLOY
2	122 60105-02	LOWER HALF SPHERE	1	PERMALLOY
1	122 60105-01	UPPER HALF SPHERE	1	PERMALLOY

General Tolerance / Tolleranza generale, UNI EN 22768/1 - M

Lunghezze/Quote	0.5	6	30	120	315	1000	2000	4000	8000
Lunghi e Diam.	6	30	120	315	1000	2000	4000	8000	Angoli
Tolleranze	±0.1	±0.2	±0.3	±0.5	±0.8	±1.2	±2.0	±3.0	±0.5°

Not dim. Fillets Raggi non quotati	0.4	Angles
	0.25	
Not dim. Chamfers Smussi non quotati	R= 1	0.5x45°
Draft Angles Sformi pen.		

	0.2 100	REMOVE ALL PUNCHING BURRS AFTER MACHINING.
	0.2 100	ELIMINARE BAVE E SPIGOLI TAGLIENTI.
Surface finish Rugosità		Ra 3.2

PROG.	A. DE LUISA		
MODEL	A. DE LUISA		
DIS.	A. DE LUISA	Jan-30-2013	

CNR - IOM

LABORATORIO TASC

MATERIALE: PERMALLOY ULTRASPIN UHV CHAMBER

TRATTAMENTO

FORMATO	SCALA	N. DISEGNO	FOGLIO
A0	2:5	12260105	1 di 2

PROPRIETÀ

Appendix C

Acknowledgements

With a wide open country in my eyes
And these romantic dreams in my head
Once we made a promise we swore
we'd always remember
No retreat, baby, no surrender
Blood brothers in a stormy night
With a vow to defend
No retreat, baby, no surrender
- B. Springsteen, No Surrender, 1984

Many people have helped me in the realization of this work, and I wish to acknowledge them dearly and deeply.

I wish to express all my gratitude to Prof. Sergio Valeri, my thesis supervisor, who took the burden of reading and commenting my dissertation, despite the numerous and challenging tasks that day by day he has to endure in order to guarantee the excellence of research in the department of Physics, Informatics and Mathematics of the University of Modena.

I cannot overstate my debt of gratitude towards Prof. Giorgio Rossi, the coordinator of the APE group, that despite the numerous responsibilities and assignments, managed to pay continuous attention to my work, offering illuminating advice during the phases of experimental work and attentively reviewing every single chapter in my thesis.

I want to thank Dr. Giancarlo Panaccione, the senior scientist of the beamline, who directly organized my work in the ULTRASPIN project. I will remember our heartfelt conversations and his recommendations for the present and the future. He taught me that research is a bet on the future results and that the higher are the expectations, the bigger is the risk. Despite this sober reality, he showed me the importance of setting several anchor points on which to build each successive step.

I am also deeply indebted to Prof. Vladimir N. Petrov, one of the leading world experts in Mott detectors. His fatherly figure supported me during the development of my thesis project, friendly passing on to me his knowledge and experience and bringing with him a peaceful atmosphere and his deep human warmth.

It was a privilege to be a part of the APE beamline team and to enjoy the company of each of its members: Dr. Ivana Vobornik, Dr. Emilia Annese and Dr. Damjian Krizmancic were always available and helpful, generously answering my questions and letting me share their experience. Dr. Piero Torelli was always attentive to my situation and explained me some of the hidden dynamics in the future of an italian scientist that I would never have guessed. Dr. Jun Fuji with his serene equilibrium and deep technical knowledge was an irreplaceable support in the most difficult situations. I would like to thank Dr. Benoît Goubaut for his friendly company in the long laboratory hours and outside of the synchrotron.

I want also to express my gratitude towards the group of University of Regensburg under the coordination of Prof. Christian Back, that hosted us in their laboratories, giving us the possibility of obtaining new and interesting results. I want to especially acknowledge Dr. Stefan Günther, who not only set his laboratory at our disposal, performed the measurements with us and helped us to give a first interpretation of the data, but also was our guide in the exploration of the city of Regensburg, being the perfect host from every point of view.

I would like to thank Dr. Carlo Spezzani, that allowed me to participate to its work, and to see the operation of a HHG beamline, gently explaining every step of the procedures.

I am thankful to the team of the Laboratory for Instrumentation and Detector of Sincrotrone Elettra, under the coordination of Dott. Giuseppe Cautero, that involved me in the development of the new electronics, gently explaining and discussing every detail of their work and allowing me to be an active part of the development.

Vorrei ringraziare la Dott.ssa Roberta Ciprian, per avermi fatto scoprire un mondo. È riuscita, stando al mio fianco, ad insegnarmi cosa significa lavorare indipendentemente, cercando di fornire il proprio contributo al procedere dell'attività del gruppo. Mi ha guidato nello sviluppo del progetto di questa tesi, avvertendomi in anticipo di quali sarebbero stati gli scogli più ardui e condividendo con me le fatiche e le difficoltà. Senza di lei, questa tesi non avrebbe assunto il respiro che ora possiede.

Vorrei ringraziare i miei amici e compagni di studi, nell'occasione di questo ciclo che sta per concludersi. Federico, con cui lo scambio di pensieri e di riflessioni scientifiche è sempre stato vivissimo, privo di orari, e tale da dare un contributo significativo a questa tesi. Ma quello che è più importante è l'affetto e l'amicizia di cui lui, i Franceschi, Gianmarco, Giulio e Giacomo mi hanno circondato in tutti questi anni.

Va ai miei genitori tutta la mia gratitudine, per avermi sostenuto in tutti i modi possibili, consentendomi la meravigliosa opportunità di scegliere il mio futuro. È stato fondamentale il fatto che abbiano incoraggiato le mie aspirazioni fino quasi ad essere delusi quando tentavo di "riportare i piedi per terra". Forse mio fratello Francesco non lo sa, ma anche lui è stato fondamentale, perchè anche lui è fra le persone il pensiero delle quali mi dà forza e serenità nell'affrontare le situazioni difficili e faticose.

Da ultimo, non esistono parole che possano esprimere la mia gratitudine per Caterina. La sua forza e la sua dolcezza sono ogni giorno sorprendenti e mi permettono di guardare al futuro con serenità. I momenti della mia trasferta triestina che ho condiviso con lei sono stati più gioiosi, sereni e facili. È soprattutto merito suo se quella che ho vissuto e sto vivendo è un'esperienza meravigliosa.

Bibliography

[1] H. Hertz. Ueber einen einfluss des ultravioletten lichtes auf die electrische entladung. *Annalen der Physik*, 267(8):983–1000, 1887.

[2] A. Einstein. Über einen die erzeugung und verwandlung des lichtes betreffenden heuristischen gesichtspunkt. *Annalen der Physik*, 322(6):132–148, 1905.

[3] C. M. Jozwiak. *A New Spin on Photoemission Spectroscopy*. PhD thesis, University of California, Berkeley, 2008.

[4] Peter D Johnson. Spin-polarized photoemission. *Reports on Progress in Physics*, 60(11):1217, 1997.

[5] L. Plucinski and C.M. Schneider. The electronic structure of spintronic materials as seen by spin-polarized angle-resolved photoemission. *Journal of Electron Spectroscopy and Related Phenomena*, 189(0):137 – 145, 2013.

[6] Igor Žutić, Jaroslav Fabian, and S. Das Sarma. Spintronics: Fundamentals and applications. *Rev. Mod. Phys.*, 76:323–410, Apr 2004.

[7] C.S. Fadley. X-ray photoelectron spectroscopy: Progress and perspectives. *Journal of Electron Spectroscopy and Related Phenomena*, 178–179(0):2 – 32, 2010. Trends in X-ray Photoelectron Spectroscopy of solids (theory, techniques and applications).

[8] Andrea Damascelli. Probing the electronic structure of complex systems by arpes. *Physica Scripta*, 2004(T109):61, 2004.

[9] M. Hoesch, T. Greber, V.N. Petrov, M. Muntwiler, M. Hengsberger, W. Auwärter, and J. Osterwalder. Spin-polarized fermi surface mapping. *Journal of Electron Spectroscopy and Related Phenomena*, 124(2–3):263 – 279, 2002. Frontiers in photoemission spectroscopy of solids and surfaces.

[10] J. H. Dil. Spin and angle resolved photoemission on non-magnetic low-dimensional systems. *Journal of Physics: Condensed Matter*, 21(40):403001, 2009.

[11] G. Rossi. Spin polarization of the photoelectrons and photon polarization of x-ray absorption: Spectroscopy and magnetometry. In Boscherini Federico Meneghini Carlo Mobilio, Settimio, editor, *Synchrotron Radiation*. Springer-Verlag Berlin Heidelberg GmbH, 2015.

[12] J. Stöhr and H.C. Siegmann. *Magnetism: From Fundamentals to Nanoscale Dynamics*. Springer Series in Solid-State Sciences. Springer, 2006.

[13] A.C. Thompson. *X-ray data booklet*. University of Berkeley, 2001.

[14] AL Cavalieri, Norbert Müller, Th Uphues, VS Yakovlev, Andrius Baltuška, B Horvath, B Schmidt, L Blümel, R Holzwarth, S Hendel, et al. Attosecond spectroscopy in condensed matter. *Nature*, 449(7165):1029–1032, 2007.

[15] Martin Schultze, M Fieß, N Karpowicz, Justin Gagnon, M Korbman, M Hofstetter, S Neppl, AL Cavalieri, Yannis Komninos, Th Mercouris, et al. Delay in photoemission. *Science*, 328(5986):1658–1662, 2010.

[16] A McPherson, G Gibson, H Jara, U Johann, Ting S Luk, IA McIntyre, Keith Boyer, and Charles K Rhodes. Studies of multiphoton production of vacuum-ultraviolet radiation in the rare gases. *JOSA B*, 4(4):595–601, 1987.

[17] Tenio Popmintchev, Ming-Chang Chen, Paul Arpin, Margaret M Murnane, and Henry C Kapteyn. The attosecond nonlinear optics of bright coherent x-ray generation. *Nature Photonics*, 4(12):822–832, 2010.

[18] C Grazioli, C Callegari, A Ciavardini, M Coreno, F Frassetto, D Gauthier, D Golob, R Ivanov, A Kivimäki, B Mahieu, et al. Citius: An infrared-extreme ultraviolet light source for fundamental and applied ultrafast science. *Review of Scientific Instruments*, 85(2):023104, 2014.

[19] C Hernández-García, JA Pérez-Hernández, T Popmintchev, MM Murnane, HC Kapteyn, A Jaron-Becker, A Becker, and L Plaja. Zeptosecond high harmonic kev x-ray waveforms driven by midinfrared laser pulses. *Physical review letters*, 111(3):033002, 2013.

[20] John MJ Madey. Stimulated emission of bremsstrahlung in a periodic magnetic field. *Journal of Applied Physics*, 42(5):1906–1913, 1971.

[21] Luis R Elias, William M Fairbank, John MJ Madey, H Alan Schwettman, and Todd I Smith. Observation of stimulated emission of radiation by relativistic electrons in a spatially periodic transverse magnetic field. *Physical Review Letters*, 36(13):717, 1976.

[22] Brian WJ McNeil and Neil R Thompson. X-ray free-electron lasers. *Nature photonics*, 4(12):814–821, 2010.

[23] E Allaria, Roberto Appio, L Badano, WA Barletta, S Bassanese, SG Biedron, A Borga, E Busetto, D Castronovo, P Cinquegrana, et al. Highly coherent and stable pulses from the fermi seeded free-electron laser in the extreme ultraviolet. *Nature Photonics*, 6(10):699–704, 2012.

[24] Patrick S Kirchmann, Laurenz Rettig, Dhananjay Nandi, Uwe Lipowski, Martin Wolf, and Uwe Bovensiepen. A time-of-flight spectrometer for angle-resolved detection of low energy electrons in two dimensions. *Applied Physics A*, 91(2):211–217, 2008.

[25] E Beaurepaire, J-C Merle, A Daunois, and J-Y Bigot. Ultrafast spin dynamics in ferromagnetic nickel. *Physical Review Letters*, 76(22):4250, 1996.

[26] CD Stanciu, F Hansteen, AV Kimel, A Kirilyuk, A Tsukamoto, A Itoh, and Th Rasing. All-optical magnetic recording with circularly polarized light. *Physical review letters*, 99(4):047601, 2007.

[27] A Scholl, L Baumgarten, R Jacquemin, and W Eberhardt. Ultrafast spin dynamics of ferromagnetic thin films observed by fs spin-resolved two-photon photoemission. *Physical review letters*, 79(25):5146, 1997.

[28] Robert Carley, Kristian Döbrich, Björn Frietsch, Cornelius Gahl, Martin Teichmann, Olaf Schwarzkopf, Philippe Wernet, and Martin Weinelt. Femtosecond laser excitation drives ferromagnetic gadolinium out of magnetic equilibrium. *Physical review letters*, 109(5):057401, 2012.

[29] A. Messiah. *Quantum Mechanics*. Dover Publications, 1999.

[30] N.W. Ashcroft and N.D. Mermin. *Solid state physics*. Saunders College, 1976.

[31] M. Born. *My life: recollections of a Nobel laureate*. Scribner, 1978.

[32] Walther Gerlach and Otto Stern. Das magnetische moment des silberatoms. *Zeitschrift für Physik A Hadrons and Nuclei*, 9(1):353–355, 1922.

[33] GE Uhlenbeck and S Goudsmit. Naturwiss. 13, 953 (1925). *Nature*, 117:264, 1926.

[34] George E Uhlenbeck and Samuel Goudsmit. Spinning electrons and the structure of spectra. *Nature*, 117:264–265, 1926.

[35] Louis De Broglie. *Recherches sur la théorie des quanta*. PhD thesis, Migration-université en cours d'affectation, 1924.

[36] FHL Koppens, Christo Buizert, Klaas-Jan Tielrooij, IT Vink, KC Nowack, Tristan Meunier, LP Kouwenhoven, and LMK Vandersypen. Driven coherent oscillations of a single electron spin in a quantum dot. *Nature*, 442(7104):766–771, 2006.

[37] *Polarized electrons*. Springer-Verlag Berlin Heidelberg GmbH, 1985.

[38] N. F. Mott. The scattering of fast electrons by atomic nuclei. *Proceedings of the Royal Society of London. Series A*, 124(794):425–442, 1929.

[39] V.B. Berestetskii, L.P. Pitaevskii, and E.M. Lifshitz. *Quantum Electrodynamics*. Number v. 4. Elsevier Science, 1996.

[40] T. J. Gay and F. B. Dunning. Mott electron polarimetry. *Review of Scientific Instruments*, 63(2), 1992.

[41] C. G. Shull, C. T. Chase, and F. E. Myers. Electron polarization. *Phys. Rev.*, 63:29–37, Jan 1943.

[42] J Kessler. Electron spin polarization by low-energy scattering from unpolarized targets. *Reviews of Modern Physics*, 41(1):3, 1969.

[43] R Feder and J g. Spin-polarized low-energy electron diffraction: Theory, experiment and analysis of results from w (001)(1x1). *Surface Science*, 103(1):75–102, 1981.

[44] J. Sawler and D. Venus. Effects of hydrogen adsorption on the performance of the w(001) spin polarized low energy electron diffraction electron polarimeter. *Journal of Vacuum Science and Technology A*, 10(2), 1992.

[45] Dehong Yu, Christian Math, Matthias Meier, Matthias Escher, Georgi Rangelov, and Markus Donath. Characterisation and application of a spleed-based spin polarisation analyser. *Surface Science*, 601(24):5803 – 5808, 2007. Wagga Symposium on Surfaces and Interfaces - 2006 Wagga Symposium on Surfaces and Interfaces - 2006.

[46] D. Tillmann, R. Thiel, and E. Kisker. Very-low-energy spin-polarized electron diffraction from fe(001). *Zeitschrift für Physik B Condensed Matter*, 77(1):1–2, 1989.

[47] F. U. Hillebrecht, R. Jungblut, and E. Kisker. Spin polarization of the metallic fe 3s photoemission spectrum. *Phys. Rev. Lett.*, 65:2450–2453, Nov 1990.

[48] R. Jungblut, Ch. Roth, F.U. Hillebrecht, and E. Kisker. Spin-polarized electron spectroscopy as a combined chemical and magnetic probe. *Surface Science*, 269–270(0):615 – 621, 1992.

[49] Riccardo Bertacco and Franco Ciccacci. Large spin asymmetry in electron absorption and reflection from oxidized single crystal fe/mgo (001) films. *Surface science*, 419(2):265–271, 1999.

[50] V. N. Petrov, V. V. Grebenshikov, B. D. Grachev, and A. S. Kamochkin. New compact classical 40 kv mott polarimeter. *Review of Scientific Instruments*, 74(3), 2003.

[51] M. Getzlaff, B. Heidemann, J. Bansmann, C. Westphal, and G. Schönhense. A variable-angle electron spin polarization detection system. *Review of Scientific Instruments*, 69(11), 1998.

[52] A. Gellrich and J. Kessler. Precision measurement of the sherman asymmetry function for electron scattering from gold. *Phys. Rev. A*, 43:204–216, Jan 1991.

[53] J. Kemmer. Fabrication of low noise silicon radiation detectors by the planar process. *Nuclear Instruments and Methods*, 169(3):499 – 502, 1980.

[54] H.A. Rijken, S.S. Klein, W. Jacobs, L.J.H.G.W. Teeuwen, M.J.A. de Voigt, and P. Burger. Subnanosecond timing with ion-implanted detectors. *Nuclear Instruments and Methods in Physics Research Section B: Beam Interactions with Materials and Atoms*, 64(1–4):272 – 276, 1992.

[55] V. N. Petrov, V. V. Grebenshikov, A. N. Andronov, P. G. Gabdullin, and A. V. Maslevtcov. Ultrafast compact classical mott polarimeter. *Review of Scientific Instruments*, 78(2):–, 2007.

[56] Vladimir N Petrov, Alexander B Ustinov, Daria V Petrova, and Andrey A Grib. Investigation of the physical properties of entangled electron spin states in a solid. *physica status solidi (c)*, 11(5-6):1068–1073, 2014.

[57] A. Weber. *Ultrafast Spindynamics in Ferromagnetic Thin Films*. PhD thesis, Fakultät für Physik der Universität Regensburg, 2010.

[58] A Fognini, TU Michlmayr, G Salvatella, C Wetli, U Ramsperger, T Bähler, F Sorgenfrei, M Beye, A Eschenlohr, N Pontius, et al. Ultrafast reduction of the total magnetization in iron. *Applied Physics Letters*, 104(3):032402, 2014.

[59] G. C. Burnett, T. J. Monroe, and F. B. Dunning. High efficiency retarding potential mott polarization analyzer. *Review of Scientific Instruments*, 65(6), 1994.

[60] V. N. Petrov, M. S. Galaktionov, and A. S. Kamochkin. Comparative tests of conventional and retarding-potential mott polarimeters. *Review of Scientific Instruments*, 72(9), 2001.

[61] J. C. Lancaster, F. J. Kontur, G. K. Walters, and F. B. Dunning. Source of potential systematic error in retarding-potential mott polarimeters. *Review of Scientific Instruments*, 70(7), 1999.

[62] S. Souma, A. Takayama, K. Sugawara, T. Sato, and T. Takahashi. Ultrahigh-resolution spin-resolved photoemission spectrometer with a mini mott detector. *Review of Scientific Instruments*, 81(9):–, 2010.

[63] L. Moreschini, G. Ghiringhelli, K. Larsson, U. Veit, and N. B. Brookes. A time-of-flight–mott apparatus for soft x-ray spin resolved photoemission on solid samples. *Review of Scientific Instruments*, 79(3):–, 2008.

[64] Christian Tusche, Martin Ellguth, Alexander Krasyuk, Aimo Winkelmann, Dmytro Kutnyakhov, Pavel Lushchyk, Katerina Medjanik, Gerd Schönhense, and Jürgen Kirschner. Quantitative spin polarization analysis in photoelectron emission microscopy with an imaging spin filter. *Ultramicroscopy*, 130(0):70 – 76, 2013. Eighth International Workshop on LEEM/PEEM.

[65] D. Kutnyakhov, P. Lushchyk, A. Fognini, D. Perriard, M. Kolbe, K. Medjanik, E. Fedchenko, S.A. Nepijko, H.J. Elmers, G. Salvatella, C. Stieger, R. Gort, T. Bähler, T. Michlmayer, Y. Acremann, A. Vaterlaus, F. Giebels, H. Gollisch, R. Feder, C. Tusche, A. Krasyuk, J. Kirschner, and G. Schönhense. Imaging spin filter for electrons based on specular reflection from iridium (001). *Ultramicroscopy*, 130(0):63 – 69, 2013. Eighth International Workshop on LEEM/PEEM.

[66] J Kirschner, F Giebels, H Gollisch, and R Feder. Spin-polarized electron scattering from pseudomorphic au on ir (001). *Physical Review B*, 88(12):125419, 2013.

[67] A. Winkelmann, D. Hartung, H. Engelhard, C.-T. Chiang, and J. Kirschner. High efficiency electron spin polarization analyzer based on exchange scattering at fe/w(001). *Review of Scientific Instruments*, 79(8):–, 2008.

[68] Taichi Okuda, Koji Miyamaoto, Hirokazu Miyahara, Kenta Kuroda, Akio Kimura, Hirofumi Namatame, and Masaki Taniguchi. Efficient spin resolved spectroscopy observation machine at hiroshima synchrotron radiation center. *Review of Scientific Instruments*, 82(10):–, 2011.

[69] A Tange, CL Gao, B Yu Yavorsky, IV Maznichenko, C Etz, A Ernst, W Hergert, I Mertig, W Wulfhekel, and J Kirschner. Electronic structure and spin polarization of the fe (001)-p (1× 1) o surface. *Physical Review B*, 81(19):195410, 2010.

[70] R. Bertacco, M. Marcon, G. Trezzi, L. Duò, and F. Ciccacci. Spin and energy analysis of electron beams: Coupling a polarimeter based on exchange scattering to a hemispherical analyzer. *Review of Scientific Instruments*, 73(11), 2002.

[71] J. Graf, C. Jozwiak, A. K. Schmid, Z. Hussain, and A. Lanzara. Mapping the spin-dependent electron reflectivity of fe and co ferromagnetic thin films. *Phys. Rev. B*, 71:144429, Apr 2005.

[72] K. Gotlieb, Z. Hussain, A. Bostwick, A. Lanzara, and C. Jozwiak. Rapid high-resolution spin- and angle-resolved photoemission spectroscopy with pulsed laser source and time-of-flight spectrometer. *Review of Scientific Instruments*, 84(9):–, 2013.

[73] David A Dahl. Simion for the personal computer in reflection. *International Journal of Mass Spectrometry*, 200(1):3–25, 2000.

[74] M. Medici. Vectorial mott polarimetry with synchrotron radiation for the study of the magnetic properties of surfaces and ultrathin films. Master's thesis, Università di Modena e Reggio Emilia, 2011.

[75] M. Venier. Progetto e sviluppo dell'elettronica di acquisizione per esperimenti di fotoemissione risolti in spin per macchine di luce di terza e quarta generazione. Master's thesis, Università degli studi di Trieste, 2013.

[76] O Paul, S Toscano, K Totland, and M Landolt. The spatial origin of the spin-polarization of secondary-electron emission from fe. *Surface Science*, 251:27–30, 1991.

[77] Giselher Herzer. Modern soft magnets: amorphous and nanocrystalline materials. *Acta Materialia*, 61(3):718–734, 2013.

[78] B.D. Cullity and C.D. Graham. *Introduction to Magnetic Materials*. Wiley, 2011.

[79] Timothy J Gay, MA Khakoo, JA Brand, JE Furst, WV Meyer, WMKP Wijayaratna, and FB Dunning. Extrapolation procedures in mott electron polarimetry. *Review of scientific instruments*, 63(1):114–130, 1992.

[80] ZQ Qiu and SD Bader. Surface magneto-optic kerr effect. *Review of Scientific Instruments*, 71(3):1243–1255, 2000.

[81] Federico Pressacco. *Magnetization Dynamics across the First Order Phase Transition in FeRh Thin Films*. PhD thesis, Universitat Regensburg, 2014.

[82] G. Panaccione, I. Vobornik, J. Fujii, D. Krizmancic, E. Annese, L. Giovanelli, F. Maccherozzi, F. Salvador, A. De Luisa, D. Benedetti, A. Gruden, P. Bertoch, F. Polack, D. Cocco, G. Sostero, B. Diviacco, M. Hochstrasser, U. Maier, D. Pescia, C. H. Back, T. Greber, J. Osterwalder, M. Galaktionov, M. Sancrotti, and G. Rossi. Advanced photoelectric effect experiment beamline at elettra: A surface science laboratory coupled with synchrotron radiation. *Review of Scientific Instruments*, 80(4):–, 2009.

[83] SS Parihar, HL Meyerheim, K Mohseni, S Ostanin, A Ernst, N Jedrecy, R Felici, and J Kirschner. Structure of o/fe (001)-p (1x1) studied by surface x-ray diffraction. *Physical Review B*, 81(7):075428, 2010.

[84] Christian Eibl, Anke B Schmidt, and Markus Donath. Appearance of the minority d z 2 surface state and disappearance of the image-potential state: Criteria for clean fe (001). *Physical Review B*, 86(16):161414, 2012.

[85] A Cattoni, D Petti, S Brivio, M Cantoni, R Bertacco, and F Ciccacci. Mgo/fe (001) and mgo/fe (001)-p (1× 1) o interfaces for magnetic tunnel junctions: A comparative study. *Physical Review B*, 80(10):104437, 2009.

[86] A Di Bona, C Giovanardi, and S Valeri. Growth and structure of fe on mgo (001) studied by modulated electron emission. *Surface science*, 498(1):193–201, 2002.

[87] Werner Smekal, Wolfgang S. M. Werner, and Cedric J. Powell. Simulation of electron spectra for surface analysis (sessa): a novel software tool for quantitative auger-electron spectroscopy and x-ray photoelectron spectroscopy. *Surface and Interface Analysis*, 37(11):1059–1067, 2005.

[88] JMD Coey and CL Chien. Half-metallic ferromagnetic oxides. *Mrs Bulletin*, 28(10):720–724, 2003.

[89] E. Dagotto. *Nanoscale Phase Separation and Colossal Magnetoresistance: The Physics of Manganites and Related Compounds*. Springer Series in Solid-State Sciences. Springer, 2003.

[90] J-H Park, E Vescovo, H-J Kim, C Kwon, R Ramesh, and T Venkatesan. Direct evidence for a half-metallic ferromagnet. *Nature*, 392(6678):794–796, 1998.

[91] Paolo Perna, Carlos Rodrigo, E Jiménez, Francisco Jose Teran, N Mikuszeit, Laurence Méchin, Julio Camarero, and R Miranda. Tailoring magnetic anisotropy in epitaxial half metallic la0. 7sr0. 3mno3 thin films. *Journal of Applied Physics*, 110(1):013919, 2011.

[92] Georg M Müller, Jakob Walowski, Marija Djordjevic, Gou-Xing Miao, Arunava Gupta, Ana V Ramos, Kai Gehrke, Vasily Moshnyaga, Konrad Samwer, Jan Schmalhorst, et al. Spin polarization in half-metals probed by femtosecond spin excitation. *Nature materials*, 8(1):56–61, 2008.

[93] Michel P de Jong, I Bergenti, VA Dediu, Mats Fahlman, M Marsi, and C Taliani. Evidence for mn 2+ ions at surfaces of la 0.7 sr 0.3 mn o 3 thin films. *Physical Review B*, 71(1):014434, 2005.

[94] YH Ren, M Trigo, R Merlin, Venimadhav Adyam, and Qi Li. Generation and detection of coherent longitudinal acoustic phonons in the la0. 67sr0. 33mno3 thin films by femtosecond light pulses. *Applied physics letters*, 90(25):251918, 2007.

[95] André Bojahr, Marc Herzog, Daniel Schick, Ionela Vrejoiu, and Matias Bargheer. Calibrated real-time detection of nonlinearly propagating strain waves. *Phys. Rev. B*, 86:144306, Oct 2012.

[96] MC Weber, B Hillebrands, V Moshnyaga, and K Samwer. Spin-lattice relaxation phenomena in manganite la0. 7sr0. 3mno3 thin films. *EPL (Europhysics Letters)*, 73(2):285, 2006.